

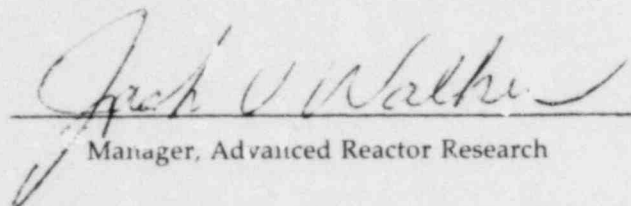
NUREG/CR-1594 (1 of 4)
SAND80-1646 (1 of 4)
Vol. 13
R-7

Advanced Reactor Safety Research Quarterly Report January-March 1980

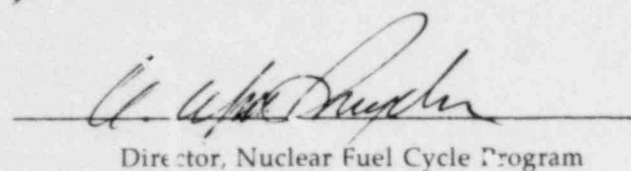
Advanced Reactor Research Department
Sandia National Laboratories
Albuquerque, NM 87185

Printed April 1980

APPROVED:



Manager, Advanced Reactor Research



Director, Nuclear Fuel Cycle Program

Sandia National Laboratories
Albuquerque, NM 87185
operated by
Sandia Corporation
for the
U. S. Department of Energy

Prepared for
Division of Reactor Safety Research
Office of Nuclear Regulatory Research
U. S. Nuclear Regulatory Commission
Washington, DC 20555
Under Memorandum of Understanding DOE 40-550-75
NRC FIN No. A-1016, -1172, -1180, -1186, -1054, -1181, -1032, -1058,
-1198, -1197

8107060054 810630
PDR NUREG
CR-1594 R
PDR

Foreword

Sandia Laboratories' Advanced Reactor Safety Research Program, initiated in FY 1975, is a comprehensive research activity conducted on behalf of the U. S. Nuclear Regulatory Commission (NRC) and is part of NRC's confirmatory research effort to assure that the necessary safety data and theoretical understanding exist to license and regulate the Liquid Metal Fast Breeder Reactor (LMFBR) or other advanced converters, breeders or advanced light water reactors which may be commercialized in the United States. The program includes a broad range of experiments to simulate accidental transient conditions to provide the required data base to understand the controlling accident sequences and to serve as a basis for verification of the complex computer simulation models and codes used in accident analysis and licensing reviews. Such a program must include the development of analytical models, verified by experiment, which can be used to predict reactor performance under a broad variety of abnormal conditions. Major program elements include studies of the coolability and containment of rubbleized cores to assure containment integrity. This work along with that of other U. S. and international researchers should provide the technology base on which licensing decisions can be made with confidence that the safety of the public is assured.

The early thrust of Sandia's program was designed to provide data associated with the hypothetical core disruptive accident, with emphasis on prompt burst (~ 1-ms period) energetics and the behavior of postaccident core debris. The scope of the program was expanded in FYs 1976 and 1977 to encompass other energetics and inherent retention concerns such as large-scale sodium containment and structural integrity; aerosol source studies; transition

phase energetics; fuel failure and motion; probabilistic accident delineation; and studies to quantify elevated temperature failure modes of critical component materials. A portion of the early effort in the program was directed toward obtaining data to support the licensing review of the Clinch River Breeder Reactor (CRBR) and the Fast Flux Test Facility (FFTF). Recently the emphasis has shifted toward applying advanced reactor safety technology to LWR Class 9 accident concerns which have been of considerable interest following the accident at TMI-2. For FY 1980, the program is organized in the following subtasks, progress on which is reported herein.

- Task 1 Energetics
 - Subtask 1.1 Prompt Burst Energetics
 - Subtask 1.2 Irradiated Fuels Response
- Task 2 Fuel Dynamics
 - Subtask 2.1 Transition Phase
 - Subtask 2.2 Initial and Extended Fuel Motion
 - Subtask 2.3 Fuel Motion Detection
- Task 3 Core Debris Behavior—Inherent Retention
 - Subtask 3.1 Molten Core Containment
 - Subtask 3.2 PAHR Debris Bed
 - Subtask 3.3 PAHR Molten Pool
 - Subtask 3.4 Fragmentation
 - Subtask 3.5 Sodium Containment and Structural Integrity
- Task 4 Aerosol Source Normalization
- Task 5 Containment Analysis
- Task 6 Elevated Temperature Design Assessment
- Task 7 LMFBR Accident Delineation
- Task 8 Test and Facility Technology

Contents

Foreword.....	5
Executive Summary.....	13
1. Energetics	27
1.1 Prompt Burst Energetics.....	27
1.2 Irradiated Fuels Response	33
2. Fuel Dynamics	57
2.1 Transition Phase	57
2.2 Initial and Extended Fuel Motion (IEFM).....	59
2.3 In-Core Fuel Motion Detection	68
3. Core Debris Behavior—Inherent Retention.....	73
3.1 Molten Core Containment.....	73
3.2 PAHR Debris Bed	85
3.3 PAHR Molten Pool	102
3.4 Fragmentation.....	108
3.5 Sodium Containment and Structural Integrity.....	110
4. Aerosol Source Normalization	125
4.1 Introduction	125
4.2 Aerosol Source Term During Sodium Concrete Interactions.....	125
5. Containment Analysis	133
5.1 Introduction	133
5.2 MAEROS, A Sectional Multispecies Model for Aerosol Dynamics.....	133
6. Elevated Temperature Design Assessment.....	147
6.1 Uniaxial Creep-Fatigue Behavior	147
6.2 Creep-Fatigue Damage Analysis	149
6.3 Structural Analysis	149
6.4 Structural Evaluation	149
7. LMFBR Accident Delineation.....	151
7.1 Engineered Safety Systems	151
7.2 Accident Phenomenology	151
7.3 Postaccident Phenomenology.....	153
8. Test and Facility Technology	155
8.1 ACRR Fuel Motion Detection System.....	155
8.2 ACRR Status	166

Illustrations

Figure

1.1-1	PBE-14S Reactor Power History	28
1.1-2	PBE-14S Bottom Pressure History	29
1.1-3	PBE-14S Top Pressure History	29
1.1-4	PBE-14S Piston Displacement History	29
1.1-5	X-Radiographs of PBE-14S	30
1.1-6	Film Growth Around UO_2 Particle in Sodium, Incompressible Model	34
1.1-7	UO_2 Wall Temperature, Incompressible Model.....	35
1.1-8	Film Growth Around UO_2 Particle in Sodium, Compressible Model	36
1.1-9	UO_2 Wall Temperature, Compressible Model	37
1.2-1	Pressure-Energy Relationships for Each of Five Versions of EOS.....	41

Illustrations (cont)

Figure

1.2-2	Spatial Mesh and Initial Fuel Configuration Used in Most of the Experiment Modeling	42
1.2-3	Energy Deposition Profile Used in Most of the Experiment Modeling	42
1.2-4	Normalized Energy Deposition Rate for Figure 1.2-3	43
1.2-5	Fuel Geometries Investigated in the Neutronics Calculations	43
1.2-6	Vapor Pressure Against the Transducer and Measured Pressure in EEOS-4	44
1.2-7	Results of a 5 x 5 Mesh Calculation	44
1.2-8	Results of C-6 and C-7 vs Specific Energy Deposited in the Sample	45
1.2-9	Cross Section of EEOS Pressure Cell	46
1.2-10	Relative Fission Density Profile vs Radius for Gold Occluder	46
1.2-11	Quantitative Estimates of Typical Fuel Pressure Sources	46
1.2-12	Pressure Sources Contributing to Measured p(E) Relation	49
1.2-13	Flow of Pressure Cell Components	52
1.2-14	Flow of Fuel and Loaded EOS Cell	53
1.2-15	Schematic Diagram of the Experimental Apparatus for Measuring the Dynamic Heat Capacity of UO ₂	55
1.2-16	Surface Temperature of a UO ₂ Sample Immediately Before, During, and After the Capacitor Discharge	56
2.1-1	Parameter Ranges Covered by ANL and French (Grenoble) Experiments on Fuel Freezing Together With Parameter Range of Planned Sandia Experiments	58
2.1-2	Fuel Velocity (V), Fuel Penetration Distance (Z), and Driving Pressure (P _D) for a Linearly-Rising Pressure Pulse With a 23-ms Rise Time	58
2.1-3	Fuel Velocity (V), Fuel Penetration Distance (Z), and Driving Pressure (P _D) for a Step-Rise Pressure Pulse	59
2.1-4	Graded-Enrichment Fuel Pellet Design	59
2.2-1	Assembly Drawing of OOP Loop	61
2.2-2	Data Acquisition and Control System for the IEFM Out-of-Pile Loop	63
2.2-3	Data Acquisition and Control System for the IEFM In-Pile Loop	64
2.2-4	Fission Thermocouple Detector Response to a SPR-III Pulse (FTC 2)	68
2.2-5	Gamma Thermocouple Detector Response to a SPR-III Pulse (GTC 3)	68
2.2-6	Fission Chamber Response to a SPR-III Pulse (CAB 16)	69
2.3-1	Seven-Pin Gross Motion Detector Locations	70
2.3-2	Radial Location of Detectors for the Seven-Pin High Resolution and Gross Motion Experiments	71
2.3-3	Thick Film Self-Powered Detector	71
3.1-1	Shear-Rate Dependence of Slurry Viscosity	74
3.1-2	Photographs of Leach Specimen	77
3.1-3	Typical Heat-Up of Leach Sample in Bomb	77

Illustrations (cont)

Figure

3.1-4	Time Dependence of Leaching of Cs and U at About 161°C.....	84
3.1-5	Cesium Concentration vs Temperature.....	84
3.1-6	Melt Furnace Test 2.....	84
3.2-1	Ultrasonic Thermometer Data for Control Run 1.....	86
3.2-2	Ultrasonic Thermometer Data for Control Run 2.....	86
3.2-3	Predicted Temperature Profile and Experiment Data From Thermocouples and UTs.....	86
3.2-4	Helium Loop Power Measurements vs Mass Flow Rate.....	87
3.2-5	Dryout Heat Flux vs Particle Diameter for a 100-mm-Deep Bed in Water.....	92
3.2-6	Dryout Heat Flux vs Particle Diameter for a 100-mm-Deep Bed in Sodium.....	93
3.2-7	Dryout Heat Flux vs Particle Diameter for a Particle Bed in Water for Various Bed Depths.....	93
3.2-8	Dryout Heat Flux vs Particle Diameter for Sodium.....	93
3.2-9	Dryout Heat Flux vs Particle Diameter for Acetone.....	94
3.2-10	Dryout Heat Flux vs Particle Diameter for Methanol.....	94
3.2-11	Dryout Heat Flux vs Particle Diameter for Freon 113.....	94
3.2-12	Predictions vs Measurements for the General Model.....	95
3.2-13	Predictions vs Measurements for the Dhir-Catton Model.....	96
3.2-14	Predictions vs Measurements for the Hardee-Nilson Model.....	97
3.2-15	Predictions vs Measurements for the Shires-Stevens Model.....	98
3.2-16	Predictions vs Measurements for the Ostensen Model.....	99
3.3-1	MP-4 Molten Fuel Pool Experiment Capsule.....	103
3.3-2	Location of Ultrasonic Thermometers and Inner Crucible Thermocouples in MP-4.....	103
3.3-3	MP-4 Reactor and Experiment Power History.....	104
3.3-4	MP-4 Ultrasonic Thermometer Data Radial Center UT.....	104
3.3-5	MP-4 Ultrasonic Thermometer Data Radius = 12.5 mm.....	105
3.3-6	MP-4 Ultrasonic Thermometer Data Radius = 25.0 mm.....	105
3.3-7	MP-4 Ultrasonic Thermometer Data Radius = 25.0 mm.....	105
3.3-8	MP-4 Ultrasonic Thermometer Data Radius = 25.0 mm— Comparison With Thermocouple Data.....	105
3.3-9	MP-4 Ultrasonic Thermometer Data Radial Profile Near Top of Fuel Bed.....	106
3.3-10	MP-4 Ultrasonic Thermometer Data Radial Profile Near Top of Fuel Bed.....	106
3.3-11	MP-4 Ultrasonic Thermometer and Thermocouple Data.....	107
3.3-12	MP-4 In-Pile Experiment (UO ₂ /MgO) Power and Pressure Histories.....	107
3.4-1	Fragment Density vs Penetration Distance for Core Sample Taken From the Center of the Bed.....	109
3.4-2	Fragment Density vs Penetration Distance for Core Sample Taken From the Bed Near the Wall.....	109
3.4-3	Elapsed Time vs Temperature (Temperature Response) at Several Selected Concrete Depths, Test FRAG 12.....	110
3.5-1	Experimental and Calculated Temperature, Test 5.....	110
3.5-2	Experimental Temperature, Test 14.....	111
3.5-3	Calculated Temperature, Test 14.....	111

Illustrations (cont)

Figure

3.5-4	Pressure Through Concrete, Test 11	111
3.5-5	Water Release Data for Magnetite	111
3.5-6	Relative Water Release Data for Magnetite	112
3.5-7	Key Features of the Physical Separate Effects Test.....	112
3.5-8	Sodium Pool and Concrete Temperatures During Physical Separate Effects Test 13	112
3.5-9	Flow Rate Data for a 0.23-mm Wide Slot	114
3.5-10	Mass Flow Rate (m) vs Mass of Water in Reservoir (m).....	114
3.5-11	Data for Two Na/O Compositions	115
3.5-12	Sodium/Concrete Ablation Model	116
3.5-13	Closeup View of the Porous Dehydrated Concrete at the Reaction Zone	117
3.5-14	Closeup View of the Condensed NaOH Liquid Layer	117
3.5-15	Calculated and Measured Temperatures at $x = 0.0351$ m for HEDL Test 1 Data	122
3.5-16	Plot of Calculated and Measured Pressures at $x = 0.0351$ m for HEDL Test 1 Data	122
3.5-17	Plot of Calculated and Measured Value of Integrated Water Release for HEDL Test 1 Data	122
4.2-1	Schematic of Parallel Plate Sampler Experiment	126
4.2-2	End View of Sampling Channels	126
4.2-3	Comparison of Particle Velocities Arising From Sampling Forces.....	126
4.2-4	Aerosol Particles Collected in Sampling Channel on Test 16	129
4.2-5	Particle Migration in the Channel	130
4.2-6	Sampler Channels Positioned Vertically	130
6.1-1	Multiaxial Specimen Geometry (All dimensions in inches).....	149
6.1-2	Low Cycle Fatigue Results for Biaxial Loadings	149
8.1-1	ACRR Fuel Motion Detection System.....	156
8.1-2	Configuration of Thermal Neutron Shield Sandwiching the Stainless Steel Window	158
8.1-3	Geometry for Testing the Effect of the Be Heat Sink on the Scene Background.....	158
8.1-4	Thermal Neutron Shielding of the Pb Shield Block	158
8.1-5	Neutron Dosimeter Package Layout.....	159
8.1-6	Photograph of the Coded Image, Upper Channel, Run 10	161
8.1-7	Axial Scan Along Central Zone of Coded Image	162
8.1-8	Radial Scan of the Coded Image.....	162
8.1-9	Density Deviation vs Log Exposures for Three Primary Noise Sources in the CAIS Active Detector System	164

Tables

1-I	PBE-145 Initial Conditions and Results.....	28
1-II	Sodium Vapor Film Growth Around UO_2	32
1-III	Energy Deposited in Each Region, Scaled From Figure 1.2-4.....	40

Tables (cont)

1-IV	Results of Neutronic Energy Deposition Calculations for Different Fuel Geometries Compared to Values Used in CSQ Modeling	43
1-V	Wall Temperatures Calculated With TAC2D	45
1-VI	Critical Temperatures and Concentrations of Gases Expected in Handling Atmospheres	48
1-VII	Classification of Common Contamination Sources.....	50
1-VIII	Summary of Cleaning Steps for EOS Pressure Cell Components	51
2-I	Proposed Experiment Sequence for Initial In-Core Fuel-Freezing Experiments	57
2-II	CABRI Detector Sensitivities in SPR-III	68
3-I	Sample Composition	76
3-II	Summary of the Tests	79
3-III	Lot Analyses of Dissolved Materials	80
3-IV	Analysis of Leach Liquors.....	81
3-V	Major Constituents of Leach Solution Before Use	83
3-VI	Particle Diameters for Transition to Fully Laminar (d_L) or Fully Turbulent (d_T) Flow for a 100-mm-High Bed With $\epsilon = 0.4$ for Various Fluids at 1-atm Pressure	92
3-VII	Ratio of Dryout Powers With Downward Boiling to That Without Downward Boiling for $L = 100$ mm, $d = 0.5$ mm, and $\epsilon = 0.4$ for Various Fluids	100
3-VIII	Downward Heat Flux Predicted by Downward Boiling and Conduction for Various Bed Depths	101
3-IX	Description of Fuel/Magnesium Oxide Interaction	108
3-X	Strength of Magnetite Concrete	111
3-XI	Future Large Scale Sodium/Concrete Interactions Tests	113
3-XII	Selected Values for the Solution Space	121
5-I	Sectional Coefficients for Equation (5.50)	142
5-II	Sectional Coagulation Coefficients With Geometric Constraint	144
6-I	Biaxial Creep-Fatigue Tests on 316 Stainless Steel at 593°C ...	148

Executive Summary

Introduction

Sandia National Laboratories, Albuquerque, New Mexico is conducting the Advanced Reactor Safety Research Program on behalf of the U. S. Nuclear Regulatory Commission (NRC). The overall objective of the program is to provide NRC a comprehensive data base essential to (1) defining key safety issues, (2) understanding the controlling accident sequences, (3) verifying the complex computer models used in accident analysis and licensing reviews, and (4) assuring the public that advanced power reactor systems will not be licensed and placed in commercial service in the United States without appropriate consideration being given to their effects on health and safety.

The NRC program is carefully planned to complement the larger DOE program, but at the same time to satisfy the NRC obligation of independent confirmatory research.

Together with other programs, the Sandia effort is directed at assuring the soundness of the technology base upon which licensing decisions are made, and includes experiments and model and code development.

Sandia has been asked to investigate eight major areas of interest which are intimately related to overall NRC needs. These are

1. Energetics
2. Fuel Dynamics
3. Core Debris Behavior—Inherent Retention
4. Aerosol Source Normalization
5. Containment Analysis
6. Elevated Temperature Design Assessment
7. LMFBR Accident Delineation
8. Test and Facility Technology

These major tasks are subdivided as necessary into subtasks to facilitate the organization of work and the interaction of subtask results into a body of coherent information which supports the requirements of the NRC.

1. Energetics

1.1 Prompt Burst Energetics

Prompt Burst Energetics (PBE) experiments provide information on the energetic response of various reactor fuel-clad-coolant systems to superprompt

critical conditions. This program is directed at characterizing the phenomena which result in pressure generation and the conversion of thermal energy to work, and reactivity effects arising from rapid coolant voiding and initial fuel motion. These experiments examine integral effects of fuel-clad-coolant interactions (FCI), fission gas release, and fuel and fission product vapor pressure during superprompt critical core disruptive accidents, and determine the potential for damage to the primary containment. The experimental work is closely interfaced with analytical efforts to develop models which uniquely describe the observed phenomena for incorporation into predictive accident analysis as well as to provide data to verify existing accident analysis codes. These experiments also provide information about the thermodynamic states and spatial distribution of fuel, clad, and coolant following a superprompt excursion. These data serve as initial conditions for postaccident heat removal (PAHR) and molten core containment analysis.

In tests performed to date, single fuel pins have been pulse fission heated in the Annular Core Research Reactor (ACRR) to temperatures resulting in fuel vaporization. The pins, which have been surrounded by helium or sodium, are contained in a rigid pressure vessel which is instrumented with thermocouples and pressure transducers and which is fitted with a movable piston at its upper end. Estimates of the conversion of thermal energy to work result from comparisons of the kinetic energy of the piston to the fission energy input to the fuel. Pressure, temperature, and piston displacement histories are determined for a variety of fuel-coolant systems and initial conditions. A series of experiments with fresh uranium dioxide fuel and sodium coolant has been completed. Additional oxide experiments are now being performed. Initial experiments with fresh uranium carbide fuel and sodium have been performed. Future pin experiments will examine fission product effects in preirradiated fuel. A seven-pin test vehicle for PBE experiments has been developed.

The scope of the PBE work is being enlarged to include separate effects experiments to examine FCI phenomena between oxide fuel and sodium. The first area to be addressed in these studies is to determine if

Executive Summary

the oxide/sodium system is capable of supporting large scale, propagating, escalating interactions and, if so, to characterize the controlling phenomena. Conceptually, the experiments will examine the response of a mixture of relatively large droplets of molten fuel in a sodium volume to externally applied pressure transients.

The PBE-14S experiment was performed in mid-February. This experiment was designed to study the energetics of the oxide/sodium system under conditions yielding pin failure at high power in the presence of significant fuel vapor. The experiment also provided additional information about the failure of fuel pins that are restrained only at one end to aid in the validation of the EXPAND fresh-fuel pin-failure model.

The pin failed ~ 7 ms after the peak of the prompt-power pulse at $\sim 20\%$ of the peak power. Failure was evidenced by a high amplitude pressure transient (recorded maximum ~ 100 MPa), consistent with the predicted fuel vapor pressure. The initial transient was followed by other pressure transients, including a massive event at the top of the capsule following piston stoppage. This large secondary event, which destroyed both top pressure transducers, is (as in other PBE experiments) attributed to an FCI triggered by the low amplitude pressurization arising from compression of the top sodium slug as the piston is decelerated at the end of its travel.

The maximum kinetic energy of the piston (170 J) represented $\sim 0.1\%$ of the thermal energy deposited in the fuel. The piston responded only to the initial fuel-vapor-driven pressure transient and stopped as the channel was pressurized by sodium vapor. Thus, the observed energy conversion represents only part of the total work potential of the system. PBE-14S represents the greatest energy input of any PBE experiment and yielded the most energetic response of any oxide-fueled experiment.

The validation of the EXPAND model is continuing with preexperiment modeling of PBE-14S and new calculations of the AXI carbide TREAT experiment. The EXPAND code predicted that PBE-14S would fail ~ 4 ms earlier than observed. This difference appears to result from the input data used. Recalculations are in progress using measured experiment parameters. The results of the AXI calculations agree with the experiment results to within the

expected accuracy of these calculations. This level of accuracy is $\pm 5\%$ of the transient time scale which, in turn, is defined as 4 times the pulse full width at half maximum (FWHM).

Examination has begun for determining the characteristics and behavior of sodium vapor films surrounding fuel droplets immersed in sodium. This work is directed at assessing the feasibility of the FCI experiments involving coarse-predispersed-fuel mixtures and will form the basis of a model to describe the initial temperature conditions of the fuel and sodium in those experiments. The current work examines the dynamic growth of a vapor film around a hot spherical particle which is suddenly immersed in coolant. Of particular interest are the stability, growth rate, and typical thickness of the film and the sensitivity of the film behavior to subcooling and particle size on the 10 ms timescale of the ACRR pulse. Preliminary analysis indicates that relatively thin vapor films and molten fuel surfaces can be attained for degrees of subcooling between 50 and 150 K for particle sizes in the range of interest (1 to 3 mm diameter).

The framework for the FCI analysis model is being assembled to permit evaluation of various phenomenological models with respect to the results of the FCI separate effects experiments.

Hardware design and procurement for future single-pin PBE experiments and coarse-predispersed-fuel FCI experiments is in progress along with improvements in data logging and reduction methods.

1.2 Irradiated Fuels Response

The Sandia National Laboratories Irradiated Fuels Response program is aimed at determining the response of fresh and irradiated reactor fuels to both prompt burst (disassembly timescale) and loss-of-flow (LOF) heating conditions. On prompt burst timescales, the pressure source from both fuel vapor and fission gases as well as the accelerations produced by these pressure sources, are of central importance. Thus, the program in this area centers on determining the effective equation-of-state (EEO) of both fresh and irradiated fuels, the dynamics of pressurization (rate effects), and the ability of this pressure to disperse fuel. On LOF timescales, the mode of initial fuel disruption and its timescale for both fresh and irradiated fuels are of crucial importance.

Executive Summary

1.2.1 LOF-Timescale Fuel Disruption

A significant ongoing effort in support of the Irradiated Fuels Response program has been the development of a high resolution optical diagnostic system to observe and record experimental results. This development work has evolved into a system which uses motion picture photography to provide a real-time record of a fuel pin response under various accident conditions as simulated in the ACRR. From the motion picture record, fuel pin swelling, modes of failure and disruption, and other phenomena of interest are determined.

In the initial series of fuel disruption experiments, FD1, a significant unexpected result was very rapid and extensive fuel swelling. In addition, this swelling, which may be the dominant initial fuel disruption mechanism in an LOF, unexpectedly occurred in the restructured, least-gassy region of the fuel. A suitable explanation for either of these two phenomena has not emerged yet, and a model remains to be developed. In an effort to provide insight into the mechanisms responsible, some of the FD1 fuel is to be shipped to KfK, Karlsruhe, FRG for post test quantitative examination.

An NRC license to export appropriate fuel was received in this quarter. The samples to be shipped include (1) mixed oxide fuel which was irradiated in the FD1 series of tests and which swelled to varying degrees but did not disrupt, (2) a sample of sibling fuel, and (3) five small disks of fresh UO_2 . KfK, Karlsruhe will perform electron microscopy and gas analysis on the mixed oxide fuel. The fresh fuel disks will be pulsed-laser heated for vapor generation and measurement. Shipment is currently scheduled for next quarter.

The current experiment program centers on the second, or FD2 series of 10 scheduled tests. This series includes experiment conditions more prototypic of an LOF than FD1. Experiment geometry, diagnostics, and fuel handling and heating conditions have been improved. Four tests, including three with fresh UO_2 fuel and one with irradiated mixed oxide, have been conducted. Results include molten fuel jetting through a solid outer annulus for the fresh fuel tests, and chunk breakup for the mixed oxide.

In this quarter, neutronic and thermal response calculations have continued for the FD2.1-2.4 tests. The calculated clad and fuel temperature histories now agree within 5% with those determined experimentally. Gap conductance, a sensitive function of

initial gas conditions, is better understood. The remaining six FD2 irradiated fuel experiments will follow later in the year, depending on other exigencies and on the availability of the ultraclean shielded glovebox.

Two gas samples obtained during the FD2.4 irradiated fuel test have been analyzed by means of gamma scanning and mass spectrometry. A number of fission products and the expected hydrocarbon gases were identified. The source of the hydrocarbons was not determined. Larger gas samples are necessary.

Program personnel have implemented a new, simplified optical path for the fuel-response cinematography. Two mirrors have been eliminated and an 8-in. Celestron telescope will be used. This increases the light-gathering by at least a factor of 4 and may allow use of the optical pyrometer.

The high ramp rate (HRR) experiments to be performed in collaboration with the UKAEA are now expected to start in June. These experiments will investigate the potential of fission product gases to cause fuel dispersal before dispersal would occur from fuel vapor pressure alone.

The principle investigator visited KfK with a threefold purpose:

- To present an invited talk on FD1 and FD2
- To discuss the upcoming microscopic analysis of the FD1 fuel by KfK
- To discuss a proposed fuel disruption experiment series, FD4, which would be collaborative between KfK and Sandia.

1.2.2 EEOS Preexperiment and Postexperiment Analysis

The Sandia EEOS experiments give a direct measurement of fuel pressure vs energy for use in accident analysis. This direct measurement eliminates the additional uncertainties in the specific heat above melt that are invoked in pressure-temperature measurements. The pressures in the EEOS experiments are a factor of 2 to 10 higher than those from pressure-temperature measurements, if currently accepted values of the specific heat are used to make the conversion.

The postexperiment analysis of the EEOS experiments is aimed at (1) investigating the discrepancy between the pressure-energy and pressure-temperature measurements, and (2) reducing the experimental uncertainty (some 20%) in the energy responsible

Executive Summary

for the pressure range quoted above. The first series of CSQ-II hydrocode calculations for EEOS analysis has been completed. The calculations are summarized and tentative results given. A second series of calculations has been started to settle questions of numerical accuracy raised in the first series and to investigate the feasibility of code modifications where necessary.

Increasing emphasis has been placed on design and preexperiment analysis of the new EEOS series. Investigators have set a design goal of 7% uncertainty in energy with reliable contamination control. A tentative neutronic design and the contamination control analysis is presented here. The design of an in-pile calorimeter for absolute calibration of in-pile sample energy deposition has been started and will be discussed next quarter.

The goal of 7% uncertainty in energy at 3000 J/g deposition appears feasible for the fresh fuel EEOS experiments. This apparent feasibility is based on TWOTRAN neutronics calculations involving an occluder ring. However, a limitation on the accuracy of TWOTRAN calculations has delayed a final design because of the need for independent corroboration.

Because fuel behavior in closed volume, in-pile EEOS experiments is very sensitive to nonprototypical contaminants, a program for contamination analysis and control during the preparation of EEOS experiments fuel had previously been started. The analysis was completed this quarter.

Estimates of the gas contributions from the different sources lead to the conclusion that the highest potential for atypical pressure contributions lies in the fuel contamination from handling, although credible contamination may also be significant. Several likely contaminants were studied and a contaminant-specific cleaning and handling procedure was established.

1.2.3 UO₂ Heat Capacity Experiments

High temperature properties of UO₂ are required for thermal transient calculations of reactor systems under accident conditions. In particular, the heat capacity of UO₂ in the solid phase is needed to establish the initial energy state for these calculations.

Sandia investigators have devised an experiment to measure the relative values of the equilibrium and instantaneous specific heat of UO₂ as well as the relaxation time. The facility for these experiments

became operational during this quarter and some preliminary measurements have been made.

The apparatus uses Joule heating to raise the sample temperature to the region of interest. After Joule heating was discontinued, surface temperatures recorded as a function of time revealed that the sample cooled linearly with time. Following a short delay, a rapid temperature excursion was introduced by discharging a capacitor into the sample. The capacitor discharge resulted in a temperature in the jump fuel of an amount corresponding to the magnitude of the instantaneous specific heat. After the capacitor discharge, the sample cooled exponentially in time while the specific heat relaxed to the equilibrium value. Then, the cooling rate again became approximately constant. A technique was developed to determine the relative magnitude of the instantaneous specific heat.

2. Fuel Dynamics

2.1 Transition Phase

Following the loss of initial geometry in a core disruptive accident, and assuming that neither early shutdown nor rapid hydrodynamic disassembly takes place, the accident enters the transition phase. The progression of the transition phase toward possible second recriticalities may strongly influence the severity of the accident and it is, therefore, important to understand in detail the phenomena associated with this accident stage. Sandia work is currently directed toward the mechanics of fuel blockage formation since this defines conditions leading to recriticality.

The formation of fuel blockages by freezing is an important aspect of the transition phase since this phenomenon controls fuel penetration through the upper core structure and hence the amount of negative reactivity available for accident termination. Heat transfer between flowing molten fuel and ablating steel walls which ultimately controls fuel penetration distance is affected by transpiration as molten steel moves away from the solid wall and is ablated into the bulk flow.

The sequence of experiments in the initial series of ACRR in-core fuel freezing experiments has been defined. These experiments will study freezing of

Executive Summary

pure, low-void-fraction, UO_2 over a steel-wall-temperature range of 673 to 1073 K (400° to 800°C), a fuel temperature range of 3273 to 3973 K (3000° to 3700°C), and a driving pressure range of 10 to 100 atm. Heat transfer and neutronic calculations have been performed to provide design information. Fabrication of the experiment packages has begun.

2.2 Initial and Extended Fuel Motion (IEFM)

The purpose of the IEFM Program is to investigate the key phenomena associated with fast reactor initiating accidents such as a loss of coolant flow (LOF) and transient overpower (TOP) without SCRAM. In these hypothetical accidents, dispersive fuel motion is a major source of negative reactivity insertion. However, depending upon failure location, failure mode and final fuel relocation, positive reactivity effects are also possible. Therefore, it is important to identify and model phenomena such as fuel motion inside the clad prior to failure, axial fuel-failure location, mode of cladding failure, fuel disruption modes, rate of dispersal, fuel plateout, and extended fuel motion into the blanket (potential for blockage). Data to support model development and verification of these phenomena are severely limited.

Irradiated fuel experiments are currently being planned that will use the newly developed coded aperture fuel motion detection system in the ACRR. Investigators hope that, because of improved resolution of this diagnostic device, direct observations of these phenomena will be possible. These tests in the ACRR will require operating modes allowing preheats at nominal power followed by ramp, or pulse power profiles. The required hardware to provide these modes has been constructed. An additional facility needed for these experiments is a flowing sodium loop. Design of a prototype in-pile loop for single fresh fuel pin tests is currently underway. An out-of-pile loop has already been designed and will be available this year. The out-of-pile loop will aid in the design of the in-pile loop and experiment planning. A program (Phase 2), involving a matrix of tests directed at specific issues, is proposed as a follow up to the prototype loop program.

These experiments are complementary to those currently being performed in the CABRI reactor in France. Consequently, cooperative efforts are underway through the ACRR/CABRI exchange agreement

to provide a continuing interchange of expected data and analysis results.

The design of the initial out-of-pile loop system has been completed. Most of the major out-of-pile loop components have been ordered. Several approaches for sodium-level-detector instrumentation are being explored. The design of the initial in-pile loop continues. Design of the loop-control and data-acquisition systems is in progress.

The CABRI A2 TOP test was recalculated by using a revised version of the EXPAND code and actual experimental data. The sensitivity of the EXPAND failure model to variations in the power level was found to be greater than the accuracy of the experimental data. The consequences of using UO_2 instead of mixed oxide fuel in CABRI tests is under evaluation. The detectors for the CABRI-calorimeter experiment have been fabricated, tested and shipped to France. Although five of the nine thermocouple detectors failed during mounting at Cadarache, the remaining detectors will provide the needed information.

2.3 In-Core Fuel Motion Detection.

The feasibility of in-core fuel motion detection is being investigated at Sandia because many facilities which can be used for NRC fast reactor safety tests do not have instrumentation slots. Also, in those reactors which do have slots, self-shielding may preclude the use of high-resolution techniques for large-scale tests. Consequently, 7-, 19-, and 37-pin experiments are being conducted in the SPR-III to test both detectors and unfolding methods. Following the completion of these experiments, fuel motion detection will be performed in the ACRR as part of prototype accident situations generated during PBE experiments.

Experiments were performed in the SPR-III this quarter to test the feasibility of in-core fuel motion detection, using platinum self-powered detectors (Pt-SPD) outside of the fuel bundle to monitor fuel motion. The detectors were located outside a seven-pin fuel bundle in such a way location simulates placement in the sodium bypass loop of a true fast reactor LOF or TOP experiment.

The unfolding analysis of these experiments is still under development. However, preliminary analysis of the detector responses has been completed. The responses appear lower than those in the high-resolution experiments, as expected. The detector

Executive Summary

responses of interest here changed by 3% to 5% as all 7 pins were moved away from the detector whereas the signal change was about 15% for the high-resolution experiments.

In addition to development of Pt-SPDs, a significant effort is ongoing to develop a thick film self powered detector (TF-SPD) which has different sensitivities from those of Pt-SPDs. More experimental and developmental work is necessary before a choice of detectors or an appropriate combination of detectors can be made.

3. Core Debris Behavior – Inherent Retention

3.1 Molten Core Containment

If, following a major reactor accident the core debris is not permanently coolable, the debris will penetrate the reactor vessel, and come into contact with structural and containment materials. The interaction of the melt with these materials causes (1) pressurization of the containment structure, (2) release of the radioactive aerosols, and (3) erosion of the containment. The attack of high temperature, reactor core materials on containment materials is the focus of this task.

This quarter has been devoted primarily to developing techniques for examination and posttest analysis on in-pile and out-of-pile experiments involving the interaction of molten $\text{UO}_2 + (\text{La}_2\text{O}_3 + \text{steel})$ with commercial grade ceramic materials. The focus is on electron microprobe chemical analysis of the products of the reactions of molten core simulant with MgO and MgAl_2O_4 bricks. This analysis is providing information on diffusion and melting reactions in the bricks. The information thus obtained leads to estimates of both equilibrium and kinetic factors controlling the mechanism of attack.

The analytical method takes full advantage of the accuracy, precision, and automated capability of the Sandia electron microprobe. The approach being considered here was tested sufficiently to assure its applicability and utility. Samples of appropriate materials from previous experiments have been selected for analyses and are now being prepared.

One aspect of melt/concrete interactions that must be addressed in modeling their long term behavior is the crust formation and growth that occurs during solidification of the oxidic phase of the melt. Crust formation is expected around the periphery of the melt where temperatures are lowest. One material property that undoubtedly plays a significant role in the process of crust formation is viscosity. The viscosity of single phase siliceous melts increases dramatically with decreasing temperature. As the melt temperature falls below its liquidus value, the precipitation of solids will produce a two-phase slurry having a viscosity different from that of the single phase melt because of the presence of the solid particulate.

Several correlations of the viscosities of slurries are available. For all the correlations, viscosity increases as solid particles are added. Viscosities become quite large when the volume fraction of solids exceeds about 0.4.

Numerous analytic attempts are being made to estimate the attack on MgO by molten reactor fuel, using a thermal ablation formalism. The formulation of the problem consists of approximating the reactor fuel as pure UO_2 , assuming some directional dependence of heat rejection from the molten pool, and using heat rejected from the pool into the MgO as the controlling factor in determining the ablation rate.

The MgO/UO_2 system is far from ideal. Consequently, the ablation rates calculated even with ideal heats of solvation will still be lower bounds on the true ablation rates.

In response to interest in the liquid pathway of fission product release following a core-meltdown accident at a nuclear power plant, an effort to examine, in an exploratory fashion, the aqueous leaching of corium mixtures with concrete was completed. Leach studies were done on a basaltic concrete-corium mixture of known composition. Acidity of leach liquor is the most important factor in the leachability of the mixtures. Water chemistry can be important if coordinating ions such as phosphate are present in solution. Cerium, lanthanum, and cesium are the most easily leached fission products.

The construction and installation of the large melt facility was completed and two shakedown experiments were performed by using a dummy graphite load. In the second shakedown experiment the furnace reached the design temperature of 3273 K (3000°C).

Executive Summary

3.2 PAHR Debris Bed

Requirements for the safe shutdown of an LMFBR have led to many studies of Post Accident Heat Removal (PAHR) from disrupted-core geometries. Studies of in-vessel and ex-vessel PAHR have been motivated largely by the significant reduction in radiological hazard potential which results from retention of fuel and coolant within the primary or secondary containments.

Following a core disruptive accident, molten core materials may exit the core region and contact sodium where solid fuel debris will be formed and collected on horizontal surfaces within the vessel. This debris is still capable of generating significant power through the decay of fission products. Should insufficient cooling be afforded by natural processes, the debris could remelt and threaten the vessel. The purpose of this task is to determine the natural cooling of such debris.

3.2.1 Debris Bed Experiment D4

Debris bed experiment D4 was the fourth in a series of experiments designed to provide quantitative information on the behavior of debris beds formed from reactor materials following a core-melt accident. The analysis of the D4 data continued with a detailed analysis of the experiment control runs and the review of the deposition and profile of the debris bed power. Control run analysis allowed observation of the debris bed at a specific power of 0.27 kW/kg and a temperature of 573 K. The debris bed was cooled primarily by conduction. Information on the effective conductivity allowed identification of bed characteristics and changes in these characteristics. These postchange conditions define the initial bed conditions for the next series of dryout experiments. A two-region conduction phenomenon observed in the first control run led to speculation that a local region of large resistance may be responsible. Agreement between the predicted and measured temperatures tends to confirm the responsibility of local resistance. Additional analysis on effective conductivity (k_{eff}) has resulted in a calculated k_{eff} of 34 W/m-K as compared to a predicted value of 27 W/m-K. Undefined uncertainties are the causes of the variance between calculated and predicted k_{eff} . These must be resolved prior to additional analysis.

Specific power profiles and deposition were subject to post-experiment analysis. This analysis revealed a discrepancy between the measured power deposition and that calculated by the neutronic code TWOTRAN II. As a result, the helium loop power diagnostics and the neutronic calculation were reviewed. The reponse of the helium loop power diagnostics was experimentally quantified.

Refinements in neutronic calculations were made to improve the accuracy of bed-power predictions.

3.2.2 Debris Bed Experiment D5

Debris bed experiment D5 is the first experiment in which bed behavior at extended post dryout conditions will be investigated. The three objectives are (1) to observe bed behavior at elevated temperatures under varying conditions of sodium subcooling, (2) to evaluate crucible design for future high temperature experiments, and (3) to evaluate double containment concepts for D-series experiments. D5 is in the early design stages. Preliminary stress analysis on the high temperature crucible is nearly completed and indicated that the present design will meet all the design measurements without crucible damage or failure. Thermal analysis has been completed and indicated a maximum temperature of 2073 K can be reached within the crucible while maintaining a subcooled temperature on the outer crucible wall. In addition, investigators have initiated thermal analysis on the overall experiment package. Analysis will follow. Various construction and fabrication projects are in progress to support D5.

3.2.3 Debris Bed Experiment D6

Debris bed experiment D6 will investigate the coolability of UO_2 debris by natural convection in sodium following an LMFBR accident. D6 differs from previous experiments in that a stratified bed is to be used to determine the characteristics of a bed in which particle size varies as a function of depth. A detailed design drawings for the D6 experiment have been completed. Fabrication of all experiment components has been initiated. A problem with vessel fabrication arose as a void was discovered in the weld of the debris-bed-vessel upper section. A reweld will

Executive Summary

be attempted but salvaging the part is doubtful. This problem is expected to delay fabrication by about a month. Various analyses are underway to assure adequate equipment performance.

3.2.4 PAHR Debris Bed Analysis

3.2.4.1 A General Dryout Model

A general model for incipient dryout in debris beds has been developed. This model includes the effects of both laminar and turbulent flow in both the vapor and the liquid phases. It also includes the driving forces of both gravity and capillary action. The laminar limit is similar to that of Shires and Stevens. The laminar limit for very deep beds is similar to that of Hardee and Nilson (and with further restrictive assumptions is similar to the deep bed model of Dhir and Catton). The very turbulent limit for very deep beds is similar to the flooding model of Ostensen. The model is based on first principles and contains only empirical constants which were obtained from areas other than dryout studies. Yet when the model is applied to published dryout data (126 points involving 5 different fluids and many different particle diameters and bed heights) agreement with the data appears to be better than in all other models (some of which include parameters determined from direct fitting of the models to the dryout data themselves).

A major prediction of the general model is that the dependence of dryout heat flux on particle diameter decreases from a square dependence to a square root dependence as the particle diameter increases. Thus the use of the Dhir-Catton or Hardee-Nilson models for beds with a large particle diameter will result in a large overprediction of the dryout flux. (The transition occurs for the particle diameters of ~ 1 mm for both sodium and water.)

3.2.4.2 Bottom Cooling and Downward Boiling

The presence of strong capillary forces in debris beds implies that downward boiling is possible in a bed, provided that the support plate is sufficiently cool to condense the downward flowing vapor. Extension of the laminar limit of the general model (above) to include downward boiling results in equations for the upward and downward heat fluxes at dryout for a bottom-cooled bed. (These equations do not include condition effects, which would add to the

downward heat-removal capability.) One prediction of the model is that the dryout power (or combined upward and downward heat fluxes) for a bed of fixed height can increase by as much as a factor of 4 with downward boiling (and even more with subcooling and conduction). This has an impact on core-catcher design since the support plate must be thin enough to pass this enhanced heat flux. The model also suggests the possibility of core catchers for water-cooled reactors since downward heat removal is no longer limited by the low thermal conductivity of water.

3.2.4.3 Zion-Indian Point Filtered Vending Containment System Studies

The general nature of events surrounding a PWR reactor vessel failure following a core meltdown was subjected to a cursory analysis to assess the impact of such events on a containment building filtered vent. The major findings are as follows:

- The location and size of a vessel rupture could significantly affect the pressure history in containment and the subsequent loading on the filtered vent.
- A significant pressure rise in a containment building could occur from molten debris dropping into the reactor cavity if there is adequate water in the cavity.
- The coolability of in-vessel or ex-vessel particle beds by natural circulation (assuming an adequate coolant supply) can neither be assured nor precluded at this time. However current data and models suggest that ex-vessel beds may be coolable, especially if less than all of the core material is involved in the bed.

3.2.5 LWR Related Activities

An interim review of current modeling of in-vessel meltdown in an LWR was performed. The objective was an assessment of the applicability of current models to the process of specifying possible accident mitigation measures. Significant uncertainties, caused either by modeling problems or phenomenological unknowns, have been identified and recommendations are made for resolution of some of the uncertainties. Bounds for the identified uncertainties could not be established without further study. Visualizations of alternate meltdown hypotheses are offered. The report will be published in April.

Executive Summary

3.3 PAHR Molten Pool

The PAHR Molten Pool program interfaces closely with both the Molten Core Containment and the PAHR Debris Bed programs. After a major reactor accident, if the core-material debris is uncoolable it will progress to a molten state. The progression of the debris to a molten state and the interaction of the melt with structural and core retention material is being experimentally investigated in the Molten Pool studies. High-temperature, laboratory furnace tests and first-of-a-kind neutronically heated experiments are providing significant data on many PAHR-related issues, including the thermal response of dried UO_2 and steel particulate beds to internal decay heating, the formation of crust and voids in pools of internally heated molten fuel material, and the interaction of hot fuel debris with core structure and retention material. As with other safety research programs, the experimental results are being used to develop and verify analytical models to study reactor behavior under a wide variety of accident conditions.

To date, Sandia has performed four in-pile fission-heated experiments in the Annular Core Pulse and Research Reactors (ACPR and ACRR) and three more are planned through FY 1981. The fourth experiment examined the effect of internal heating on the attack of magnesium oxide brick by overlying hot solid UO_2 particulate. Ultrasonic thermometry was used successfully in these experiments to measure temperatures up to 3150 K in environments hostile to thermocouples and optical pyrometry. The temperature measurements from these experiments are being used to obtain heat flux distributions (i.e., the amount of heat lost to surroundings vs the amount of heat directed toward the attack of supporting structure) and material property data (i.e., thermal conductivity of mixed UO_2 /steel particle beds).

This quarter, reduction of the data from the recently conducted MP-4 in-pile experiment was completed. Temperature and energy deposition profiles were compared against existing heat transfer and neutronic models. The comparisons, which are preliminary, indicate some discrepancies in the models and are pointing to the fact that radiation heat transfer may be more dominant in particulate beds than previously believed. As with previous molten pool experiments, uncertainties in material properties, and in the ultrasonic thermometry and fuel bed energy deposition data have made the thermal analysis of these tests very difficult. Resolution of some of

these uncertainties has received high priority attention this quarter. A new ultrasonic thermometer system is under development with the objective of improving its overall reliability and accuracy. A significant part of this development will require that signal reflections from containment seals be eliminated, as they have been a cause of substantial error in in-pile experiments. Power measurement techniques for use in large debris beds of fuel particulate are also being developed. Both tasks should be completed in time for the next in-pile molten pool experiment, MP-5S, which is scheduled to be conducted shortly after next quarter.

In addition to the above activities, the experimental matrix of out-of-pile UO_2 /MgO interactions discussed in the last two quarterlies was extended to include the effect of ZrO_2 and La_2O_3 to better simulate fuel melt compositions. In all tests, the rate of the interaction increased while the threshold temperature for the interaction decreased. The effect of La_2O_3 was significantly greater than that of ZrO_2 . These tests have shown the need to properly simulate fuel material compositions in the study of core retention material interactions.

3.4 Fragmentation

Most severe accident scenarios for advanced sodium-cooled reactor systems involve the production of significant amounts of molten fuel and steel. The ultimate dispersal of this molten material often depends on either bulk freezing the melt or establishing coolable particulate beds. Scenarios which differentiate between the dispersal modes involve questions of the fragmentation of substantial quantities of melt when contacted with coolant. Previous investigations yielding quantitative information involve very small quantities of fuel melt, leaving unanswered the question as to whether or not large quantities would yield different particulate size distribution because of vapor blanking of the bulk stream. A knowledge of particle size distributions is crucial to the resolution of postaccident coolability of cores which have been reduced to rubble.

Following whole-core accidents in which all, or most, of the sodium remains in the reactor vessel, molten/vaporized core materials and sodium will come in contact, resulting in sudden freezing and fragmentation of the core debris, which may then

Executive Summary

settle on various surfaces within the vessel. If recriticalities do not occur, this fragmentation and onset of settling roughly denotes the beginning of the post-accident sequence.

In this program, melts of core material about a factor of 10 larger than previously used are contacted with sodium. Characterization of the fragmented debris size and the settling of this debris within the residual sodium pool are the most important results expected from this program.

Gamma ray densitometry measurements of the residual sodium pool in test FRAG 11 are reported this quarter. This test involved deposition of sodium coolant onto a pool of molten core material. Initial results from the densitometry measurement indicate the presence of large fragments (> 28 mm diameter) throughout the bed and that the debris had not leveled within the sodium pool. Large debris has not been encountered in previous tests involving molten core material streaming into a sodium pool.

The unusual results from test FRAG 11 on debris size and bed leveling may be a consequence of premature freezing of portions of the core debris before it was quenched by sodium.

Test FRAG 12 was run during this quarter. This test was similar to test FRAG 11 except the pool of molten core debris was formed in contact with concrete rather than MgO. The debris/coolant interaction was quite vigorous in this test. The 2000-kg test apparatus was moved laterally about 2 cm as a result of this interaction. Early results on the posttest examination suggest both vigorous attack on the concrete and MgO cavity walls took place. No data are yet available on the debris formed during the interaction test.

Gamma-ray densitometry measurements were made of core samples from fragmentation test FRAG 11. Several core samples were taken, of which some were unsuccessful, probably because of fragments comparable in diameter to the sampling tubes. A full core sample could usually be obtained within a few centimeters of an unsuccessful attempt.

Gamma-ray scans were made 90 degrees apart for each sample. The density variations between the two directions were quite large and the density variations in the bed were also very large. These variations were due to the large fragments. For the scale of the samples, the bed structure was nonuniform, the high density portion of the bed being thicker near the walls than in the center. The average density in both of these regions was 3.7g/cm^3 . These results, together

with measurements of fragment-weight fraction, will give the variation in the void fraction of the bed.

Test FRAG 12, performed during this quarter, was designed to investigate the effect of the melt/concrete and sodium/concrete interactions on the fragmentation process and the formation of the debris bed. Twenty kg of metallosilic melt, produced in a crucible with a limestone concrete bottom and MgO sidewalls, were subject to a team of 23 kg of high temperature sodium. The sodium was released 10.7 s after ignition of the melt. Audio signals indicated six separate interactions lasting a total of 1.87 s. Other phenomena accompanied the interactions. The temperature response of the concrete, as monitored with thermocouples embedded in the concrete, shows that the reaction front of the sodium/concrete interaction reached a depth of 63 mm at 8 min and 1.27 mm at 21.5 min. As a result of the interaction, the MgO sidewalls were heavily eroded up to 20 mm. This phenomenon did not appear in previous fragmentation experiments.

3.5 Sodium Containment and Structural Integrity

The interaction of sodium with concrete will appear in a variety of fast reactor scenarios. Such interactions could develop in severe, core-disruptive accidents and in milder accidents that do not involve the core. Research in this program has shown that sodium/concrete interactions involve two distinct phases. The first phase is relatively mild and involves only the exothermic reaction of the sodium with water from the concrete. The rate of this reaction is believed to be controlled by the rate of heat transfer into the concrete and the consequent thermal decomposition of hydrates and hydroxides in the concrete. The USINT code, developed as part of this program, is a useful model of the heat and mass transfer within the concrete during the mild first stage of sodium/concrete interactions.

During this quarter, the USINT code was improved and used to predict data from tests conducted at HEDL on heated concrete. Predicted and measured temperatures within the concrete agree quite closely. Pressures within the concrete were less accurately predicted. Also during this quarter, magnetite concrete was characterized to provide data for the USINT code.

The second phase of sodium/concrete interactions is exceptionally exothermic. During this phase,

Executive Summary

actual erosion of the concrete takes place. The sodium temperature rises to near boiling. Temperatures at the reaction front are even higher.

Prediction of transition from the mild to the energetic phase of sodium/concrete interactions and prediction of the rate of the energetic phase are required for analysis of the safety of fast reactors. Once these predictions can be made, heat generation, aerosol generation and gas generation can be easily derived.

Experimental characterization of the transition from the mild to the energetic phase of the interaction has been handicapped because the transition has been observed only in relatively large-scale tests. Energetic interactions have never been observed in small tests (< 50 lb sodium) either in this research program or in work elsewhere. Without the ability to do rapid, low cost tests, empirical description of the transition is a time-consuming effort.

During this quarter, some promising results arose in the small-scale testing program to suggest that small-scale tests may be triggered to enter the energetic phase. A small-scale test with basaltic concrete proceeded much the same as in the past. That is, only the mild phase of the interaction was observed. However, after some time the test cell ruptured and sodium drained away from the heaters and the concrete. As the sodium drained away, exothermic excursions were recorded by thermocouples used in the test. This suggests that the energetic reaction was triggered by either increased heating of the pool that resulted when much of the sodium was lost from the cell or flow of the sodium across the concrete as the sodium drained. These possibilities will be pursued in future small-scale tests.

Characterization of the transition of the sodium/concrete interactions, that has been possible in this program, has been significant. Enough data have been accumulated to begin construction of a model of the interaction. The early form of this model is described here. Though the model is far from complete, it contains operative phenomena now believed to be important in the interaction. This model should guide future experimentation and, eventually, constitute the basis for systematizing data generated by this research program.

4. Aerosol Source Normalization

During an energetic hypothetical core disruptive

accident, fuel vapor may be produced which subsequently condenses to form small particulate debris (molten or solid) which can be transported to the upper vessel regions and through breaks which may have occurred in the vessel. The possibility of transporting this material depends strongly on its initial character.

Particulate debris produced from in-pile (ACRR) experiments is being characterized to determine the physical properties of fuel particles resulting from the vaporization and melt breakup of fuel pins subjected to simulated overpower excursions. The characteristics of these particles are being compared with those produced by out-of-pile experiments at ORNL which are part of the NRC sponsored aerosol transport program. Subsequent in-pile studies will examine the interaction of particles with the supporting structure and with sodium.

In a recent series of experiments at ORNL, fuel debris was sampled and fuel temperatures measured by methods previously demonstrated at Sandia's ACPR.

Previous quarterlies have described the temperature response of an exposed fuel pellet in a stack of fuel pellets when the stack was resistively heated to vapor. Calibrated photographic film was used to measure the temperatures of the fuel surface and of the bottom of a hole drilled to the pellet centerline. Several tests established the accuracy of the temperature measurements.

Sandia has continued to cooperate with ORNL in a joint program of aerosol studies in which the results of out-of-pile and in-pile aerosol experiments are being compared and analyzed. The purpose of these studies is to determine the validity of each type of test to portray the behavior of aerosols in actual reactor-accident situations. This joint effort is expected to continue.

5. Containment Analysis

This task is directed toward developing a general comprehensive containment systems code (CONTAIN) which will be a basic computational tool for the analysis of a variety of possible postaccident sequences, generally beginning with primary containment failure and proceeding to the determination of the radiological release from the secondary

Executive Summary

containment failure. Core-melt accidents, energetic disassemblies, reactor vessel rupture, and large scale sodium spills are addressed. Existing containment models are being adapted where feasible and new models are being supported by containment-related experiment programs, some of which are described in previous sections. Major phenomena are

- Postaccident heat removal
- Debris bed behavior
- Vessel failure
- Concrete-sodium interactions
- Concrete-melt interactions
- Melt-sodium interactions
- Liner response
- Sodium pool/spray burning
- Chemical reactions products and kinetics
- Gas flow, pressurization and venting characteristics
- Heat transfer (pool/wall/atmosphere)
- Fission product chemistry and inventory
- Aerosol transport behavior

During this quarter, CONTAIN's capabilities continued to increase. The principal improvement has been the inclusion of a new aerosol module. MAEROS, a new state-of-the-art aerosol code, has now been incorporated into CONTAIN. MAEROS uses a sectional treatment of the size distribution function for aerosol particles. Further, MAEROS allows simulation of multispecies aerosols under the assumption that agglomeration and settling effects are functions solely of particle size. This treatment provides new capabilities in aerosol modeling which will allow more mechanistic treatment of aerosol composition in CONTAIN. MAEROS also calculates the effects of vapor condensation on aerosol dynamics. Sensitivity calculations with MAEROS have investigated aerosol behavior in a light water reactor (LWR) TMLB' scenario as part of the Zion-Indian Point (ZIP) Study.

The reconstructed version of CONTAIN, reported last quarter, has now successfully run a test problem. CONTAIN now has a more general heat transfer model which allows an arbitrary number of heat transfer nodes in a cell. This permits the heat-sink and surface deposition effects of piping, equipment, etc, to be modeled in addition to the walls, floor, and roof. A major revision of the plot package is underway. When it is completed, a more useful set of plots will be available to allow more efficient assessment of the voluminous output from CONTAIN.

As part of the current ZIP Study, CONTAIN is being modified for application to problems with condensable atmosphere such as the steam encountered in LWR events. When completed, the atmosphere calculation in CONTAIN will handle mixtures of noncondensable and condensable gases and their condensation on aerosols and structures.

6. Elevated Temperature Design Assessment

The primary objectives of the elevated-temperature design assessment studies are to (1) develop correlative NDE techniques that can be used to monitor progressive creep, fatigue, and combined creep-fatigue damage in materials used in advanced reactor primary- and secondary-loop components; (2) evaluate analytical methods (and correlate with experimental data) for creep buckling of advanced-reactor components operating at elevated temperatures; and (3) design, fabricate, and operate a multiaxial creep-fatigue facility for the purpose of evaluation of creep-fatigue damage rules.

6.1 Uniaxial Creep-Fatigue Behavior

A 2.25Cr-1Mo steel specimen from ORNL was examined with transmission electron microscopy (TEM). The specimen was cycled at 811 K at the low strain range of 0.001 with a 0.05-h compressive hold period. These conditions prevailed for 8124 h after which the strain range was increased to 0.004 and cycling was continued to failure. Examination of the sample revealed that only thermal aging effects had occurred and that the strain range-temperature combination used in the test did not cause added carbide precipitation. Further, the dislocation density was very low considering the 3733 cycles given the specimen prior to failure. These observations indicate that accelerated testing of 2.24Cr-1Mo steel at high than service temperatures needs to be re-evaluated.

Thirteen experiments were conducted on tubular biaxial specimens of 316 stainless steel at 866 K to checkout the multiaxial test facility and specimen design and to compare the biaxial results with existing data. The specimens were cycled until leaking

Executive Summary

was noted, the pressure was then shut off, and cycling was continued until a crack had propagated approximately 50% around the circumference. This effort revealed that much more energy was required to initiate cracking than to propagate it. In addition, results were reproducible and indicated that tubular specimens had shorter lifetimes than did solid specimens, that the amount of wall thickness of tubular specimens had minimal effect on life length, and that tensile holds significantly shorter life.

7. LMFBR Accident Delineation

The principal objective of this program is to determine the applicability of event tree methodology to all phases of LMFBR accidents. The results of the study are intended to (1) provide a demonstrated methodology for developing accident sequence diagrams for an LMFBR, (2) identify and systematize the key phenomena and phenomenological or system uncertainties in the accident sequences, and (3) illustrate the methodology by determining the dominant accident sequences.

Sandia National Laboratories initiated the LMFBR Accident Delineation Study to examine the applicability of logic techniques, such as event and fault tree methods in the overall safety assessment of advanced reactor power systems. The purpose of this study is to (1) delineate the significant accident sequences in candidate advanced reactors, (2) develop the methodologies necessary to estimate the relative importance of both specific accident sequences and key phenomena within these sequences, and (3) utilize this perspective on important accident sequences to focus research resources on the most crucial reactor safety issues. This is a broad based program which combines logical and analytic methodologies in an attempt to present a state-of-the-art view of important accident features. Early phases of this study have used the CRBRP as an illustrative facility. Future efforts will be directed toward proposed candidate LMFBR designs when design information becomes available.

Fault trees for detection, SCRAM, and shutdown heat removal systems (SHRS) in the CRBRP were completed during this quarter and data collection for quantification during Phase II of the Accident Delineation Study was initiated. Sandia program personnel became aware that a major portion of the effort in the Engineered Safety Systems area during Phase II

must focus on quantification of the SHRS fault tree because of its complexity, its sensitivity to common mode and common cause effects, and the importance of protected accident sequences to the analysis of overall LMFBR uses. Assessment of the applicability of several computer codes to Phase II efforts was initiated; codes considered included the LMFBR-plant-systems code BRENDA, the fault tree evaluation code SETS, and the AUTOET event tree evaluation code. The accident initiation and engineered safety-systems response portions of the *LMFBR Accident Delineation Study Phase I Final Report* (henceforth called the *Phase I Report*) were completed in draft form.

In the accident phenomenology area, the major task for this quarter was the preparation of the Phase I Report, with work centering on four subtasks. These were:

- A substantial expansion and revision of protected accidents
- Delineation of the late stages of local fault propagation accidents
- Incorporation of recent SIMMER-II computer code calculations into the delineation of ULOF transition and fuel dispersal phases
- Exploring the applicability of two representation techniques, other than event trees, to delineation of LMFBR accident phenomenology.

Of these subtasks, the first (protected-accident delineation) is considered to be the most important. It further highlighted the need for the LMFBR safety community to devote much more attention to protected accident delineation and related issues, since protected accidents may contribute more to the total societal risk of LMFBR systems than do unprotected accidents.

In the postaccident phenomenology area, the event trees defining the postaccident phenomenology were modified during this period. These modifications improved the capability of the trees to represent in-vessel and ex-vessel energetic recriticalities, to represent primary sodium spills not involving a CDA, and to reflect feedback from experimental and analytical information in the future. Substantial efforts were devoted to preparation of the Phase I Report. At NRC request, a listing of LMFBR containment research and development needs was compiled.

Executive Summary

8. Test and Facility Technology

8.1 ACRR Fuel-Motion Detection System

The Coded Aperture Imaging Fuel Motion Detection System (CAIS) is being declared operational because recent tests prove that it will supply very useful information during experiments simulating core disruptive accidents. Added shielding in the instrumentation chamber has increased the signal-to-noise ratio at the detector plane by a factor of 10. The recent tests have also shown that CaWO_4 is still the best scintillator among those tested. The major remaining background at the detector plane is generated in the region of the canister, in the center of the core, which holds the fuel pin. Quality coded images have been obtained through the active system and were recorded on 35mm film. The major source of

noise in the active detector recordings appears to be film grain.

The CAIS is being prepared for full-scale Prompt Burst Energetics Tests to be conducted in August 1980.

8.2 ACRR Status

During this quarter, modification of the ACRR continued with the objective of improving its performance in several ways including giving it a capacity for increased power levels, faster control rod drive speeds, an enhanced pulse shaping capability. This modification was not only applicable to the reactor itself, but also involved the installation and testing of several pieces of auxiliary equipment for programming ACRR operating modes.

The initial characterization of the programmed transient rod withdrawal (TRW) mode was performed under control of the eight-segment hard-wired programmer. The initial attempt at a high-power square wave resulted in a power level of 37 ± 5 MW for 4 s with an energy release of 150 MJ.

Advanced Reactor Safety Research Program Quarterly Report January-March 1980

1. Energetics

1.1 Prompt Burst Energetics (K. O. Reil, 4423; M. F. Young, 4425; J. T. Hitchcock, 4424)

1.1.1 Introduction

Prompt Burst Energetics (PBE) experiments provide information on the energetic response of various reactor fuel-clad-coolant systems to superprompt critical conditions. This program is directed at characterizing the phenomena which result in pressure generation and the conversion of thermal energy to work, and at understanding the reactivity effects arising from rapid coolant voiding and initial fuel motion. These experiments examine integral effects of fuel-clad-coolant interactions (FCI), fission gas release and fuel and fission product vapor pressures during superprompt critical core disruptive accidents and determine the potential for damage to the primary containment. The rate of coolant voiding in a positive reactivity void-coefficient system determines the reactivity insertion rate and hence the magnitude of the transient under accident conditions. The experimental work is closely interfaced with analytical efforts to develop models which uniquely describe the observed phenomena for incorporation into predictive accident analysis as well as to provide data to verify existing accident analysis codes. These experiments also provide information about the thermodynamic states and spatial distribution of fuel, clad, and coolant following a superprompt excursion. These data serve as initial conditions for postaccident heat removal (PAHR) and molten core containment analysis.

In tests performed to date, single fuel pins have been pulse fission heated in the Annular Core Research Reactor (ACRR), (and previously in the Annular Core Pulse Reactor (ACPR)) to temperatures resulting in fuel vaporization. The pins, which have been surrounded by helium or sodium, are contained in a rigid pressure vessel which is instrumented with

thermocouples and pressure transducers and fitted with a movable piston at its upper end. Estimates of the conversion of thermal energy to work result from comparison of the kinetic energy of the piston to the fission energy input to the fuel. Pressure, temperature, and piston displacement histories are determined for a variety of fuel-coolant systems and initial conditions. A series of experiments with fresh uranium dioxide fuel and sodium coolant has been completed. Additional oxide experiments are now being performed. Future pin experiments will examine fission product effects in preirradiated fuel. A seven-pin test vehicle for PBE experiments has been developed.

The scope of the PBE work is being enlarged to include separate effects experiments to examine FCI phenomena between oxide fuel and sodium. The first area to be addressed in these studies is to determine if the oxide/sodium system is capable of supporting large-scale, propagating, escalating interactions and if so, to characterize the controlling phenomena. Conceptually, the experiments will examine the response of a mixture of relatively large droplets of molten fuel in a sodium volume to externally applied pressure transients.

During this quarter the PBE-14S experiment was assembled and performed. This experiment was designed to study the energetics of the oxide/sodium system under conditions yielding pin failure at high power in the presence of significant fuel vapor. The experiment also provided additional information about the failure of fuel pins that are restrained only at one end to aid in the validation of the EXPAND fresh-fuel pin-failure model. Current EXPAND work has involved preexperiment modeling of PBE-14S

and postexperiment calculation of the AX1 carbide experiment in TREAT.

Examination has begun to determine the characteristics and behavior of sodium vapor films surrounding fuel droplets immersed in sodium. This work is directed at assessing the feasibility of the FCI experiments involving coarse predispersed fuel mixtures. Current work will also form the basis of a model to describe initial temperature conditions for fuel and sodium in those experiments.

An FCI analysis model is being assembled to permit evaluation of various phenomenological models with respect to the results of FCI separate effects experiments.

1.1.2 Prompt Burst Energetics Experiment PBE-14S

The PBE-14S experiment was performed in February 1980 and was the second experiment in the current series of PBE experiments. The objectives were to obtain information about the energetics of the fresh oxide/sodium system for high energy deposition in the fuel and to provide more data about failure of pins that are restrained only at one end. PBE-14S was designed to produce pin failure during the reactor pulse in the presence of significant fuel vapor pressure. To achieve this design goal, a 14%-enriched fresh UO_2 fuel pin surrounded by sodium was irradiated in the ACRR during a single maximum pulse with a 6.35 mm-thick polyethylene moderator. The resulting maximum-radially-averaged fission energy deposited in the test fuel was 3980 J/g above the isothermal initial condition of 773 K. This represents the highest energy deposition attained in any PBE experiment.

Preliminary results of PBE-14S are shown in Table 1-1 and in Figures 1.1-1, 1.1-2, 1.1-3 and 1.1-4. Considerable data reduction remains to be completed; thus these results (many of them raw data) must be considered preliminary and subject to change as noise signals, signal biases, and other factors are corrected. Figures 1.1-1 through 1.1-4 show, respectively, the reactor power history, a bottom pressure history, a top pressure history, and the piston displacement.

Pin failure was indicated by the initial pressure transient observed at the bottom of the capsule at 38.7 ms. As shown in Figure 1.1-1, pin failure occurred 6.6 ms after the peak of the prompt pulse at $\sim 20\%$ of the maximum power. The pressure histories observed at both the top and bottom of the capsule are characterized by multiple pressure transients (Figures 1.1-2 and 1.1-3). The observed amplitude of the initial

pressure transient is consistent with the fuel vapor pressure predicted by the EXPAND pin failure model (see Section 1.1-3). The channel remained pressurized for ~ 40 ms after the initial transient.

Table 1-1 PBE-14S Initial Conditions and Results

Fuel material	UO_2
Fuel enrichment (% U-235)	14
Polyethylene moderator thickness (mm)	6.35
Initial temperature (K)	773
Initial pressure (MPa)	0.22
Reactor pulse mode	Single maximum
Reactor yield (MJ)	340
Pulse full width at half maximum (ms)	7.1
Maximum radially averaged energy deposition (J/g)	3980
Total energy deposition (kJ)	237
Maximum pressure at top of capsule (MPa)	82
Maximum pressure at bottom of capsule (MPa)	100
Maximum piston kinetic energy (J)	170
Piston energy conversion ratio	1×10^{-3}

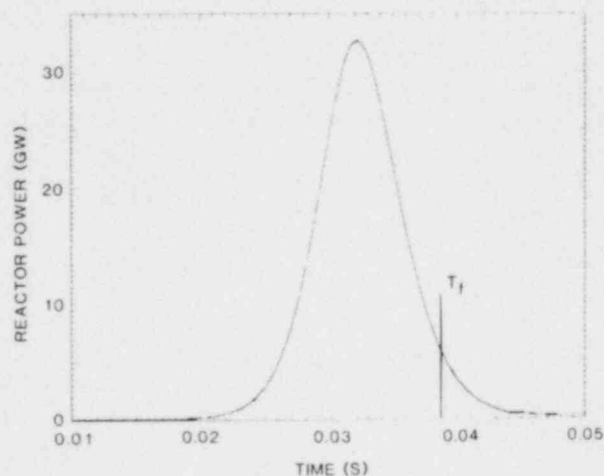


Figure 1.1-1 PBE-14S Reactor Power History (T_f = failure time = 38.7 ms)

A comparison of Figures 1.1-3 and 1.1-4 reveals that a large pressure transient occurred at the top of the capsule following stoppage of the piston. Both top pressure transducers were destroyed during that pressure transient. The transient reached ~ 60 MPa before the transducers were destroyed. Since each transducer was statically calibrated to ~ 60 MPa, it is doubtful that such a transient would destroy the

transducers. Thus, a sharp, high amplitude transient apparently occurred in the vicinity of the transducers between 43.5 and 44.0 ms resulting in their destruction. Lower amplitude (< 50 MPa) pressure transients have been observed immediately following piston stoppage in other PBE experiments^(1-1.1-2); these transients were attributed to FCIs triggered by small pressurizations resulting from deceleration of the sodium slug moving with the piston.

Another pressure transient was observed at the bottom of the capsule ~ 4 ms after the piston stopped (Figure 1.1-2). This transient appears to have resulted from compression of the two-phase region in the central portion of the channel as sodium and pin debris were driven back into the channel by the pressure event occurring at the top.

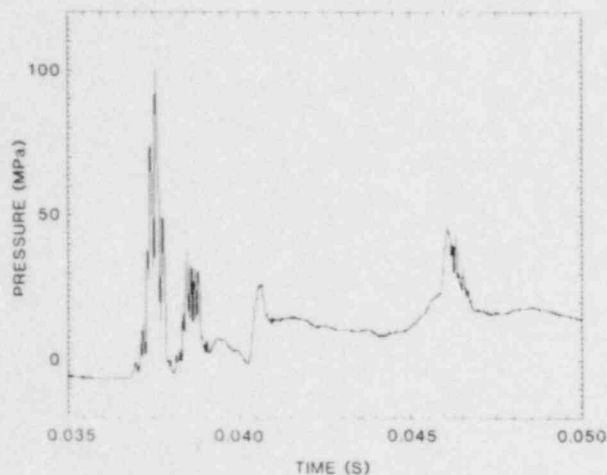


Figure 1.1-2 PBE-14S Bottom Pressure History (Time of peak of reactor power = 32.1 ms)

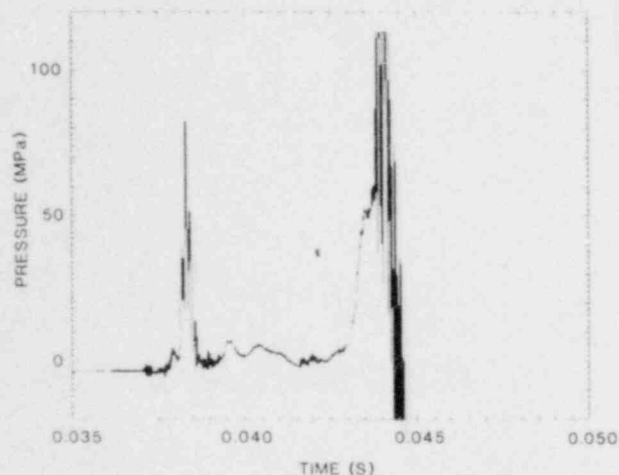


Figure 1.1-3 PBE-14S Top Pressure History (Time of peak of reactor power = 32.1 ms)

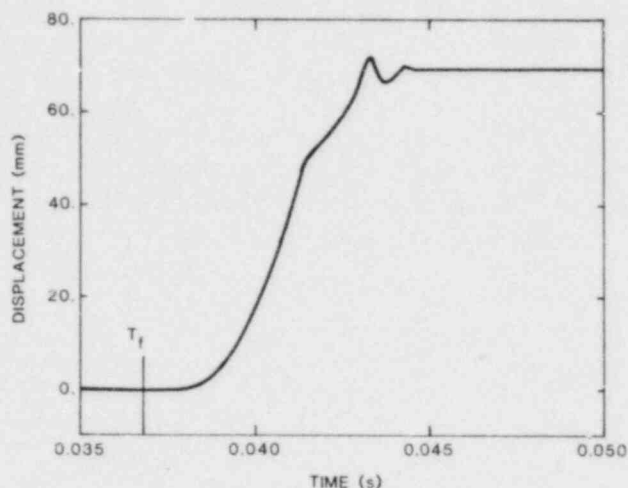


Figure 1.1-4 PBE-14S Piston Displacement History (T_f = failure time = 38.7 ms) (Time of peak of reactor power 32.1 ms)

From the piston displacement history, the maximum kinetic energy of the piston can be derived and was found to be ~ 170 J. When this value is compared to the total fission energy deposited in the fuel pin at that point (~ 166 KJ), the fraction of thermal energy that was converted to work is 1×10^{-3} . This is greater than that observed in other oxide-fueled PBE experiments. Note that, as in previous experiments, significant pressurization occurred following piston stoppage; thus the piston motion reflects only a part of the total work potential of the system.

Pretest and posttest radiographs of the experiment package are shown in Figure 1.1-5. The posttest radiograph shows that the fuel pin was totally destroyed. An accumulation of debris is seen below the core centerline with very little debris above the core centerline. (The fuel column as shown in the pretest radiograph was centered in the ACRR core.) The accumulation of most of the debris in the bottom of the capsule supports the conclusion that the late pressure transient at the bottom was caused by material driven back down the channel. In all but one of the other PBE experiments, the plenum portion of the fuel pin including the top end cap, clad section, plenum spring and scratch gauge was found more or less intact after the experiment. No evidence of this structure is seen in PBE-14S. An image near the top of the debris accumulation may be the scratch gauge. The total disruption of the top of the pin may be the result of the total energy deposited in the fuel or may be indicative of the pressure transient which destroyed the top pressure transducers.

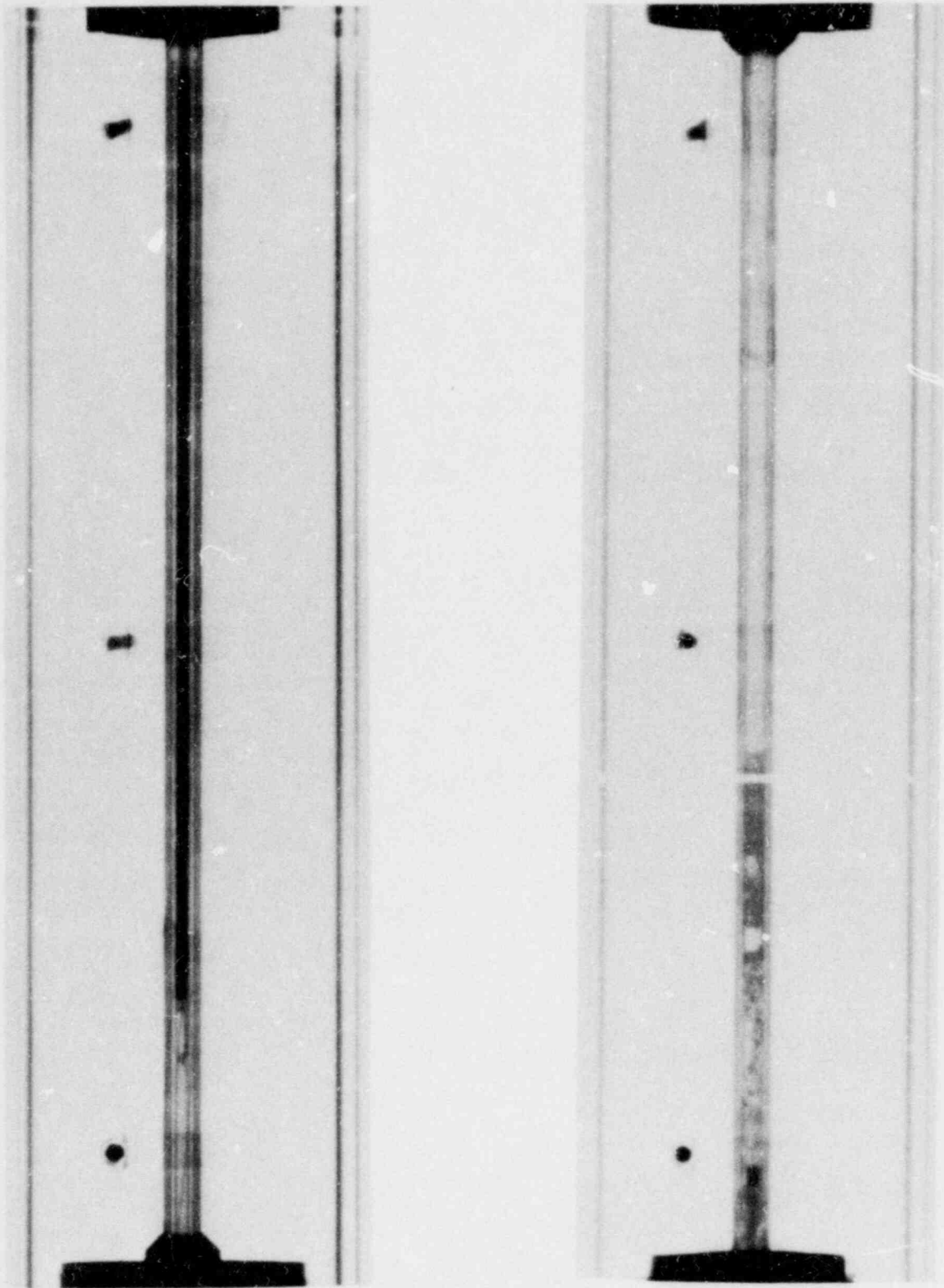


Figure 1.1-5 X-Radiographs of PBE-14S

PBE-14S represents the greatest energy input of any PBE experiment and yielded the most energetic response of any oxide-fueled experiment. The initial pressure transient appears to have been fuel vapor. The balance of the pressure history, particularly the transient following piston stoppage and the slowly decaying sustained pressure that followed, must be attributed to sodium. While different in degree, similar phenomena were observed in other oxide experiments, particularly PBE-9S, PBE-12S, and PBE-13S (see References 1-1 and 1-2).

1.1.3 Preexperiment Calculations for PBE-14S

Preexperiment calculations for PBE-14S, using the EXPAND pin failure model, indicated that the experiment objectives would be met with pin failure occurring at high power on the backside of the prompt pulse.

In modeling PBE-14S, a pulse shape characteristic of the ACPR was used. This pulse shape is narrower (5 ms full width at half maximum—FWHM) than the present ACRR pulse (7 ms FWHM) with a greater fraction of the total energy in the prompt pulse. A coupling factor was chosen to yield ~ 3800 J/g total-radially-averaged energy deposition at the axial maximum. The molten fuel-clad-contact conductance was assumed to be between 2.5 and 5 W/cm² K (the latter value corresponding to previous analysis of PBE experiments) and the stress correction factor was set at 1.5 (see Reference 1-3 for description of these parameters). A radial peak-to-minimum fission-density ratio of 1.44 was assumed. The two values of the contact-conductance gave predicted failure at 2.3 ms after peak power at an internal pin pressure of 59 MPa and at a 1.7 ms with 33 MPa, respectively. The later predicted failure (2.3 ms) is still at high pin power (100 kW/g) and pressure and should result in an initial pressure pulse due to fuel vapor as in PBE-4S through PBE-7S.⁽¹⁻¹⁾

In the experiment the pin failed at 6.6 ms after the power peak. The later failure is thought to be primarily due to differences between the actual power history and that used in the calculations. The calculations will be redone when the actual detailed power history data is available.

1.1.4 AX1 Recalculation

Recalculation of the TREAT carbide fuel test AX1⁽¹⁻⁴⁾ was performed with EXPAND using the stress correction factor⁽¹⁻⁵⁾ and molten fuel-clad coolant conductance (2.5 W/cm² K) determined from the

PBE carbide tests PBE-SG1, PBE-SG2, and PBE-SG3.⁽¹⁻⁵⁾ Failure occurred at 93 ms before peak power for the nominal power calibration (3.34 W/g/MW reactor) and at 70 ms before peak power for 90% of nominal power (3.01 W/g/MW reactor). Internal pin pressure for the nominal case was 1.06 MPa and for the 90% case, 1.07 MPa. The AX1 experiment was observed to fail at 60 ms before peak power.

The error in EXPAND pin-failure predictions depends on the rate of energy input (power level); a rough rule-of-thumb for pin failure at high power (>10 kW/g) is $\pm 5\%$ of the transient time scale, defined as four times the FWHM. Pin power at failure for AX1 was 22 kW/g and the FWHM was ~ 220 ms, thus the expected error in the prediction is roughly ± 40 ms. Both predictions are in rough agreement with the experimental result. This expected error is of the same order as observed error in LAFM predictions⁽¹⁻⁶⁾ for irradiated fuel pins subjected to similar TREAT transients. (Note: Since the time of the AX1 recalculation, the nominal power calibration has been revised downward by 3% to a value of 3.25 W/g/MW reactor.)⁽¹⁻⁷⁾

1.1.5 Calculations for FCI Experiments Involving Coarse Predispersed Fuel Mixtures

Calculations have been completed which investigate the characteristics of the film of boiling sodium around small UO₂ droplets in preparation for the detailed specification of the coarse-predispersed-mixture FCI experiments. In these experiments small particles (1 to 3 mm diameter) of UO₂ will be predispersed in sodium and rapidly heated in the ACRR. Pressures, temperatures, and the conversion of thermal energy to mechanical energy will be measured for both triggered and untriggered configurations. The objectives of these experiments are to determine the capability of the oxide/sodium system to support large scale, propagating, escalating thermal interactions and to map the sensitivity of such interactions to various initial conditions.

In the ACRR the bulk of the energy deposition occurs over about 10 ms. During this heating period stable film boiling is desirable in order to obtain the accompanying low heat transfer rate and high fuel temperature. However, a very thick film, which would be difficult to collapse, is undesirable. Calculations were performed which examine the effect of particle size and sodium subcooling on the stability of the film boiling, on the film thickness, and on the fuel surface temperature.

The analysis was based on a method developed by Kazimi for investigating the dynamic growth of a

vapor film around a hot spherical particle which has been suddenly immersed in a coolant.⁽¹⁻⁸⁾ The following assumptions are made:

- The system is spherically symmetric.
- All the generated vapor is retained in the film.
- A small gaseous film initially exists at the surface of the sphere.
- The pressure in the film is uniform.
- The liquid and vapor are at equilibrium at the film/liquid interface.
- Heat is transferred across the film only by conduction.
- The vapor and gases in the film may be treated as perfect gases.
- Buoyancy effects may be neglected.
- Convective heat transfer in the liquid may be neglected.
- The liquid may be treated either as incompressible or as acoustically infinite.
- The physical properties of the sphere and liquid may be considered temperature independent.

The use of this method for examining the predisposed fuel experiments has several obvious limitations. First, the method examines only the cool-down

behavior of a hot particle initially at a uniform temperature. Second, there is no modeling of phase change in the particle. Work is currently underway to improve the models, but preliminary calculations have been completed using Kazimi's approach.

The primary objective of this study was to investigate the dynamics of the growth of a sodium vapor film around a molten UO₂ particle. Investigators sought answers to the following questions:

- How rapidly does the film grow?
- Does it stabilize?
- What is a typical film thickness?
- What is the sensitivity of the film behavior to subcooling and particle size?
- Does the particle surface remain molten?

Information in all these areas can be obtained by cool-down calculations.

The boiling of the sodium film around UO₂ particles of 0.5 to 2.0 mm radius was investigated for various values of subcooling ranging from 39 to 231 K. The initial UO₂ temperature was 3470 K and the bulk sodium temperature was 920 K. Subcooling was adjusted by varying the pressure in the bulk sodium. The calculations follow the film growth for 10 ms. Table 1-II summarizes the various cases run and the final values for film thickness and UO₂ wall temperature.

Table 1-II Sodium Vapor Film Growth Around UO₂

Radius of UO ₂ (mm)	Sodium Subcooling (K)	Corresponding Pressure (10 ⁵ Pa)	Model ^(a)	UO ₂ Wall Temp ^(b) at 10 ms (K)	Film Thickness at 10 ms (μm)
1	39	0.12	C	3380	39
1	39	0.12	I	3320-3400	13-83
0.5	100	0.257	C	3170	11
0.5	100	0.257	I	3150-3230	6-14
1	100	0.257	C	3250	15
1	100	0.257	I	3200-3280	9-21
2	100	0.257	C	3290	18
2	100	0.257	I	3240-3320	10-38
1	160	0.5	C	3120	8
1	160	0.5	I	3080-3150	6-11
1	231	1.0	C	2960	5
1	231	1.0	I	2680-3120	2-14
2	231	1.0	C	3050	6
2	231	1.0	I	2990-3110	4-9

(a) I = incompressible
C = compressible, acoustically infinite

(b) Melting temperature of UO₂ = 3138 K

For a particle having a 1-mm radius, vapor film and wall-temperature behavior during the calculations are illustrated for various values of subcooling in Figures 1.1-6 through 1.1-9. Predictions from both the incompressible and compressible, acoustically infinite models are shown. The incompressible coolant model predicts a continued oscillatory behavior, while the compressible model shows rapid damping. As these are bounding approximations, the actual behavior is expected to be intermediate. Table 1-II and the figures reveal that both film thickness and particle-surface temperature decrease with increased subcooling. Decreasing the particle size over the range examined had the same effect as increasing the subcooling. In the planned predispersed-fuel experiments a relatively thin film and a molten surface temperature is desired. From the current work, a subcooling of between 50 to 150 K appears to give reasonable conditions for the range of particle sizes of interest.

1.1.6 EPIC Modification

The progressive fuel-fragmentation model for the EPIC FCI code⁽¹⁻⁹⁾ has been debugged. Some further work may be required to extend the code algorithms to handle supercritical sodium; in particular, calculations of channel pressure and energy partitioning are changed if the state of the sodium coolant is off the saturation curve. In this model, fragmentation is controlled by local hydrodynamic conditions in the coolant channel, as interpreted by the assumed fragmentation model. This work and the model used were reported in more detail previously (see Reference 1-2).

1.1.7 Status

Preparations for future experiments are continuing. These include design of a nuclear heated channel boundary for single pin PBE experiments, design of the fuel dispersing system for the Coarse Predisposed Mixture FCI experiments, and definition of instrumentation for those experiments. Long lead time items such as pressure transducers and raw metal stock have been ordered.

An FCI analysis model is being assembled to analyze results of the FCI separate effects experiments using various phenomenological models. The governing equations and possible numerical-solution methods for a one-dimensional FCI analysis code are being researched.

The necessary hardware and software are being assembled to fully use the new data acquisition and display system. When that work is sufficiently complete to permit reduction of the PBE-13S and PBE-14S

data, data reports will be assembled for each of those experiments.

The evaluation of the fast transient response of the Kaman pressure transducers is continuing. This involves the measurement of the transient response by using a shock tube and unfolding that response from the measured pressure data by using an inverse digital filtering technique.⁽¹⁻¹⁰⁾

A report describing the EXPAND fresh fuel pin failure model has been prepared and is being reviewed for publication.

1.2 Irradiated Fuels Response (G. L. Cano, 4423; W. R. Trebilcock, 4424; K. K. Murata, 4425; W. Breitung, 4425; J. Smaardyk, 4422; M. J. McNamee, 5534)

1.2.1 Introduction

The Sandia National Laboratories Irradiated Fuels Response program is aimed at determining the response of fresh and irradiated reactor fuels to both prompt burst (disassembly timescale) and loss-of-flow (LOF) heating conditions. On prompt burst timescales, the pressure source from both fuel vapor and fission gases as well as the accelerations produced by these pressure sources are of central importance. Thus, the program in this area centers on determination of the effective equation-of-state (EEO) of both fresh and irradiated fuels, the dynamics of pressurization (rate effects) and the ability of this pressure to disperse fuel.

On LOF timescales, the modes of initial fuel disruption and its timescale for both fresh and irradiated fuels are of crucial importance. Various mechanisms for disruption have been proposed: liquid fuel slumping, rapid solid/liquid-state swelling, solid-state breakup, and liquid/gas froth formation. Of these, the last two are dispersive and would tend to reduce reactivity, while the first two are not dispersive and thus would not diminish reactivity. Indeed, they could have deleterious effects on the accident progression. Thus, determining the disruption mechanisms operating under various LOF heating conditions is important. To assist in this determination, the FD1 series of fuel disruption experiments was performed and the FD2 series, with significant improvements over FD1, has been initiated. The first series involved multipulse heating of single fresh and irradiated pellets, individually, in the ACPR. Film records of fuel behavior were obtained for all 12 experiments. Significant results from this series include the observation of rapid swelling as a disruption mechanism.

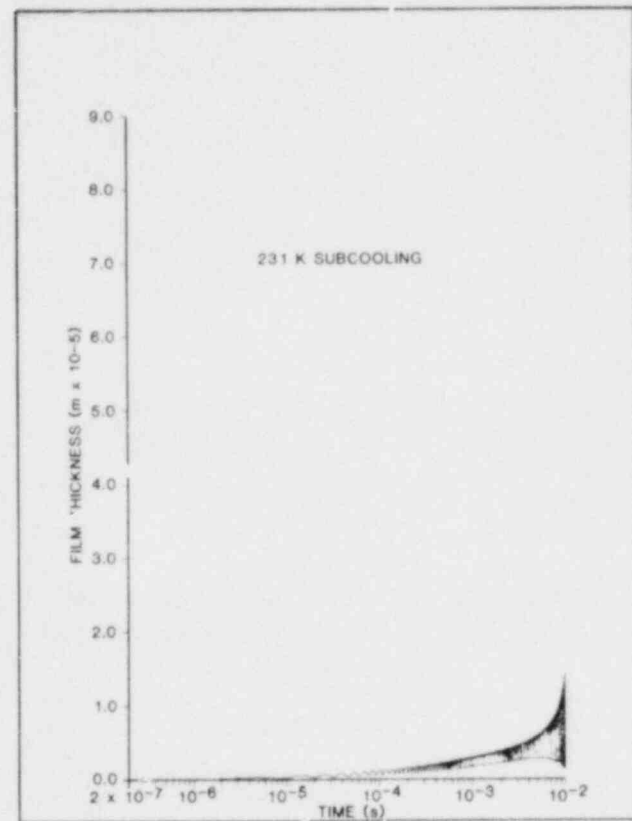
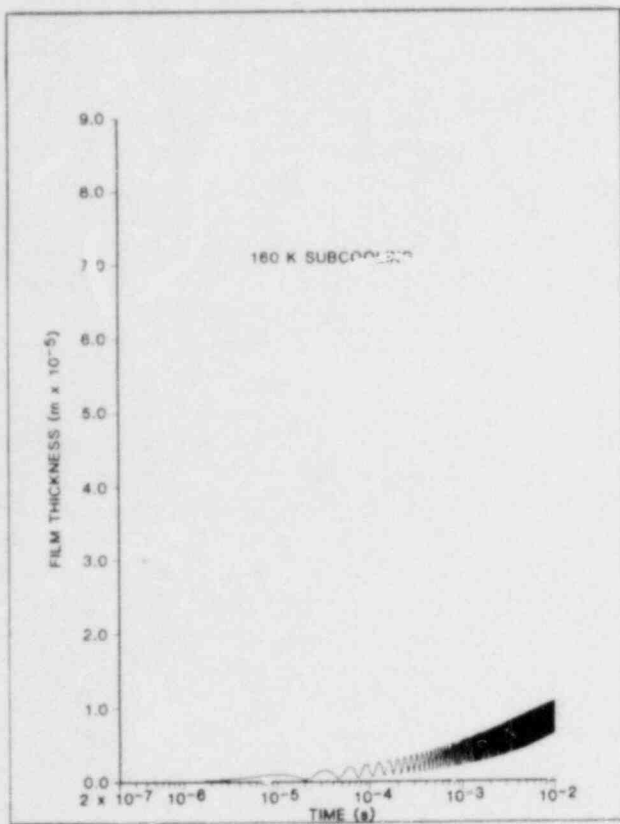
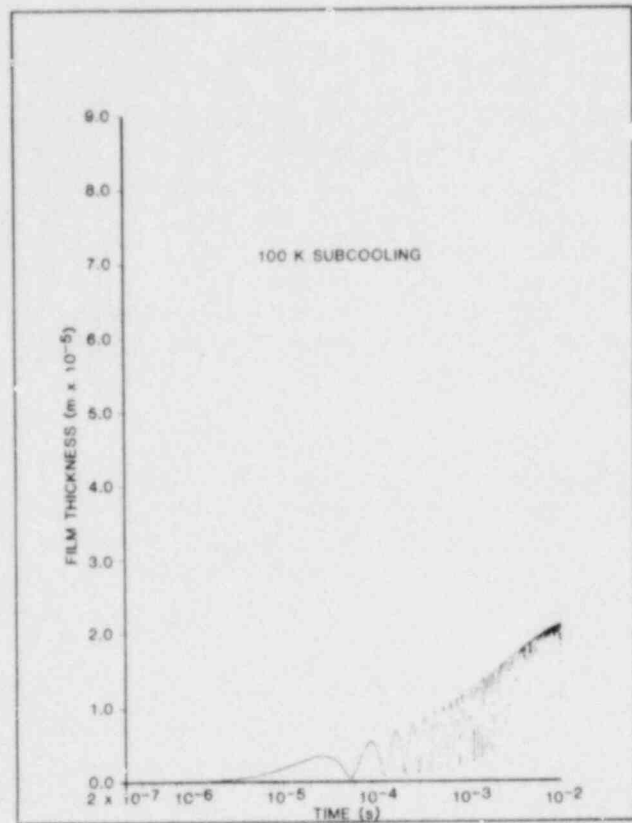
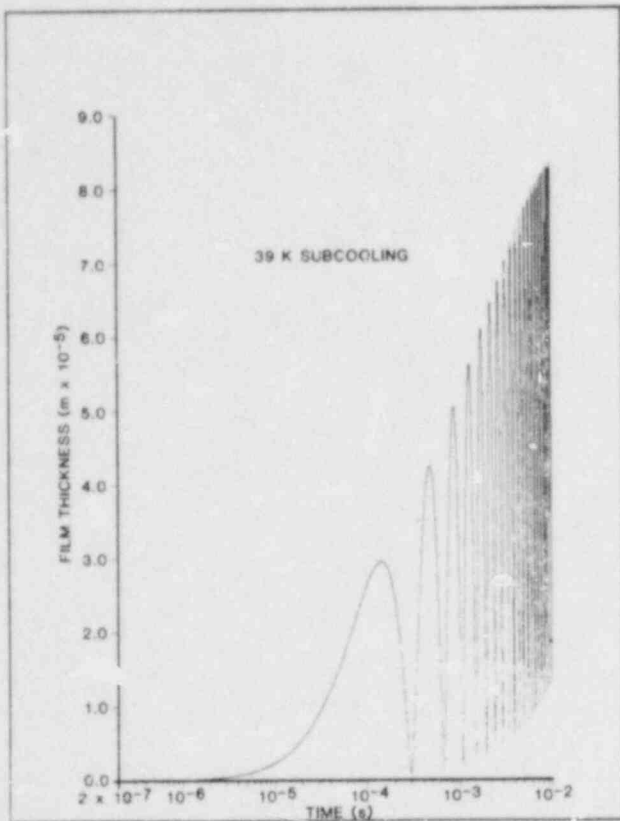


Figure 1.1-6 Film Growth Around UO_2 Particle in Sodium, Incompressible Model

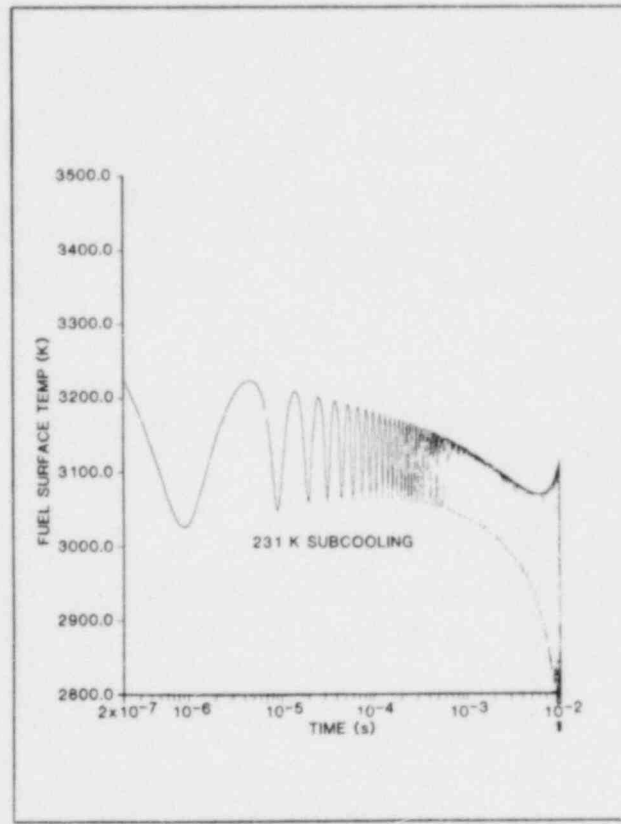
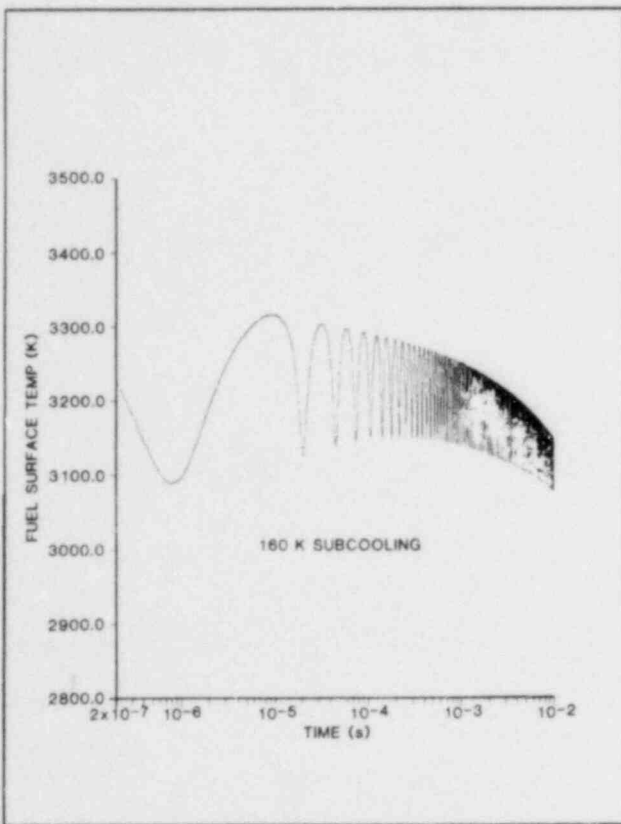
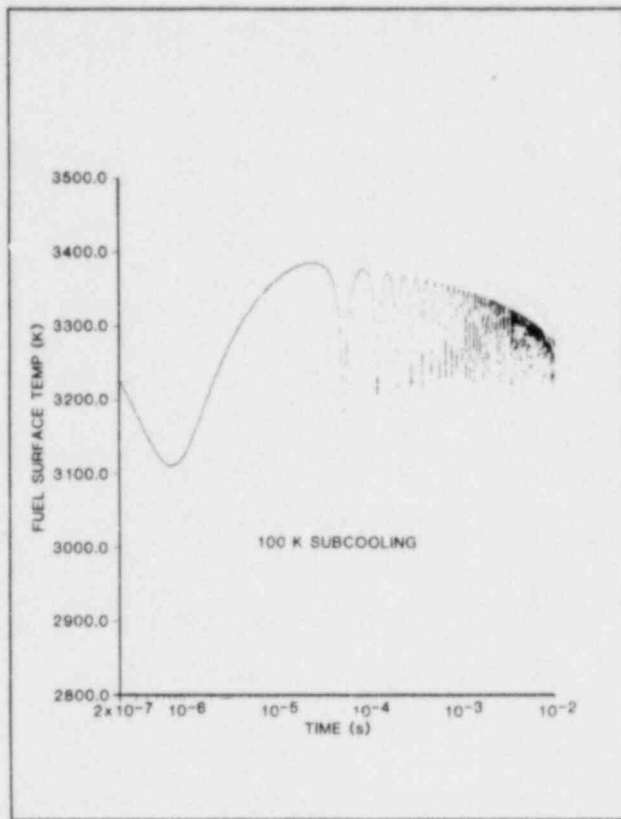
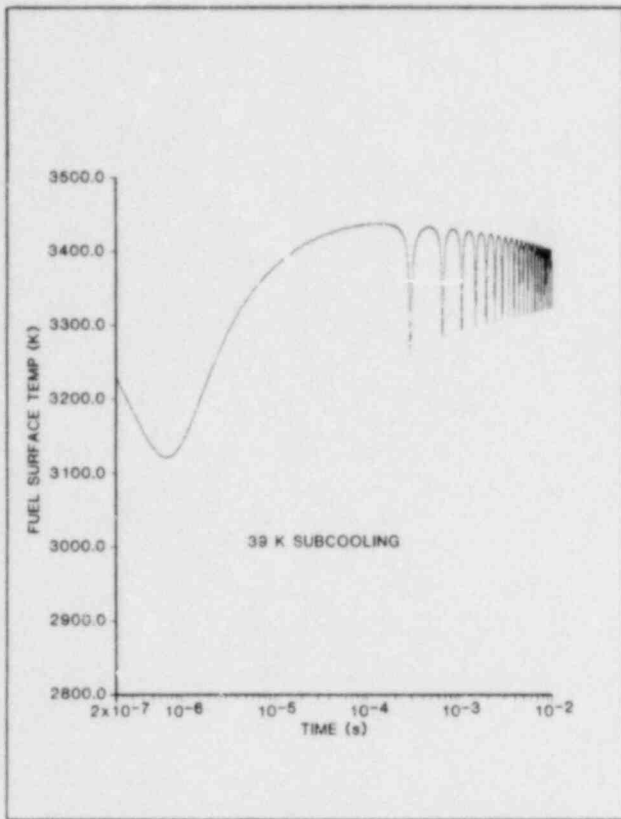


Figure 1.1-7 UC₂ Wall Temperature, Incompressible Model

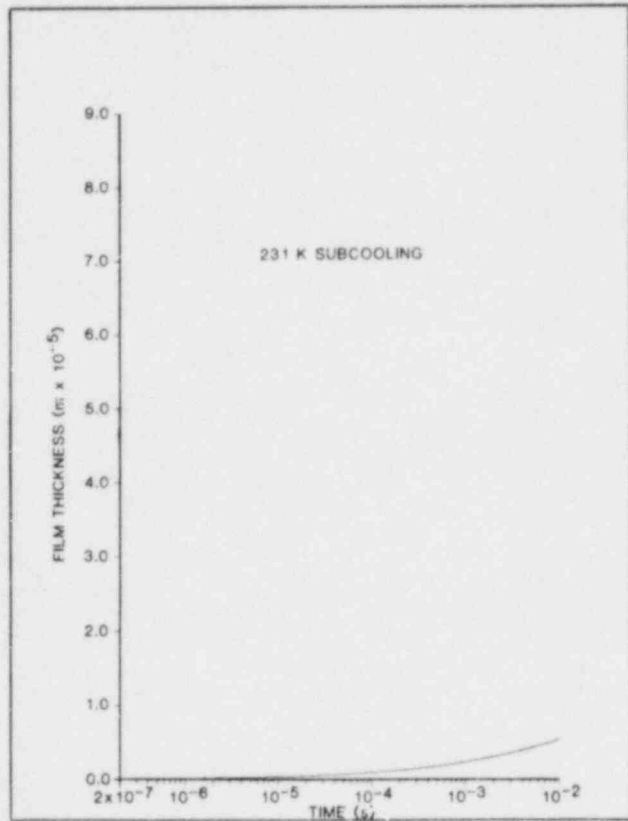
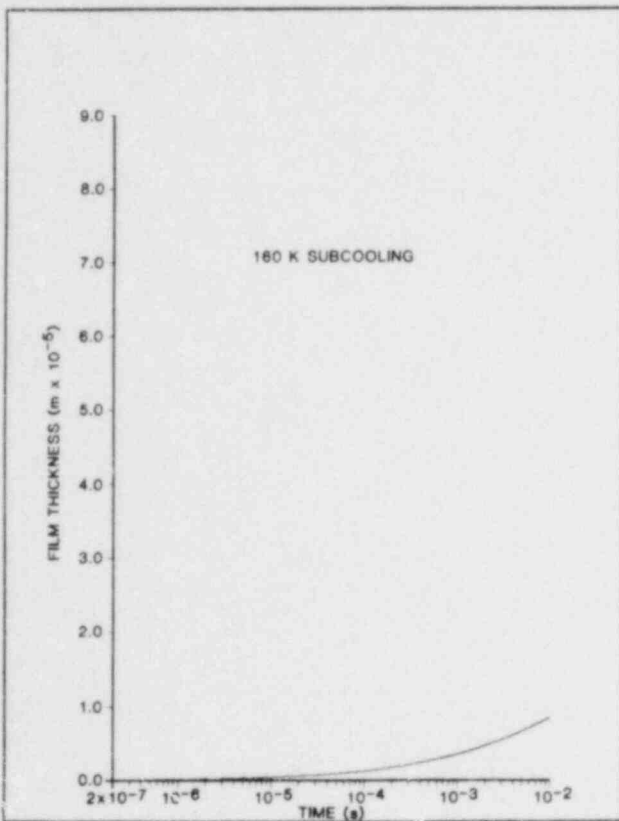
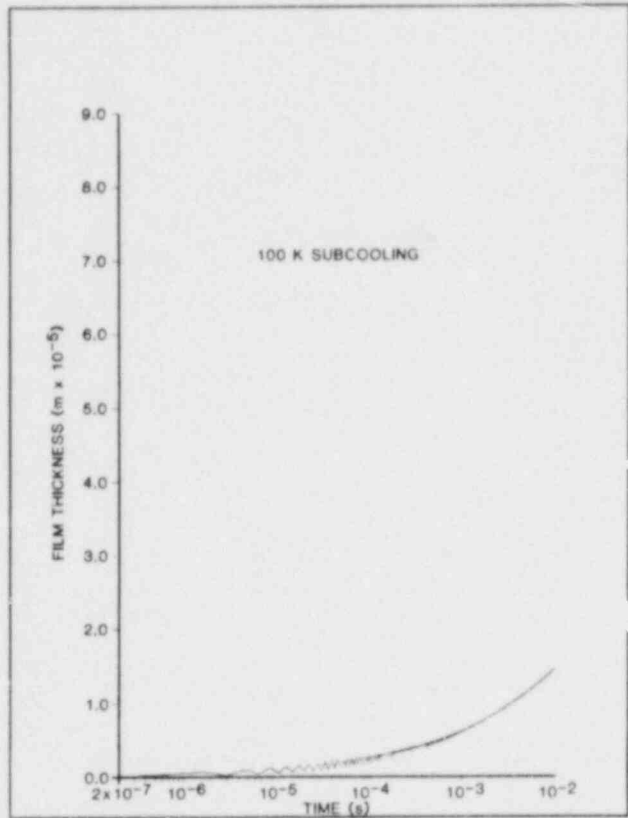
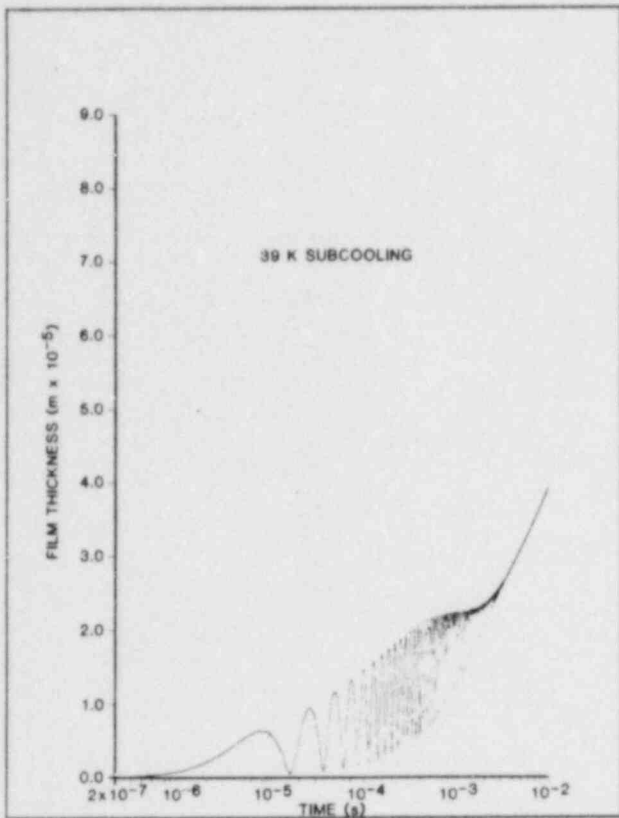


Figure 1.1-8 Film Growth Around UO_2 Particle in Sodium, Compressible Model

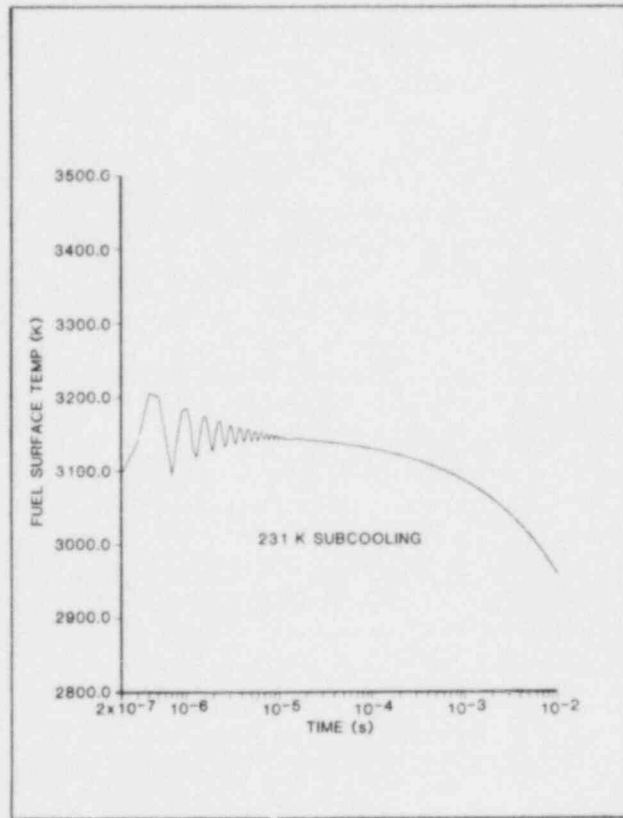
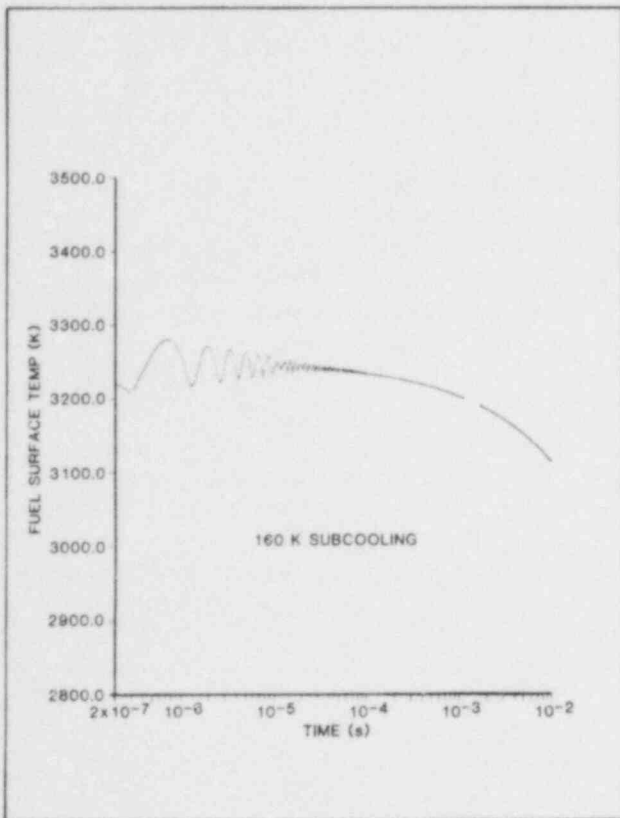
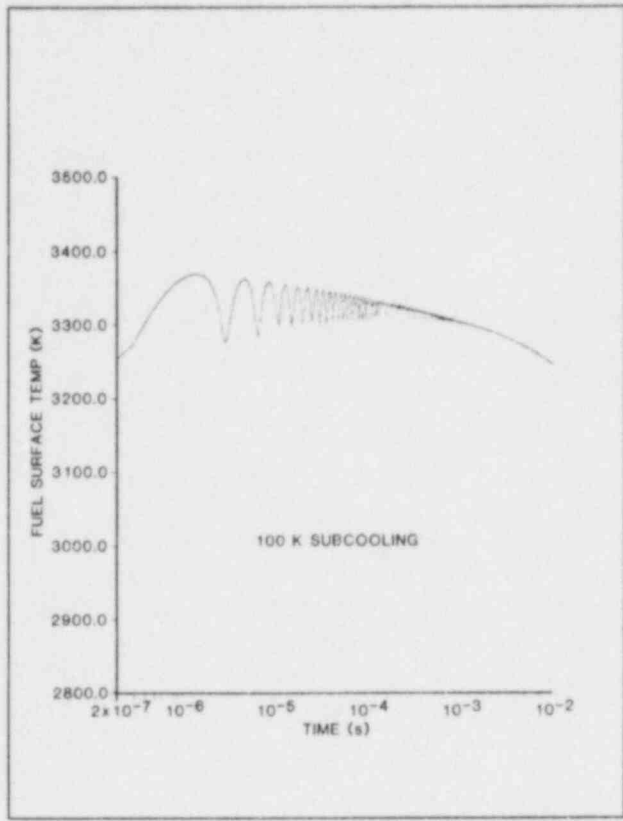
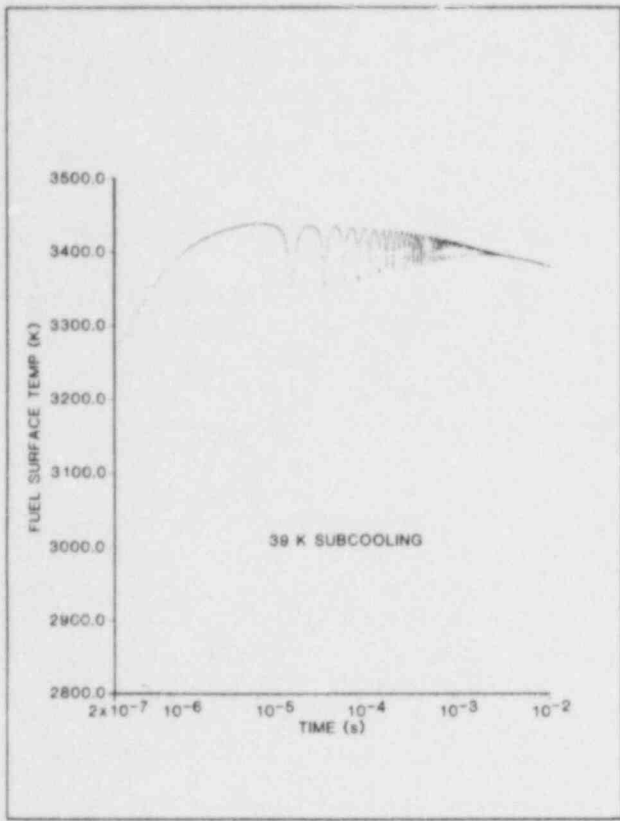


Figure 1.1-9 UO₂ Wall Temperature, Compressible Model

Currently, the experimental program centers on the FD2 series in which larger fuel sections (three pellets) are being irradiated in the ACRR with heating conditions much more typical of LOF conditions than those which were obtainable in the ACPR. Additional improvements include filming of both sides of the pellet stack, gas sampling, dynamic clad thermometry for the fresh fuel, and contamination-free fuel-handling facilities for sectioning the preirradiated fuel. Four tests have been conducted in this series; three used fresh UO_2 fuel, and one used preirradiated, mixed-oxide fuel.

Analytical work in the EEOS and LOF/FD programs continued with neutronic and thermohydrodynamic analysis of the experiments. In the case of the EEOS program, the CSQ hydrodynamics code is being used in an attempt to unfold the equilibrium pressure from the dynamic pressure. In the case of LOF/FD experiments, analysis is being performed with the FISGAS code. FISGAS is intended to calculate fuel mechanics including swelling, cracking, frothing, and gas release. In its current form, FISGAS concentrates on the dynamics of gas release and fuel swelling. An advanced module, TIGRS, which also includes cracking is being incorporated in FISGAS II.

1.2.2 LOF—Timescale Fuel Disruption Phenomenology

1.2.2.1 FD1 Experiments and Analysis

An NRC license to export fuel samples to KfK, Karlsruhe, FRG was received. The fuel includes both irradiated mixed-oxide and fresh UO_2 fuel. The mixed-oxide consists of three half-pellet samples reirradiated in FD1.4, 1.7 and 1.8 respectively, and one half-pellet sample of sibling, irradiated fuel. This mixed-oxide fuel is enriched to 67% effective fissile atoms. The fresh UO_2 samples, enriched to 30% ^{235}U , are in the form of five disks each weighing 1 g.

KfK will perform electron microprobe analysis, scanning electron microscopy and finally, will analyze the total gas content of each sample by dissolving the fuel and spectrometrically determining the constituents. KfK will study the concentration and distribution of fission gases and Cs in the lattice and in the pores, and the distribution and quantity of fission gas bubbles within grains and on grain surfaces. KfK will study and identify metallic precipitates in the central void, and finally, will determine the Pu-distribution. The fresh fuel will be pulse-laser heated to generate UO_2 vapor; vapor pressures will

then be measured. Shipment is scheduled for the next quarter.

A semiempirical dynamic gap-conductance model of the form

$$h_g = A e^{aT^2}$$

is being used in the calculations of heat transfer through the fuel-clad gap for the FD2 experiments conducted so far. This model replaced the constant value that was used in FD1. Preliminary results show $\pm 5\%$ agreement between this representation and four fresh fuel tests. The exponential representation applies only in the molecular flow regime as used in the FD2 tests so far ($\sim < 2$ Torr). At this pressure, gas type is not very important. In the viscous flow regime (as in FD1), the gap-conductance depends primarily on gap width and strongly on gas type. A model for gap-conductance, as used in the EXPAND, and other codes, will be modified and integrated into Sandia's TAC2D heat transfer code. The new model will calculate gap-conductance as a function of pressure and temperature in the gap. The TAC2D calculations will be used with the gas release and swelling code TIGRS to compare fuel disruption calculations with observations.

Two samples of gases which were taken from the disassembling FD2.4 fuel have been analyzed by means of gamma scanning and mass spectrometry. The gamma scanning identified only the condensable fission products and mass spectrometry identified the corresponding non-condensables and also hydrocarbons. The results are very similar for both samples, and include ^{51}Cr , ^{88}Zr , ^{124}Sb , ^{110}Ag , ^{58}Fe and ^{60}Co by gamma scanning, and H_2 , $\text{CO} + \text{N}_2$, O_2 , CO_2 and cleaning solutions by mass spectrometry. Kr and Xe were not detected. This is probably due to the level of detection capability of the spectrometer being about an order of magnitude greater than the expected availability of Kr and Xe. The atmospheric hydrocarbon constituents may have come from the fuel and/or from the residual gases. Relative amounts were measured. Further tests in which greater quantities of gas samples are captured are necessary.

A new simplified optical path has been implemented and tested for the fuel response cinematography. This new system has eliminated two mirrors and now includes an 8-in.-diameter Celestron telescope. The present system allows viewing the fuel directly through the line-of-sight (LOS) tube. The changes have increased the f-number of the optical system by at least a factor of 2; thus, at least four times the light obtained previously is collected now. The two-color optical pyrometer, which was obtained to determine the clad temperature to meltoff and fuel temperature

after clad meltoff, and which was discarded due to light gathering limitations of the old optical system, may now be usable. It will be tested in the next quarter.

The high ramp rate (HRR) experiments to be performed in collaboration with the UKAEA now are planned to commence in June. These experiments will investigate the potential of fission gases to cause fuel dispersal milliseconds before dispersal would occur from fuel vapor pressure alone. A tentative matrix of 10 tests has been defined. The current experiment matrix consists of eight tests using a pellet stack and two tests using powdered fuel. The eight-test series will consist of four contaminated-fuel tests, two uncontaminated fuel tests and two fresh fuel tests. The final two tests will use fuel uncontaminated by atmospheric gases, and which has been pulverized. These powdered-fuel experiments are for direct comparison with results of companion tests in the EOS series.

Preliminary neutronic and heat transfer calculations have commenced for this series. An ACRR double pulse, as in FD1.6, will be used. The first, single-rod pulse will serve to preheat the fuel for a short time (~ 2.5 s) to a specified temperature. The second, or double-rod pulse will take the fuel at $\sim 10^5$ K/s to disruption either by occluded fission gases or fuel vapor generation. Cinematography at 5000 to 10000 frames/s is planned.

1.2.2.2 Proposed Additional Experiments

An additional series of experiments, FD4, has been planned for performance in collaboration with the Nuclear Research Center (KfK) of West Germany. The main reason for these experiments is to determine the response of SNR-300 type fuel to both LOF and LOF/TOP accident simulations. SNR-300 fuel with the requisite parameter values is not available and none will be for about 3 yr. The only fuel available for these experiments was irradiated in PHENIX and is of low (1 atom percent) burnup. Fuel available in the U.S. (some immediately available and some to be obtained), has been proposed for these tests. Besides fuel type, the most important test parameters are the fuel temperature profile at the time of fuel disruption, and the power history. The energy generation profile must be as low as possible to attain these conditions.

A test matrix which includes up to 10 experiments has been proposed. Up to seven of these will be of the LOF variety with the remainder being LOF/TOP type tests. In both test categories, the fuel will be heated at $\sim < 10^3$ K/s to ~ 2100 to 2400 K during the preheat

and then at either 10^3 K/s or 10^5 K/s to disruption, if that occurs.

Neutronic and heat transfer calculations for the proposed LOF experiments have been completed. These include energy generation profiles, temperature profiles, and temperature histories for both bare and filtered neutron-energy spectra from the ACRR. These calculations illustrate that the desired power, energy, and temperature conditions can be met by using available fuel and the ACRR. KfK will evaluate these results and will inform Sandia concerning the KfK views on this proposed collaborative project.

1.2.3 EEOS Preexperiment and Postexperiment Analysis

1.2.3.1 Introduction

In this quarter, the first series of EEOS experiments,⁽¹⁻¹¹⁾ was analyzed to obtain a more precise equation-of-state of UO_2 . Preliminary results of this analysis have already been presented, along with separate neutronic and heat transfer analyses at the Seattle Fast Reactor Safety Conference.⁽¹⁻¹²⁾

Questions as to the numerical accuracy of the 10×10 mesh in the first series have, however, been raised and are presently not resolved. The goal of the hydrodynamic analysis is to reduce the experimental uncertainty of some 20% in the EEOS experiment. This uncertainty is attributed to nonuniform fission-energy deposition in the UO_2 sample. Therefore, a hydrocode should be capable of calculating the energy profile, after dispersal, with considerably less than 20% uncertainty in order for the associated analysis to be defensible. Because of, for example, numerical diffusion in the two-dimensional Eulerian mesh, CSQ may have extreme difficulty in achieving this level of precision on the 10×10 mesh.

To resolve the questions of numerical accuracy, a second analysis series, using 20×30 mesh and 40×60 mesh, has been started. Special techniques, including scaling methods, have also been implemented to reduce the running times normally required by these smaller mesh sizes. The 20×30 and 40×60 mesh sizes normally require running times that are longer than that for the 10×10 mesh by factors of 18 and 144, respectively. The results from the second series will address several questions related to numerical accuracy, and possible improvements to the code, but are still too preliminary to discuss here.

To provide some familiarity with the hydrocode analysis, a brief presentation of the results from the

first series is given in Sections 1.2.3.2 to 1.2.3.7. But, a bottom-line appraisal of the results is being deferred. Consensus on various aspects of the calculation has been delayed because of the absence of one of Sandia's key investigators. A topical report on the first series, however, is being written and will discuss the results in more detail as will future quarterly reports.

1.2.3.2 Equation-of-State of UO_2

Five different versions of the UO_2 equation-of-state (EOS) have been generated and used in CSQ for modeling the EEOS experiments. The pressure-energy relationships (the saturation curve) are plotted for each version in Figure 1.2-1, along with the specific energy of the liquid at melt. As is customary, the energy axis is the specific energy of the condensed phase in Joules/gram, relative to the room temperature value, $E - E_{298}$. The first UO_2 EOS (EOS-1) has been used in the past at Sandia and predicts the solid phase properties of UO_2 quite well. The saturation curve pressure-energy relation, however, is not well represented by this EOS. For this reason, Sandia has not employed it in the EEOS modeling. The second UO_2 EOS (EOS-2) has been used for fast-executing scaled calculations with CSQ which have been reported elsewhere.⁽¹⁻¹²⁾

Relative to the melt-energy or if plotted against temperature, the vapor pressure from EOS-2 lies in the German "best estimate" band. Its apparent shift to the right is due to its poor treatment of the solid-state specific heat at low temperature. Thus, this EOS can only be used with initial conditions near or above melt with an appropriate energy shift. The final three equations-of-state have been used in the CSQ modeling reported here and have been developed to reproduce the Harwell saturation curve (EOS-3)⁽¹⁻¹³⁾ to lie within the German "best estimate" band (EOS-4)⁽¹⁻¹⁴⁾ and to reproduce more closely previous EEOS⁽¹⁻¹¹⁾ and REBA⁽¹⁻¹⁵⁾ series vapor pressure results (EOS-5). The circled points are the REBA results.

1.2.3.3 Experiment Modeling With CSQ

An important consideration in modeling the EEOS experiment series⁽¹⁻¹²⁾ with CSQ, which is an explicit code, has been to keep the running time at a reasonable level. The time steps in CSQ are never longer than the shock-wave transit time in a single cell. For the 10×10 mesh used for most of the results discussed here, the timestep, Δt is of the order of 10^{-7} s. The experimental pressure-energy data are taken

over a duration of 3 ms, requiring 3×10^4 iterations to model the experiment. This is very large and requires ~ 2 hr of central processing time on Sandia's CDC 7600. For this reason, the graphite container could not be modeled. Figure 1.2-2 shows the spatial mesh and initial fuel configuration used in most of the experiment modeling and Figure 1.2-3 shows the energy deposition profile used in most of the experiment modeling.

CSQ cannot exactly simulate neutronic (fission) heating of material because its specific energy deposition rate (watts/gram of UO_2) is space fixed. For the EEOS experiments, the code was set up to deposit specific energy in each of 15 regions shown in Figure 1.2-3 at a normalized rate shown in Figure 1.2-4. The energy deposited in each region has been scaled from Figure 1.2-4 as shown in Table 1-III. The values of the scale factors, in the regions where there is no UO_2 initially, anticipates that dispersal will proceed from disk to "100% smeared" to "shell" geometry as Figure 1.2-5 shows. Comparison of the coded deposition profile from Figure 1.2-3 and Table 1-IV with that of a TWOTRAN neutronics calculations for the geometries in Figure 1.2-5 is shown in Table 1-IV.

Table 1-III Energy Deposited in Each Region, Scaled From Figure 1.2-4

Region	Scale Factors
1, 13	1.03
2	0.89
3, 10	1.00
4, 14	1.09
5	0.94
6, 11	1.04
7, 15	1.18
8	1.11
9, 12	1.16

1.2.3.4 Preliminary Modeling

The parameters of interest for the EEOS-4 experiment are the dynamic pressure on the transducer face and the time-dependent internal energy of the sample. The energy used here in reporting the results of the calculations is the average specific energy deposited in the sample at a given time. In the CSQ and also the experimental pressure-energy relationships discussed here, the specific energy deposited ($E - E_{298}$) can be used interchangeably with that deposited in the predominant condensed phases. Note that the specific energy of the vapor phase is not the same as the condensed-phase energy on the saturation curve, but the vapor phase will not be referenced.

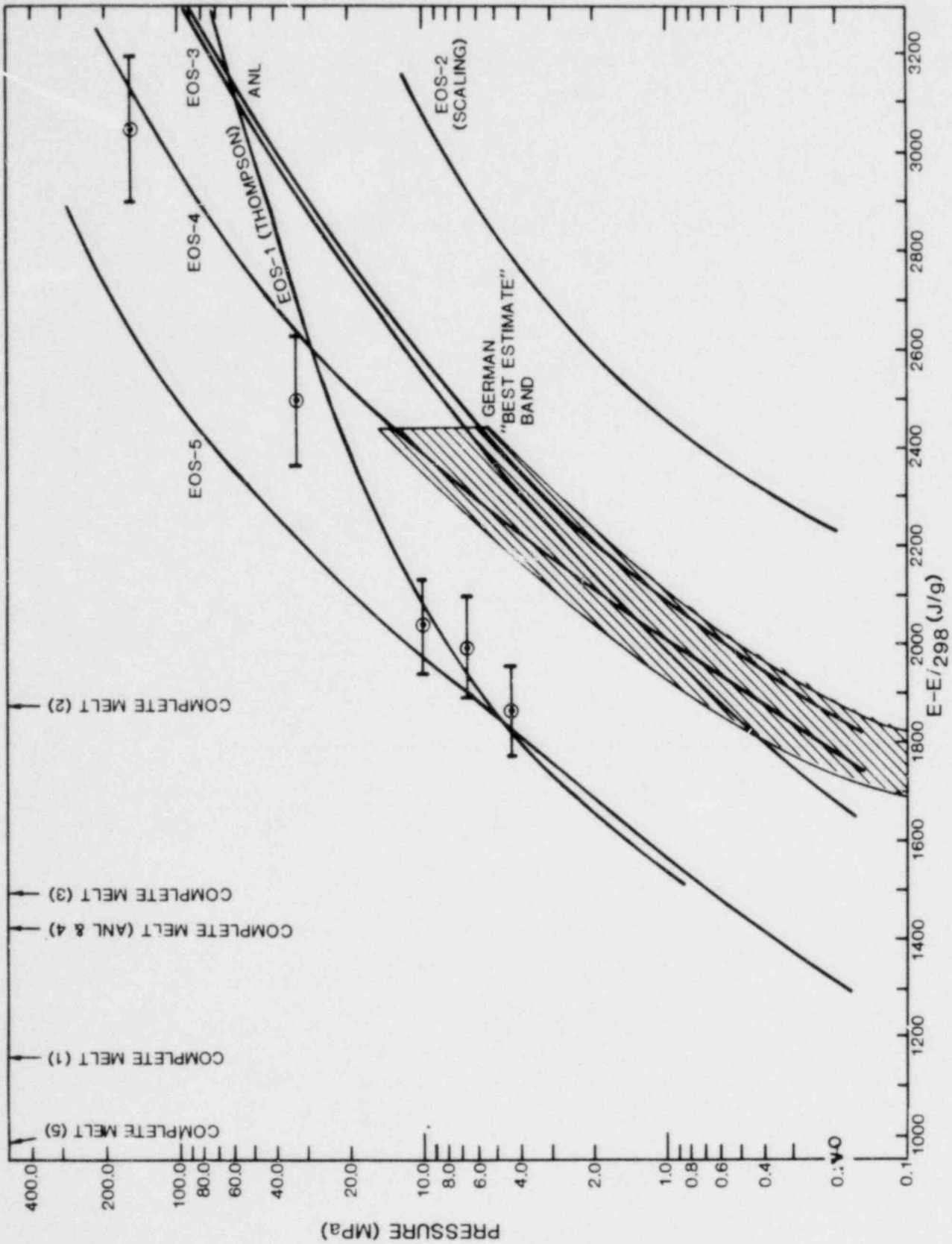


Figure 1.2-1 Pressure-Energy Relationships for Each of Five Versions of EOS

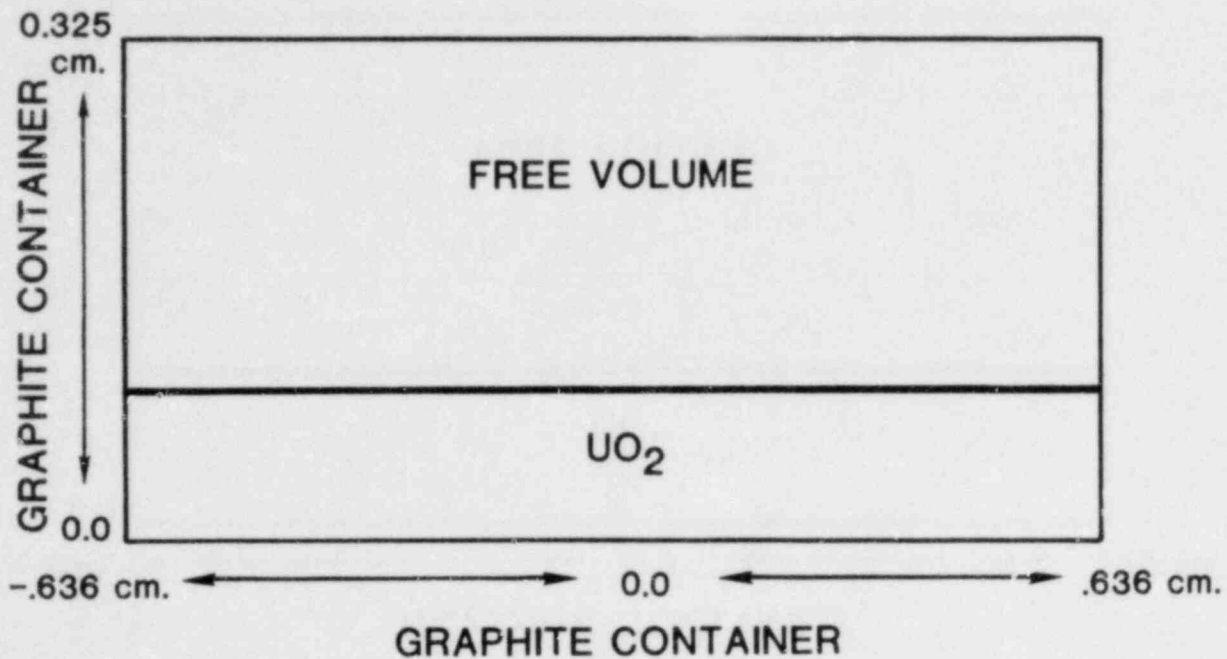


Figure 1.2-2 Spatial Mesh and Initial Fuel Configuration Used in Most of the Experiment Modeling

15	14	13	14	15	1.18
		1.03	1.09		
12	11	10	11	12	1.16
		1.00	1.04		
9	6	3	6	9	1.16
		1.00	1.04		
8	5	2	5	8	1.11
		.89	.94		
7	4	1	4	7	1.18
		1.03	1.09		

Figure 1.2-3 Energy Deposition Profile Used in Most of the Experiment Modeling

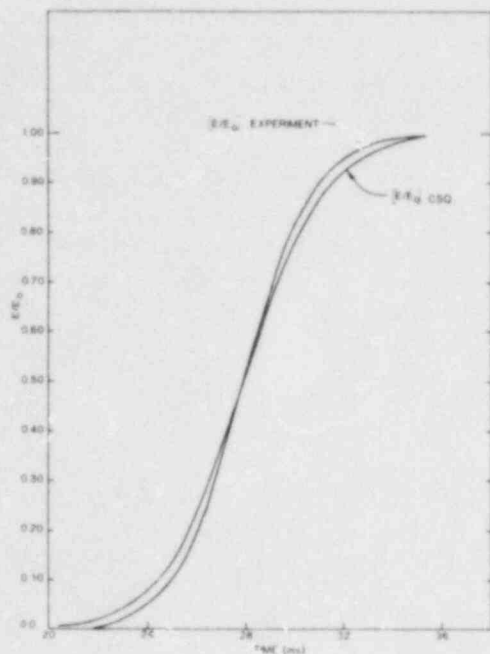


Figure 1.2-4 Normalized Energy Deposition Rate for Figure 1.2-3

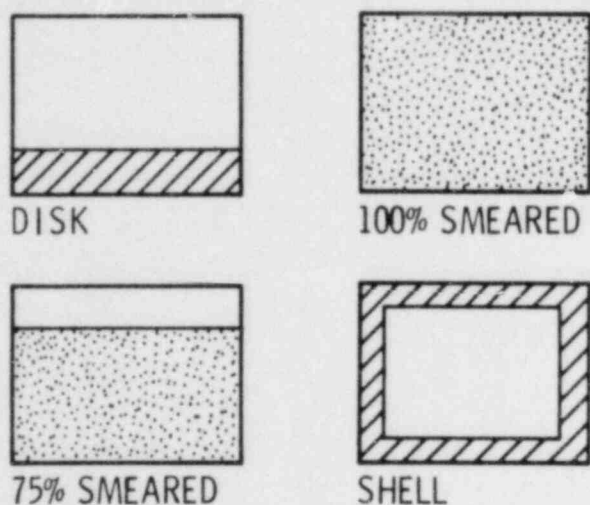


Figure 1.2-5 Fuel Geometries Investigated in the Neutronics Calculations

Initial calculations with CSQ did not include heat transfer. Indeed, calculations C-1 through C-4 with CSQ were scoping and were run under nominal rather than actual conditions in order to investigate the basic characteristics of the code and the important experimental parameters. In addition, these initial runs sought to determine the nature of the UO_2 dispersal predicted by CSQ. These runs will not be detailed here.

1.2.3.5 Modeling of E₂OS-4

To model the EEOS series more closely (in particular, EEOS-4), an additional five calculations, C-5 through C-9, were performed all using EOS-5. In C-5, the calculation was begun at 26.5 ms when the UO_2 has attained a specific energy of $E - E_{298} = 565$ J/g. This is a 1.5 ms before the peak of the reactor pulse at 28.0 ms. All segments of the UO_2 are assumed to be in the solid phase at rest with the added energy distributed throughout the same as in Figure 1.2-3. The UO_2 is assumed to be at 100% density.

The calculation predicts that until 27 ms, the UO_2 remains stationary at the bottom of the capsule. At 27.1 ms, brittle fractures begin and are complete by 27.4 ms. At this point, only small amounts of UO_2 are liquid. Material continues to fracture and disperse, but with less force, so that the effective pressure on the transducer diaphragm decreases to the pressure generated by the vapor only. This occurs at about 27.7 ms. The pressure against the transducer diaphragm after this time is vapor pressure and is shown in Figure 1.2-6 along with the measured pressure in EEOS-4. The circles represent impact pressures.

Table 1-IV Results of Neutronic Energy Deposition Calculations for Different Fuel Geometries Compared to Values Used in CSQ Modeling

Fuel Geometry	Peak to Average Ratio		Peak to Minimum Ratio		Relative Total Energy Input (%)	
	TWOTRAN	Used in CSQ	TWOTRAN	Used in CSQ	TWOTRAN	Used in CSQ
Disk	1.34	1.18	1.53	1.32	100	100
75% smeared	1.25	-	1.49	-	107	-
100% smeared	1.24	-	1.48	1.33	112	104
Shell	1.17	-	1.24	1.15	117	110

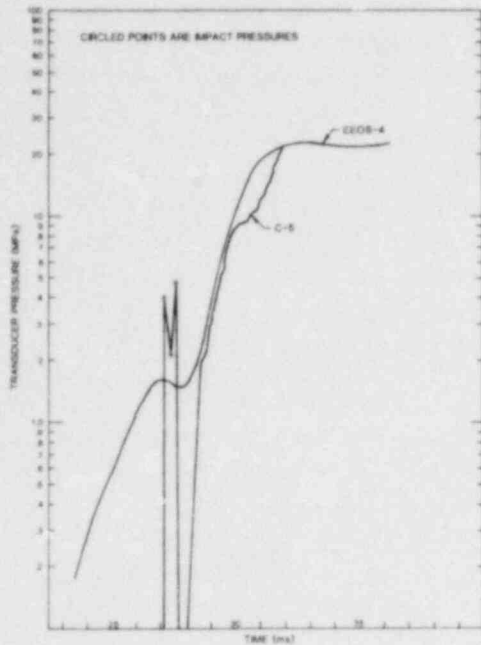


Figure 1.2-6 Vapor Pressure Against the Transducer and Measured Pressure in EOS-4

Because of the energetic early fragmentation, the UO_2 is distributed throughout the free volume in chunks when vapor pressure becomes appreciable. Because of the predispersal, the subsequent vapor-pressure dispersal of UO_2 to essentially uniform densities is rapid compared to that observed in runs started at melt. The vapor-pressure-caused dispersal requires on the order of a few tenths of a millisecond.

Unfortunately in this run, nonuniform energy accounting errors appeared to distort the energy profile even though the average specific energy in the sample was adjusted to follow Figure 1.2-4 with $E_0 = 2257 \text{ J/g}$. The distortion of the profile resulted in an increase in peak-to-average ratio to a value of 1.35 at 27.7 ms from an initial value of 1.18. Thus, the comparison of vapor pressures from this run with experiment and with runs C-6 through C-9 (to be discussed), is difficult even though the pressure-time trace most closely approximated that in EOS-4.

Because of creep and plastic strain (neither of which was present in CSQ in C-5), the fracturing caused by thermal stresses seen in C-5 may not occur. The thermal expansion may also be taken up somewhat by the porosity. Because of these uncertainties, the second modeling calculation, C-6, with EOS-5 was begun when the UO_2 had attained a total specific energy of $E - E_{298} = 1047 \text{ J/g}$ at 27.7 ms (0.3 ms before the peak of the reactor power). Investigators assumed that fuel was at rest at this point, and that fission

energy was distributed within the sample as in Figure 1.2-3. They further assumed the sample to be under a constraint pressure of 0.1 MPa. The hottest part of the fuel was molten, but below the boiling point at 0.025 MPa vapor pressure and the coldest part was well into the melt. Implicit in the condition that the UO_2 is initially at rest is the assumption that surface-tension constraints on the internal porosity serving as nucleation sites minimizes dispersal of the molten outer edges of the fuel before starting. Figure 1.2-7 is the pressure vs time plot.

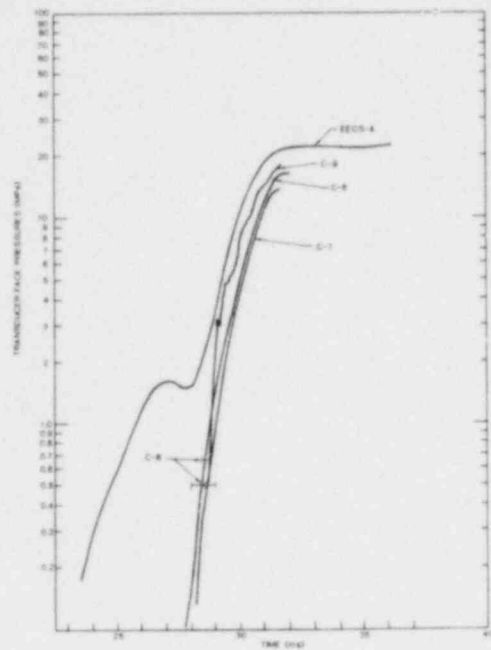


Figure 1.2-7 Results of a 5 x 5 Mesh Calculation

The third calculation, C-7, done with EOS-5, includes heat transfer within the sample and to the surrounding walls. Because the graphite walls were not explicitly included in the CSQ calculation, the temperatures calculated with TAC2D⁽¹⁻¹⁵⁾ have been used. These values are given in Table 1-V. A thermal conductivity for UO_2 of $1.74 \times 10^{10} [T(\text{eV})]^{1.02} \text{ ergs/cm/s/eV}$ was used. In all other respects, the calculation is identical to C-6. Figure 1.2-7 is the pressure vs time plot for this calculation also.

In C-8, only the mesh size was altered; otherwise the calculation is identical to C-6. C-8 used a 20×20 cell mesh and was run only for 1 ms because of the large amount of computing time used. The results are shown in Figure 1.2-7 by circles and coincide exactly to C-6 with a 10×10 mesh. Figure 1.2-7 also shows the results of a 5×5 mesh calculation (C-9).

In Figure 1.2-8, the results of C-6 and C-7 are

plotted vs specific energy deposited in the sample. For comparison, the measured pressure vs energy in EEOS-4 is given, assuming that the energy is deposited along the experimental curve in Figure 1.2-4. (This curve is the integral of the reactor pulse. Geometry changes as in Figure 1.2-5 during the experiment can modulate the energy deposition as in Table 1-IV). Since EEOS-4 is somewhat atypical of the EEOS series, a more representative curve, labeled EEOS-series, is also given. It would be misleading to plot results from C-5 on this figure until the problem of nonuniform energy accounting errors is investigated.

Table 1-V Wall Temperatures Calculated With TAC2D

t Start (ms)	T Top* (K)	T Sides** (K)	T Bottom*** (K)
0	298	298	298
7	298	337	337
8	298	1014	950
9	298	1200	1100
10	1200	1344	1200
11	1300	1400	1300
12	1400	1500	1400
13	1420	1550	1420

*Temperature of inside surface of graphite at top of container.

**Temperature of inside surface of sides of container.

***Temperature of inside surface of bottom of graphite container.

1.2.3.6 Evaluation

The difficulty in EEOS analysis is that the problems of heat transfer, neutronics, and hydrodynamics are coupled. The existence of coupled phenomena severely complicates the prediction of behavior within the experiment capsule. Because of the small sample size, the neutronics could be simplified and calculated correctly by replacing the driver core with a source. But, on the other hand, the large surface-to-volume ratio and the fact that thermal diffusion lengths are not completely negligible compared to sample size means that intercellular heat transfer should be included. The CSQ hydrodynamic code with well-developed EOS, quasi-static energy source, and heat transfer options provides a calculational tool, but because of its explicit nature and lack of neutronic options, it is not entirely appropriate.

CSQ has been used here to attempt to plot the

equilibrium vapor pressure vs energy relationship which will produce the dynamic pressures measured in the EEOS experiments. Dynamic pressures have been calculated explicitly for comparison to EEOS-4. However, for reasons discussed in the introduction, an analysis of the errors in the calculations has been deferred and will not be presented here.

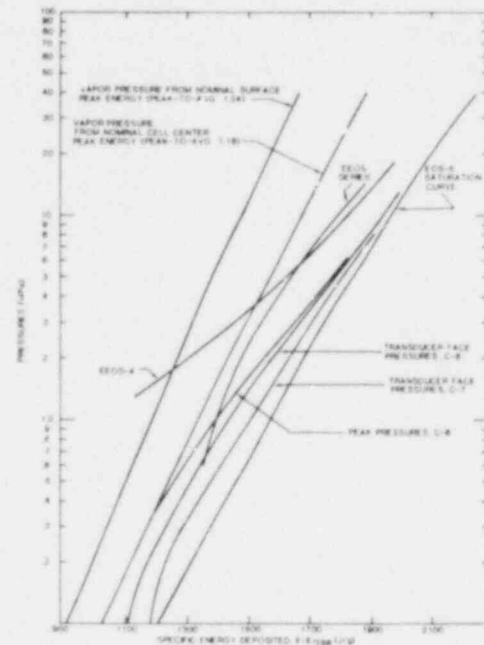


Figure 1.2-8 Results of C-6 and C-7 Specific Energy Deposited in the Sample

1.2.4 Occluder Neutronic Design of the New EOS Experiments

The current design philosophy for the new EOS experiments is to ensure, if possible, that uncertainties in experiment analysis do not lead to uncertainties of greater than 7% in the energy corresponding to the experimentally measured pressure. This objective can apparently be achieved in the ACRR for fresh fuel by careful neutronic design. After designing for low peak-to-average energy deposition, the only requirement is to assure that heat transfer cannot decrease the peak energy in the sample below some bound, for example, the average energy deposited during the measurement time. Such bounds using worse case estimates are probably much more reliable than pinpointing the actual energy in an uncertainty band initially much broader than 7%.

The TWOTRAN calculations discussed here incorporate a short cylindrical gold filter positioned as shown in Figure 1.2-9 some distance from the fuel

disk. The filter in this geometry is primarily a solid angle occluder, the isotropic flux in the filter mid-plane in the absence of the fuel disk decreases as a function of radius from solid angle considerations. The normal increase in fission density with radius in the fuel disk can thereby be offset and even reversed as Figure 1.2-10 shows. Although TWOTRAN is not capable of more elaborate occluder designs, split ring and double ring designs could be considered in principle to gain more flexibility in tailoring the radial profile.

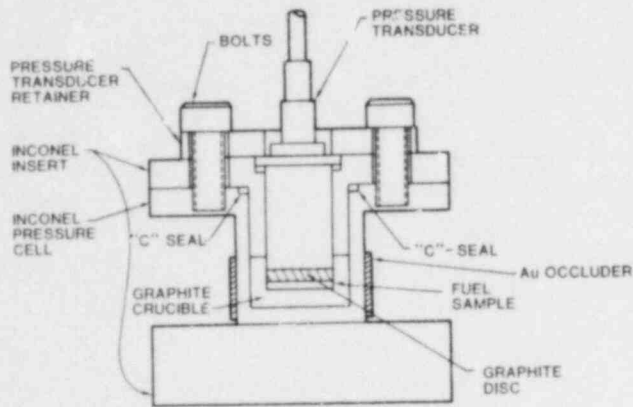


Figure 1.2-9 Cross Section of EEOS Pressure Cell

TEST CASE:
GOLD OCCLUDER-
NOMINALLY 1.0 cm. HIGH
.15 cm. THICK

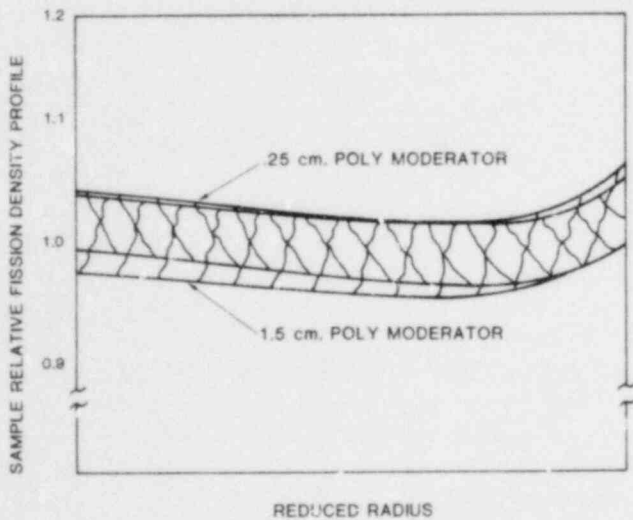


Figure 1.2-10 Relative Fission Density Profile vs Radius for Gold Occluder

The thickness of the fuel disk can be adjusted to minimize the axial variation of the energy deposition, but, the practical lower bound is determined by heat transfer considerations.

A test-case TWOTRAN calculation for the geometry in Figure 1.2-9 gives a radial variation for the energy deposition in the fuel disk as shown in Figure 1.2-10. This calculation corresponds to 1 g of 15%—enriched UC fuel at 50% density and a gold occluder nominally 1 cm high and 0.15 cm thick. A lower Inconel plate is included in the calculation to assure top-to-bottom symmetry along with top and bottom polyethylene reflectors (not shown) and a tall cylindrical polyethylene moderator (not shown). The bands for different moderator thicknesses represent the probable peak-to-minimum axial variation at a given radius. The axial variation could not be calculated with any certainty, due to what is believed to be a space mesh-angular quadrature interaction effect and an inadequate angular quadrature (S16). Attempts were made to use nonstandard angular quadrature sets but were not particularly successful. The uncertainties in the bands in Figure 1.2-10 correspond to peak-to-average values between 1.07 and 1.03. The variation in the disk-core energy coupling factor with moderator thickness is shown in Figure 1.2-11.

TEST CASE:
GOLD OCCLUDER-
NOMINALLY 1.0 cm. HIGH
.15 cm. THICK

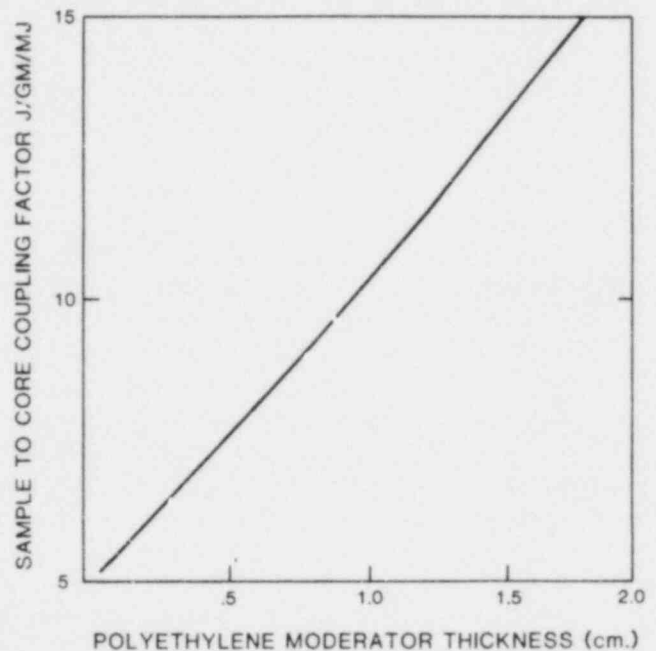


Figure 1.2-11 Quantitative Estimates of Typical Fuel Pressure Sources

1.2.5 Contamination Control in Sandia EOS Experiments

This quarter, the design of a cleaning and handling procedure for the EOS experiment series at Sandia was completed and documented. The aim is prevention of additional pressure contributions from contaminant substances. For the design of this procedure, the various aspects of the contamination phenomenon were investigated in detail.⁽¹⁻¹⁸⁾ The main results are:

1.2.5.1 Starting Point of Contamination

There are two sources for contaminant pressures in EOS experiments, namely fuel contamination and crucible contamination. To determine which contributions from these sources are tolerable in EOS experiments, quantitative estimates were made of the reactor-typical fuel pressure sources (Source C in Figure 1.2-11). Two results from this estimation are noteworthy.

- Prototypical fuel impurities which must be considered typical of the particular reactor, represent a pressure source which has the potential for dominating the pressures contributed by pure or even irradiated fuel (Figure 1.2-12). So far, this pressure potential from fuel impurities has not been accommodated in EOS studies on nuclear fuels. They very likely contributed to the pressures measured in closed in-pile volume experiments.⁽¹⁻¹¹⁾
- The experience from the VIPER experiments has demonstrated that pressures from fuel and crucible contaminants can easily invalidate the results of in-pile EOS measurements on nuclear fuels, sources D and E in Figure 1.2-12. Thus, ultra-pure environments are required for the EOS-test preparation.

1.2.5.2 Required Degree of Cleanliness

The desired upper pressure limit from contaminants is determined by the pressure transducer resolution, which translates into about 1 μmol of contaminant gases in the EOS capsule. If this quantity is expressed as the number of monolayers which can be formed on the available fuel and crucible surface, it is equivalent to three monolayers for PNL 9, 10, 11 fuel.

1.2.5.3 Contamination Causes

Contamination of a particular part requires a source of contaminants and a transfer mechanism. The following transfer mechanisms exist in the EOS experiment preparation:

- *Direct Contact* The contamination potential from direct contact is rather large because only a few tens of micrograms of volatile materials are tolerable in the EOS experiments. As an example, one single fingerprint can be transfer 10^{-4} g.
- *Physical Adsorption* Physisorption of gases or vapors from the atmosphere can result in multilayer formation on the substrate. Therefore, physisorption was investigated in detail with respect to its general properties, the attractive forces and heats of physical adsorption. A kinetic adsorption model was set up to determine the gases and p-T-conditions for which multilayer physisorption has to be expected. It turns out that gases capable of multilayer adsorption during the experiment preparation are polar gases having a critical temperature above 300 K. The most important gases of this class are water vapor and polar hydrocarbons which can be very abundant in ambient air (Table 1-VI). The kinetic model predicts that at room temperature partial pressure less than 1 Pa (which corresponds to 10 ppm at 1 bar) are required to keep the surface coverage below one monolayer. Other gases, in air or in the hot cell atmosphere, are not critical for the contamination of EOS experiment parts.
- *Chemical Adsorption* Chemisorption may be regarded as a chemical surface reaction. It is a single layer process because there are no longer binding forces available once the adsorbing surface is covered with a complete monolayer of adsorbed molecules. Since monolayers of contamination are tolerable for the EOS tests, and since chemisorbed molecules are in general strongly bound, chemisorption is not critical.
- *Bulk Absorption* Both physical and chemical adsorption of molecules can give rise to bulk absorption. However, at or slightly above room temperature, absorption proceeds slowly because either an activation energy or slow non-activated transport is involved. Thus, investigators expect no significant bulk absorption of gases during handling of EOS experiment parts. On the other hand, the existing bulk gas within pressure cell components must be removed prior to the EOS experiment.
- *Deposition of Aerosols* Exposure of surfaces to an atmosphere results in deposition of solid or liquid airborne materials (aerosols). The most important transport mechanisms are sedimentation under the influence of gravity, and

movement of the suspending atmosphere itself. Aerosols that come into contact with a solid surface will adhere to it due to bonding forces. Liquid aerosols almost always spread into thin films spontaneously. Solid aerosols can be very strongly bound with forces equivalent to up to 10^5 g.

1.2.5.4 Contamination Sources

The contamination sources present in a given technical process depend on the materials involved, process parameters and handling. Contamination sources common to many procedures and environments, and thus also important for EOS experiments, were collected from the contamination literature (Table 1-VII). Two unexpected sources are low-molecular-weight hydrocarbons which are added to virtually all plastic materials to increase their flexibility

(plasticizers), and a wide variety of human contamination (skin components, cosmetics, smoking).

1.2.5.5. Removal of Contamination

From a review of the relative effectiveness of available cleaning techniques, costs and influence on the base material properties, the following cleaning processes appear appropriate for pressure cell components:

- Solvent cleaning combined with mechanical and ultrasonic cleaning
- UV-ozone cleaning
- Thermal treatment, and eventually, if necessary
- Plasma cleaning.

Table 1-VI Critical Temperatures and Concentrations of Gases Expected in Handling Atmospheres

Component	Critical Temperature (K)	Expected Content in Laboratory Air (Vppm)	[Volume ppm] in Hot Cell Atmosphere
N ₂	126	780 900	
O ₂	155	209 500	
CO ₂	304	300	
Ar	151	9 300	>55.5%
Ne	44	18	
He	4	5	Other gases < 10 ppm (design goal)
Kr	209	1	
H ₄	181	2	
H ₂ O	647	11 500 (293 K, 50% rel. hum.)	
CO	133	5...50†	
Hydrocarbons*	{ 300 to 600 K (for 2 to 6 atoms of C, N, O or Cl)	0.1...2+ (vapors) 3800 weight ppm (sol. + liq.)	
N ₂ O*	310	---	
NO	180	} 0.05...1.3†	
NO ₂ *	431		
O ₃	268	0.5...3†TC	
SO ₂ *	431	0.15...7†	

* Gases capable of multilayer adsorption at room temperature.

† Nonsmoggy day in Los Angeles.

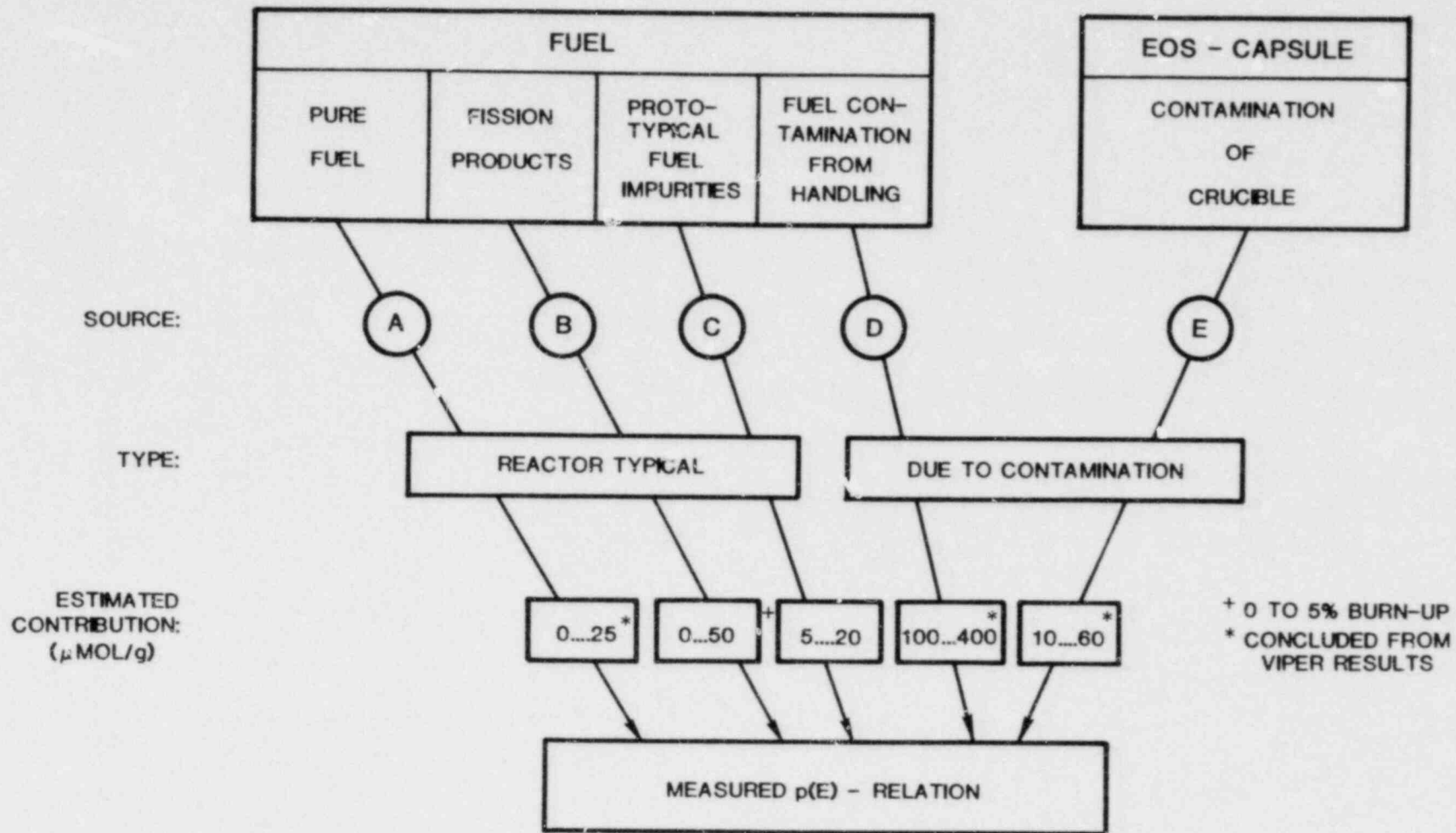


Figure 1.2-12 Pressure Sources Contributing to Measured $p(E)$ Relation

Table 2-7/II Classification of Common Contamination Sources

State of Contaminant	Mode of Contamination Transfer	
	Direct Contact of Condensed Phases	Transfer From Ambient Atmosphere
Gaseous		Atmospheric gases (O ₂ , N ₂) Atmospheric vapors (H ₂ O, hydrocarbons) Impurities in bottle gases Vacuum pump exhausts Gases from cured resins (H ₂) Plasticizers Human breath
Liquid	Cutting fluids (H ₂ O, oils) Grinding, polishing, buffering compounds Cleaning solvent residues Machine oils Grease Skin oils (finger prints)	H ₂ O droplets Water soluble acids Pump oils Bearing lubricants Fluxes Human breath
Solid	Rust, scale Nonadherent metal oxides Metallic microfragments Cosmetics Perspiration salts (finger prints) Human hair	Dust particulates Microbial contaminants Clothing fibers Skin flakes Smoking residues

Also addressed were the problems of recontamination, storage and transport of cleaned samples. Experiments described in the literature lead to the conclusion that exposure of a cleaned sample to ambient air will result in significant recontamination with water in less than 1 min and with hydrocarbons in 10 min. Cleaned samples must be stored and transported in cleaned stainless steel containers containing a high purity inert gas.

1.2.5.6 Measurement of Residual Contamination

Information will be needed about the actual surface states at different stages of cleaning and processing. A survey of the available techniques for contamination detection revealed several suitable spectroscopic methods:

- Electron spectroscopy for chemical analysis (ESCA)
- Auger electron spectroscopy (AES)
- Secondary ion mass spectroscopy (SIMS)
- Mass spectrometry in the UHV-system.

With SIMS, all the relevant elements (H, C, N, O, Ar) can be detected. More suitable for bulk analysis are

- X-ray fluorescence analysis (XFA)
- Electron microprobe analysis (EMP).

All these spectroscopic techniques are available at Sandia.

Proper indirect methods for the detection of hydrocarbon contamination are

- The water break test which examines the wetting behavior of water
- Measurement of the contact angle of water on the sample surface.

The wetting behavior of water was investigated theoretically. Based on the available surface energies of various substrates, water should spread spontaneously on clean solid inorganic surfaces like glass, oxides, and hard metals. Already a fraction of a monolayer of water-insoluble hydrocarbon contamination on these surfaces causes nonwetting. Contact angle measurements yield numbers which are directly related to the hydrocarbon coverage of the test surface. This can be used to control working environments by measuring contact angles as a function of time or environment parameters.

1.2.5.7 Preparation Route for EOS Experiment

Components:

- Pressure Cell Components** Cleaning is designed to be done in three different environments with increasing degrees of cleanliness (Table 1-VIII). Because physically adsorbed multilayers of water and hydrocarbons are expected to be major causes for contamination, the least two cleaning steps especially aim at removal of these compounds. The flow of pressure cell components through the various stages of cleaning and processing is summarized in Figure 1.2-13.
- Fuel** The EOS fuel must be characterized prior to the experiments with regard to its chemical composition and physical structure. The designed preparation route tries to retain the fuel in a prototypical state. Maintaining this state requires avoidance of contamination via the various transport mechanisms (see section 1.2.5.3) and no loss of prototypical fuel pressure sources like gases and fission products. A procedure for the preparation of clean fuel powder has been proposed. At present, investigators plan fuel cleaning only by means of the final bakeout in the UHV-system prior to EOS cell closure in situ. Figure 1.2-14 summarizes the flow of fuel material through the various stages of processing. Figures 1.2-13 and 1.2-14

also show the most important points for contamination control. The information from contamination measurements will be used to confirm or improve the designed preparation route.

1.2.6 UO₂ Heat Capacity Experiments

1.2.6.1 Dynamic Heat Capacity Measurements on UO₂

High temperature properties of UO₂ are required for thermal transient calculations of reactor systems under accident conditions. In particular, the heat capacity of UO₂ in the solid phase is needed to establish the initial energy state for these calculations. Previous vaporization experiments by Benson⁽¹⁻¹⁶⁾ and others suggest that the heat capacity of UO₂ is heating-rate dependent. A dynamic heat capacity model has been proposed^(1-16,1-17) in which the instantaneous heat capacity varies from 1.0 to about 0.5 times the equilibrium values in the temperature range from 1500 K to melt. The difference between the instantaneous and equilibrium values has been attributed to the formation and diffusion of defects with characteristic relaxation times of up to several tens of milliseconds.

Table 1-VIII Summary of Cleaning Steps for EOS Pressure Cell Components

Contamination Source and Expected Contaminants	Primary Cleaning	Secondary Cleaning (Combined With Storage)	Final Cleaning
1. Contact Contamination	Mechanical cleaning in water-ethanol, affected: B, C	UV-ozone cleaning supported by active adsorbents for water and hydrocarbons	Heating in UHV - system to 500 K
Gross hydrocarbons A			
Inorganic salts B			
Particulates C			
	Ultrasonic cleaning in trichlorethylene, A, F	Affected contaminants: E, F	Affected contaminants: E, F
2. Airborne Contamination	Ultrasonic cleaning in water ethanol, affected: B, C, D		
Particulates D			
Water E			
Film hydrocarbons F			
	UV-ozone cleaning prior to outgassing affected: A, F		
3. Bulk Gases G	Outgassing in vacuum affected: G		

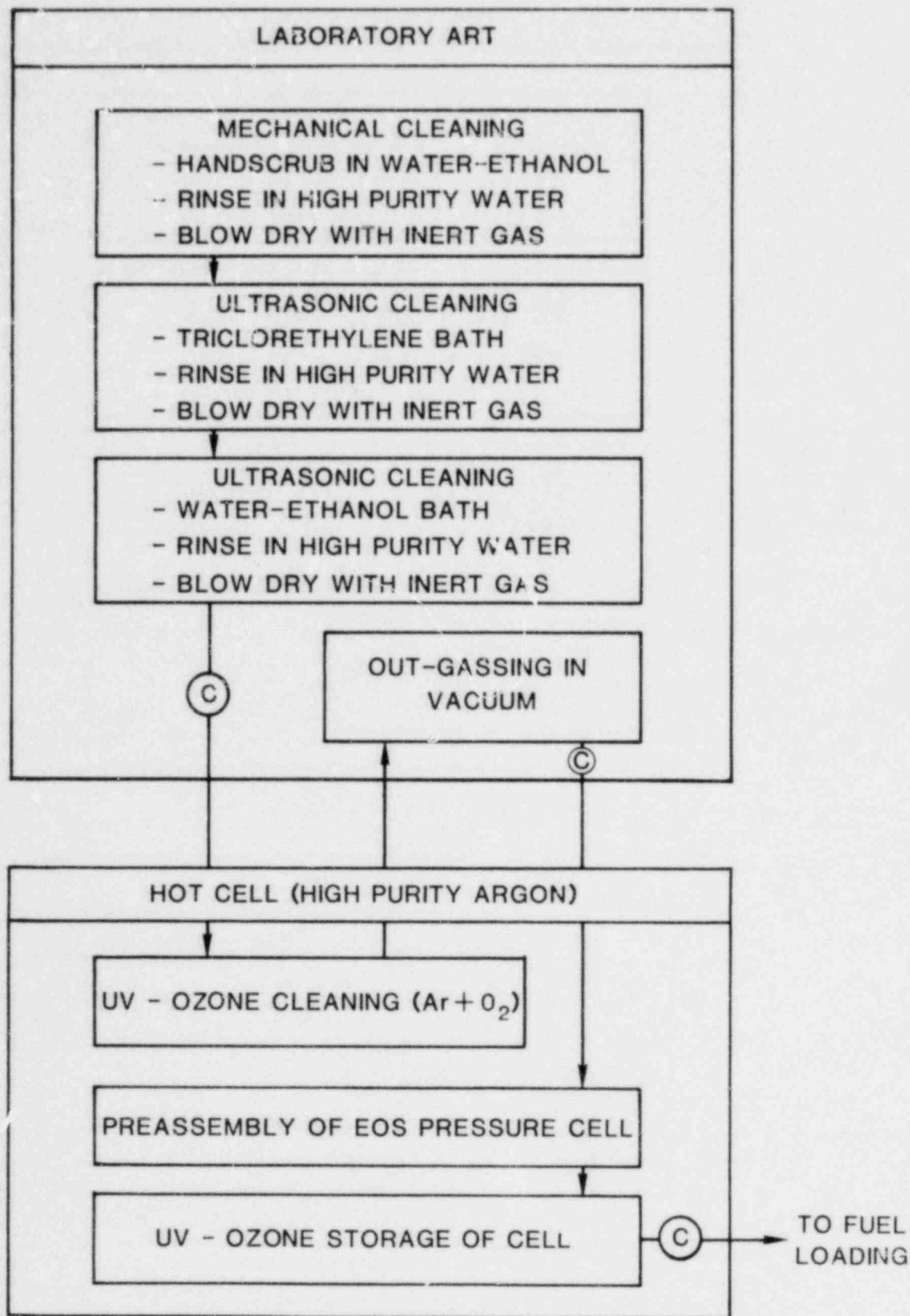


Figure 1.2-13 Flow of Pressure Cell Components (C = most important points of contamination control)

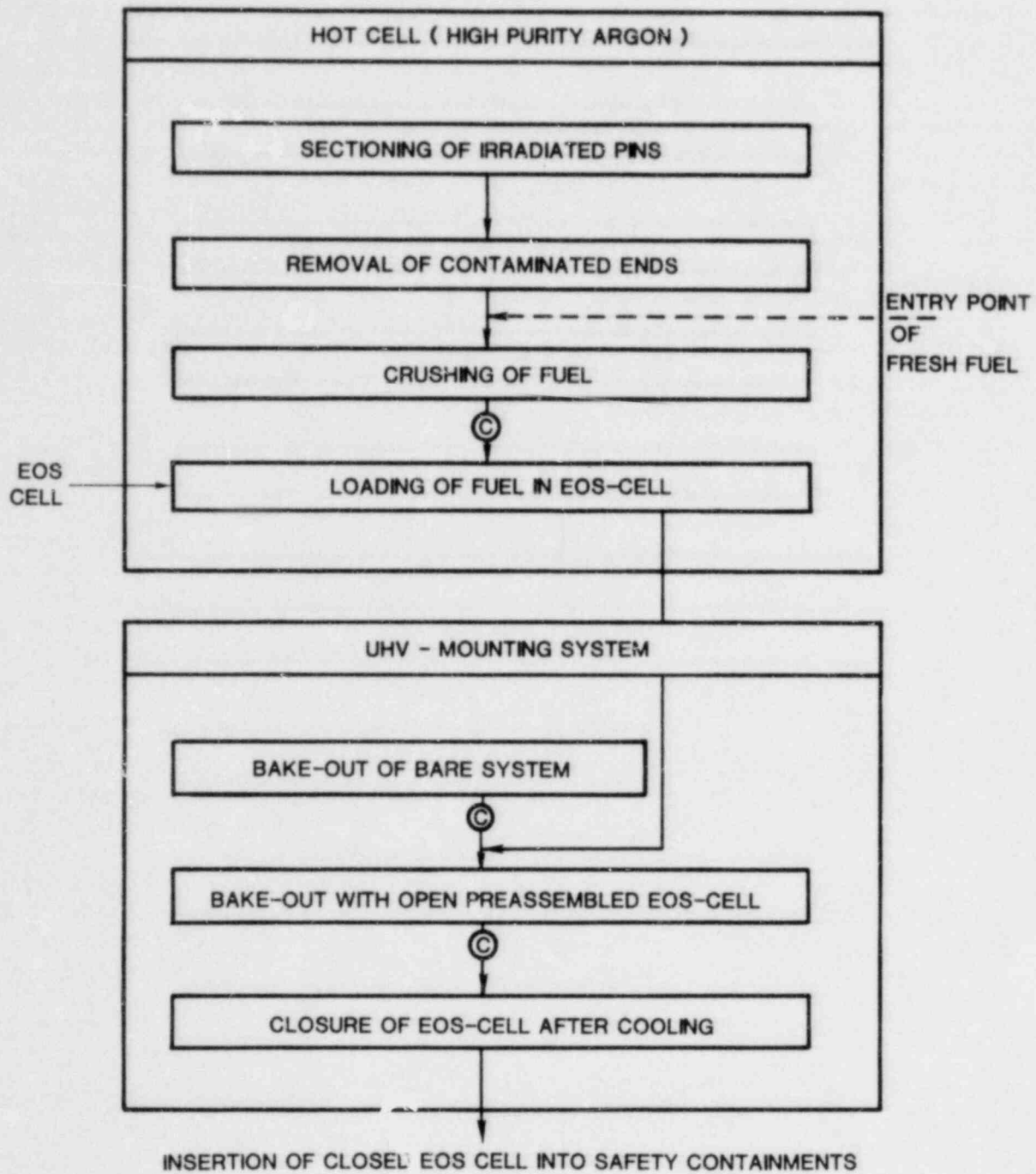


Figure 1.2-14 Flow of Fuel and Loaded EOS C-II (⊙ = most important points of contamination control)

Sandia investigators have devised an experiment to measure the relative values of the equilibrium and instantaneous specific heat of UO_2 as well as the relaxation time. The facility for these experiments became operational during this quarter and some preliminary measurements have been made.

1.2.6.2 Experimental Apparatus

The apparatus uses Joule heating to raise the sample temperature to the region of interest. Then, after a short delay, a rapid temperature excursion is induced by discharging a capacitor into the sample.

Major limitations to rapid resistive heating of UO_2 arise from the negative temperature coefficient of resistance. These include high resistance at ambient temperature, radial temperature gradients in the sample, and the possibility of hot filaments in the sample interior. To minimize these limitations, small diameter samples are used and the heating is accomplished in steps with time for thermal equilibration between each step.

The apparatus is shown schematically in Figure 1.2-15. The high-voltage (low-current) ac power supply is used to overcome the high-initial resistance of the sample and heat it to about 1200 K. The low-voltage (high-current) ac power supply raises the sample temperature to the desired point and holds it to establish equilibrium conditions. The capacitor bank generates a rapid temperature excursion defined by the proposed instantaneous specific heat. The high-voltage dc power supply is for charging the capacitor bank. The power supplies and capacitor bank are switched by mercury relays which are controlled by a microprocessor. The sample is contained in a vacuum system to minimize heat losses by convection and to provide electrical insulation between the electrodes. The surface temperature of the sample is measured by a fast optical pyrometer, the output of which is recorded on a digital oscilloscope.

1.2.6.3 Data Analysis

Analysis of the data is not entirely straightforward, but the essential features will be described.

Investigators have assumed that sample heating proceeded as outlined above and the surface temperature was recorded as a function of time. The sample cooled linearly with time after the low-voltage (high-current) power supply was switched off and until the capacitor discharge began. The temperature then jumped an amount determined by the magnitude of the instantaneous specific heat. Following discharge, the sample cooled exponentially in time while the specific heat relaxed to the equilibrium value. Then the cooling rate was again approximately constant.

The relative magnitude of the instantaneous specific heat was determined as follows. First, the linear, post-pulse cooling curve was extrapolated back to the time of the heating pulse. This defined the temperature jump expected if there were no dynamic effect. The ratio of this jump to the observed jump was multiplied by the known value of the equilibrium specific heat to give the instantaneous value. Finally, the difference between the actual temperature and the linear extrapolation could be fit to an exponential curve to determine the relaxation rate of the heat capacity. This relative technique eliminates the need to measure the energy deposited in the sample and minimizes the effects of thermal gradients.

1.2.6.4 Preliminary Measurements

A series of preliminary measurements was completed on several UO_2 samples to check out the apparatus. Figure 1.2-16 shows the results of one such measurement. It appeared that some sort of dynamic effect was occurring. The same general shape of this curve was observed in all of the measurements made so far.

The greatest unresolved difficulty at this time arises from poor electrical contact between the sample and sample holder. This results in only a small fraction of the energy stored in the capacitor being deposited in the sample. To achieve the desired temperature rise, the capacitor voltage has to be higher causing arcing across the sample surface. Several modifications are being tried out to alleviate the problem.

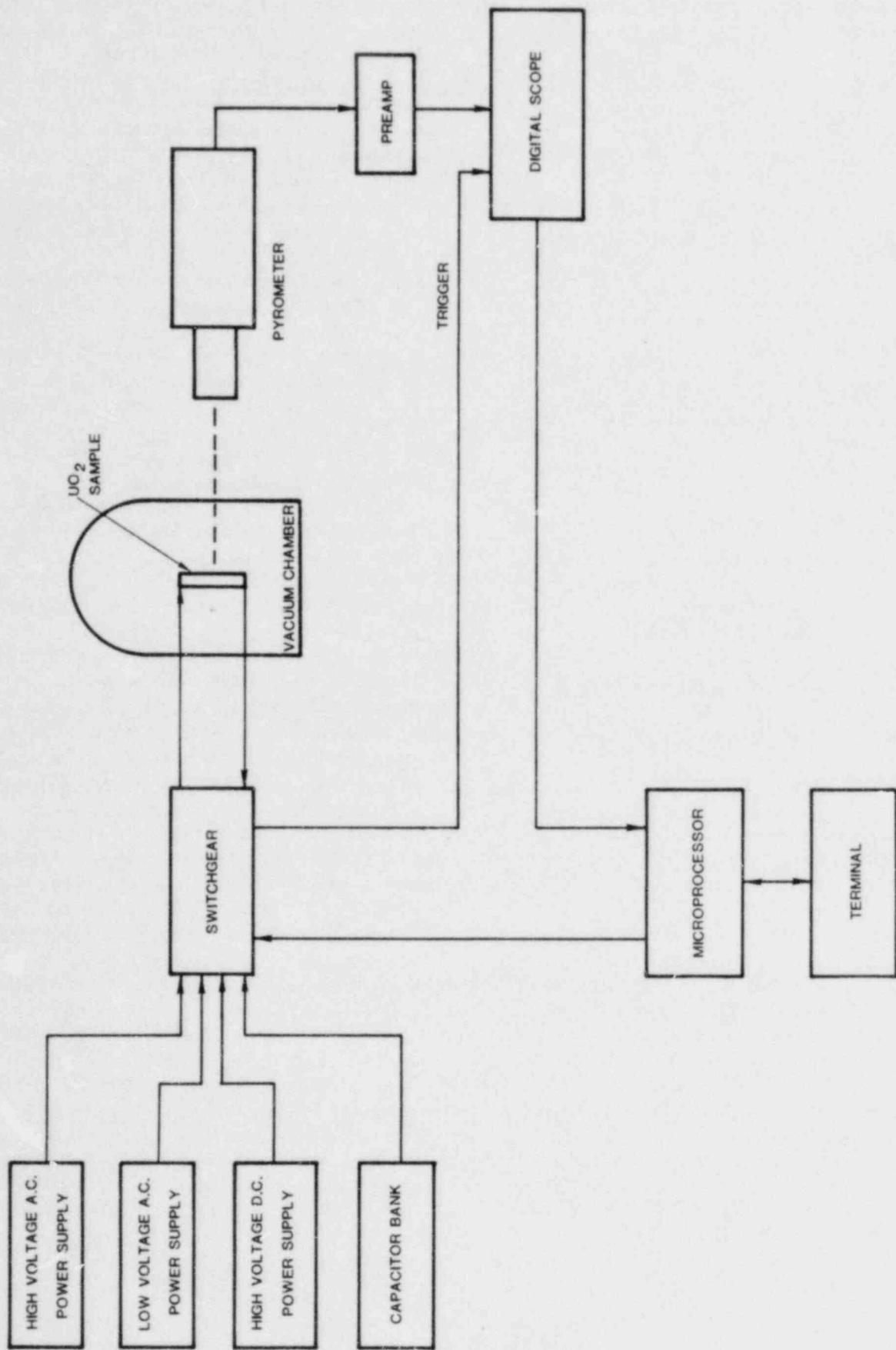


Figure 1.2-15 Schematic Diagram of the Experimental Apparatus for Measuring the Dynamic Heat Capacity of UO_2

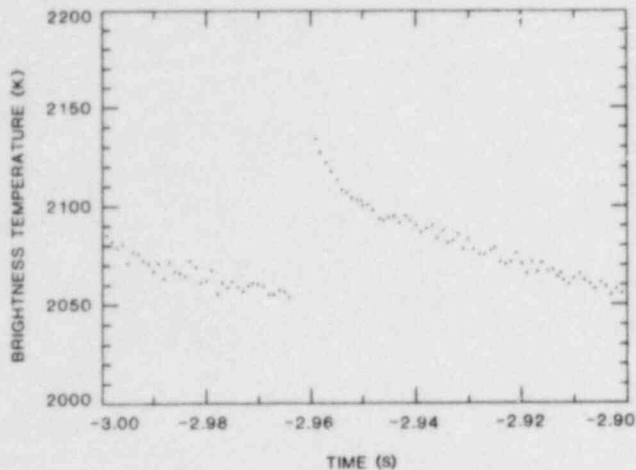


Figure 1.2-16 Surface Temperature of a UO_2 Sample Immediately Before, During, and After the Capacitor Discharge. (The relaxation phenomena observed following the discharge is tentatively attributed to a dynamic heat capacity.)

References for Section 1

- 1-1 K. O. Reil, M. F. Young, and T. R. Schmidt, *Prompt Burst Energetics Experiments: Fresh Oxide/Sodium Series*, SAND78-1561, NUREG/CR-0367 (Albuquerque, NM: Sandia Laboratories, August 1978).
- 1-2 *Advanced Reactor Safety Research Quarterly Report April-June 1979*, SAND79-1597, NUREG/CR-0984, Advanced Reactor Research Department (Albuquerque, NM: Sandia Laboratories, November 1979).
- 1-3 *Advanced Reactor Safety Research Quarterly Report July-September 1979*, SAND79-2158, NUREG/CR-1141, Advanced Reactor Research Department (Albuquerque, NM: Sandia National Laboratories, May 1980).
- 1-4 A. E. Wright, R. C. Doernor, and P. H. Fruehle, *Data Report for Carbide-Fuel MFCI Test AX1 in TREAT*, ANL/RAS 79-3 (Argonne, IL: Argonne National Laboratory, 1979).
- 1-5 K. O. Reil, M. F. Young, H. Jacobs, and H. Plitz, *Prompt Burst Energetics Experiments: Fresh Uranium Carbide/Sodium Series*, SAND80-0820, NUREG/CR-1396 (Albuquerque, NM: Sandia National Laboratories, June 1980).
- 1-6 P. K. Mast, *The Los Alamos Failure Model (LAFM-A) Code for the Prediction of LMFBR Fuel Pin Failure*, LA-7161-MS (Los Alamos, NM: Los Alamos Scientific Laboratory, 1978).
- 1-7 *Reactor Development Program Progress Report, July 1979*, ANL-RDP-85 (Argonne, IL: Argonne National Laboratory, 1979), p 2.44.
- 1-8 M. S. Kazimi, *Theoretical Studies on Some Aspects of Molten Fuel-Coolant Thermal Interaction*, MITNG-155 (Cambridge, MA: MIT, May 1973), pp 93-127.
- 1-9 P. A. Pizzica and P. B. Abramson, "EPIC-FCI A Numerical Model of Fuel and Coolant Motions Following Pin Failure," *Nucl Sci and Eng*, 64:465, 1977.
- 1-10 S. D. Stearns, *Non Recursive Wiener Filter Design*, SAND79-1319, (Albuquerque, NM: Sandia Laboratories, 1979).
- 1-11 K. O. Reil, "Effective Equation-of-State Measurements on Uranium Dioxide," *Nuc Eng Dept*, University of New Mexico, Albuquerque, NM, May 1977.
- 1-12 W. Breitung, E. Bergeron, and K. K. Murata, "Analysis of Sandia In-Pile EOS Experiments," *ENS/ANS Proceedings of the Int'l Meeting on Fast Reactor Safety Technology*, Seattle, WA, August 19-23, 1979, p 1059.
- 1-13 P. Browning, M. J. Gillen, and P. E. Potter, *The Equation of State-of-Uranium Dioxide: A Comparison of the Corresponding States and Significant Structures Theories*, AERE-R8129 (UK: Atomic Energy Research Establishment, March 1977).
- 1-14 M. Bober, W. Breitung, and M. U. Karow, *Thermodynamic Calculation and Experimental Determination of the Equation-of-State of Oxide Fuels up to 5000 K*, KfK-2689 (Karlsruhe, West Germany: KfK, June 1978).
- 1-15 D. A. Benson and E. Bergeron, "Measurement and Analysis of Transient Vaporization in Oxide Fuel Elements," *IAEA International Symposium on Thermodynamics of Nuclear Materials*, Julich, Germany, January 29-February 2, 1979.
- 1-16 D. A. Benson, *Application of Pulsed Electron Beam Vaporization to Studies of LiO_2* , SAND77-0429 (Albuquerque, NM: Sandia Laboratories, June 1977).
- 1-17 E. Bergeron, *Theoretical Considerations of Rate Effects in UO_2* , SAND78-1745 (Albuquerque, NM: Sandia Laboratories, 1979).
- 1-18 W. Breitung, *Contamination Control in Sandia Equation of State Experiments*, SAND80-1277 (Albuquerque, NM: Sandia National Laboratories, October 1980).

2. Fuel Dynamics

2.1 Transition Phase (D. A. McArthur, 4423; A. Suo-Anttila, 4425; W. E. Nelson, 4452)

2.1.1 Introduction

Following the loss of initial geometry in a core disruptive accident, and assuming that neither early shutdown nor rapid hydrodynamic disassembly takes place, the accident enters the transition phase. At this point, one or a number of subassemblies have melted down and radial propagation takes place as subassembly hexcans are melted through. The progression of the transition phase may strongly affect the severity of the accident, and it is, therefore, important to understand the phenomena associated with this accident stage in detail. In particular, several key questions need to be answered. First, in the early stages of the accident is the fuel dispersive, that is, how far can the molten core material and fission gas mixture move axially before it freezes? Secondly, if blockages form and the core is bottled up, what is its configuration—does it remain boiled up, or does the pool collapse followed by the occurrence of a recriticality? Answers to these questions depend upon resolving the uncertainties in transition phase phenomenology. Work at Sandia is directed toward the mechanics of fuel blockage formation and boiling pool behavior. Both analytic and experimental studies are included in this effort.

2.1.2 Initial In-Core Fuel Freezing Experiment Series

Heat transfer and neutronics calculations (described in greater detail below), have been performed to determine a final design for the fuel freezing apparatus. Some modifications were incorporated for the first experiment series. The diameter of the fuel pellet was reduced from 1.0 to 0.8 cm, and the maximum initial steel wall temperature was reduced from 1273 K (1000°C) to 1073 K (800°C), to prevent overheating of the stainless steel wall next to the molten fuel. At 1073 K, the steel adjacent to the fuel is expected to melt rapidly upon contact with molten fuel, so this steel temperature restriction is not expected to reduce the utility of the initial experiment series. To allow more room for fuel expansion upon melting, the initial average fuel-pellet density was reduced to 80% of theoretical density. The initial experiments will therefore involve about 45 g of UO_2 for a 10-cm-long fuel-pellet stack. The maximum fuel temperature was also reduced somewhat to ~ 3973 K

(3700°C), to insure that transient fuel-vapor pressure would be small compared to the applied He driving pressure.

Table 2-1 shows the proposed experiment sequence for the initial series. The experiments at the lowest temperatures and pressures are to be performed first, to allow accumulation of safety-related data on experiment performance. Figure 2.1-1 compares this experiment series with the parameter ranges covered in previous work performed at ANL and Grenoble.^(2-1, 2-2, 2-3)

Table 2-1 Proposed Experiment Sequence for Initial In-Core Fuel-Freezing Experiments

Experiment	T _{steel} (°C)	P _{He} (atm)	T _{fuel} (°C)
1	400	10	3000
2	400	100	3000
3	400	10	3700
4	400	100	3700
5	600	55	3350
6	800	10	3000
7	800	100	3000
8	800	10	3700
9	800	100	3700

2.1.3 Apparatus Design and Fabrication

Most features of the apparatus have been determined by the desired length of the fuel freezing tube, the physical size of the pressure system, and the need for good thermal insulation around the preheated freezing tube. However, two changes were necessary compared to the design reported in the preceding Quarterly Report. First, all-welded construction was chosen for the fuel freezing tube and the fuel pellet housing to provide greater reliability, simplicity, and strength. Second, neutronics and heat transfer calculations showed that greater heat capacity was required in the stainless steel wall of the melting chamber.

Maintenance of a constant pressure on the molten fuel is desirable until freezing is complete (i.e., for times approaching 1 min). In considering experiment safety, the conservative assumption was made that a

blockage would form very early, in which case practically all the molten fuel would remain in the melting chamber. The 316 stainless steel used for the melting chamber wall becomes very weak near 1473 K (1200°C)⁽²⁻⁴⁾ so a maximum wall temperature of about 1323 K (1050°C) was set. Transient heat transfer calculations showed that the maximum wall temperature after the pulse is determined to a good approximation by the initial fuel temperature and the relative heat capacities of the fuel pellet and the steel wall. On the other hand, an excessive wall thickness reduces energy deposition in the fuel pellet and makes the deposition less uniform by requiring higher pellet enrichments. Therefore, a wall thickness of 0.87 cm and a pellet diameter of 0.8 cm were chosen. Detailed heat transfer calculations for these dimensions, using conservative assumptions for the conductivities and gap resistances, show that a maximum wall temperature of about 1373 K (1050°C) is reached at about 30 s after the reactor pulse, followed by a slow decay to lower temperatures. This wall temperature rise appears to be acceptable from a safety standpoint. The wall temperature will be monitored on the earlier experiments at low steel temperatures, to verify the thermal behavior.

Transient flow calculations were also performed to estimate the time required for the molten UO₂ to flow into the freezing tube. The effects of gravity, of the ~4 centipoise viscosity of molten UO₂, and of a 1-atm back pressure in the freezing tube were included in the analysis, but freezing and wall ablation were neglected. At the lowest driving pressure, 10 atm, the front of the molten UO₂ is calculated to be 20 cm into the freezing tube at 15 to 25 ms after the pressure pulse is applied, depending on the precise shape of the pressure pulse. Figures 2.1-2 and 2.1-3 show the molten fuel velocity (V) and the distance (Z) into the freezing tube reached by the leading edge of the fuel, for two assumed shapes of the applied pressure pulse. The differences between Figures 2.1-2 and 2.1-3 show that the shape of the pressure pulse is significant. However, similar calculations at 30 and 100 atm show that the pulse shape is less important at high pressures.

Figure 2.1-4 shows the final fuel pellet design, the result of a compromise between adequate margin for reaching the desired energy deposition in these initial experiments, and maximum uniformity of energy deposition in the fuel. The pellet has two radial zones of slightly different enrichment, but with the same average energy deposition in each zone. The radial variation of energy deposition was calculated with a two-dimensional neutron transport code, including

realistic material compositions and the actual dimensions of the experiment containment canisters. If no radial mixing is assumed, roughly half of the molten fuel will have an energy deposition within ±5% of the desired average value, corresponding to roughly a ±200 K temperature variation.

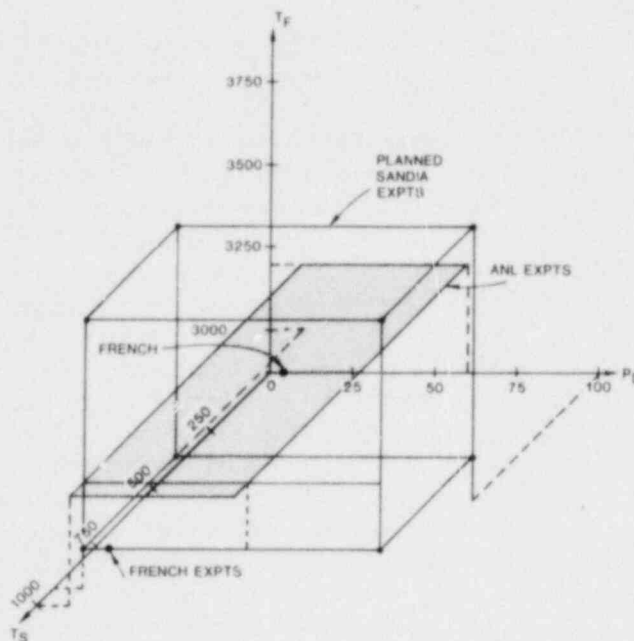


Figure 2.1-1 Parameter Ranges Covered by ANL and French (Grenoble) Experiments on Fuel Freezing Together With Parameter Range of Planned Sandia Experiments. (Parameters are steel wall temperature, T_F (°C), and driving pressure, P_D (atm).)

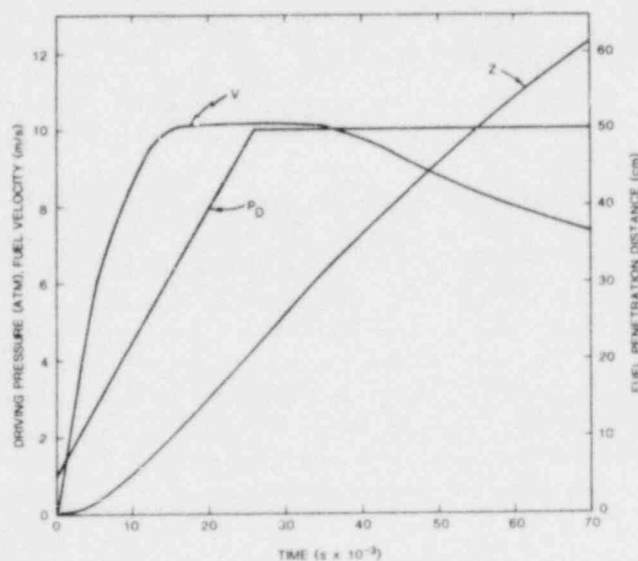


Figure 2.1-2 Fuel Velocity (V), Fuel Penetration Distance (Z), and Driving Pressure (P_D) for a Linearly-Rising Pressure Pulse With a 23-ms Rise Time

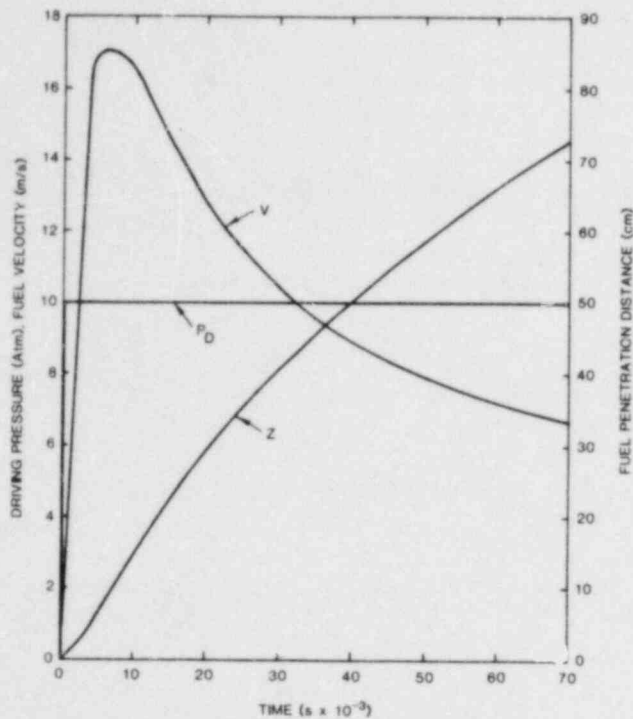


Figure 2.1-3 Fuel Velocity (V), Fuel Penetration Distance (Z), and Driving Pressure (PD) for a Step-Rise Pressure Pulse

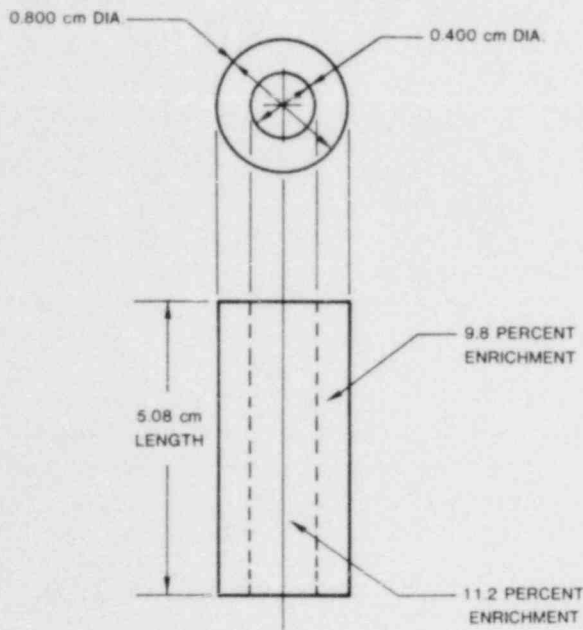


Figure 2.1-4 Graded-Enrichment Fuel Pellet Design. (Two pellets would be used to obtain 45 g of fuel total. Average pellet density is 8.78 g/cm^3)

Fabrication of the smaller items in the driving pressure system is complete. Work is in progress on the containment canisters and their covers, which

include feedthroughs for control cables and diagnostic instrumentation. Orders for some of the diagnostic instrumentation have been placed. The final design for the freezing tube and melting chamber is currently being reviewed by Sandia safety consultants.

2.2 Initial and Extended Fuel Motion (IEFM)

(A. C. Marshall, 4423; R. Craven, 4423; W. H. Sullivan, 4423; S. A. Wright, 4423; W. Trebilcock, 4424; G. Randall, 4452; M. F. Young, 4425; W. J. Camp, 4425.)

2.2.1 Introduction

Phenomenological investigations are being conducted in transient overpower (TOP), loss-of-flow (LOF), and LOF-driven-TOP advanced reactor accident sequences. To support accident analysis, detailed phenomena associated with core disruption must be identified and modeled. These phenomena include fuel motion inside the clad prior to failure, axial fuel failure location, mode of cladding failure, fuel disruption modes, rate of dispersal, fuel plateout and extended fuel motion into the blanket (potential for blockage).

Current activities in the program are directed toward planning for preirradiated fuel tests of up to 19 pins in the ACRR and participation in the NRC international exchange program on CABRI through preanalysis of series tests A and B (TOP and LOF-driven-TOP respectively) with single-pin geometries.

Some reactor safety tests that involve larger bundle sizes and full length pins may be required. Facilities in which to conduct these tests are, therefore, being evaluated on a continuous basis. Work on LOF and TOP accidents has been done in the DOE program at TREAT and will continue in the TREAT upgrade. The Sandia program will be coordinated with the DOE program to take the maximum advantage of the available data.

The tests being planned for the ACRR will require an in-pile flowing sodium system, a loop-control system, high power operating modes in the reactor, preirradiated fuel, hot-fuel handling facilities, and a high resolution fuel-motion-diagnostics system. The fuel-motion-diagnostics system has been completed and installed in the ACRR tank. The design of the initial out-of-pile loop has been completed and most of the loop components have been ordered. Work on the design of the in-pile loop continued. Design of

the loop control and data acquisition systems are in progress.

2.2.2 Out-of-Pile Loop Design

The design of the initial out-of-pile (OOP) loop has been completed. An assembly drawing of the OOP loop is shown in Figure 2.2-1. The loop is designed to operate at a nominal temperature of 773 K (500°C) and a maximum pressure of 3 MPa (450 psi). Sodium and gas valves in the OOP loop design permit a variety of test operations as well as fill, drain, clean, and reconfiguration operations. During high pressure operations, valves will be operated remotely. The OOP loop will also contain a remotely actuated valve for depressurizing the loop during a potential accident (leak) situation. All major loop components and instrumentation, except heaters, insulation, sodium level detectors, and flow meters, have been ordered.

Several approaches are being explored for sodium level detection methods that are compatible with the space and temperature constraints of the Sandia loops. The level detection methods given the most attention follow.

2.2.2.1 Time Domain Reflectometer (TDR) Concept

The system consists of a fast-rise-time pulse applied to a high speed interval timer and air dielectric coaxial cable immersed in sodium. The timer is both started and stopped on the rising edge of the appropriate pulse. The initial pulse is reflected when it hits the short caused by the sodium on the coaxial cable. The reflected pulse is 180° out of phase with the initial pulse, so that its trailing edge is the rising edge which stops the timer. With time and velocity information, the distance, or level, may be computed. The time interval has 40-ps resolution (40×10^{-12} s); this resolution allows the sodium level to be determined within 1/2 in. The mechanical parts for this device are now complete. Testing of this approach will begin soon.

2.2.2.2 Temperature Compensated Resistance Wire

The concept uses the change in resistance in a conducting loop immersed in sodium to indicate sodium level change. Temperature changes will, however, also change the resistance producing inaccurate level indications. To correct for temperature changes, one leg of the conducting loop will be a thermocouple. Appropriate electronics are used with

the thermocouple to correct for temperature changes in the sodium. This approach will also be tested.

2.2.2.3 Sweep Generator Concept

This approach uses a sweep generator and detects sodium level by observing the resonance frequency. At 473 K (200°C) the resonance frequency is approximately 25 kHz for an air column of 2.5 cm down to 1 kHz for an air column of 60 cm. This approach is considered as a backup should the other two approaches fail; consequently, no testing of this approach is planned yet.

2.2.3 Data Acquisition and Control

The electronics for the Data Acquisition system and the controllers for the heating of the sodium were chosen from many possible systems. The same system and controller will be used on both in-pile and out-of-pile loops with minimum changes or additions. An HP 3052 Data Acquisition system was chosen. The HP 3052 is compatible with the existing HP 9845T terminal/controller and HP 1000 computer.

The HP 3052 provides 76 channels of thermocouple and/or pressure transducer information and 10 channels of relay closures for status or alarm conditions. These channels would be used on both loops.

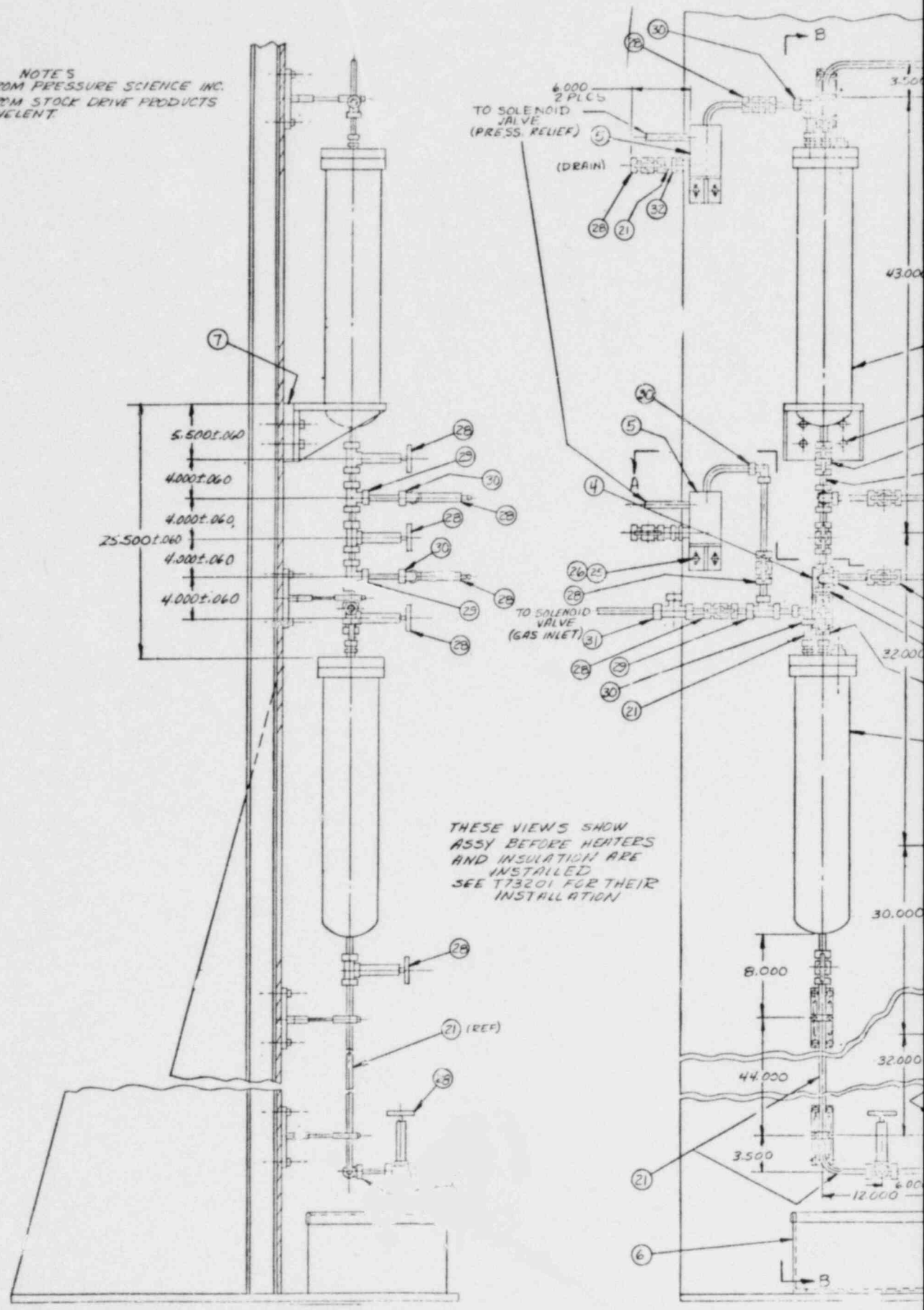
An LSI-11 microprocessor is being used as a test bed to evaluate loop-heater-controller approaches. The management consists basically of solid-state relays (zero crossing type), activated by TTL compatible logic, operating the trace heaters and thermocouples as the feedback. Under software control, sodium is melted from the free surface in zones until all the sodium is melted, and then brought up to operating temperature. Either the LSI or the 3052 system will then continue to run the heaters.

The previously mentioned electronics are all common to both loops and represent a cost savings over two complete systems. A 15-channel FM tape deck will provide backup data in the event that primary data acquisition is lost. The data acquisition and control systems for the out-of-pile and in-pile loops are illustrated in Figures 2.2-2 and 2.2-3 respectively.

2.2.4 ACRR Control System

The ACRR control system has been modified to provide a programmed transient rod withdrawal mode which will be used in the IFFM experiments. The switch preset and microprocessor based rod drive programmers have been installed and electro-mechanical acceptance testing was completed for the

NOTE'S
 1. OBTAIN FROM PRESSURE SCIENCE INC.
 2. OBTAIN FROM STOCK DRIVE PRODUCTS
 OR EQUIVALENT



THESE VIEWS SHOW
 ASSY BEFORE HEATERS
 AND INSULATION ARE
 INSTALLED
 SEE T73201 FOR THEIR
 INSTALLATION

77206					
-------	--	--	--	--	--

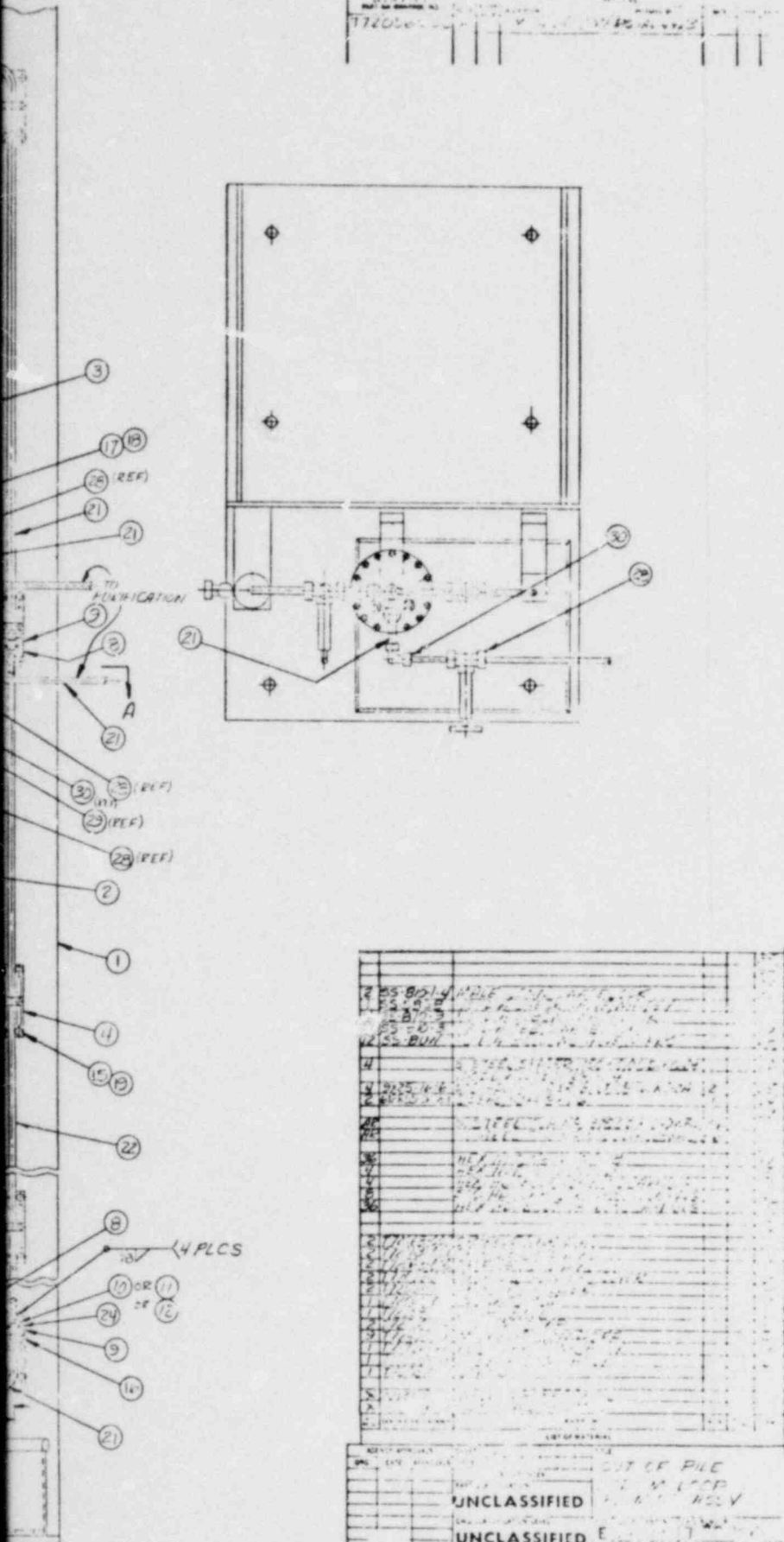
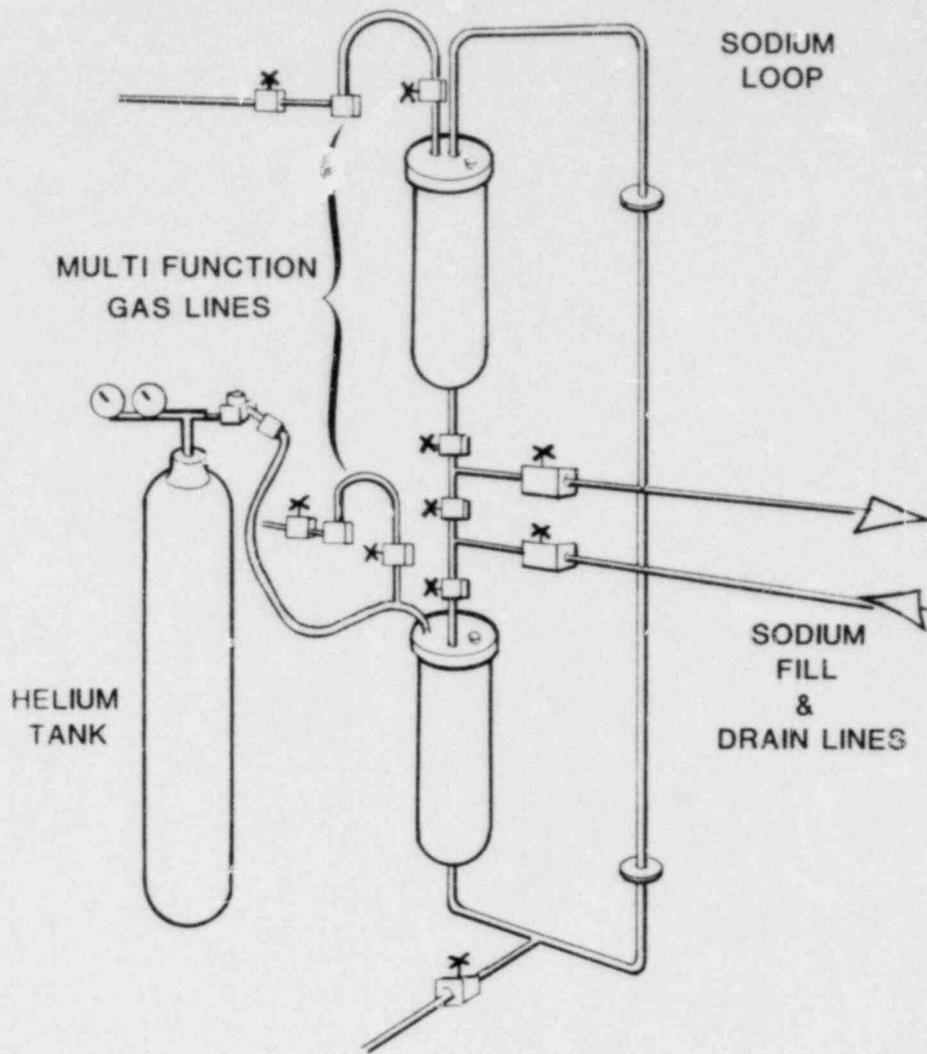
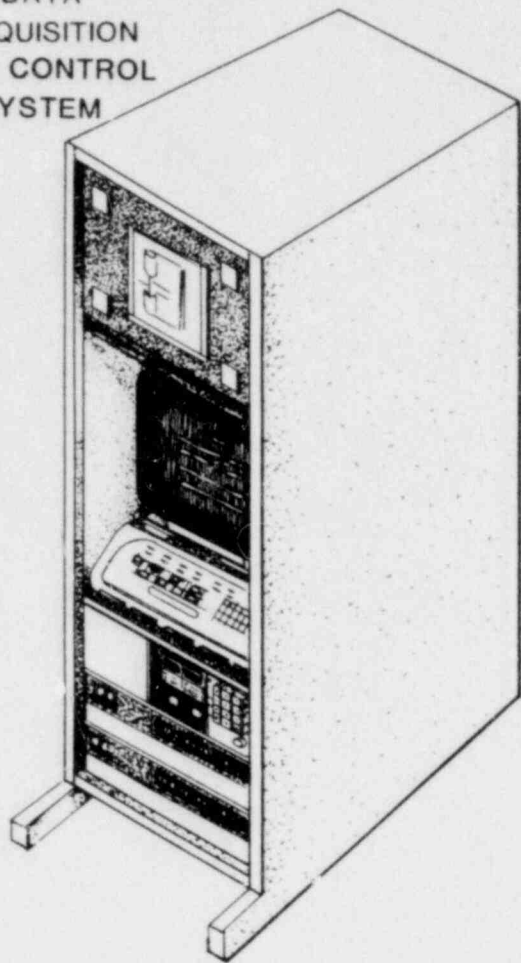


Figure 2.2-1 Assembly Drawing of OOP Loop

DATA
ACQUISITION
AND CONTROL
SYSTEM



IEFM OUT-OF-PILE LOOP

Figure 2.2-2 Data Acquisition and Control System for the IEFM Out-of-Pile Loop

DATA ACQUISITION AND CONTROL SYSTEM FOR IN-PILE AND OUT-OF-PILE IEFM LOOP

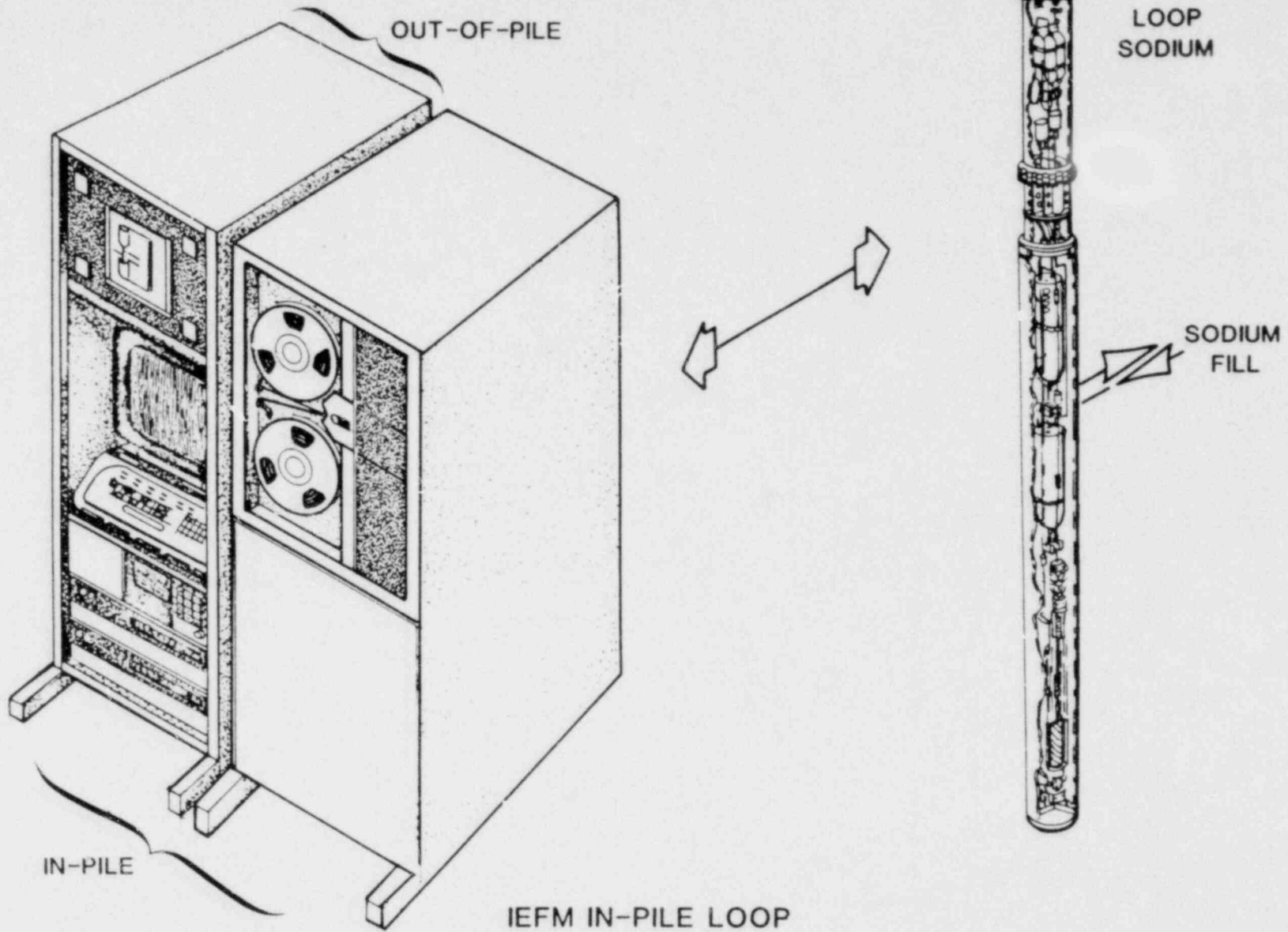


Figure 2.2-3 Data Acquisition and Control System for the IEFM In-Pile Loop

switch preset system. This system is now fully operational and has been used for several extended transient operations. Electromechanical testing of the microprocessor-based system is continuing.

Kinetics calculations have shown that a simulation of an LOF-driven-TOP cannot be fully simulated by using a single pulse or transient rod withdrawal since the rod withdrawal speed required for this test falls between these two modes. Additional kinetics and heat transfer calculations have shown, however, that an operating mode in which the transient rods are withdrawn for a preheat followed by firing the two rods in succession could yield an acceptable power history.

2.2.5 CABRI Calculations

The CABRI A2 TOP test was recalculated by using a revised version of the EXPAND code and actual experimental data. The previous EXPAND prediction of late failure in A2 when no failure occurred was due to the uncertainty in the failure model at low power levels plus the differences between the previous and present EXPAND versions. In the case of A2, the sensitivity of the failure model to variations in the power level is greater than the experimentally attainable accuracy. This difference is demonstrated by the fact that no failure is predicted when the coupling factor is reduced by only 2% compared to the experimental error of about $\pm 10\%$.

Steady-state results are in fair agreement with thermocouple data, although calculated temperatures are roughly 20 K higher than experimental temperatures over the pin length. This difference, around 11%, could be due to several experimental and calculational factors.

Transient results are in general agreement with the PHYSURA calculations except that a permanent maximum clad strain of 0.002 was calculated, corresponding to a permanent deformation of 7.6×10^{-4} cm.

Comparisons between the coolant thermocouple responses and calculated results are in fair agreement; the major differences appear to be a slower rise time in the thermocouple data (TC transient response) and a hump in the latter half of the TC data, probably due to gamma heating.

2.2.6 UO₂ vs Mixed Oxide

The implications of the use of UO₂ instead of mixed oxide fuel in CABRI tests have been evaluated. The primary reason for using UO₂ instead of mixed oxide is to reduce the radial-energy-deposition gradient during transient tests; this gradient is a problem

that is more pronounced in the large diameter CABRI test pins than in the SNR-300 or PFR pins.

The substitution of irradiated UO₂ for mixed (U, Pu)O₂ fuels has been addressed on the basis of the phenomenology impacting the experiments under consideration. Slightly different concerns emerge for TOP experiments than for LOF experiments; and considerably different concerns would enter if PAHR experiments were under consideration.

2.2.6.1 LOF Experimental Concerns

Under LOF conditions, the loss of coolant flow means that either the clad melts off prior to significant fuel disruption or at least that clad is so weak at the time of fuel disruption that mechanical loading of clad is of no consequence. So, for LOF experiments the crucial phenomenologies are fission gas release and fission-gas-driven fuel disruption. The disruption can be mild (e.g., solid-state swelling followed by liquid-state slumping) or violent (e.g., fission-gas-driven fuel micro-fracturing and dispersal). The trade-off between various microprocesses determines which type disruption occurs.

The basic cause of fuel disruption is the growth, pressurization, and motion of inert-gas bubbles within the fuel matrix. The amount of gas retained in bubbles (vs that released during steady-state operation) and its location depend primarily on power level at burnup and percent burnup. Low power fuel retains more gas than high power fuel; the location of gas depends on restructuring radii which are determined again by power level and burnup. In both cases, the dependence on power level is dominant.

Gas release during the transient is in a sense a phenomenon that complements fuel disruption. It arises by growth of intragranular bubbles, their movement to grain-boundary bubbles, and release of grain-boundary gas through interconnected porosity. The questions of fuel swelling vs brittle or ductile fracture, and of these two phenomena vs gas release depend on temperature and temperature ramp rates, metal-atom vacancy concentrations and mobilities, the diffusivity of metal atoms on bubble surfaces, fuel strength properties (e.g., ultimate tensile stress and yield stress), fuel creep rates, and the nature of steady-state fuel restructuring. In turn, these properties depend directly or indirectly on fuel surface tension, grain boundary tensions, thermal expansivity, thermal conductivity, and fuel specific heat as well as melting points and heats of fusion. Finally, for both UO₂ and (U,Pu)O₂ these properties are generally quite sensitive to oxygen stoichiometry. In addition, should Pu migration toward the hotter central regions of the fuel pin become significant, it can

effect changes in radial temperature profiles during transients and thus possibly the nature and timing of fuel disruption.

2.2.6.2 TOP Experimental Concerns

Under TOP conditions, coolant flow may normally be assumed to be sufficient to cause mechanical clad failure rather than clad melt-through. Mutual fuel-clad mechanical loading is thus very important. The clad properties will play an important role in TOP failure; they are unaffected by differences between UO_2 and mixed-oxide fuels.

Many of the same concerns that enter for LOF experiments also impact TOP experiments. However, fuel mechanical properties play a more dominant role here. The thermal expansion of fuel is especially important. The contribution from fission gas release can be equally important for some experiments, and the nature of fuel cracking is also of significant influence on failure modeling. For very high ramp rate TOPs, fuel vapor pressure can also have a major impact on failure and fuel motion.

2.2.6.3 Comparison of Relevant UO_2 and $(U, Pu)O_2$ Properties

2.2.6.3.1 Thermal Properties

- **Melting Points.** The mixed oxide system melts incongruently with a solidus-liquidus range of about 25 K for 10% Pu. In addition, the melting point is depressed by 35 K in the mixed oxide. These effects are roughly twice as large for 20% PU fuels. The net effect is not terribly significant for either a LOF or a TOP. ⁽²⁻⁵⁾
- **Specific Heats.** In the solid, except just below the melting points, the mixed-oxide specific heat is nearly identical to that of UO_2 . In the liquid, these specific heats are within 10% of each other. ⁽²⁻⁵⁾
- **Boiling Point.** The mixed-oxide boiling point is nearly 200 K below that of UO_2 . This is of no importance for LOF and would only impact very high ramp rate TOPs. ⁽²⁻⁵⁾
- **Latent Heat of Fusion.** These are nearly identical for the two systems. ⁽²⁻⁵⁾
- **Latent Heat of Vaporization.** The mixed-oxide latent heat is about 15% lower than that of UO_2 . This compensates for the low-

er boiling point in the mixed oxide and again would only be important for very high ramp rate TOPs. ⁽²⁻⁵⁾

- **Thermal Conductivity.** In the solid state, there are no discernable changes due to Pu addition. ⁽²⁻⁶⁾ The liquid state thermal conductivity is not well known even for UO_2 . No important effects are expected.
- **Thermal Emissivity.** This property has not been measured for Pu- UO_2 , but from theoretical considerations it should be nearly the same as for UO_2 . Differences will not have significant effects.
- **Surface Tension.** Again, although not measured for $(U, Pu)O_2$, no major differences are anticipated. A major change in surface tension could have a significant effect on bubble dynamics and fuel failure.
- **Thermal Expansion.** The expansivity of mixed oxides is closely similar to that of UO_2 . This is important since thermal expansion is a determining parameter under some TOP conditions.

2.2.6.3.2 Mechanical Properties

- **Elastic Moduli.** These differ by roughly 25% between UO_2 and 25% Pu mixed oxides. This can have quantitative but no qualitative effects. ^(2-5, 2-6)
- **Ultimate Tensile Stress and Yield Stress.** These are both very temperature dependent and decrease rapidly above 2000 K. 50% uncertainties exist in the data. To this kind of accuracy, there is no difference between $(U, Pu)O_2$ and UO_2 . ^(2-5, 2-6)
- **Fracture Stress.** Brittle fracture stress increases with temperature and is closely similar in both oxides. ^(2-5, 2-6)
- **Creep.** Creep is an activated process which varies strongly with temperature, oxygen stoichiometry and burnup. The activation energies are similar in the two materials. The oxygen stoichiometry variation has not been as well studied for mixed oxides as for UO_2 . Nevertheless, it is strong: a 5% reduction in oxygen stoichiometry from $(U, Pu)O_2$ to $(U, Pu)O_{1.95}$ leads to an order of magnitude increase in creep rate. In general, $(U, Pu)O_2$ creep rates are somewhat higher than UO_2 rates. In UO_2 as in $(U, Pu)O_2$ deviations from stoichiometry lead to enormous increases in creep rates: for $UO_{2.001}$ the creep rate is more than two

orders of magnitude less than $UO_{2.05}$.⁽²⁻⁶⁾ In addition, creep rates become greatly enhanced at temperatures near melt.⁽²⁻⁷⁾ Although the differences in creep rate between UO_2 and $(U,Pu)O_2$ should be taken into account, the oxygen stoichiometry and temperature dependences dwarf the Pu stoichiometry effects and they have not been carefully established.⁽²⁻⁶⁾

2.2.6.3.3 Microscopic Properties

- Defect Formation Energies. Vacancy and interstitial-formation energies as well as dislocation formation energies are seen from statistical mechanical theories to scale like the melting temperature or other disorder temperatures, none of which are grossly different in $(U,Pu)O_2$ systems from UO_2 systems. So no major differences are expected.
- Diffusivities. Bulk and surface diffusivities should be quite similar (except, perhaps, near the melting point) in the two systems because the fundamental cohesive forces and lattice structures are very similar.

In neither of the above cases does there exist sound experimental data. Thus, fundamental physical principles have been invoked to decide that significant differences are not expected.

2.2.6.4 Radial Dependence of (U,Pu) Stoichiometry

In mixed oxides which are stoichiometric or hyperstoichiometric, during burnup, Pu migrates to the hotter central region of the fuel pin. Thus, for example, a fuel pin initially 20% Pu uniformly distributed, will have ~30% Pu at centerline ~15% Pu at the outer radial edge after 5% burnup.⁽²⁻⁶⁾ This has a significant effect on temperature profiles. However, UO_2 fuels with 5% burnup will show some of this effect since they contain several percent Pu. Furthermore, the thermal effect apparently is more than compensated by the difference in fission and capture cross sections between U and Pu.

2.2.6.5 Conclusions on the Use of UO_2 vs Mixed Oxide Fuel

For both TOP and LOF experiments, the use of preirradiated UO_2 fuels in place of $(U,Pu)O_2$ fuels is justified if experimental exigencies mandate such a

substitution. This is because (1) the two fuels are very similar in nearly all relevant properties; and (2) where significant differences between fuels exist, either these differences are masked by larger effects due, for example, to oxygen stoichiometry and/or temperature, or to the current uncertainties in the UO_2 and $(U,Pu)O_2$ properties which are greater than expected differences. As a practical matter, in fuel with significant burnup some of the thermal profile improvement gained through the use of UO_2 is lost because of efficient $U^{238} \rightarrow Pu^{239}$ breeding. Finally, the mixed-oxide profile problems are exacerbated by the rather large diameter of CABRI common test pins. The problem should be lessened with SNR-300 or PFR fuel pins. Conversely, it would be worsened with Super-Phenix pins.

2.2.7 CABRI Calorimeter Experiment

The detectors for the CABRI calorimeter experiments were fabricated, calibrated, and shipped to France this quarter. The five fission-thermocouple detectors (FTCs) and the gamma-thermocouple detectors (GTCs) were fabricated at Sandia during the previous quarter. These detectors, along with five fission chambers fabricated by Reuter Stokes Inc, were calibrated in the SPR-III to determine their impulse response functions, sensitivities to neutron and gamma fluxes, and to determine the effect of temperature on the voltage output of the fission and gamma thermocouple detectors.

The SPR-III calibration experiments consisted of exposing the detectors to six reactor pulses. The six reactor pulses consisted of two free-field glory hole pulses at room temperature, two free-field glory hole pulses at 553 K (280°C), and two glory hole pulses with a lead pig insert at room temperature. The dosimetry for all reactor pulses consisted of TLDs, ^{235}U -foils, and ^{238}U foils. The lead pig perturbs the neutron-to-gamma flux ratio allowing a determination of the neutron and gamma-ray sensitivities of the detectors (summarized in Table 2-II).

Figures 2.2-4, 2.2-5, and 2.2-6 show the measured detector responses for the three types of detectors (FTCs, GTCs, and fission chambers) for the 280 K free-field reactor pulse. Note that the fission chamber response follows the reactor pulse while the FTC and GTC responses are significantly altered by heat transfer characteristics of the detectors. Because the pulse width of the SPR-III is so small ($<100 \mu s$) compared to the pulse width of the CABRI reactor, these responses are, to a good approximation, the impulse response function. These functions are fit to a series

of polynomials and exponentials and used in a deconvolution program to determine the energy deposition rate in the detector.⁽²⁻⁸⁾

At the conclusion of the SPR-III calibration experiments 9 out of the 10 thermocouple detectors were operating correctly. Radiographs made prior to the experiments and after the experiments showed no changes or damages to the detectors caused by either handling or high-temperature operation. In January the detectors were shipped to France and arrived on schedule in mid-February. Upon arrival of the detectors in France, continuity checks showed that all nine of the thermocouple detectors were functioning properly. However, after mounting the detectors only four of the thermocouple detectors passed the continuity checks. Examination of the failed detectors revealed that the gold lead wire bonds within the detectors had broken. Since the calorimeter experiments were not scheduled for several months, attempts are being made in France to effect repairs. The primary dynamic instrumentation in the calorimeter experiments consists of five fission chamber detectors. Consequently, even if the five broken detectors cannot be repaired, the remaining four detectors can still provide valuable time dependent information which is unavailable otherwise.

Table 2-II CABRI Detector Sensitivities in SPR-III

Detector	Sensitivity	
	cal/g (u10Mo)	Type of Sensitivity
Fission TC (FTC2)	$0.53 \times 10^{-4} \pm 8\%$	Neutron and gamma
Gamma TC (GTC3)	$1.34 \times 10^{-4} \pm 5\%$	Neutron and gamma
Fission chamber (CAB16)	$*1.85 \times 10^{-17} \pm 16\%$	Neutron

*(V x s) / (fis/g (9.3% U))

2.3 In-Core Fuel Motion Detection

(S.A. Wright, 4426; P. J. McDaniell, 4424)

2.3.1 SPR-III Fuel Motion Detection Experiments

Experiments to test the feasibility of in-core fuel motion detection were performed in the SPR-III this quarter. The specific goal of these experiments was to

test the capability of platinum-self powered detectors (Pt-SPD) to monitor fuel motion when the detectors are located outside the fuel bundle. Previous experiments were performed with detectors inside the fuel bundle.⁽²⁻⁹⁾ In these gross motion experiments, the detectors were located outside a seven-pin fuel bundle approximately 15 mm from the central fuel pin. This location simulates placing the detectors in the sodium bypass loop of a true fast reactor LOF or TOP experiment.

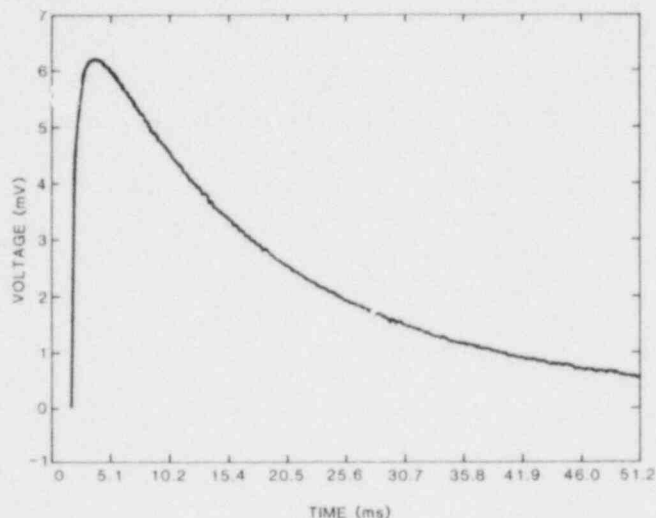


Figure 2.2-4 Fission Thermocouple Detector Response to a SPR-III Pulse (FTC 2)

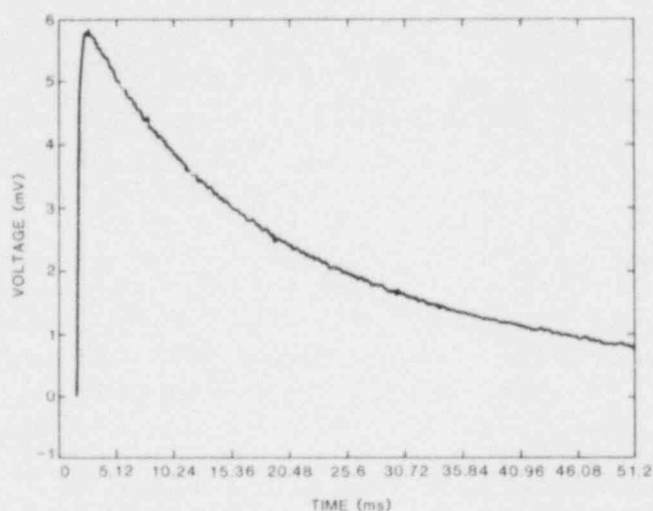


Figure 2.2-5 Gamma Thermocouple Detector Response to a SPR-III Pulse (GTC 3)

Figures 2.3-1 and 2.3-2 illustrate the Seven-pin fuel bundle geometry and the detector locations. Figure 2.3-1 shows a schematic of the axial view of the seven-pin bundle and the detector locations. The

fuel pins come in two sections, a fixed section and a movable section. The fixed section is attached to the bottom of the experiment stand. The movable portion, which is above the fixed fuel pin section can be withdrawn to simulate fuel motion. The detectors are placed at 10 axial elevations around the fuel bundle. At each elevation there are at least two detectors. Each elevation is separated by 25.4 mm which corresponds to the active length of each detector. The total axial coverage of the 22 detectors is 254 mm.

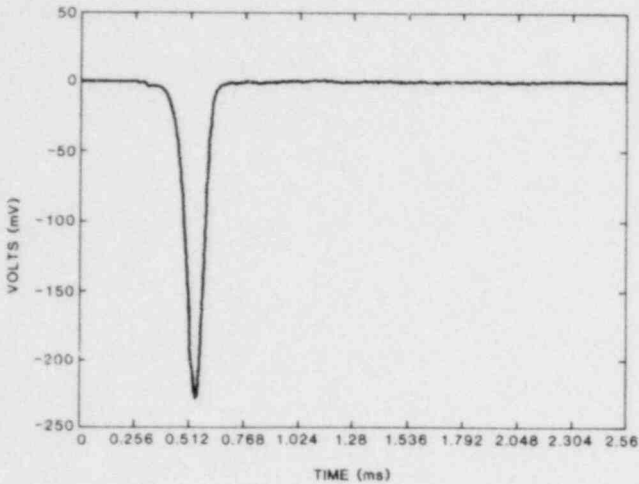


Figure 2.2-6 Fission Chamber Response to a SPR-III Pulse (CAB 16)

Figure 2.3-2 shows a top view of the seven-pin bundle and the location of the detectors for the gross motion experiments. For comparison, the location of the detectors in the seven-pin high resolution experiments is also shown. Additionally, the groups of fuel pins which are moved together are connected by dotted lines. Configuring the fuel-pin bundle and detector locations in this manner allows assessment of the three-dimensional resolution capabilities of the unfolding techniques for these gross motion experiments.

The unfolding analysis of these experiments is still under development. However, preliminary analysis of the detector responses has been completed. In general, the detector responses observed in these gross motion experiments are lower than in the high resolution experiments. This was expected since the detectors are farther away from the fuel. The average change in detector response for a fuel motion in which all seven pins were moved away from the detector is 3% to 5%. In the high resolution experiments, the average change in signal for this amount of motion was 15%.

The unfolding analysis of these experiments will be performed after the completion of the 19- and 37-

pin experiments. These experiments are scheduled for the next two quarters.

2.3.2 Detector Development

One of the keys to a successful in-core fuel motion detection system is having detectors which are sensitive to fuel motion. The detectors currently used to observe fuel motion are Pt-SPDs. These detectors are sensitive to the gamma-ray flux and have no angular distribution in their sensitivity. Another detector which is being considered for use as a fuel motion monitor is the thick film self-powered detector (TF-SPD). This detector operates in a similar manner to the Pt-SPD; however, it has a significant neutron sensitivity and is very sensitive to the angular distribution of the neutron and gamma-ray flux.

Before these detectors can be effective as fuel motion monitors, the detector must be fully characterized with respect to its neutron sensitivity, gamma sensitivity, and its sensitivity to the angular flux distribution. The basic physics of how these detectors work must also be understood in order to choose materials and design characteristics that will make the detectors even more sensitive to fuel motion. The theory for these detectors is currently being developed. Several reactor experiments were performed which reinforce many of the theoretical concepts.

The TF-SPDs are fabricated at Sandia, using thick film hybrid microcircuit electronic techniques. Figure 2.3-3 illustrates one of the detectors. Electronically, the detector is really a parallel plate capacitor ($c \approx 3$ pf).

Accordingly to present theoretical understanding, the detector operates in the following manner. When gamma radiation is incident on the top side of the detector, the gamma rays have Compton interactions in the aluminum and gold. Since Compton interactions are forward scattered, there is a net flow of electrons from the top electrode to the bottom electrode through the dielectric. This produces a positive current in the external circuit. However, when neutron radiation is incident on the top of the detector, the fast neutrons produce energetic charged particle interactions (n,α) or (n,p), with the aluminum. These (n,α) and (n,p) interactions are also forward scattered to produce a net flow of positive charged particles between the top and bottom dielectrics. This creates a negative current in the external circuit. These two processes compete with each other to produce the total external current. When the radiation is incident from the bottom of the detector, the neutron and gamma-ray currents are reversed in sign.

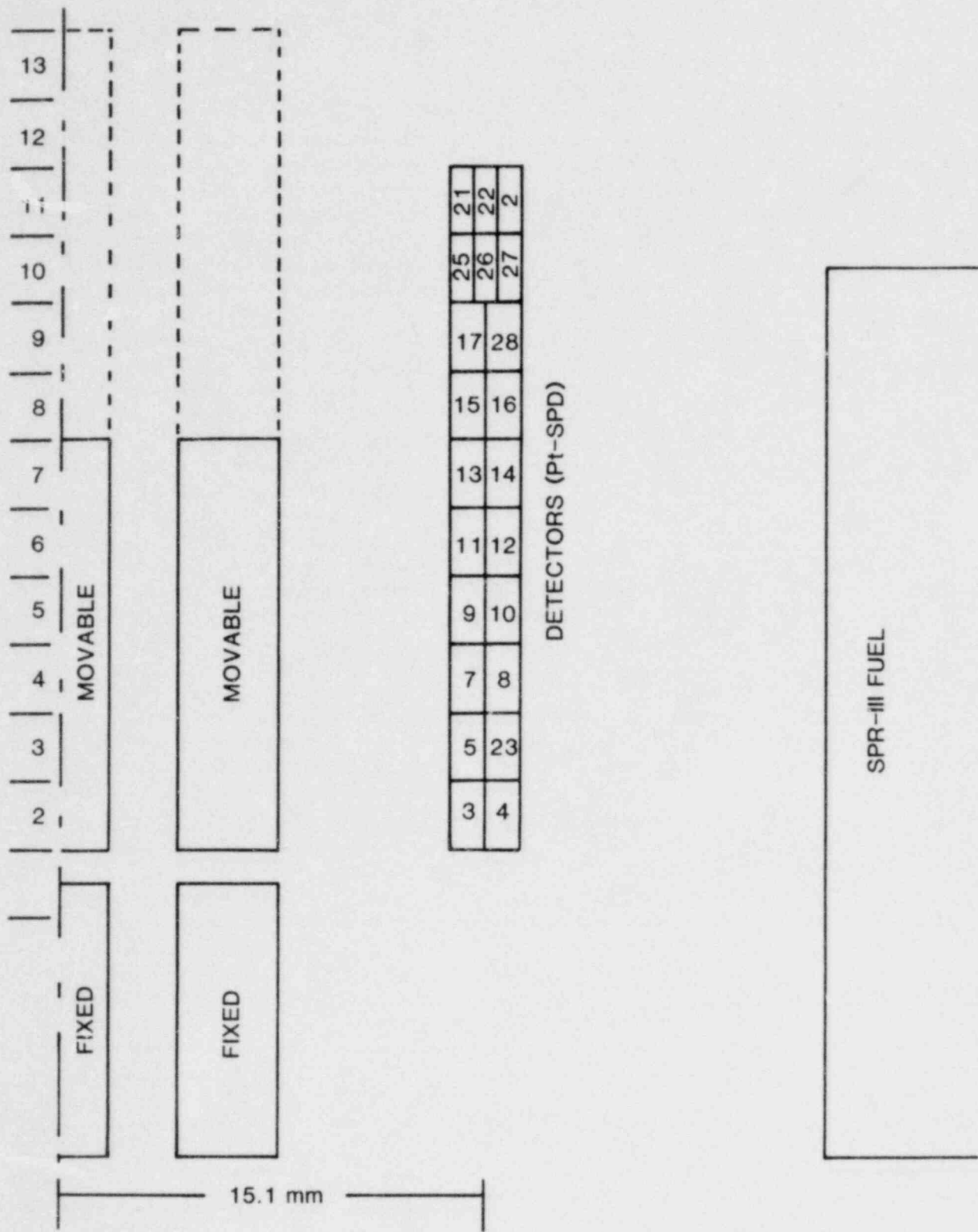


Figure 2.3-1 Seven-Pin Cross Motion Detector Locations

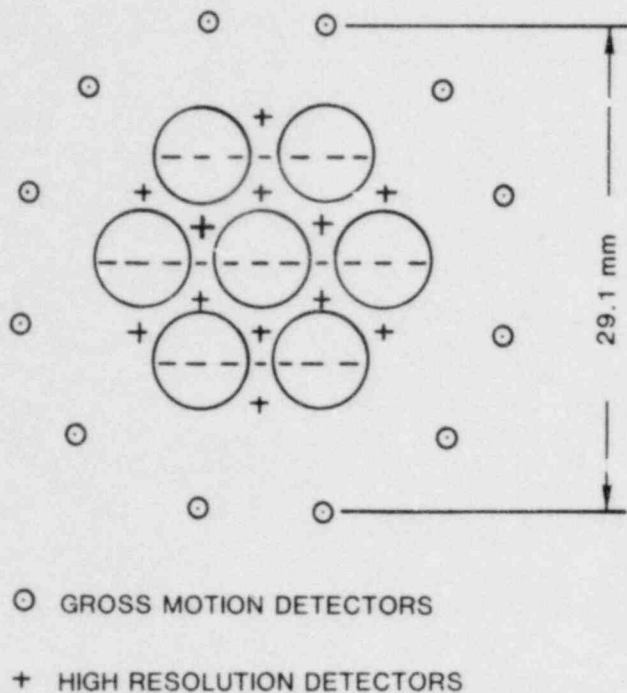


Figure 2.3-2 Radial Location of Detectors for the Seven-Pin High Resolution and Gross Motion Experiments

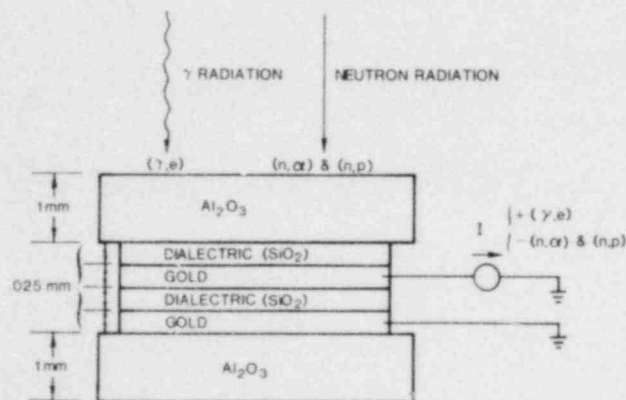


Figure 2.3-3 Thick Film Self-Powered Detector

Experiments performed in the SPR-III reactor confirmed most of the above speculation on how these detectors operate. These experiments were performed by placing the detectors outside the SPR-III reactor approximately 0.584 m from the core centerline. The radiation incident on the detector was perturbed from free-field conditions by placing blocks of lead or polyethylene between the reactor and the detector. For each configuration (i.e., lead, poly, or free field) the gamma-ray fluence and the number of charged particle interactions were recorded. The

gamma-ray fluence was determined by using TLDs. The charged particle interactions were determined by counting the specific activity of the residual ^{24}Na nucleus resulting from the $^{27}\text{Al}(n,\alpha)^{24}\text{Na}$ nuclear interaction. These results confirmed that the forward and backward (top-bottom) sensitivities of the detector to the incident radiation are of nearly equal magnitude and of opposite sign. In addition, they showed that the sign of the (n,α) sensitivity of the detector was opposite to that of the gamma-sensitivity of the detector. This seems to confirm that the major charged particle interactions which cause signals to be developed are due to fast neutron interactions competing with gamma induced Compton electrons. Also, the magnitude of the gamma-sensitivity (γ,e) was approximately twice that of the fast neutron (n,α) and (n,p) sensitivity for the SPR-III flux.

The transport and slowing down of these highly energetic charged particles through the dielectric significantly alters its conductivity. Replacement currents flowing between the electrodes may also be created and could affect measured output currents. In addition, charge trapping in the dielectric may cause the detector to have long term changes in sensitivity because of the total radiation dose to which the detector is exposed. The theory to take these effects into account is being developed. To aid in the development of this theory, future detectors will be fabricated from very pure materials for which many of the electronic properties (e.g. radiation induced conductivity, density of traps, etc) are known. More experiments will then be performed to determine the sensitivity characteristics of the detector and to assess how these electronic characteristics affect the detector response.

References for Section 2

- 2-1 M. Epstein, et al, "Transient Freezing of a Flowing Ceramic Fuel in a Steel Channel," *Nucl. Sci. Eng.*, 61, pp 310-323, 1976.
- 2-2 R. W. Ostensen, et al, "Fuel Flow and Freezing in the Upper Subassembly Structure Following an LMFBR Disassembly," *Trans. Am. Nucl. Soc.*, 18, 1974, pp. 214-215; M. E. Epstein, et al, "Analytical and Experimental Studies of Transient Fuel Freezing," *Proc. Int'l Mtg. on Fast Reactor Safety and Related Physics*, USERDA-CONF-761006, Chicago, IL, 1976; B. W. Spencer, et al, *Reactor-Material Fuel Freezing Experiments Using Small-Bundle, CRBR-Type Pins*, ANL/RAS 79-11 (Chicago, IL: Argonne National Laboratory, July, 1979), p 14.
- 2-3 M. Amblard, unpublished presentation at Brookhaven National Laboratory, Upton, NY, December, 1979.
- 2-4 E. F. Nippes, et al, "An Investigation of the Hot Ductility of High Temperature Alloys," *Welding Research Supplement*, pp 183-s through 196-s, April, 1955.
- 2-5 L. Leibowitz, et al, *Properties for LMFBR Safety Analysis*, ANL-CEN RSD-76-1 (Chicago, IL: Argonne National Laboratory, 1976).

- 2-6 D. R. Olander, *Fundamental Aspects of Nuclear Reactor Fuel Elements*, TID 26711-P1 (Springfield, VA: USDOE Technical Information Center, 1976).
- 2-7 O. D. Slagle, *Deformation Behavior of UO_2 at Temperatures above 2400°C* (HEDL-TME 78-31, UC796, 1978).
- 2-8 S. A. Wright and H. L. Scott, "Energy Deposition Measurements in Fast Reactor Safety Experiments with Fission Thermocouple Detectors," *Transactions of the ANS Winter Meeting*, San Francisco, CA, November 1979.
- 2-9 *Advanced Reactor Safety Research Combined Quarterly Report, October 1978 - March 1979*, SAND79-1566, NUREG/CR-0983 (Albuquerque, NM: Sandia National Laboratories, September, 1980).

3. Core Debris Behavior – Inherent Retention

3.1 Molten Core Containment

(D. A. Powers, 4422; J. F. Muir, 4441; W. Luth, 5541; T. Y. Chiu, 1537)

3.1.1 Introduction

The Molten Core Containment program is an experimental and analytical effort to identify and quantify the safety-related processes that could occur during interaction of core debris with nuclear-reactor containment structures. The experimental program involves the interaction of prototype core materials at realistic temperatures with structures representative of those found in existing and planned nuclear reactors. The program emphasizes the generic aspects of the interactions. Results of the program are useful in the analysis of light-water and gas-cooled reactors as well as LMFBRs during accident situations.

The initial thrust of the program was the investigation of molten core-debris interactions with various types of concrete and steel liners. These studies established that melt/concrete interactions are quite vigorous. The generation of gases by thermal decomposition of the concrete is a dominant process during the interaction. The rapid erosion of concrete and the generation of gas continues even after the core materials have solidified. Recently, experimental efforts in this program have been redirected toward the study of solidified debris with concrete and the study of molten core debris with candidate materials that would be more suitable than concrete for the retention of molten core materials. Candidate materials being examined in the program are magnesia, firebrick, high alumina cement, and borax.

Phenomenological models developed from the experimental results of this program will be of use in the analysis of the structural integrity of reactor containments during severe accident situations. These phenomenological models will be incorporated in the containment analysis program.

3.1.2 Interaction of Molten Oxides With Core Retention Materials

Activities during the past quarter have centered development of techniques for examination and

posttest analysis of in-pile and out-of-pile experiments involving the interaction of molten UO_2 (+ La_2O_3 + steel) with commercial grade ceramic materials. The focus is on electron microprobe chemical analysis of the products of the reactions of molten core simulant with MgO and $MgAl_2O_4$ bricks. This analysis is providing information on diffusion and melting reactions in the bricks. The information thus obtained leads to estimates of both equilibrium and kinetic factors controlling the mechanism of attack.

The analytical method takes full advantage of the accuracy, precision, and automated capability of the Sandia electron microprobe, and has been developed with the collaboration of W. F. Chambers of Sandia. To assure full potential in treating chemically complex systems with a large (≈ 9) number of independent chemical components, the approach has been tested on natural basaltic rocks containing 4 to 6 crystalline phases (all of which are solid solutions) and a multicomponent glass.

A polished thin section is prepared and examined optically to identify particular areas of interest. The electron microprobe is calibrated relative to standards of known composition and the sample of interest is placed in position under the electron beam. Preliminary analyses on selected areas are conducted by using 2 to 5 μm (square raster) electron beam incident on the sample to identify phases and their local variability. Subsequent to this "hands-on" data collection, the analyses are obtained in a fully automated manner. The procedure is to identify points which define the ends of 1 to 6 vectors on the sample, specify the number of analysis points per vector (not necessarily the same for all vectors), and conduct the analyses of all points. The data can be collected overnight and typically (depending on number of element, counting precision, and background counting interval) 300 to 600 data points are obtained. This method, employing wave-length dispersive rather than energy dispersive analysis, provides high precision information on

- Weight and volume percent of phases present
- Chemical composition, range and variability within and between phases
- Average bulk chemical composition of the sample
- Spatial distribution of phases along the vector(s) employed.

As noted previously, this approach has been tested on more complex (chemically) natural system. Sandia's

analyses of both in-pile and out-of-pile experiments will be based on this method. Samples of appropriate materials from previous experiments have been selected for analyses and are now being prepared.

Experimental studies of molten UO_2 with potential sacrificial materials are in the planning stage for out-of-pile static and dynamic experiments. Sandia staff members are examining potential natural materials which may serve to quench the molten material while simultaneously forming a high-viscosity-silicate melt which would serve as a possible hot medium for radionuclides and as a barrier for the concrete reactor substructure and the environment. Preliminary experiments planned for the next quarter will emphasize molten core materials interacting sequentially with granite, MgO , and concrete.

3.1.3 Analysis of Melt/Concrete Interactions

One aspect of melt/concrete interactions that must be addressed in modeling their long-term behavior is the crust formation and growth that occurs during solidification of the oxidic phase of the melt. Crust formation is expected around the periphery of the melt (on the exposed surface of the slag layer and at the oxidic-phase/concrete interface) where temperatures are lowest. One material property that undoubtedly plays a significant role in the process of crust formation is viscosity. The viscosity of single phase siliceous melts increase dramatically with decreasing temperature. As the melt temperature falls below its liquidus value, the precipitation of solids produces a two-phase slurry having a viscosity different from that of the single-phase melt because of the presence of the solid particulate.

The viscosities of molten siliceous materials have been correlated into an empirical formulation described by Bottinga and Weil.⁽³⁻¹⁾ This correlation has been implemented in a computer subroutine, VISRHO,⁽³⁻²⁾ that has been incorporated into the CORCON and WECHSEL computer models of melt/concrete interactions. The subroutine provides density and viscosity data for siliceous melts of varying composition and temperature. The viscosity data provided by the subroutine are for single-phase liquids.

Precipitation of solids in the siliceous melts will cause the viscosity of the resulting slurry to differ from that of the single-phase melt. It is generally observed that such slurries are thixotropic. That is, the viscosity is a nonlinear function of shear rate. The viscosity of a model thixotropic eutectic slurry as a function of shear rate is shown in Figure 3.1-1. This

dependence of viscosity on shear rate is approximately exponential:

$$\eta = \eta_0 \exp(-\alpha \dot{\omega})$$

where

η = viscosity

η_0 = viscosity at zero-shear rate

$\dot{\omega}$ = shear rate

α = parameter.

The viscosity at zero-shear rate is not the viscosity of the pure liquid. Rather it is the viscosity of the liquid-solid slurry.

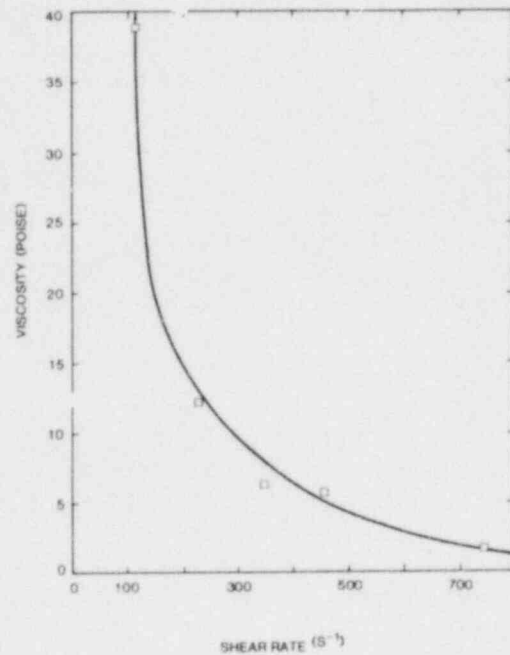


Figure 3.1-1 Shear-Rate Dependence of Slurry Viscosity

Several correlations of the viscosities of slurries are available. For slurries containing less than 50 v/o solid, Kunitz⁽³⁻³⁾ has suggested

$$\frac{\eta_s}{\eta_l} = \frac{1 + 0.5\phi}{(1 - \phi)^4}$$

where

η_s = viscosity of the slurry

η_l = viscosity of the pure liquid

ϕ = volume fraction of solids.

Ting and Luebbbers⁽³⁻⁴⁾ found the following correlations:

- (1) Spherical particles, $\phi < 0.3$:

$$\frac{\eta_s}{\eta_l} = \left[\frac{1}{1 - \left(\frac{\phi}{0.46 - 0.00158 \left(\frac{\eta_l}{R} \right)^{0.469}} \right)} \right]$$

(2) Cubic particles, $\phi < 0.4$:

$$\frac{\eta_s}{\eta_l} = \frac{0.403}{0.403 - \phi}$$

where

$$R = \rho_s / \rho_l$$

ρ_s = density of the particle.

Note that for all the correlations viscosity increases as solid particles are added. Viscosities become quite large when the volume fraction of solids exceeds about 0.4. For a precipitating system of a typical binary oxidic mixture, a slurry of 40% solids could be achieved when the temperature of the system was the average of the solidus and liquidus temperatures at the bulk composition.

3.1.4 Analysis of Melt/MgO Interactions: Heat of Fusion of MgO

Numerous analytic attempts are being made to estimate the attack on MgO by molten reactor fuel using a thermal ablation formalism.^(3-5, 3-6) The formulation of the problem consists of approximating the reactor fuel as pure UO₂, assuming some directional dependence of heat rejection from the molten pool, and using heat rejected from the pool into the MgO as the controlling factor in determining the ablation rate. A variety of other explicit, but usually implicit, assumptions such as treating MgO as a monolithic nonporous mass are typically made in constituting the problem within the ablation formalism.

The rate of ablation of the MgO is found by dividing the rate of heat input into the MgO by the "heat of ablation" of MgO. Sometimes conduction of heat by the MgO is also considered. The estimation of the "heat of ablation" is formulated as

$$\Delta H_{abl} = \int_{T_0}^{T_{abl}} C_p(\text{MgO}) dt + L_{\text{MgO}}$$

where

T_0 = initial temperature of the MgO

T_{abl} = ablation temperature of the MgO

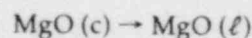
$C_p(\text{MgO})$ = heat capacity of MgO

L_{MgO} = latent heat of fusion.

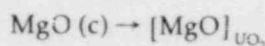
T_{abl} is often taken to be the eutectic temperature between MgO and UO₂ though, occasionally, the true melting point of MgO is used.

Without commenting on the applicability of the ablation formalism to the treatment of fuel-melt interactions with MgO, an error must be noted in the formulation of the problem within the assumption delineated above.

As outlined above, the formulation involves assuming the latent heat of fusion of MgO is temperature independent. The ablation treatment is, in essence, a treatment of MgO undergoing the reaction



when, in fact, the true reaction is



where the square brackets are read "solvated in the subscripted system." As constituted, the formulation neglects any enthalpic effects of solvation and presumes that they will be compensated by using the low eutectic temperature of the system rather than the melting point of MgO as the ablation temperature. No information is yet available to refute this contention. Data are available, however, to refute the subsequent use of a hypothetical, temperature-independent heat of fusion.

At the normal melting point of MgO, the free-energy of melting is

$$\Delta G(T_m) = \Delta H(T_m) - T_m \Delta S_m = 0$$

where

T_m = melting point

$\Delta H(T)$ = enthalpy of melting at temperature T

ΔS_m = entropy of melting.

Now if by some "magical" effect (that is, the solvation process), the melting temperature is reduced to T_e the free-energy is given by

$$\Delta H(T_e) - T_e \Delta S_m = \Delta G(T_e) = 0.$$

If heat capacity effects are ignored, then ΔS_m is independent of temperature, and

$$\Delta S_m = \frac{\Delta H(T_m)}{T_m},$$

then

$$\Delta H(T_e) = \Delta H(T_m) \left(\frac{T_e}{T_m} \right).$$

That is, the latent heat of fusion must, within the approximation, decrease linearly with temperature. Then $\Delta H(T_m)[(T_e - T_m)/T_m]$ may be considered the ideal "heat of solvation." At a eutectic temperature of 2473 K the absolute value of the ideal heat of solvation is 20% of the latent heat of fusion at the normal melting point.

Inclusion of the heat effect because of the solvation of the eroded MgO in the analysis of ablation will result in faster ablation rates. The MgO/UO₂ system is, of course, far from ideal. Qualitative considerations of the manifestations of nonideal behavior that could occur in the system (such as preferential stabilization of MgO, deviation of UO₂ from stoichiometry) suggest that the real heat of solvation will be even more negative than the ideal heat of solvation calculated here. Consequently, the ablation rates calculated even with idealized heats of solvation will still be lower bounds on the true ablation rates.

3.1.5 Survey of Leaching Characteristics of Corium-Concrete Mixtures

In response to interest in the liquid pathway of fission product release following a core-meltdown accident at a nuclear power plant, an effort to examine, in an exploratory fashion, the aqueous leaching of corium mixtures with concrete was initiated. Preliminary results of this effort are reported here.

Leach studies were done on a basaltic concrete-corium mixture having the composition shown in Table 3-I. The composition of the basaltic concrete used in the sample mixture is shown at the bottom of the table. These compositions are based on the constitution of the mixture before firing. The compositions have been corrected for loss of water, carbon dioxide, and sulfur oxides during the firing process. But, no determination of postfiring composition has been made. It is likely that the firing process did lead to some volatilization of some species such as the alkali metal oxides, oxides of chromium and oxides of molybdenum. However, some studies have suggested that the siliceous matrix provided by the concrete would sharply reduce the volatility of these two

species. Molybdenum and cesium were charged into the mixture as calcium molybdate and cesium uranate to reduce their volatilities until any stabilization by the siliceous matrix became available.

Table 3-I Sample Composition

Species	Weight (g)	Weight (%)
Basaltic concrete (dry)	0.400	48.08
Cs ₂ O (constituted as Cs ₂ U ₄ O ₇)	0.0085	0.044
SrO	0.016	0.082
ThO ₂	0.020	0.10
Nb ₂ O ₅	0.020	0.10
CeO ₂	0.020	0.10
La ₂ O ₃	0.020	0.10
MoO ₃ (constituted as CaMoO ₄)	0.028	0.14
SrO ₂	0.020	0.10
ZrO ₂	1.84	9.41
UO ₂ corium	6.16	31.50
Fe ₃ O ₄	1.00	5.11
Cr ₂ O ₃	1.00	5.11

Basaltic Concrete Composition

Fe ₂ O ₃	6.25%
TiO ₂	1.05
K ₂ O	5.38
Na ₂ O	1.8
CaO	8.8
MgO	6.15
SiO ₂	54.73
Al ₂ O ₃	8.3

Wt loss on drying at 700°C = 6.5%

The mixture of powders was fired at 1673 ± 20 K for 16 hr in a platinum crucible. The mixture was air-quenched, crushed to about a 100-μm mean particle size, and refired for 16 hr. At the conclusion of this second firing, the sample was cooled in the furnace to ~ 873 K (3 hr) and then air-quenched.

A photograph of the sample and micrographs of the sample after it has been extracted from the crucible are shown in Figure 3.1-2. The fused material had a grey-brown color. It appeared macroscopically to be glassy. The micrographs show the material to be very porous. Gross pores 0.07 to 0.3 mm in diameter are readily apparent. The porous structure suggests the mixture may have not been a single phase during the firing. Some of the pores have a shiny collar. This shiny material is most likely glass though it could be metal produced by thermal decomposition of oxides in the mixture.

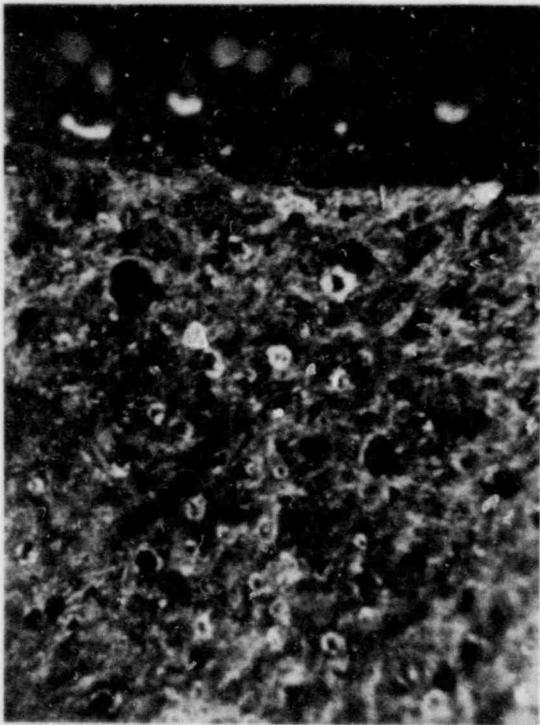
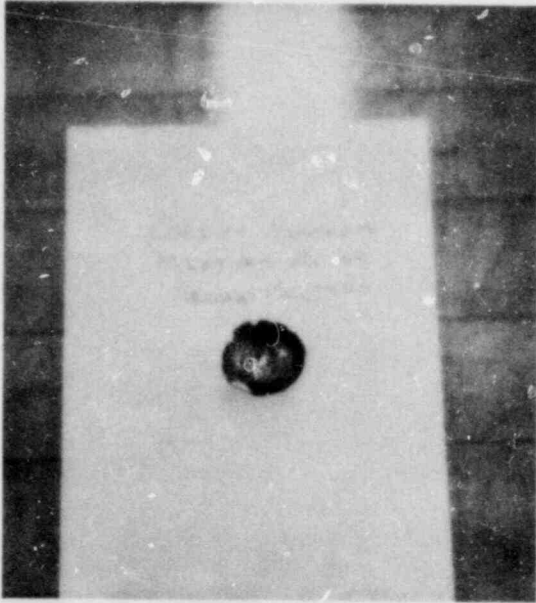


Figure 3.1-2 Photographs of Leach Specimen
(Micrographs are at 21x)

The mixture was hand crushed in a steel mortar until it would all pass through a 150 mesh screen. All the material, save a 1.5-g chunk, was crushed so that any macroscopic segregation of the material—which was not visually apparent—would not influence the leaching results.

No attempt has yet been made to characterize the particle size or surface area of the crushed material used in the leach tests. The screening of the sample

suggests the surface area will be greater than $125 \text{ cm}^2/\text{g}$.

The leaching procedure was to charge a sample of 0.3 to 1.0 g of sample into a 25 ml teflon crucible with about 15 ml of the leach liquor. The liquor had previously been deaerated with N_2 and filtered. The crucible was capped with a teflon top and sealed in a Parr acid dissolution bomb. The bomb and its contents were then heated with little agitation in a laboratory drying furnace. After the desired time at temperature, the bomb was removed from the furnace and set into a massive steel fixture to rapidly quench it. A typical example of the early time-temperature profile for the leach treatment is shown in Figure 3.1-3. Heatup of the sample was rapid enough in comparison to the duration of the leach experiments that the early temperature transient ought not to have unduly influenced the results.

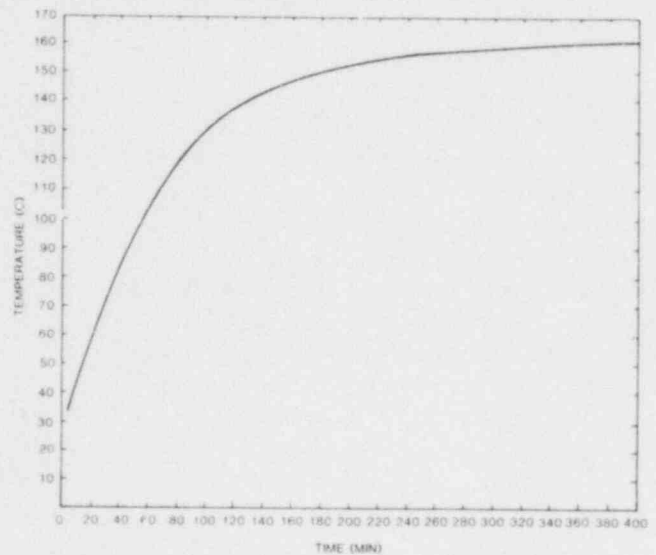


Figure 3.1-3 Typical Heat-Up of Leach Sample in Bomb

Once the leach treatment was complete, the liquor was decanted from the particulate and placed in a steamed glass vial with a plastic stopper. Neutron activation analysis by General Activation Analysis, Inc (11575 Sorreto Valley Road 214, San Diego, CA) was used to determine the compositions of the samples. For samples 1 through 13 and for blank analyses of the leach liquors prior to the leach experiments the following procedure was used:

Samples were irradiated for 30 min in a TRIGA Mark I Nuclear Reactor at a flux of $1.8 \times 10^{12} \text{ n/cm}^2\text{-s}$. After decay periods of 1h, 1d, 7d and 21d, the samples were monitored with a Ge(Li) detector coupled to a multichannel gamma-ray spectrometer. For data on very short half-life isotopes, the samples were re-exposed for 1 min at a flux of $2.5 \times 10^{12} \text{ n/cm}^2\text{-s}$

and then monitored for 1 min after a decay of 1 min.

The procedure for analysis of samples 19 through 23 was:

Samples and comparator standards were irradiated for 30 min at a flux of 1.8×10^{12} n/cm²-s in the TRIGA Mark I Nuclear Reactor. After decay periods of 1h, 4d, and 21d the samples were monitored with a Ge(Li) detector coupled to a multichannel gamma-ray spectrometer. The isotopes and their half-lives used in the data analysis were

Element Sought	Irradiation Production	Half-Life
U	No ²³⁹	2.35d
Cs	Cs ¹³⁴	2.1 y
Ce	Ce ¹⁴¹	32.5 d
La	La ¹⁴⁰	1.67d
Sr	Sr ^{87m}	2.8 h
	Sr ⁸⁹	50.8 d

Neutron activation was chosen as the analytic tool for its convenience and because in the multielement survey mode it provides upper bounds on constituents not actually observed in the solution. This multielement survey method was used for samples 1 through 13 and for the solution blanks. In some cases (Zr, Fe, etc), the upper bounds are so large they are useless. However, in other cases (Th, etc) the bounds do provide meaningful estimates. The vendor supplying the neutron activation services claimed an accuracy of $\pm 20\%$ to 40% . However, he cautioned that interferences might influence this estimated accuracy. One such interference came from sodium. First day counts on the irradiated solutions that contained large concentrations of sodium were done with a detector 2 ft from the sample. This, of course, had a drastic effect on the detectability limits as well as the accuracy.

Another difficulty was encountered when uranium was present at even moderate concentrations in the solution. The uranium spectrum would then be sufficiently intense that it would severely reduce the detectability of other elements.

A more sensitive method based on comparator standards was used for samples 19 through 23. Only the specific elements U, Ce, Cs, Sr, and La were determined by this method.

During the course of the work, some of the liquors were observed to contain flocculent suspended solids. A crude Tyndell effect experiment suggested that they also contained colloidal species. No identification of these species was made. Whether they

were formed during the leaching process or were precipitated from the liquor during cooling is not known. To remove the contribution of the solid material from the analytic results, some of the samples were filtered by pressure through a Millipore filter (0.22 μ).

The variables studied in the leach experiments were

- Time of leaching
- Temperature of leaching
- The effect of water chemistry on leaching.

A summary of the tests is presented in Table 3-II.

Water chemistry was investigated by looking for a pH effect and for liquid phase reactions. Parallel tests were done with liquors having pH values of 7.8 and 4.2. (pH was adjusted with 1 M HNO₃ and 10 M NaOH solutions.) However, the solutions were not buffered. After leaching, the pH of the solution was found to have risen to 9.1 ± 0.3 regardless of the initial pH. Dissolution of alkali metal and alkaline earth oxides is believed to have been responsible for the increase in pH. The increase in pH probably obliterated any differences in the leaching ability of the solutions of different initial pH values.

Leaching of uranium, and perhaps other elements, ought to be susceptible to solution chemistry. The aspects of solution chemistry that were investigated were complex formation and oxidation. Stabilization of a dissolved species in solution (as a complex) ought to enhance the species' apparent solubility. Complexing anions that might arise in ground water were included at very high concentration in some of the solutions as follows:

0.53 M NaCl

0.49 M Na₂HPO₄

Saturated CaCO₃ solution.

All the anions in the above list are well-known to complex uranium. Chloride and phosphate anions also complex rare-earths. Manufacturer analyses of the NaCl and Na₂HPO₄ used in the tests are shown in Table 3-III.

Many species, but especially uranium, are stable in melts as low valence species. Oxidation markedly enhances the solubility of uranium in water. To examine the effect of oxidation, leach experiments were conducted with the following solutions:

0.1 M Fe(NO₃)₃ · 9H₂O

0.1 M K₂Cr₂O₇.

Potassium dichromate is, of course, an obvious oxidant. Ferric nitrate is not so clearly an oxidant. Ferric ions will oxidize uranium by



In air, this is a catalytic process since the product ferrous ion can be oxidized back to ferric ion. In the sealed bombs used for these experiments, such reoxidation was sharply limited.

The ferric nitrate hydrolyzed during leaching precipitated as a light brown very fine-particulate mass that is probably similar to the Towe and Bradly hydroxide. This precipitated mass, which incorporated nearly all the iron from solution (residual iron < 1400 ppm), must surely have acted as "carrier" to

absorb many of the dissolved species from the leach liquor. Some of the effects of ferric ions on the leaching may have been obscured by the hydrolysis and precipitation. But as will be noted below, the main effect of accelerated uranium leaching was not missed.

The dichromate solution also precipitated a greenish-orange mass. It may be that dichromate is a sufficiently powerful oxidant that it was converted at least partially to Cr_2U_3 or CrO(OH) at the elevated temperature of the test.

Table 3-II Summary of the Tests

Test	Liquor	Sample Wt (g)	Time (hr)	Maximum Temperature (c)	Filtration (μ)	Comment
1	pH7.8 H ₂ O	1.0003	119.5	149	2.0	
2	pH4.0 H ₂ O	1.0003	119.5	149	2.0	
3	pH7.8 H ₂ O	0.99996	119.7	199	none	20 ml solution v. much ppt.
4	pH4.0 H ₂ O	1.00007	119.7	199	0.22	20 ml solution
5	pH7.8 H ₂ O	1.00044	88.9	129	0.22	
6	pH4.0 H ₂ O	1.00012	88.8	129	none	
7	pH7.8 H ₂ O	0.99862	116.1	79	0.22	
8	pH4.0 H ₂ O	1.00048	116.1	79	0.22	
9	0.54M NaCl ^(a)	1.0003	121.4	157	0.22	
10	0.49M Na ₂ HPO ₄ ^(b)	0.99981	121.4	157	0.22	
11	0.10M Fe(NO ₃) ₉ H ₂ O	0.997112	93.0	161	0.22	
12	0.10M K ₂ Cr ₂ O ₇	1.00132	93.0	161	0.22	
13	saturated CaCO ₃ solution	1.00570	110.5	161	0.22	
19	pH7.8 H ₂ O	0.49266	1.55	138	0.22	
20	pH7.8 H ₂ O	0.49852	47.0	161	0.22	
21	pH7.8 H ₂ O	0.49778	24.1	161	0.22	
22	pH7.8 H ₂ O	0.49610	14.0	161	0.22	
23	pH7.8 H ₂ O	0.50063	6.7	161	0.22	

(a) Lot analysis, Table 3-III

(b) Lot analysis, Table 3-III

Table 3-III Lot Analyses of Dissolved Materials

NaCl		Na ₂ HPO ₄	
I	0.001%		
Insol.	0.002	Insol.	0.002%
N	0.002	N	0.001
PO ₄	2.0 ppm		
SO ₄	0.001	SO ₄	0.005
Ba	0.001		
Ca, Mg, R ₂ O ₃	0.002		
Pb	0.5 ppm	Pb [*]	0.0003
Fe	0.7 ppm	Fe	0.0005
K	0.003		
Br	0.001	Cl	0.001
		Wt loss on dry- ing at 105°C	0.041%
		Assay as Na ₂ HPO ₄	100.1%

3.1.6 Results From the Leach Tests

Analytic results from the leach tests are presented in Table 3-IV. Data accompanied by uncertainty bounds in this table were actually determined by the neutron activation analysis. Data with parentheses are calculated upper bounds on the species concentration in solution. The upper bounds are computed based on the inability to detect an activation product from the species in question. Consequently, the upper bound data should be used with caution.

Upper bound data were reported by the vendor for every element. Results are reproduced here only for elements deliberately included in the corium-concrete and for common major contaminants of the sources of these elements. Unfortunately, the actual concentrations of these contaminants in the leached mixture are not known.

The compositions of the leach liquors before use are shown in Table 3-V. Bound estimates in this table must be carefully used. In no case should the bounds be subtracted from either bound data or determinations in Table 3-IV.

Some qualitative conclusions that can be reached from the data in Table 3-IV are

- Ce, La, Cs, and U are definitely leached from the corium-concrete mixture.

- Al, Mn, and V are also leached. Both Mn and V were introduced into the charge as contaminants in other constituents of the mixture.
- With one exception, no definitive leach data save upper bound data were obtained for zirconium.
- Similarly, no definitive data for Fe, Si, or Ca were obtained.
- Upper bound data for Sr and Th suggest these elements are not readily leached.
- Comparison of data for sample 3 and sample 4 does not suggest the composition of the flocculent precipitate in sample 3.
- As expected, initial pH of the unbuffered leach liquor had no statistically significant impact on leaching. The more acidic solution may have been slightly more efficient in leaching rare-earth from the matrix.
- Sodium chloride in the leach liquor did not make the liquor a more efficient leaching medium relative to water. Analytic difficulties caused by the high Na concentration may have masked some of the effects of chloride ion on leaching.
- Phosphate ion did appear to enhance leaching of U, Zr, Al, and possibly La. Enhancement of zirconium leaching was dramatic.
- Ferric ion dramatically increased the leaching of uranium and zirconium. It may also have accelerated leaching of cerium and cesium. The increase in surface area due to removal of the major constituents U and Zr of the matrix may have been responsible for this apparent accelerated removal of cerium and cesium. The naturally low pH of the solution may have been responsible for all the effects.
- Interestingly the dichromate solution did not have the same effect as did the ferric solution even though the dichromate anion is a much stronger oxidant than the ferric cation.
- CaCO₃ saturated water was not an exceptional leach liquor.

The effect of water chemistry on the leaching of uranium and zirconium is startling. Clearly, leach liquors containing ferric ion or phosphate ion are the most potent leach media used in this study. Phosphate ion accelerated leaching of uranium by about an order of magnitude. Leaching of zirconium was also accentuated by at least an order of magnitude.

Table 3-IV Analysis of Leach Liquors (Entries in ppm)

Test	Arsenic	Barium	Calcium	Cerium	Chromium	Cesium	Iron	Hafnium	Lanthanum
1	(0.23)	(0.94)	(93)	0.238 ± 0.057	(0.51)	0.993 ± 0.20	(32)	(0.018)	0.044 ± 0.012
2	(0.44)	(1.20)	(43)	0.257 ± 0.061	(0.75)	0.714 ± 0.14	(46)	(0.02)	0.0492 ± 0.018
3	(0.31)	(1.8)	(41)	0.136 ± 0.042	(0.40)	0.672 ± 0.14	(46)	(0.013)	(0.097)
4	(0.26)	(1.10)	(35)	0.142 ± 0.042	(0.52)	0.667 ± 0.13	(62)	(0.018)	(0.067)
5	(0.21)	(0.70)	(31)	(0.11)	(0.45)	0.0656 ± 0.016	(32)	(0.0061)	(0.037)
6	(0.10)	(1.3)	(40)	0.168 ± 0.064	0.748 ± 0.180	0.132 ± 0.03	(66)	(0.035)	0.0398 ± 0.018
7	(0.084)	(0.72)	(34)	(0.18)	(1.0)	0.0888 ± 0.023	(55)	(0.009)	(0.047)
8	(0.097)	(1.10)	(35)	(0.71)	(3.5)	(0.095)	(580)	(0.0084)	(0.070)
9	(3.4)	(35.0)	(1700)	(0.27)	(0.49)	1.68 ± 0.34	(69)	(0.031)	(0.74)
10	(10.0)	(340.0)	(1800)	(9.5)	(1.4)	1.61 ± 0.33	(110)	(0.29)	0.722 ± 0.32
11	(49.0)	(600.0)	(700000)	733 ± 150	(30.0)	8.26 ± 1.70	(1400)	(11.0)	(86)
12	(0.75)	(6.5)	(150)	(48)	19600 ± 3900	2.33 ± 0.48	(130)	(0.12)	(0.23)
13	(0.17)	(0.61)	(120)	(0.2)	(1.3)	(0.25)	(100)	(0.034)	(0.051)
19				< 0.025		0.076			< 0.015
20				0.054		0.348			< 0.017
21				< 0.031		0.203			< 0.019
22				0.081		0.273			< 0.019
23				< 0.021		0.176			< 0.019

Test	Magnesium	Molybdenum	Niobium	Rubidium	Antimony	Silicon	Tin	Strontium	Thorium
1	(130)	(6.4)	(100)	(1.8)	(0.074)	(490)	(3.7)	(3.5)	(0.074)
2	(39)	(7.8)	(110)	(2.1)	(0.15)	(440)	(4.2)	(1.6)	(0.092)
3	(63)	(3.6)	(160)	(1.1)	(0.1)	(1800)	(3.9)	(3.0)	(0.054)
4	(45)	(3.5)	(110)	(1.1)	(0.081)	(1900)	(6.0)	(3.4)	(0.053)
5	(24)	(1.6)	(62)	(0.68)	(0.063)	(130)	(2.2)	(1.0)	(0.034)
6	(44)	(17.0)	(99)	(0.97)	(0.032)	(590)	(3.9)	(2.6)	(0.073)
7	(26)	(7.0)	(75)	(0.8)	(0.025)	(130)	(2.6)	(1.2)	(0.070)
8	(19)	(12.0)	(77)	(0.84)	(0.028)	(170)	(2.0)	(2.6)	(0.30)
9	(1900)	(2.9)	(1300)	(5.0)	(0.37)	(4200)	(42.0)	(92.0)	(0.06)
10	(2800)	(58.0)	(2000)	(8.6)	(1.2)	(9900)	(120.0)	(140.0)	(0.22)
11	not det'm	(4300.0)	(21000)	(120.0)	(3.2)	not det'm	(780.0)	(310.0)	(2.3)
12	(170)	(63.0)	(400)	(6.4)	(0.24)	(340)	(13.0)	(8.4)	(71.0)

Table 3-IV (cont)

Test	Magnesium	Molybdenum	Niobium	Rubidium	Antimony	Silicon	Tin	Strontium	Thorium
13	(58)	(2.8)	(200)	(1.5)	(0.098)	(760)	(3.5)	(1.2)	(0.082)
19							<2.5		
20							<2.2		
21							<3.1		
22							<2.3		
23							<2.6		

Test	Uranium	Zirconium	Vanadium	Sodium	Aluminum	Potassium	Ruthenium	Manganese
1	3.81 ± 0.76	(190)	(0.065)	73.2 ± 15	2.87 ± 0.58	41 ± 11	(1.5)	0.351 ± 0.071
2	3.81 ± 0.76	(140)	(0.077)	61.9 ± 12	2.37 ± 0.48	33.2 ± 9.5	(1.2)	0.0482 ± 0.010
3	1.91 ± 0.38	(280)	0.0427 ± 0.011	104 ± 21	11.0 ± 2.2	(88)	(1.1)	0.0172 ± 0.0057
4	1.66 ± 0.33	(240)	0.0532 ± 0.012	65 ± 13	11.8 ± 2.4	25.9 ± 8.8	(1.1)	0.0363 ± 0.0081
5	0.0304 ± 0.063	(140)	0.0248 ± 0.0055	31.7 ± 6.3	0.754 ± 0.15	(37)	(0.73)	0.0115 ± 0.0035
6	5.21 ± 1.00	(150)	0.0141 ± 0.0055	37.8 ± 7.6	3.52 ± 0.71	9.95 ± 4.6	(0.97)	0.0246 ± 0.0057
7	0.126 ± 0.028	(140)	0.0272 ± 0.0059	26.9 ± 5.4	0.835 ± 0.17	(35)	(0.8)	0.0222 ± 0.0051
8	0.307 ± 0.064	(130)	0.0138 ± 0.0037	32.5 ± 6.5	1.03 ± 0.21	(35)	(3.5)	0.0225 ± 0.0054
9	(0.34)	(510)	(2.5)	15900 ± 3200	(34)	(14000)	(1.90)	(4.4)
10	80.3 ± 16	2820 ± 610	(1.5)	29500 ± 5900	43.3 ± 9.5	(21000)	7.73 ± 1.6	(7.3)
11	7740 ± 1500	344000 ± 690000	not det'm	542 ± 110	not det'm	(4300)	923 ± 180	65.3 ± 13
12	4.64 ± 1.00	(770)	not det'm	200 ± 40	1.84 ± 0.39	13200 ± 2600	(5.4)	0.124 ± 0.03
13	1.11 ± 0.23	(96)	0.068 ± 0.017	63.3 ± 13.0	4.72 ± 0.96	29.7 ± 7.7	(1.5)	(0.02)
19	0.133							
20	0.382							
21	0.130							
22	0.546							
23	0.395							

Table 3-V Major Constituents of Leach Solution Before Use (Entries in ppm)

Solution	Aluminum	Gold	Barium	Bromine	Chlorine
pH7.8 H ₂ O	0.543 ± 0.11	(7.4x10 ⁻⁴)	(0.34)	0.0197 ± 0.0081	7.29 ± 1.50
pH4.0 H ₂ O	0.378 ± 0.08	(0.0014)	(0.37)	0.0243 ± 0.0094	4.46 ± 1.00
NaCl sol'n	(31)	(0.008)	(28.0)	(2.3)	25900 ± 5300
Na ₂ HPO ₄ sol'n	42 ± 8.8	(0.0057)	(170.0)	(0.81)	(8500)
Ferric sol'n	3.07 ± 0.63	(0.0016)	(5.9)	(0.28)	(53)
K ₂ Cr ₂ O ₇ sol'n	0.447 ± 0.11	(0.0046)	(3.0)	(0.44)	4.95 ± 2.00
Sat'd CaCO ₃	(0.79)	7.78 ± 3.7x10 ⁻⁴	0.159 ± 0.047	0.0606 ± 0.016	0.905 ± 0.270

Solution	Cobalt	Copper	Chromium	Iodine	Iron
pH7.8 H ₂ O	3.02 ± 0.62	(0.4)	(1.2)	(0.13)	(240)
pH4.0 H ₂ O	5.85 ± 1.20	(0.37)	(1.2)	0.277 ± 0.064	(140)
NaCl sol'n	(0.11)	(300.0)	(1.10)	(340.0)	(110)
Na ₂ HPO ₄ sol'n	(0.12)	(230.0)	(1.9)	(680.0)	(110)
Ferric sol'n	(0.31)	5.46 ± 1.10	7.56 ± 1.20	(1.5)	6330 ± 1300
K ₂ Cr ₂ O ₇ sol'n	(0.11)	(5.30)	13100 ± 2600	(1.4)	(90)
Sat'd CaCO ₃	(0.12)	(0.20)	(0.99)	0.0514 ± 0.014	(78)

Solution	Potassium	Manganese	Antimony	Sodium	Vanadium
pH7.8 H ₂ O	(16)	0.00948 ± 0.0023	(0.013)	2.63 ± 0.55	(0.013)
pH4.0 H ₂ O	(11)	0.00592 ± 0.0019	(0.011)	2.86 ± 0.58	(0.014)
NaCl sol'n	(11000)	(9.6)	(0.16)	16400 ± 3300	(3.6)
Na ₂ HPO ₄ sol'n	(9400)	(8.7)	(0.20)	15200 ± 3000	(0.7)
Ferric sol'n	(49)	13.6 ± 2.7	0.0651 ± 0.016	10.9 ± 2.2	(0.083)
K ₂ Cr ₂ O ₇ sol'n	12300 ± 2500	(0.095)	0.0685 ± 0.019	11.20 ± 2.30	2.62 ± 0.52
Sat'd CaCO ₃	(5.2)	0.00819 ± 0.0017	0.0614 ± 0.0140	3.42 ± 0.68	(0.021)

Ferric ion accelerated uranium leaching by about three orders of magnitude. It also accelerated zirconium leaching by a factor of at least 1000. The reason for the accelerated leaching of zirconium is not clear. Certainly no redox chemistry involving zirconium ought to be operative under the conditions of these tests. The low pH of the ferric nitrate solution may have been responsible for all the effects. The fact that dichromate did not produce accelerated uranium leaching cast doubt on the oxidation mechanism. A low pH is the only way to explain how such

enormous concentrations of Zr could be sustained in solution.

Quantitative analysis of the leach data is complicated by the lack of control on the time and temperature of the leach processes. The time-dependence of uranium and cesium concentrations of the solutions are shown in Figure 3.1-4. The data are indeed scattered. It is tempting to impart some curvature to the data, but such curvature cannot be justified. The scatter in the short-time data and the errors attached to the long-term data are too great to allow such

curvature. Consequently a linear least-squares regression line has been drawn along with the data.

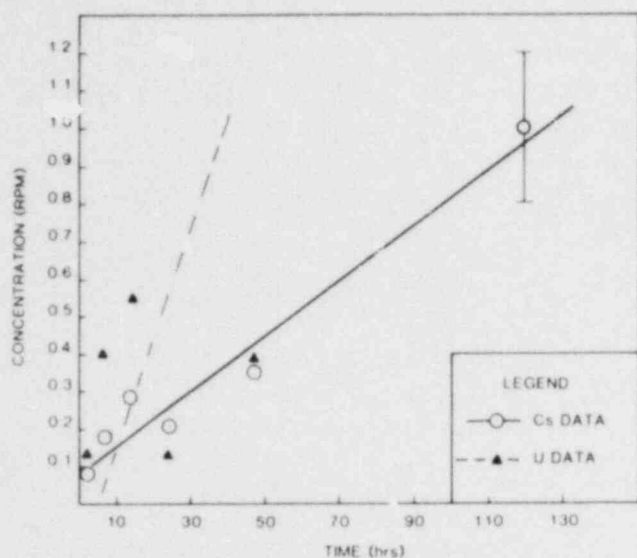


Figure 3.1-4 Time Dependence of Leaching of Cs and U at About 161°C

Scatter also frustrates any intuitively pleasing correlation of the concentrations with temperature. A plot of cesium concentration vs temperature is shown in Figure 3.1-5. The data for a sample treated at 472 K (199°C) suggest a plateau in the leach rate. Even correcting for the larger volume of this sample does not relieve this inconsistency. Similar results are obtained for data for Ce and La. Data for UO_2 show scatter at lower temperatures.

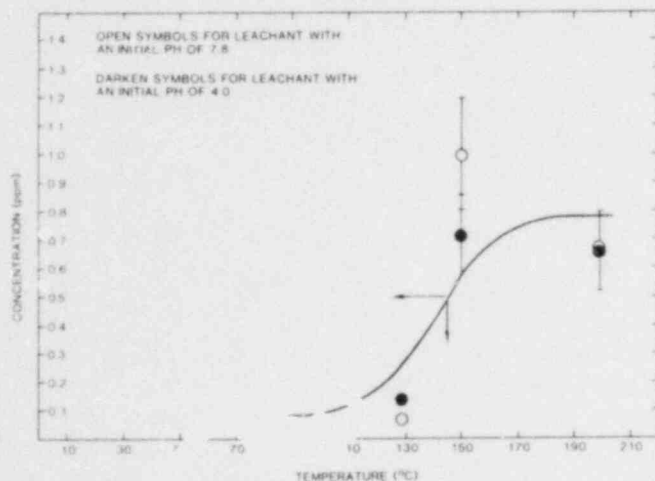


Figure 3.1-5 Cesium Concentration vs Temperature

3.1.7 Large Melt Facility

During this reporting period the construction and installation of the melt facility was completed and two shakedown experiments using a dummy graphite load were carried out. In the second shakedown experiment the furnace reached the design temperature of 3273 K (3000°C).

The first shakedown test was carried out the week of January 28. During preliminary checkout of the power supply, a defective capacitor was discovered and replaced. With 100 kW of applied power, the furnace reached 1273 K (1000°C) in about 2 hr. At this point the test was terminated due to two problems:

- The rigidized insulating cylinder was coupled to the coil and was being heated excessively.
- The bursting diaphragm at the bottom of the furnace was exceeding its operation temperature due to direct radiation from the load.

To rectify these problems, the rigidized cylinder was replaced by insulating felt wrapped directly on the susceptor and three radiation shields were installed between the load and the bursting diaphragm. In addition, a flexible bellows section was installed in the vacuum line to isolate the furnace platform from the vibration of the vacuum pump; a ground detector was installed to shut off the power supply if the induction coils were grounded; the coil was painted with electrical insulation paint.

A second shakedown experiment was carried out the week of February 25. Figure 3.1-6 shows the load temperature as a function of time, and the applied power. During the test for temperatures beyond 2273 K (2000°C), temperature of the load is monitored by pyrometry. A piece of the actual crucible material, Ta-19W, was used as the target for the pyrometer. Since the surrounding is not at the same temperature as the load and the target is nonblack, it is necessary to make an emissivity correction to the pyrometer temperature readings. An apparent emissivity of 0.64 was obtained by matching the pyrometer reading with thermal couple readings at 2348 K (2075°C).

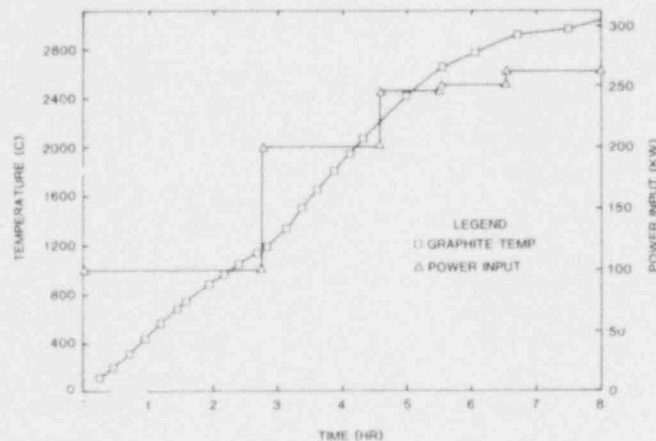


Figure 3.1-6 Melt Furnace Test 2

Posttest metallurgical examinations were made of the Ta-10W. The bottom of the sample showed both

Ta and Ta₂C formation. The top of the sample was melted and has a smooth meniscus appearance. From the Ta-W-C phase diagram, it was concluded that the sample reached at least 3273 K (3000°C).

During this quarter, a preliminary design of the MgO crucible was made. The crucible bottom will be three bricks thick and the sides will be two bricks thick. The cavity will be 16 in. in diameter and 26 in. deep.

3.1.8 Future Activities

Further shakedown experiments are planned to obtain the operating characteristics of the furnace.

3.2 PAHR Debris Bed (J. E. Gronager, 4421; G. W. Mitchell, 4421; J. B. Rivard, 4421; R. J. Lipinski, 4425; M. Schwarz, 4425)

3.2.1 Introduction

The PAHR Debris Bed program addresses issues concerned with the formation of solid fuel debris and its collection on horizontal surfaces within the containment vessel. This debris remains capable of generating significant power through the decay of fission products. Should natural processes fail to provide sufficient cooling, the debris could remelt and threaten containment. The PAHR Debris Bed program seeks to determine the natural cooling of such debris. During this period, experiments and analysis of debris bed studies continued.

3.2.2 Debris Bed Experiment D4

Experiment D4 is the fourth in a series of experiments designed to provide quantitative information on the behavior of debris beds formed from reactor materials following a core-melt accident.

The principal objectives of the D4 experiment were to

- Determine the incipient dryout heat flux for two levels of sodium subcooling, large subcooling (460 K) and small subcooling (190 K)
- Investigate the possible repeatability of the dryout heat fluxes
- Investigate bed characteristics at heat fluxes above incipient dryout (postdryout)
- Evaluate the performance of ultrasonic thermometry for debris bed experiments.

3.2.2.1 D4 Experiment Analysis

The analysis of the D4 data continued. The bulk of the effort consisted of a detailed analysis of the experiment control runs and the review of the deposition and profile of the debris bed power. This activity constitutes the ground work necessary to examine the various phenomena observed during D4.

3.2.2.1.1 Control Run Analysis

The control run resulted in observation of the debris bed at low specific power (0.27 kW/kg) and constant bulk-sodium temperature (573 K). Under these conditions, the debris bed was cooled primarily by conduction. Subsequent determinations of the effective conductivity enabled investigators to identify the bed's characteristics. Control runs performed before and after a series of dryout transients led to the identification of bed-characteristics changes caused by these dryout transients. These postchange conditions define the initial bed conditions for the next dryout series.

The first control run was performed before the initial dryout transient series, and with the aid of the ultrasonic thermometer (UT), led to the observation of an unexplained phenomenon. This phenomenon is illustrated by Figures 3.2-1 and 3.2-2. Figure 3.2-1 shows the pretransient axial temperature profile through the bed (as measured by the UT). Note that two separate regions of conduction appear to exist at 5.5 cm from the bottom of the bed. Figure 3.2-2 shows the UT axial temperature profile after the dryout transient. Note the relatively smooth conduction behavior in the wetting properties of sodium and UO₂. Earlier investigations⁽³⁻⁷⁾ of sodium wetting of UO₂ indicate that wetting is insignificant below a temperature of 673 K (400°C). From the axial temperature profiles, the upper 20 mm of the bed appear to be below 673 K. To characterize this condition, one-dimensional calculations have been initiated. Investigators speculate that a local region of large resistance may be responsible for the two-region conduction in the first control run. The large resistance may be due to a local pocket of gas, caused by poor wetting conditions. One-dimensional calculation (Code HTCID*1) of the first control run were performed to model a large resistance at 5.5 cm from the bottom of the bed. Figure 3.2-3 shows both the predicted temperature profile, and the experiment data from thermocouples and UTs. The agreement between the predicted and measured temperatures tends to indicate that a local resistance may indeed be responsible

for the two region conduction. Further analysis will be performed to determine the very nature of this resistance.

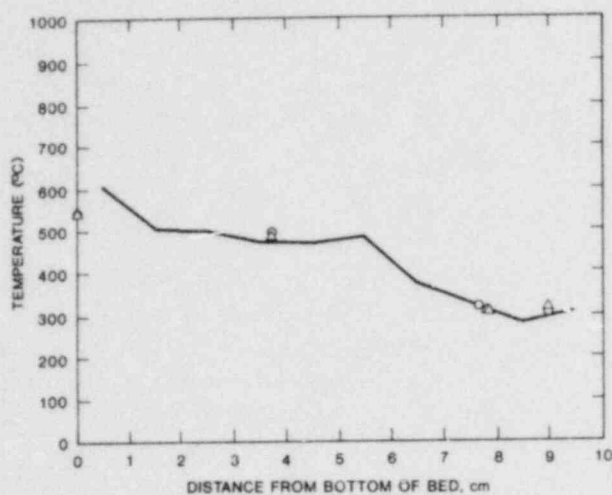


Figure 3.2-1 Ultrasonic Thermometer Data for Control Run 1. ("Δ" Indicates Thermocouple Data. The Top of the Bed is at 8.2 cm. Reactor Power is ~ 100 kW and Bed Power is ~ 0.27 W/g.)

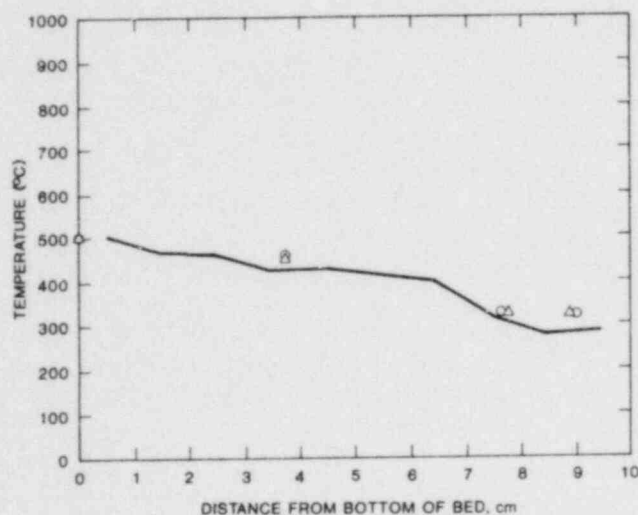


Figure 3.2-2 Ultrasonic Thermometer Data for Control Run 2. ("Δ" Indicates Thermocouple Data. The Top of the Bed is at 8.2 cm. Reactor Power is ~ 100 kW and Bed Power is ~ 0.27 W/g.)

Additional analysis on the effective conductivity (k_{eff}) of the bed during the second and third control runs is continuing. Initial calculations indicated a high k_{eff} of 34 W/m-K, as compared to 37 W/m-K predicted. Application of the axial power profile as well as radial heat losses, have reduced the k_{eff} , but uncertainties in the axial power profile of the bed must be resolved before further analysis continues.

3.2.2.1.2 Specific Power Profiles and Deposition

The postexperiment analysis developed a discrepancy between the measured power deposition

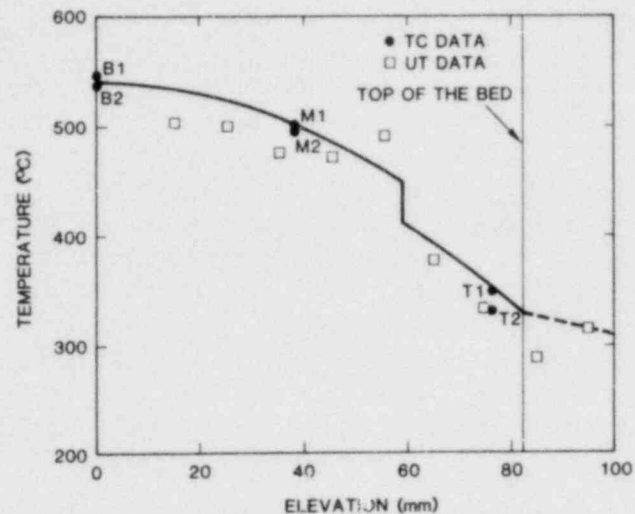


Figure 3.2-3 Predicted Temperature Profile and Experiment Data From Thermocouples and UTs

and that calculated by the neutronic code TWOTRAN II. As a result, the helium loop power diagnostics and the neutronic calculation were reviewed.

An experiment was conducted to assess the relative errors of the helium power diagnostic equipment. Briefly, the experiment consisted of using the in-line electric heaters of the helium cart to provide a source of energy to be removed by the helium system. The energy removed by the helium was calculated by using

$$\dot{Q} = \dot{M} C_p \Delta T$$

The term \dot{M} , mass flow rate, was measured with metering tubes equipped with both high flow rate and low flow rate orifices (90 to 270 lb/hr and 30 to 90 lb/hr respectively). The term ΔT is the difference in helium temperature between the inlet and the outlet of the heater section. At various flow rates, the input energy to the heaters was compared with the energy removed by the helium. The results (Figure 3.2-4) reveal that for large flow rates the power diagnostics indicate within 3% of the input power to the heaters. Also, at large flow rates the heater surface temperature was at a minimum, thus minimizing the losses caused by radiation. As the flow rate decreased below 100 lb/hr, the difference between input and measured power was observed to increase for both the large and small flow rate diagnostics. This difference was due to heater losses to the surrounding housing by radiation and conduction. These heater losses were confirmed by the rapid temperature rise of the heater housing at low flow rates. The difference between the low mass-flow-rate data for the large and small diagnostics was due to errors in the

large metering tube at low flow rates. (In fact, this is the reason for having the smaller metering tube.)

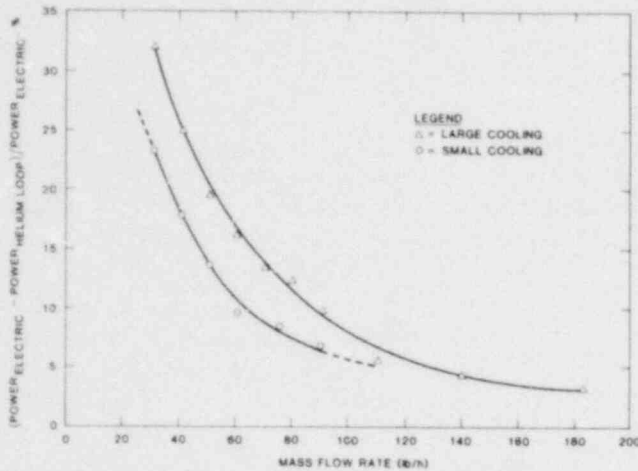


Figure 3.2-4 Helium Loop Power Measurements vs. Mass Flow Rate

Thus, based on the accuracy demonstrated at large flow rates, the helium power diagnostics can be used with confidence to measure the energy removed from the experiment package.

3.2.3 Debris Bed Experiment D5

Debris bed experiment D5, the high-temperature, extended dryout experiment, is in the preliminary design stages. The current status of the project is reported below.

3.2.3.1 Experimental Equipment Analysis

Preliminary stress analysis on the high temperature crucible is nearly completed. The initial results indicate that the present design will meet all the design requirements without crucible damage or failure. The material selected for the crucible shells was Ta-10W alloy. Selection was based upon its low temperature mechanical properties, its high temperature strength, and material compatibility.

Thermal analysis has been completed on the crucible design. Results indicated a maximum temperature of 2073 K (1800°C) can be reached within the crucible, while maintaining a subcooled temperature on the outer crucible wall. Calculations show about 5% heat loss through the crucible walls.

Investigators have initiated thermal analysis on the overall experiment package. Following the analysis, stress calculations will be performed.

A review of the neutronic calculations showed that a region-weight cross-section set was used to

represent the boron carbide neutron filter. This cross-section set incorporates little self-shielding in the filter, providing a larger effective number density than actually seen by the neutron flux. This in turn decreases the energy deposition within the bed. A new cross-section set is now being generated to include self-shielding effects.

Additional calculations of the gamma heating contribution indicated about a 4% overall increase in the experiment energy deposition.

3.2.3.2 Construction and Fabrication Techniques

Crucible construction techniques have been identified with the selection of a shear-spin method for Sandia's application. With this method, only one weld seam will be made in a low temperature region of the crucible. The Ta-10W shells of the crucible will be fabricated at Rocky Flats. Sandia National Laboratories will perform final assembly.

The primary-secondary containment vessels will be constructed from standard size stainless steel tubing available "off the shelf" from local suppliers. This should reduce fabrication costs.

Evaluation of assembly procedures for assembling the primary-secondary containment are being evaluated. Mock-up assemblies have been constructed and various methods for assembly are being investigated.

3.2.3.3 Component Development and Material Compatibility

The present UT design is currently being modified. Changes necessary for the higher-temperature applications of D5 will require additional experimentation. A new ceramic insulation has become available, enabling the electronic pulse coil to function at temperatures of up to 873 K (600°C).

A high temperature, vacuum sealed, instrumentation feedthrough is presently being tested. Initial results indicate that a multipin connector is feasible for thermocouples lead applications. Several tests are planned to expose the feedthrough to severe environments over long periods of time (50 hr).

The zirconia foam for the high temperature insulation within the crucible is presently undergoing sodium compatibility experiments. Small samples of the zirconia foam will be exposed to sodium for several hours with peak sodium temperatures of 1073 K (800°C).

Ta-10W material is undergoing similar testing in sodium to evaluate the sodium interaction rate.

3.2.3.4 Out-of-Pile System Test (OPST)

An OPST to evaluate primary and secondary containment compatibility with the present He loop temperature controller is in the assembly stages with the experiment to be performed in late April. Additional equipment is under construction for evaluating the new helium heat exchanger.

3.2.4 Debris Bed Experiment D6

All detailed design drawings for experiment D6 have been completed. Fabrication of all experiment components has been initiated.

Fabrication of the debris bed vessel is proceeding; however, during the week of March 23, an x-ray of the upper section of the vessel revealed a significant void in the weld, making it unsuitable for use in experiment D6. A reweld will be attempted, however, salvaging the part is doubtful because of shrinking that will occur in the welding operation. This will delay fabrication of the vessel by about 1 mo.

Thermal analysis of the experiment is proceeding. A model of the lower part of the experiment section, including the debris bed and surrounding insulation has been constructed and some temperature profiles have been generated.

Initiation of the stress analysis has been delayed until the first of April because of the Zion-Indian Point studies.

In support of the D6 safety evaluation, the state of fission products expected to be present in the debris bed experiments has been characterized. This characterization will be presented to the ACRR Safety Committee.

Sandia project personnel anticipate that fabrication of components for the experiment will continue during April. Also during April, the stress analysis will be initiated. Compiling of assembly checklists for the experiment will begin in April as will the writing of the experiment D6 plan.

3.2.5 PAHR Debris Bed Analysis

3.2.5.1 A General, Zero-Dimensional, Laminar-Turbulent, Gravity-Capillary Dryout Model

3.2.5.1.1 Introduction

A general model for incipient dryout in debris beds has been developed. This model includes the effects of both laminar and turbulent flows in both the vapor and the liquid phases. It also includes the

driving forces of both gravity and capillary action. The laminar limit is similar to that of Shires and Stevens.⁽³⁻⁸⁾ The laminar limit for very deep beds is similar to that of Hardee and Nilson⁽³⁻⁹⁾ (and with further restrictive assumptions is similar to the deep bed model of Dhir and Catton⁽³⁻¹⁰⁾). The turbulent limit for very deep beds is similar to the flooding model of Ostensen.⁽³⁻¹¹⁾ The model is based on first principles and contains only empirical constants which were obtained from areas other than dryout studies. Yet when the model is applied to published dryout data (126 points involving 5 different fluids and many different particle diameters and bed heights) agreement with the data appears to be better than for all other models.

3.2.5.1.2 Model Development

The conservation equations for two-phase flow through a porous medium (including gravity and capillary forces) may be expressed in one dimension as

$$\frac{\rho_v}{\eta\eta_v} v_v^2 + \frac{\mu_v}{\kappa\kappa_v} v_v + \frac{dP_v}{dz} + \rho_v g = 0 \quad (3.1)$$

$$-\frac{\rho_l}{\eta\eta_l} v_l^2 + \frac{\mu_l}{\kappa\kappa_l} v_l + \frac{dP_l}{dz} + \rho_l g = 0 \quad (3.2)$$

$$\frac{d}{dz} (\rho_v v_v h_{fg}) = S \quad (3.3)$$

$$\frac{d}{dz} (\rho_v v_v + \rho_l v_l) = 0 \quad (3.4)$$

$$P_c = P_v - P_l \quad (3.5)$$

where ρ is density, v is superficial velocity, μ is dynamic viscosity, P is pressure, g is gravitational acceleration, z is elevation above the bed bottom, h_{fg} is latent heat of vaporization, S is volumetric heat source, and the subscripts v , and l , refer to vapor and liquid respectively. In addition, κ is the bed permeability, κ_v and κ_l are (dimensionless) specific permeabilities, and η , η_v , and η_c are similar factors for turbulent flow and shall be called "passability" and "specific passability." Equations (3.1) and (3.2) are the Ergun equations⁽³⁻¹²⁾ for momentum conservation and varies smoothly from Darcy's law (for laminar flow) to the Burke-Plummer equation (for turbulent flow)

as κ or η dominate. Equations (3.3) and (3.4) are the energy and mass conservation equations respectively.

The permeability may be obtained from the Kozeny-Carman relation.⁽³⁻¹³⁾

$$\kappa = \frac{d^2}{180} \frac{\epsilon^3}{(1-\epsilon)^2} \quad (3.6)$$

where d is the particle diameter and ϵ is the interparticle volume fraction. The "passability" is

$$\eta = \frac{d}{1.75} \frac{\epsilon^3}{1-\epsilon} \quad (3.7)$$

The capillary force is suggested by Scheidegger⁽³⁻¹³⁾ to be

$$P_c = \frac{6\sigma(1-\epsilon)}{d\epsilon} \quad (3.8)$$

where σ is the surface tension. Combining Eq (3.8) with Eq (3.6) yields

$$P_c = \sigma \sqrt{\frac{\epsilon}{5\kappa}} \quad (3.9)$$

The simplifying assumption that the capillary pressure varies linearly in the bed yields

$$\frac{dP_c}{dz} = \frac{\sigma}{L} \sqrt{\frac{\epsilon}{5\kappa}} \quad (3.10)$$

where L is the total bed height. This assumption is most valid at incipient dryout since conditions then vary from fully saturated at the top of the bed to fully dry at the bottom. It also essentially reduces the problem to zero-dimensions since it has eliminated the freedom of the equations in the vertical direction.

a. Laminar Limit. In the limit of small particles, both the liquid and vapor flow will be laminar. In that case $\kappa \gg \eta$ and the v^2 term in Eqs (3.1) and (3.2) drop out. Combining the reduced Eq (3.1) and (3.2) with Eqs (3.3), (3.4), (3.9), and (3.10) (along with the lower boundary condition of no net heat or mass flow) and integrating over z yields

$$q = \frac{(\rho_l - \rho_v) g \kappa h_{fg} \left(1 + \frac{\lambda_c}{L}\right)}{\frac{v_v}{\kappa_v} + \frac{v_l}{\kappa_l}} \quad (3.11)$$

where q is the heat flux at the top of the bed, ν is the dynamic viscosity, and λ_c is the characteristic capillary force length:

$$\lambda_c = \frac{\sigma}{(\rho_l - \rho_v)g} \sqrt{\frac{\epsilon}{5\kappa}} \quad (3.12)$$

For typical beds in sodium, λ_c is about 0.5 m.

The specific permeabilities κ_l and κ_v are functions of the average saturation γ . They are flow attenuation coefficients which reflect the increased flow resistance for one phase caused by the other phase occupying some of the interparticle space. An estimate of κ_v and κ_l can be made by comparing two cases; one in which the flow is partitioned into two separate streams and one in which it is mixed. (This is essentially the approach taken by Shires and Stevens⁽³⁻⁸⁾ and by Hardee and Nilson.⁽³⁻⁹⁾) For the vapor flow in the partitioned case, κ_v is 1 and (remembering that v_v is the superficial velocity)

$$v_v = -(1-\gamma) \frac{\kappa}{\mu_v} \left(\frac{dP_v}{dz} + \rho_v g \right) \quad (3.13)$$

Comparing this to the laminar vapor flow in the mixed case Eq (3.1) suggests that

$$\kappa_v = 1 - \gamma \quad (3.14)$$

A similar analysis suggests that

$$\kappa_l = \gamma \quad (3.15)$$

Equations (3.12) and (3.15) shall be called the linear specific permeability relations.

Inserting Eqs (3.14) and (3.15) into Eq (3.11) yields a heat flux as a function of the average saturation γ . The dryout flux may be obtained by maximizing q with respect to variations in γ . The maximizing γ is the same as that originally found by Hardee and Nilson:⁽³⁻⁹⁾

$$\gamma = \left(1 + \sqrt{\frac{v_v}{v_l}} \right)^{-1} \quad (3.16)$$

Inserting Eq (3.16) into Eq (3.11) yields

$$q_d = \frac{(\rho_l - \rho_v) g \kappa h_{fg} \left(1 + \frac{\lambda_c}{L}\right)}{\left(\sqrt{v_v} + \sqrt{v_l}\right)^2} \quad (3.17)$$

This is the dryout heat flux based on zero dimensions, laminar flow, gravitational and capillary

forces, and linear specific permeability. It is very similar to that obtained by Shires and Stevens:⁽³⁻⁸⁾

$$q_d = \frac{A(\rho_1 - \rho_v) g \kappa h_{fg} \left(1 + \frac{\lambda_c}{CL}\right)}{(\sqrt{v_v} + \sqrt{v_1})^2} \quad (3.18)$$

where $C \approx 1$ and A is empirically determined from dryout data. The two are identical when $A = 1$. Note that although Eq (3.17) is based on packed, nonchanneled behavior and is thus valid for deep beds, there is nonetheless some bed depth dependence in it.

In the limit of negligible capillary forces ($L \gg \lambda_c$) and $\rho_v \gg \rho_1$, Eq (3.17) becomes that determined by Hardee and Nilson:⁽³⁻⁹⁾

$$q_d = \frac{\rho_1 g \kappa h_{fg}}{(\sqrt{v_v} + \sqrt{v_1})^2} \quad (3.19)$$

Thus, the Hardee-Nilson model would be expected to underpredict the dryout flux.

As pointed out by Hardee and Nilson, Eq (3.19) is similar to the Dhir-Catton⁽³⁻¹⁰⁾ deep bed dryout criterion:

$$q_d = \frac{0.177(\rho_1 - \rho_v) g \kappa h_{fg}}{v_1} \quad (3.20)$$

where 0.177 is an experimentally determined constant (and much reduction of the author's dimensionless terms was required to obtain this more understandable form). Note that there is no bed depth dependence in Eq (3.20). Since the empirical constant (0.177) was determined by using data from beds around 70 mm deep (for which $\lambda_c \gg L$), Eq (3.20) would be expected to overpredict the dryout flux for beds deeper than about 150 mm.

The linear specific permeabilities expressed in Eqs (3.14) and (3.15) are not strictly true. More accurate expressions have been determined experimentally to be⁽³⁻¹³⁾

$$\kappa_v = 1.11 \gamma \quad (3.21)$$

$$\kappa_1 = \gamma^3 \quad (3.22)$$

Inserting these into Eq (3.11) and maximizing q with respect to variations in γ yield

$$q_d = \frac{(\rho_1 - \rho_v) g \kappa h_{fg} \left(1 + \frac{\lambda_c}{L}\right)}{\left(\frac{v_v}{1 - 1.11 \gamma} + \frac{v_1}{\gamma^3}\right)} \quad (3.23)$$

with

$$\gamma = \sqrt{0.833 \frac{v_1}{v_v} + \sqrt{2.70 \frac{v_1}{v_v} - \sqrt{0.833 \frac{v_1}{v_v}}}} \quad (3.24)$$

This is the dryout heat flux based on zero dimensions, laminar flow, gravitational and capillary forces, and empirical specific permeability. It gives values about 70% of those given by Eq (3.17). Hardee and Nilson⁽³⁻⁹⁾ noted the existence of this solution (in the very deep bed limit), but did not present it (in closed form).

When the dryout fluxes predicted by the one-dimensional model presented last quarter⁽³⁻¹⁴⁾ are compared with those given by Eq (3.23), the agreement is within 10%. This is fortunate since Eq (3.23) is much easier to implement than the nonclosed form one-dimensional solution presented last quarter. In the very deep bed limit, the agreement can be shown rigorously;⁽³⁻¹⁵⁾ unfortunately no rigorous connection could be found with capillary forces included.

b. Turbulent Limit. In the limit of large particles, both the liquid and vapor flow will be fully turbulent. In that case, $\eta \gg \kappa$ and the v term in Eqs (3.1) and (3.2) drop out. Combining the reduced Eqs (3.1) and (3.2) with Eqs (3.3), (3.4), (3.9), and (3.10) yields

$$q = h_{fg} \sqrt{\frac{(\rho_1 - \rho_v) g \eta \left(1 + \frac{\lambda_c}{L}\right)}{\left(\frac{1}{\rho_v \eta_v} + \frac{1}{\rho_1 \eta_1}\right)}} \quad (3.25)$$

The specific passabilities η_v and η_1 may be determined in the same way that the specific permeabilities were determined, that is, by considering partitioned flow vs mixed flow. For partitioned flow, $\eta_v = 1$ and (remembering that v is the superficial velocity)

$$V_v = (1 - \gamma) \sqrt{\frac{\eta}{\rho_v} \left(\frac{dP_v}{dz} + \rho_v g\right)} \quad (3.26)$$

Comparing Eq (3.26) with the turbulent form of Eq (3.1) ($\eta \gg \kappa$) suggests the following form for the specific passability:

$$\eta_v = (1 - \gamma)^N \quad (3.27)$$

with N most likely equal to 2. Similarly,

$$\eta_1 = \gamma^N \quad (3.28)$$

Inserting Eqs (3.27) and (3.28) into Eq (3.25) and maximizing q with respect to γ yields

$$\gamma = \left(1 + N+1 \sqrt{\frac{\rho_1}{\rho_v}}\right)^{-1} \quad (3.29)$$

Inserting this into Eq (3.25) yields

$$q_d = \frac{h_{fg} \sqrt{\rho_1 (\rho_1 - \rho_v) g \eta \left(1 + \frac{\lambda_c}{L}\right)}}{\left(1 + N+1 \sqrt{\frac{\rho_1}{\rho_v}}\right)^{\frac{(N+1)}{2}}} \quad (3.30)$$

and

$$= \frac{0.756 \epsilon h_{fg} \sqrt{\rho_1 (\rho_1 - \rho_v) g d \left(\frac{\epsilon}{(1-\epsilon)}\right) \left(1 + \frac{\lambda_c}{L}\right)}}{\left(1 + N+1 \sqrt{\frac{\rho_1}{\rho_v}}\right)^{\frac{(N+1)}{2}}} \quad (3.31)$$

Note that the dryout flux varies with the square root of the particle diameter (as opposed to the square of the diameter in the laminar case). Note also that this is very similar to the flooding model of Ostensen:⁽³⁻¹¹⁾

$$q_d = \frac{0.245 h_{fg} \sqrt{\rho_v \rho_1 g d \frac{\epsilon}{(1-\epsilon)}}}{\left(1 + 4 \sqrt{\frac{\rho_v}{\rho_1}}\right)^2} \quad (3.32)$$

and

$$= \frac{0.245 h_{fg} \sqrt{\rho_1^2 g d \frac{\epsilon}{(1-\epsilon)}}}{\left(1 + 4 \sqrt{\frac{\rho_1}{\rho_v}}\right)^2} \quad (3.33)$$

Since Eq (3.31) is valid only for very turbulent flow (large particles), capillary forces will be small and the λ_c/L term will be negligible making the agreement with Eq (3.32) even better. In fact, the agreement is very close if N is chosen to be 3 rather than 2. (This is similar to the additional power dependence found in the empirical specific permeability.) Therefore, choose

$$N = 3 \quad (3.34)$$

c. **General Solution.** Equations (3.1), (3.2), (3.4), (3.9), and (3.10) may be combined to yield

$$\left(\frac{1}{\rho_v \eta_v} + \frac{1}{\rho_1 \eta_1}\right) \frac{\rho_v^2 v_v^2}{\eta} + \left(\frac{v_v}{\kappa_v} + \frac{v_1}{\kappa_1}\right) \frac{\rho_v v_v}{\kappa} - (\rho_1 - \rho_v) g \left(1 + \frac{\lambda_c}{L}\right) = 0 \quad (3.35)$$

where γ_c is given by Eq (3.12). This may be solved for v_v and inserted into Eq (3.3) and integrated to obtain:

$$q = \rho_v h_{fg} (\sqrt{v_L^2 + v_T^2} - v_L) \quad (3.36)$$

where

$$v_L = \frac{\eta}{2\kappa \rho_v} \frac{\left(\frac{v_v}{\kappa_v} + \frac{v_1}{\kappa_1}\right)}{\left(\frac{1}{\rho_v \eta_v} + \frac{1}{\rho_1 \eta_1}\right)} \quad (3.37)$$

and

$$v_T = \sqrt{\frac{\eta (\rho_1 - \rho_v) g \left(1 + \frac{\lambda_c}{L}\right)}{\rho_v^2 \left(\frac{1}{\rho_v \eta_v} + \frac{1}{\rho_1 \eta_1}\right)}} \quad (3.38)$$

The specific permeabilities and passabilities are given by Eqs (3.21), (3.22), (3.27), (3.28), and (3.34). The dryout heat flux may be determined by maximizing q with respect to variations in γ between the limits set by Eqs (3.24) and (3.29). This is most easily done by trial and error on a programmable machine. This then constitutes the general zero-dimensional laminar-turbulent gravity-capillary dryout model.

Equation (3.36) is cumbersome and it would be preferable to use the limiting Eqs (3.23) and (3.31) for the laminar and turbulent limits respectively whenever possible. Equation (3.36) reduces to Eq (3.23) whenever $v_L^2 \gg v_T^2$ and it reduces to Eq (3.31) whenever $v_T \gg v_L$. The former condition yields the laminar requirement

$$d_L < 13 d_M \quad (3.39)$$

where

$$d_M = \frac{1-\epsilon}{\epsilon} \frac{\left(\frac{v_v}{1-1.11\gamma} + \frac{v_1}{\gamma^3}\right)^{2/3}}{\left[(\rho_1 - \rho_v) g \left(1 + \frac{\lambda_c}{L}\right) \left(\frac{1}{\rho_v (1-\gamma)^3} + \frac{1}{\rho_1 \gamma^3}\right)\right]^{1/3}} \quad (3.40)$$

in which λ_c is a function of d_L and γ is given by Eq (3.24). The latter condition yields the turbulent requirement

$$d_T > 50 d_M \quad (3.41)$$

where d_M is given by Eq (3.40) in which λ_c is a function of d_T and γ is given by Eq (3.29). For particle diameters not satisfying either of these conditions, Eq (3.36) must be used. Table 3-VI displays the laminar and turbulent limiting diameters for a 100-mm-deep bed with $\epsilon = 0.4$ for various fluids at 1-atm pressure. A comparison of the dryout fluxes predicted by Eqs (3.36), (3.23), and (3.31) is also shown. As can be seen, the transition from laminar to slightly turbulent occurs at less than 1 mm for all fluids considered. The transition from slightly turbulent to very turbulent occurs at about 6 mm. Thus the turbulent (or flooding) models would apply to fractured (but not melted) fuel pellets. This is important since the turbulent model predicts a much lower heat flux for large particles than an extrapolated laminar model.

A comparison of the general model with the Dhir-Catton,⁽³⁻¹⁰⁾ Hardee-Nilson,⁽³⁻⁹⁾ Shires-Stevens,⁽³⁻⁸⁾ and Ostensen,⁽³⁻¹¹⁾ models is shown in Figure 3.2-5 for a 100-mm-deep bed with water at 1-atm pressure and $\epsilon = 0.40$. A similar plot for sodium is shown in Figure 3.2-6. All of the models come into agreement in the particle diameter range of 300 to 1000 μ . (This is where virtually all of the measured dryout data lie.) The Ostensen (flooding) model agrees with the turbulent (large particle) limit and the Shires-Stevens model agrees with the laminar (small particle) limit. Both the Dhir-Catton and Hardee-Nilson models are lower than the general model in the laminar limit due to neglect of capillary forces. All models except the Ostensen model are higher than the general model in the turbulent limit suggesting they may be grossly in error in the nonconservative direction for large (3 mm or more) particle diameters.

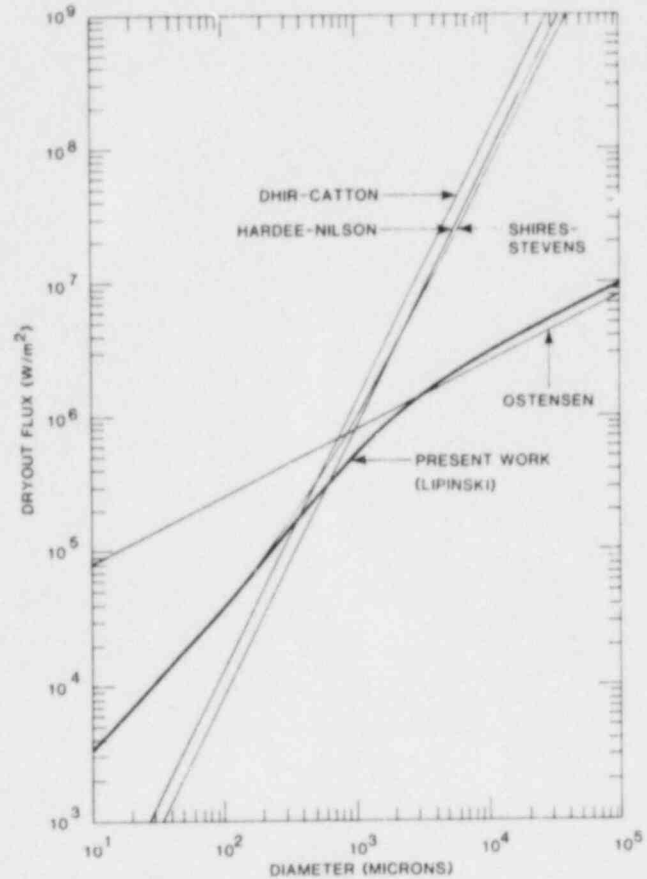


Figure 3.2-5 Dryout Heat Flux vs Particle Diameter for a 100-mm-Deep Bed in Water. (The heavy curve is the general model. The curves are labeled to indicate the model each represents.)

For water at 1-atm pressure, Figure 3.2-7 shows a plot of the dryout heat flux predicted by the general model vs particle diameter for various bed heights (and $\epsilon = 0.40$). Note that in the turbulent limit the dryout flux is proportional to the square root of the particle diameter and in the laminar limit it is proportional to the first power of the diameter. Only for deep beds with particle diameters of about 300 to

Table 3-VI Particle Diameters for Transition to Fully Laminar (d_L) or Fully Turbulent (d_T) Flow for a 100-mm-High Bed With $\epsilon = 0.4$ for Various Fluids at 1-atm Pressure*

Material	d_L (mm)	$q_{3.36}$ (kW/m ²)	$q_{3.23}$ (kW/m ²)	d_T (mm)	$q_{3.36}$ (kW/m ²)	$q_{3.31}$ (kW/m ²)
Water	0.54	291	322	6.4	2270	2610
Sodium	0.89	491	542	6.7	2510	2940
Acetone	0.36	61	67	5.6	680	780
Methanol	0.62	127	140	7.2	1230	1410
Freon-113	0.27	34	37	4.8	480	550

*Also shown are the exact heat flux ($q_{3.36}$) as given by Eq (3.36) and the approximate heat flux ($q_{3.23}$ and $q_{3.31}$) as given by Eqs (3.23) and 3.31) respectively.

1000 μm is the heat flux proportional to the square of the diameter as is assumed in the Dhir-Catton and Hardee-Nilson models. Similar plots are shown in Figures 3.2-8; -9; -10; and -11 for sodium, acetone, methanol, and freon-113. Note that water and sodium exhibit very similar dryout behavior.

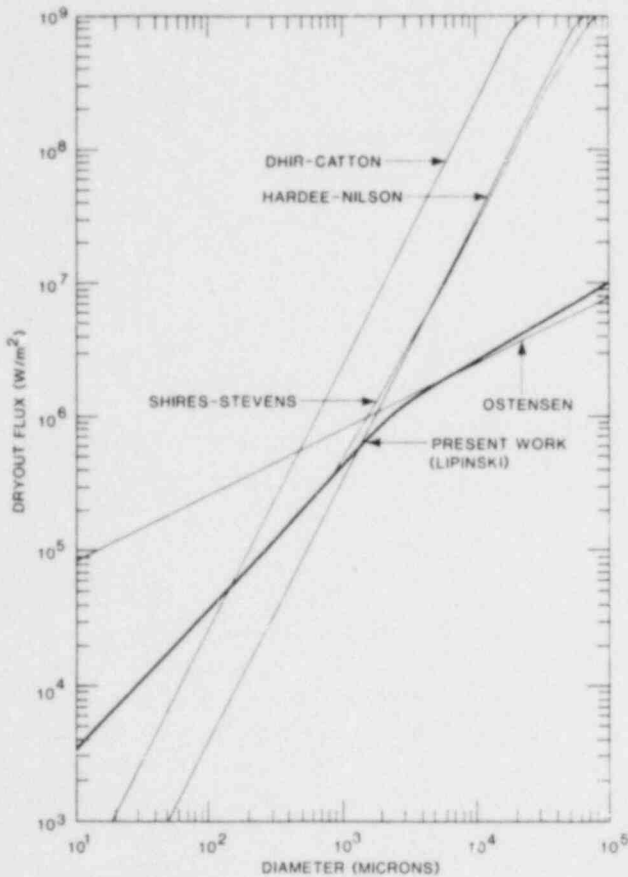


Figure 3.2-6 Dryout Heat Flux vs Particle Diameter for a 100-mm-Deep Bed in Sodium. (The heavy curve is the general model. The curves are labeled to indicate the model each represents.)

d. Comparison to Data. Several dryout measurements have been made⁽³⁻¹⁶⁻³⁻²¹⁾ involving water, sodium, acetone, methanol, and freon as fluids and steel, lead, and uranium as particles. The dryout predictions of the general (zero-dimensional laminar-turbulent gravity-capillary) dryout model Eq (3.34) is compared with the measurements in Figure 3.2-12. (A log-log scale is used so that overestimates and underestimates receive the same visual weight.) For comparison similar plots for the Dhir-Catton,⁽³⁻¹⁰⁾ the Hardee-Nilson,⁽³⁻⁹⁾ the Shires-Stevens,⁽³⁻⁸⁾ and the Ostensen,⁽³⁻¹¹⁾ models [Eqs (3.20), (3.19), (3.18), and (3.33) respectively] are shown in Figures 3.2-13, -14, -15, and -16 respectively.

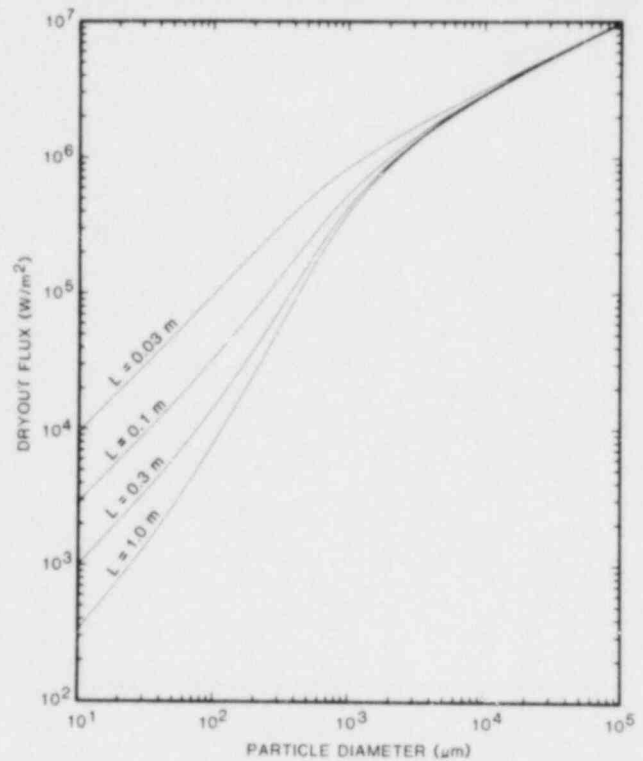


Figure 3.2-7 Dryout Heat Flux vs Particle Diameter for a Particle Bed in Water for Various Bed Depths (Indicated in meters.)

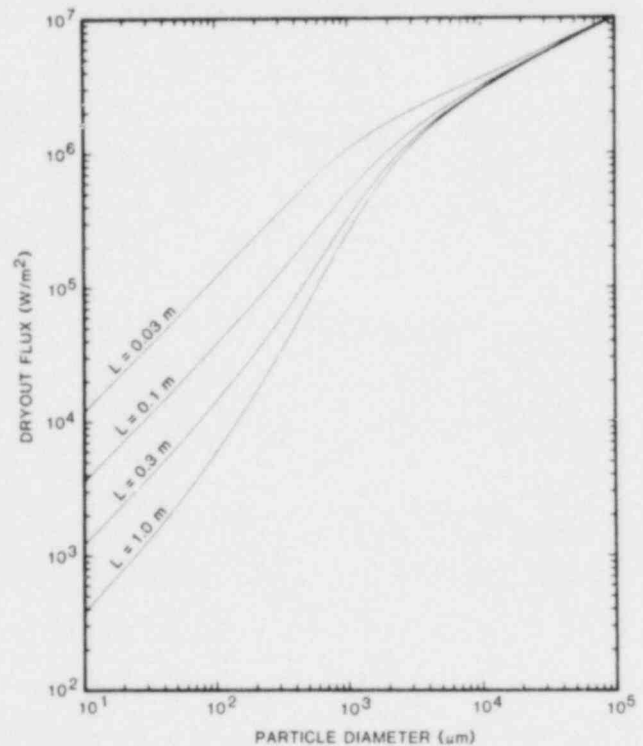


Figure 3.2-8 Dryout Heat Flux vs Particle Diameter for Sodium

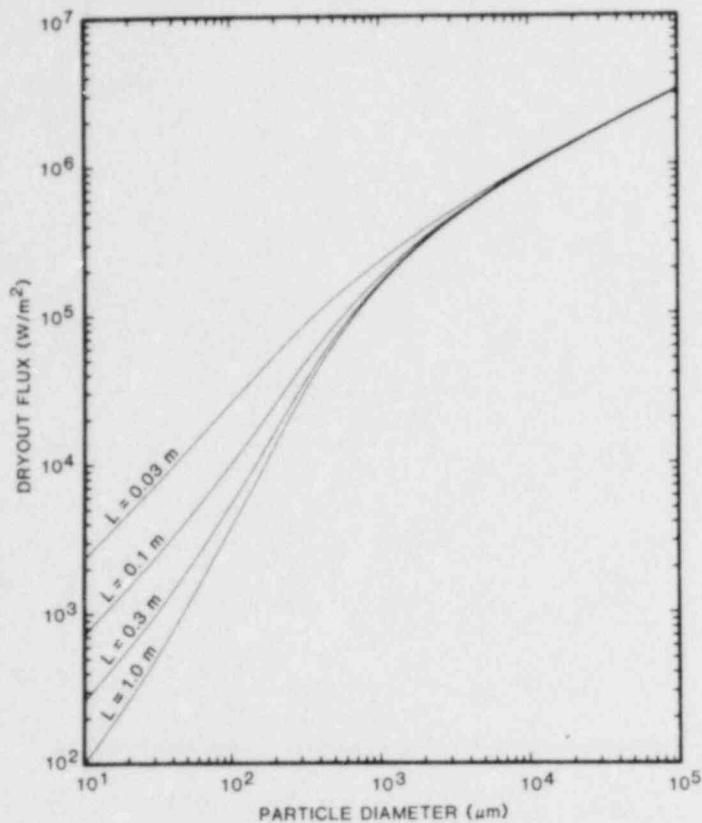


Figure 3.2-9 Dryout Heat Flux vs Particle Diameter for Acetone

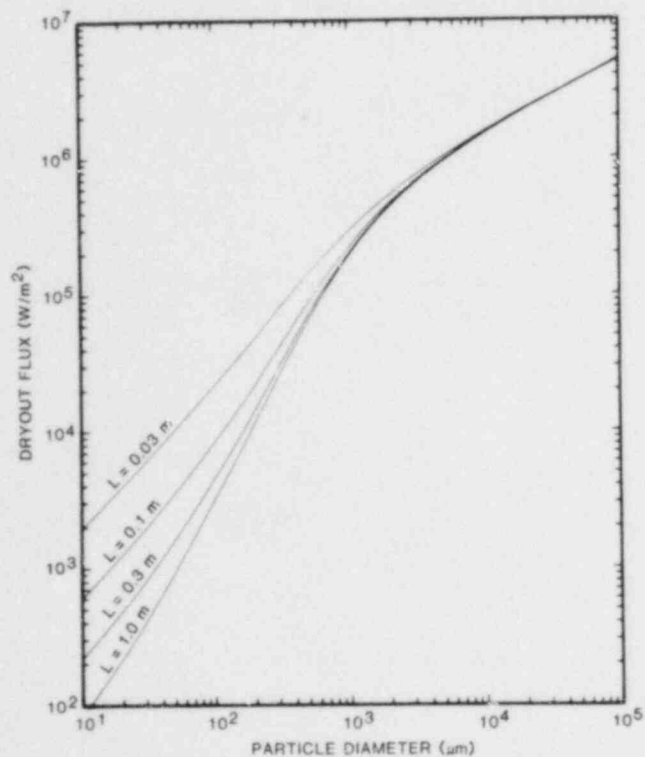


Figure 3.2-10 Dryout Heat Flux vs Particle Diameter for Methanol

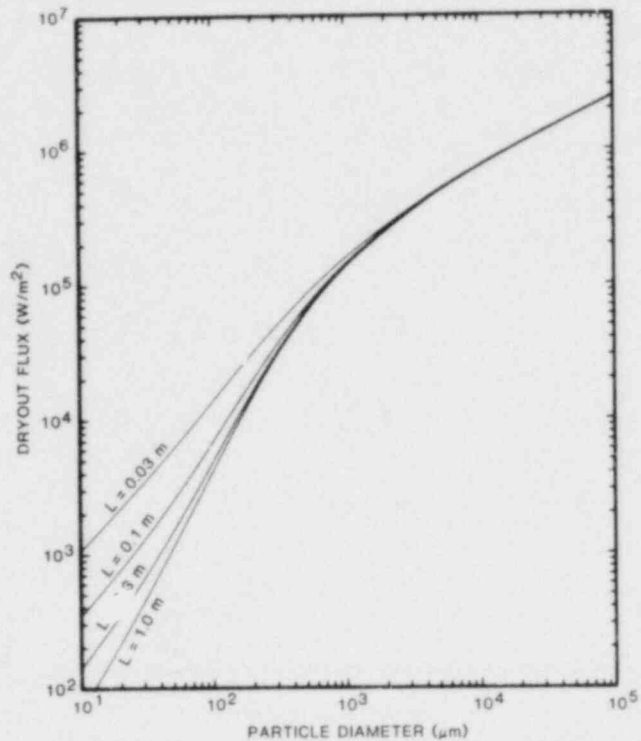


Figure 3.2-11 Dryout Heat Flux vs Particle Diameter for Freon-113

The general model correlates a wide range of data within a factor of about 2. Although this is not particularly accurate, it is better than the alternate models. Most significant is that the model was not fit directly to the dryout data; thus the fact that the data came close to the predictions at all is encouraging. Furthermore, since the model is mechanistic, the model may be extrapolated beyond the present data base with more confidence. Evidence of this is given by the freon data set which contains the only measurements with particle diameters in excess of a millimeter (2 mm and 3 mm). The Dhir-Catton,⁽³⁻¹⁰⁾ Hardee-Nilson,⁽³⁻⁹⁾ and Shires-Stevens⁽³⁻⁸⁾ models all overpredict this data (some points are even off scale) since the vapor flow becomes turbulent at those larger diameters. Even larger errors can be expected for larger particles. Similarly, the Ostensen⁽³⁻¹¹⁾ model underpredicts much of the data because it is essentially turbulently based and much of the data is in the laminar regime. The Hardee-Nilson⁽³⁻⁹⁾ model underpredicts most of the data (except the highly turbulent freon) data set since it does not include capillary forces. In contrast, the general model accounts for all these diverse effects and predicts all the data reasonably well and can thus be used with the most confidence over wide ranges of situations. (However, it is not applicable to shallow beds where channeling dominates; in those cases it would predict a lower limit to the dryout flux.)

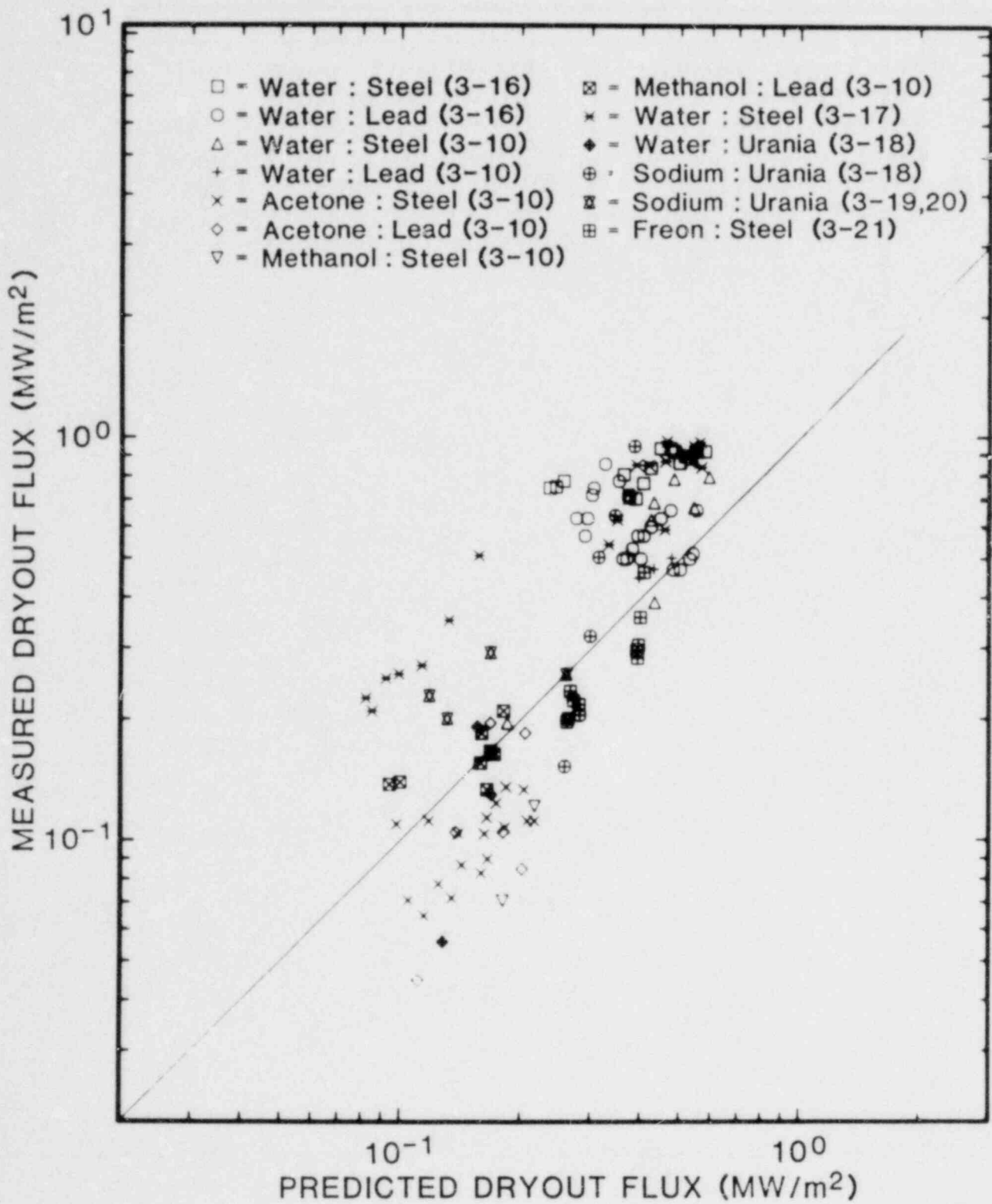


Figure 3.2-12 Predictions vs Measurements for the General Model (Eq 3.36)

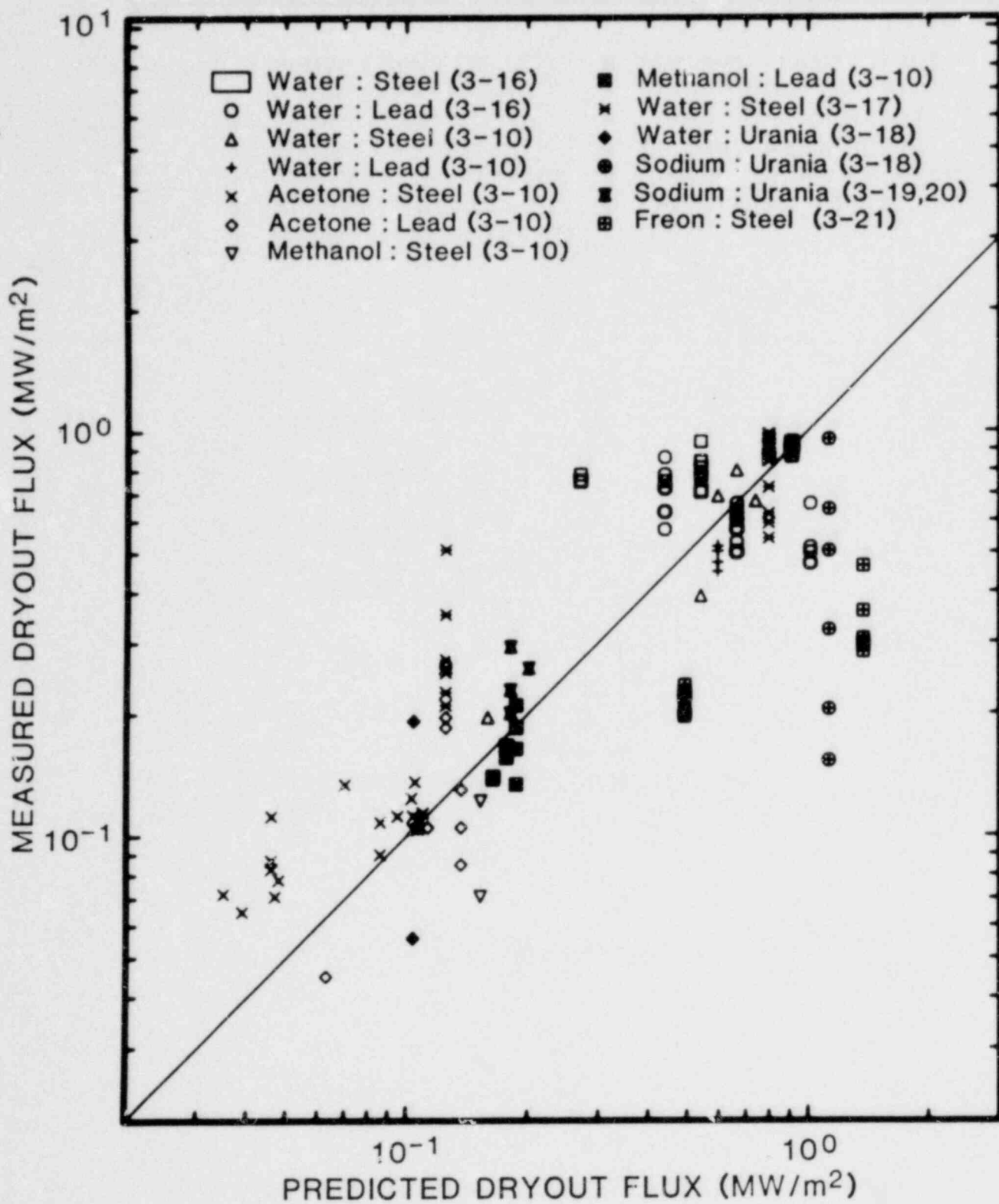


Figure 3.2-13 Predictions vs Measurements for the Dhir-Catton Model (Eq 3.20)

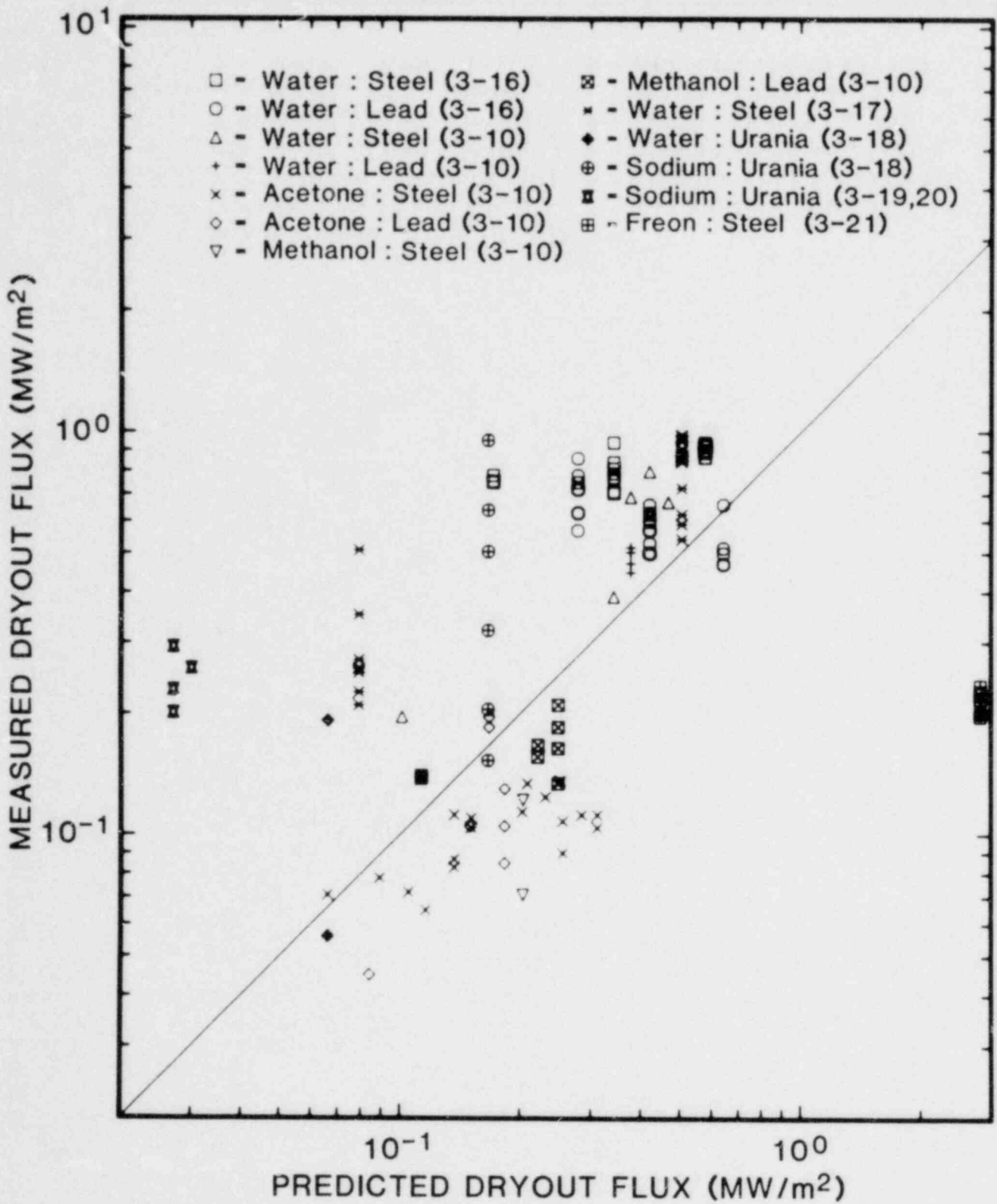


Figure 3.2-14 Predictions vs Measurements for the Hardee-Nilson Model (Eq 3.19)

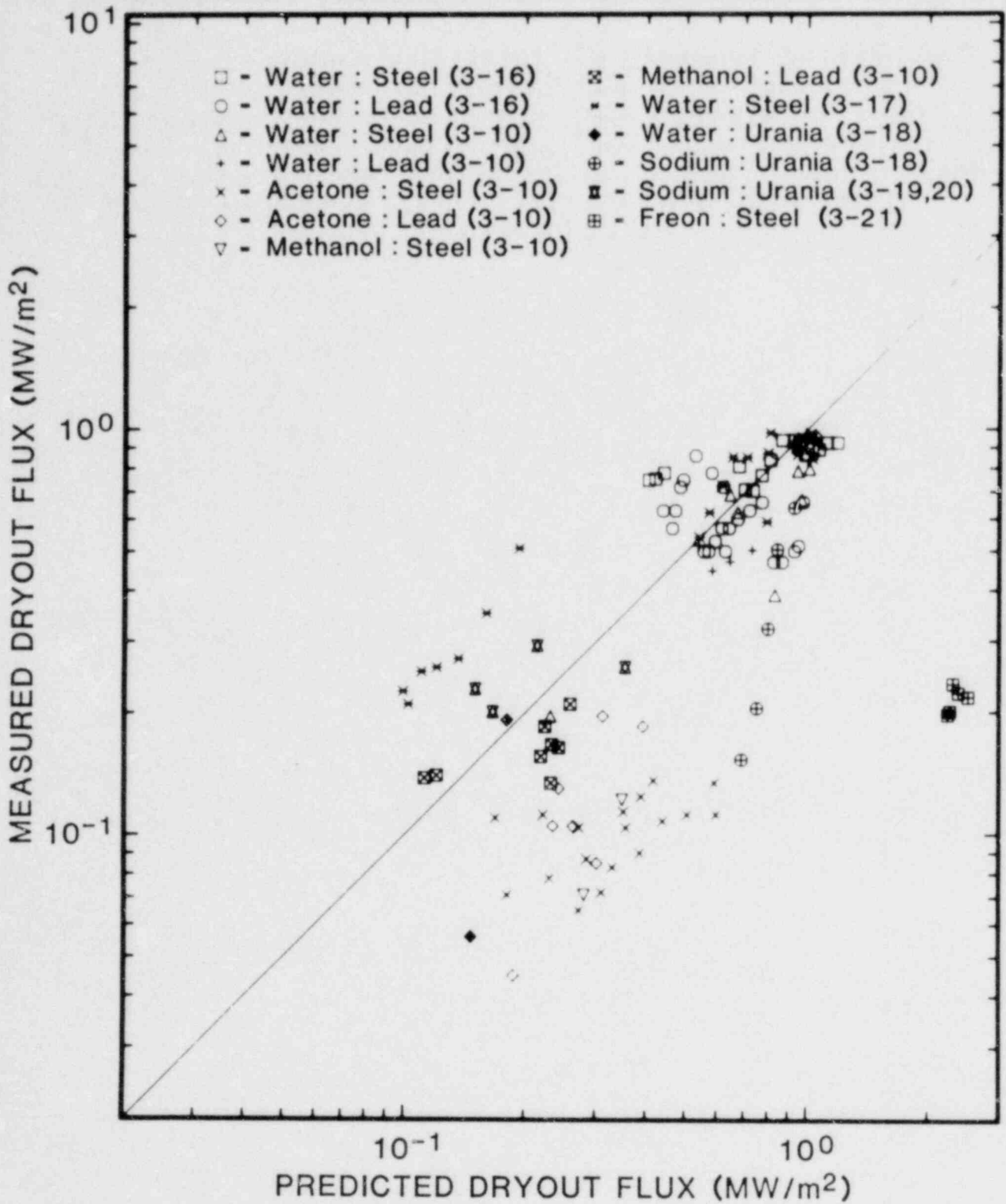


Figure 3.2-15 Predictions vs Measurements for the Shires-Stevens Model (Eq 3.18)

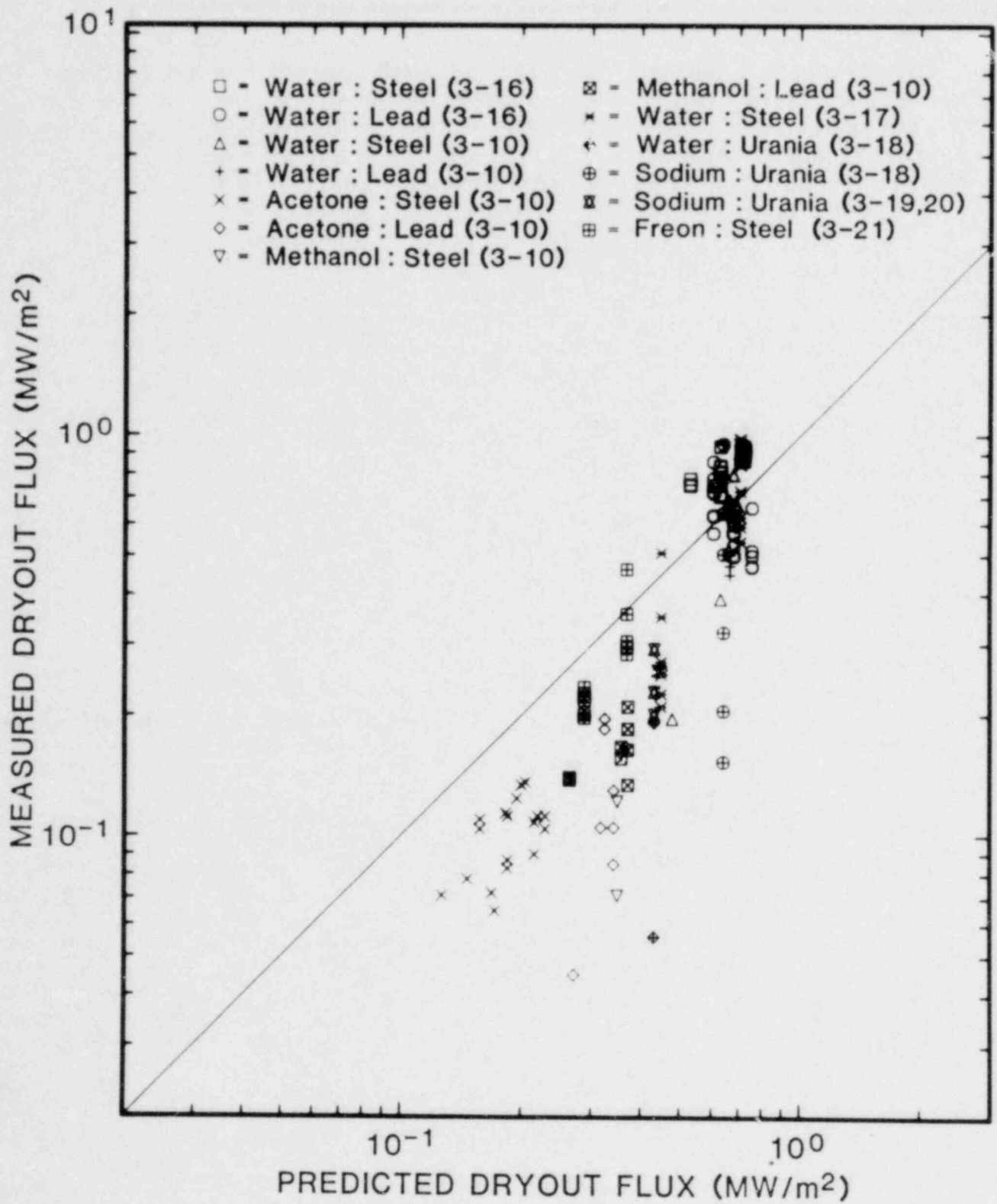


Figure 3.2-16 Predictions vs Measurements for the Ostensen Model (Eq 3.33)

3.2.5.2 Bottom Cooling and Downward Boiling

Heat removal from a particulate bed can be enhanced by cooling the bed bottom (or support plate). Models have been proposed in which the downward heat removal is by conduction alone.^(3-15,3-22) For this mode to be effective, large temperature drops (below the coolant boiling point) and high thermal conductivities in the bed are required. (The latter restriction is particularly limiting in LWRs.) However, recognition of the capillary forces acting in a bed leads to another possible mechanism of downward heat removal which would be greater than condition. That possibility is downward boiling. In most beds of interest, capillary forces are stronger than gravitational forces. Thus, if an adequate supply of liquid was maintained at both the top and the bottom of the bed, capillary forces would draw the liquid into the bed from both above and below. When the decay heat vaporized some of the liquid in the bed, the liquid would be driven out of the bed (both upward and downward) by the pressure gradient established by the capillary force (and altered somewhat by the gravitational force). Normally the downward-driven vapor would collect at the bottom support plate, build up a back pressure, and stop the vapor flow. However, if the support plate were cool enough to condense all the vapor (or if the plate were permeable) the flow could continue and the condensed liquid (or new liquid passing upward through a permeable plate) could be drawn back up into the bed. This process is downward boiling and can be just as effective at heat removal as upward boiling (if the capillary force is much greater than the gravitational force).

The equations for combined upward and downward boiling have been developed. Since capillary forces are not strong for large particles (which induce turbulent flow) it is convenient to use the laminar limit of the general dryout model Eq (3.23). The upward and downward heat fluxes at dryout are then respectively:

$$q_u = \frac{\frac{q_o}{2} \left(\frac{2\lambda_c}{L} + \sqrt{\left(\frac{2\lambda_c}{L} \right)^2 + 1 + 1} \right)}{\left(1 + \frac{\lambda_c}{L} \right)} \quad (3.42)$$

and

$$q_d = \frac{\frac{q_o}{2} \left(\frac{2\lambda_c}{L} + \sqrt{\left(\frac{2\lambda_c}{L} \right)^2 + 1 - 1} \right)}{\left(1 + \frac{\lambda_c}{L} \right)} \quad (3.43)$$

where q_o and λ_c are given by Eqs (3.23) and (3.12), respectively, and L is the total bed depth. For a bed of fixed depth L , the ratio of the volumetric power at dryout with downward boiling to that without boiling is

$$r = \frac{\left(\frac{2\lambda_c}{L} + \sqrt{\left(\frac{2\lambda_c}{L} \right)^2 + 1} \right)}{\left(1 + \frac{\lambda_c}{L} \right)} \quad (3.44)$$

This is also the ratio of the combined (upward and downward) heat fluxes. The values of this ratio for a 100-mm high bed, with a particle diameter of 0.5 mm, and with $\epsilon = 0.4$ are given in Table 3-VII for various fluids (at 1-atm pressure).

Table 3-VII Ratio of Dryout Powers With Downward Boiling to That Without Downward Boiling for $L = 100$ mm, $d = 0.5$ mm, and $\epsilon = 0.4$ for Various Fluids

Fluid	λ_c (mm)	Ratio
Water	125	2.31
Sodium	330	3.09
Acetone	51	1.62
Methanol	50	1.61
Freon-113	18	1.20

The downward boiling model may be compared to the bottom-cooled dryout data of reference 3-23. A steel-acetone bed was cooled through a 3-mm-thick aluminum support plate by running water. Two particle diameters (0.69 mm and 0.90 mm) with $\epsilon = 0.4$ were used. Table 3-VI indicates that with acetone vapor flow is becoming turbulent for diameters this large. Thus Eqs (3.42) and (3.43) should predict larger heat fluxes than were observed and only the 0.69-mm diameter data will be analyzed. (The equations would be more accurate for water or sodium.) The downward heat flux was fixed at 60 kW/m² for all the dryout runs (presumably by varying the running water flow). Thus 60 kW/m² represents a lower limit to the downward heat removal capability of the bed. If the downward heat removal were by conduction alone, heat flux would be⁽³⁻¹⁵⁾

$$q_d = \sqrt{2k\Delta TS} \quad (3.45)$$

where k is the bed thermal conductivity, ΔT is the temperature drop across the bed bottom, and S is the volumetric heat source in the bed. The conductivity of a particle bed is⁽³⁻²⁴⁾

$$k = \frac{(\epsilon k_f + (1 - \epsilon) F k_p)}{(\epsilon + (1 + \epsilon) F)} \quad (3.46)$$

where

$$F = \frac{2}{3 + \frac{3}{8} \left(\frac{k_p}{k_f - 1} \right)} + \frac{1}{3 + \frac{9}{4} \left(\frac{k_p}{k_f - 1} \right)} \quad (3.47)$$

and where k_p and k_f are the conductivities of the particles and the fluid respectively. For a steel-acetone bed, $k = 1.5 \text{ W/m}^2$. The temperature drop ΔT is less than or equal to the boiling temperature minus the running water temperature minus the temperature drop in the support plate. This is $\Delta T = 329 \text{ K} - 285 \text{ K} - 7 \text{ K} = 37 \text{ K}$. Table 3-VIII shows the downward heat fluxes predicted by downward boiling Eq (3.42) and conduction Eq (3.44) for various bed depths for 0.69-mm-diameter particles. The downward flux from conduction is much too small to account for that observed. Conversely, the downward boiling model predicts a large enough flux to account for that observed. A true test of the model awaits a measurement with a fluid for which the vapor flow is laminar (water or sodium) and a measurement in which the downward flux is not externally limited.

The possibility of downward boiling has an impact on core catcher design. In previous considerations, the downward flux was assumed to be due to conduction alone. However, with the addition of the heat flux from downward boiling, the support plate thermal resistance may become a limiting factor. For a 200-mm-high bed in sodium with $d = 0.5 \text{ mm}$ and $\epsilon = 0.4$, the downward boiling heat flux at dryout will be 210 kW/m^2 . If this heat flux is to pass through a steel plate with a temperature drop of less than 200 K, the plate must be less than 25 mm thick. One additional impact of downward boiling is the bottom-cooled core catchers become a reasonable consideration for water-cooled reactors (whereas previously bottom cooling was assumed to be ineffective because of the low thermal conductivity of water).

3.2.5.3 Zion-Indian Point Filtered-Vent Containment System Studies

The events surrounding a PWR reactor-vessel failure following a core meltdown was subjected to a cursory analysis to assess the impact of such events on a containment building filtered vent. Specific accidents considered included a loss of AC power and auxiliary feedwater (TMLB'), a small-break LOCA (S2D), and a large-break LOCA with failure of the containment heat removal system (ABG). The MARCH computer code⁽³⁻²⁵⁾ analysis of these accidents (with respect to the Indian Point 3 and Zion reactors) was used as a basis for comparison. The major findings are

- The location and size of a vessel rupture in the TMLB' accident could significantly affect the pressure history in containment and the subsequent loading on the filtered vent.
- A significant containment building pressure rise could occur from molten debris dropping into the reactor cavity if there is adequate water in the cavity. MARCH calculations have assumed less than adequate water in the TMLB' and ABG accidents. However, other accident sequences may have more water in the cavity.
- The coolability of in-vessel or ex-vessel particle beds by natural circulation (assuming an adequate coolant supply) can neither be assured nor precluded at this time. However, current data and models suggest that total-core particle beds may be coolable in some cases.

3.2.6 LWR Related Activities

As part of a larger study⁽³⁻²⁶⁾ of Class 9 accidents at the Zion and Indian Point nuclear power stations, an interim review of current modeling of in-vessel meltdown in an LWR was performed during the period January 7 through March 31, 1980. The objective of the study was to assess the risk reduction measures which may be applied to the reactors at those two sites.⁽³⁻²⁷⁾

Table 3-VIII Downward Heat Flux Predicted by Downward Boiling and Conduction for Various Bed Depths*

Bed Depth (mm)	q_{down} (Conduction) (kW/m ²)	q_{down} (Downward Boiling) (kW/m ²)	q_{down} (Observed Lower Limit) (kW/m ²)
72	12.4	93	60
60	14.6	115	60
52	15.0	137	60

*The downward heat fluxes observed in Reference 3-27 (a lower limit of that possible for the bed) are also shown.

The objective of the review was to assess the applicability of current meltdown models, as contained in the MARCH computer code, to the process of specifying risk factors and possible mitigation measures. In particular, investigators considered it desirable to estimate the degree of realism which may be assigned to the calculated results when treated as source terms which assault the containment.

Reactor meltdown sequences are treated in the Reactor Safety Study,⁽³⁻²⁸⁾ and Appendix VIII of the Study discusses the physical processes of meltdown and the modeling of those processes. This modeling was employed by the participants in the Study.

The principal meltdown computer model, developed for use in the Safety Study, was the BOIL code⁽³⁻²⁸⁾ originated by Battelle Columbus Laboratories (BCL) personnel.⁽³⁻²⁵⁾ Additional modeling of the accident sequences was performed by hand calculation.⁽³⁻²⁵⁾

Subsequent to the Reactor Safety Study, improvements and extensions to BOIL were undertaken at BCL to generalize the code's application to various LWRs and to accident sequences other than the large LOCA. These modifications were intended to enhance consistency and to incorporate new experimental data.⁽³⁻²⁹⁾ The current version is entitled MARCH, an acronym for "meltdown accident response characteristics,"⁽³⁻²⁵⁾ and BOIL is incorporated as a subroutine in MARCH. MARCH is designed to provide a continuous, coupled analysis of the thermal and hydraulic behavior of the containment building and reactor from the time of accident initiation.

The MARCH code has been constructed by using simple models of in-vessel meltdown processes. In several instances, these models are mechanistic only to the extent of satisfying conservation laws for mass and energy. This approach has four advantages. First, because the models are simple and are generally derived from basic considerations, the results are unlikely to contain gross errors hidden in complicated attempts at detailed analysis. Second, the models have been selected with the desire to bound (in some way) processes that are poorly understood. Third, the lack of detailed calculation allows the code to run rapidly and inexpensively. Fourth, unwarranted optimism concerning the treatment of poorly understood phenomena is not introduced by inappropriate elegance in the calculation.

MARCH produces a sequence of events which is believed to approximate the sequence which might be observed during a reactor meltdown. Uncertainties exist in the treatment of certain processes; these uncertainties are discussed in the body of the review.

The uncertainties arise because of (1) faulty or inadequate modeling, or (2) poorly understood phenomenology. The uncertainties give rise, in turn, to uncertainty in the timing of some events, and to some uncertainty in the magnitude of calculated conditions (pressure, temperatures, etc).

Because of significant uncertainties in the phenomena, the single greatest modeling uncertainty in MARCH concerns core melting and fuel motion, where much of what the code predicts results from selection of input options, rather than from models of evolving coupled physical processes.

The weakening (failure?) of structure, including core barrel, below core structure, and reactor vessel, are inadequately modeled, partly because of inadequate heating models, and partly because of inadequate structural treatment. Steam explosions are modeled only to the extent of providing a heat balance.

Based on this interim review, bounds for the identified uncertainties cannot be assigned. To some extent the range of possible outcomes is limited by energy-balance considerations. But detailed quantitative output from MARCH, such as that which is required for the mitigation study, must be regarded as subject to considerable variation and uncertainty.

The resolution of the uncertainties identified in the review requires additional work which may be divided into several categories:

- Continued review of meltdown modeling
- Short-term MARCH changes and studies
- Auxiliary calculations
- Experiments
- Improvements to MARCH.

Each of these categories is discussed in the body of the review. Performance of the recommended items should result in increased understanding of the in-vessel sequence. This knowledge can subsequently be used to improve the modeling in MARCH.

3.3 PAHR Molten Pool

(D. W. Varela, 4422; T. M. Kerley, 4422)

3.3.1 Introduction

The molten fuel pool studies are using prototypic and reactor materials to investigate experimentally the progression of a debris bed from dryout to melt and the interaction of the melt with structure and core retention material.

This quarter, the data from the recently conducted MP-4 in-pile experiment was reduced. Temperature and energy deposition profiles were compared against existing heat transfer and neutronic models. Furnace tests were conducted to examine the effect of second phase material (ZrO_2 and La_2O_3) on the interaction of UO_2 with magnesium oxide. Development of a new ultrasonic thermometer (UT) system was initiated with the objective of improving the reliability and accuracy of the temperature data. Investigators are giving high priority to the completion of this system in time to incorporate it in the next in-pile experiment, MP-5S, currently scheduled to be conducted late in the next quarter. Fabrication and testing of components for the assembly of this next experiment are underway.

3.3.2 MP-4 (UO_2/MgO) In-Pile Experiment

In the fourth in-pile molten pool experiment MP-4, conducted last quarter, 615 g of fully enriched UO_2 particulate formed a bed overlying a MgO disk (Harklase-type, 98% pure, burned magnesite). The objective of MP-4 was to examine the effect of fission heating on the penetration of UO_2 into the MgO brick at temperatures below the MgO dissolution temperature ($1873 < T < 2473$ K). Temperatures were measured with UTs and TCs (thermocouples). These measurements will allow determination of heat-flux partitioning in the bed (i.e., the amount of heat available for erosion of the MgO brick), an important goal of the in-pile part of the molten pool program. The actual penetration depth of UO_2 into the MgO brick will be measured when the capsule is disassembled. This measurement will be compared to recent out-of-pile correlations obtained from a series of molten pool furnace experiments.^(3-30,3-31)

Figure 3.3.1 shows the configuration of the capsule used in MP-4. Temperatures in the fuel bed and MgO brick were monitored with three UTs located at $r = 0$, $r = 12.5$ and $r = 25.0$ mm as shown in Figure 3.3-2. The center UT had eight axial sensor elements while the other two had five elements (each element gives a temperature reading averaged over its length). The length of each element was 10 mm with the exception of the end element which was 15 mm.

Figure 3.3-3 shows the reactor and fuel bed power history. As in previous experiments the low power portion of the run (150 kW for ~54 min) was used to confirm proper operation of all systems and diagnostics. Following this confirmation, the ACRR power was increased to 650 kW corresponding to an average fuel bed power of 2.93 kW/kg as calculated by the

two-dimensional neutronic code TWOTRAN.⁽³⁻³²⁾ The maximum temperature of 2400 K at the UO_2/MgO interface, called for in the experiment plan, was reached in ~9.7 min at this power level and resulted in a maximum temperature of ~3000 K in the overlying UO_2 -fuel bed. Once these temperatures were achieved, the experiment called for sequentially decreasing power levels to sustain the UO_2/MgO interactions while maintaining the overlying UO_2 below melt (for safety considerations). The power was therefore decreased first to 550 kW and then to 300 kW. Shortly after this last power level the pressure limitation on the capsule was exceeded and the reactor was scrammed.

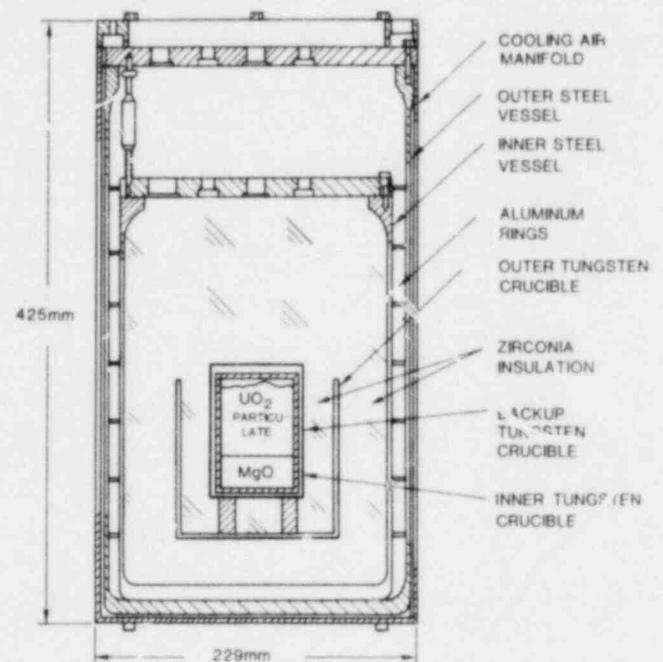


Figure 3.3-1 MP-4 Molten Fuel Pool Experiment Capsule (UO_2/MgO)

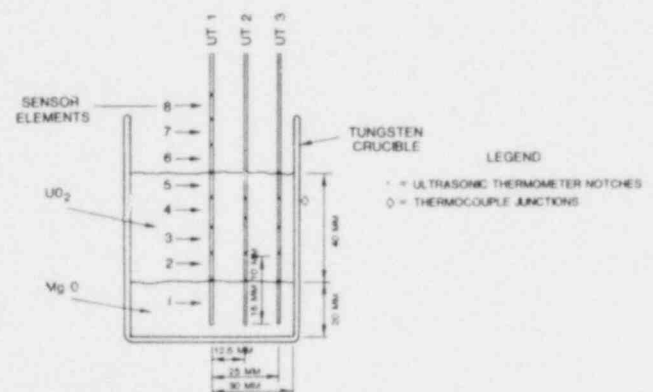


Figure 3.3-2 Location of Ultrasonic Thermometers and Inner Crucible Thermocouples in MP-4

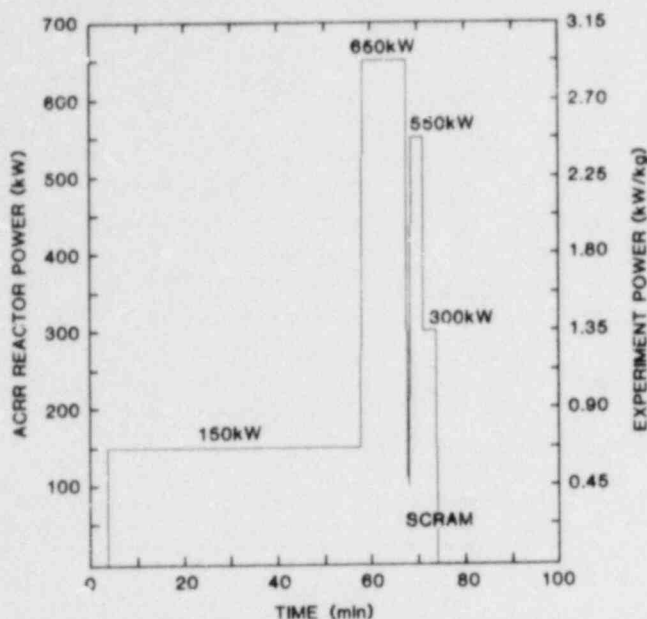


Figure 3.3-3 MP-4 Reactor and Experiment Power History

Figures 3.3-4, -5, and -6 show the data from the three UT sensors. The central sensor failed at ~ 65 min into the experiment during the latter part of the 650-kW-power portion of the test. The pulse signal was lost indicating a problem in the electronic components rather than in the sensor itself. Also, during the low power portion of the test, the data acquisition system failed to record some of the UT measurements. This time interval has been labeled "extrapolated UT data" in Figures 3.3-4, -5, and -6.

The UT data obtained from this experiment are of the same general quality as that of previous in-pile molten pool experiments, reflecting inaccuracies in some of the temperature measurements caused by distorted acoustic reflections. The source of error can generally be traced to one or more of the following: (1) hard contact and/or "sticking" between the sensor and the protective sheath or surrounding environment, (2) containment sealing around the sensor, and (3) the weld interface between the magnetostrictive and nonmagnetostrictive parts of the sensor. Any of these effects will cause unwanted signal reflections which can overlap the primary signal reflections. This overlap will in turn distort the reflected waves which yield temperatures.

To interpret the UT data shown in Figures 3.3-4, -5, and -6, the nature and effect of any distortions in the acoustic data must be understood. Take, for example, elements 4 and 5 in sensor 3, which have been extracted from Figure 3.3-6 and redrawn for Figure 3.3-7 for clarity. In general, a high reading from element 5 is compensated by a low reading in element 4. An interference reflection overlapping the reflection from the notch between elements 4 and 5

would cause this behavior. In this particular case, the average of these two readings would represent the correct temperature over the length of the two elements. This average has been plotted in Figure 3.3-8 and compared against the data of a thermocouple placed on the outer surface of the inner tungsten crucible (Figure 3.3-2). The location of the thermocouple junction corresponds to the axial center of elements 4 and 5 and is displaced radially by ~ 8.5 mm. As Figure 3.3-8 shows, the comparison is excellent, reflecting a consistent radial temperature gradient and a smooth and continuous temperature rise and decay throughout the duration of the experiment. Unfortunately, interference reflections do not always occur between two elements, but instead can affect the element signal in a variety of other ways, making interpretation of the data more difficult and sometimes impossible. For example, element 8 in sensor 1 yielded data during the experiment which is clearly erroneous. Analysis of the ultrasonic thermometer signals showed that a reflection, either from the primary containment seal or the weld interface, was overriding the signal from element 8 but was not significantly affecting element 7. This was reflected in the temperature measurements as the data from element 7 was fairly consistent with expected results while that of element 8 was spurious. Similar behavior was noted in several other elements.

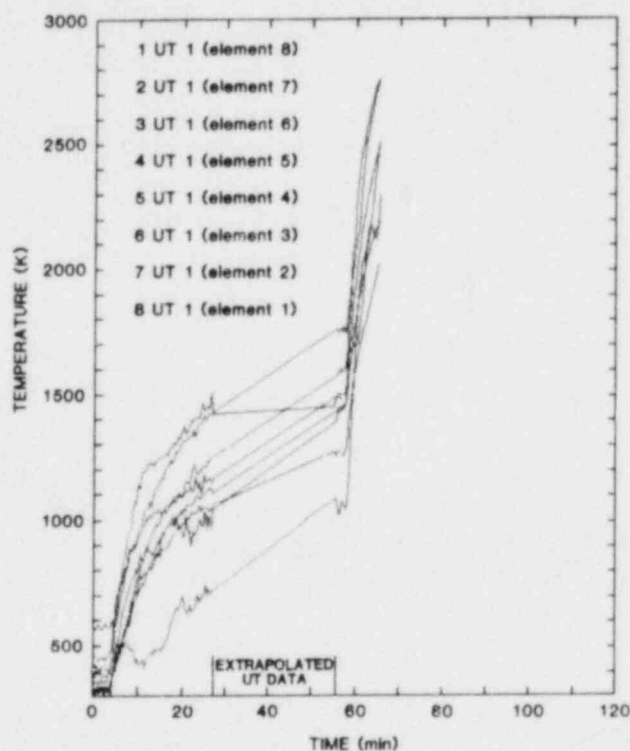


Figure 3.3-4 MP-4 Ultrasonic Thermometer Data Radial Center UT

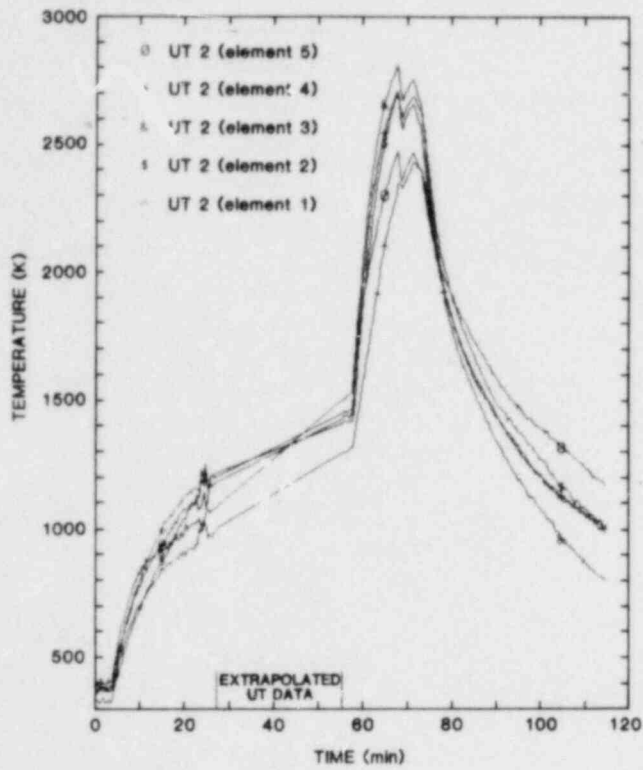


Figure 3.3-5 MP-4 Ultrasonic Thermometer Data
Radius = 12.5 mm

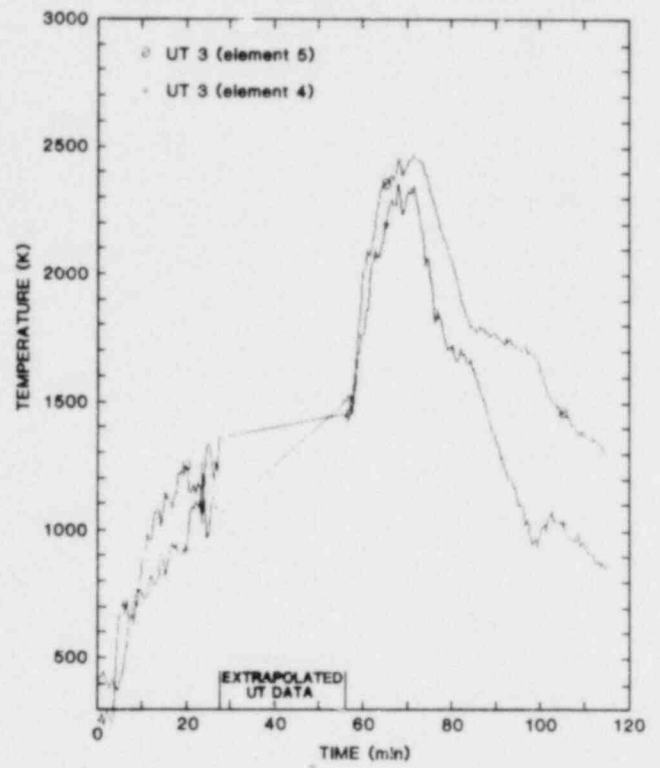


Figure 3.3-7 MP-4 Ultrasonic Thermometer Data
Radius = 25.0 mm

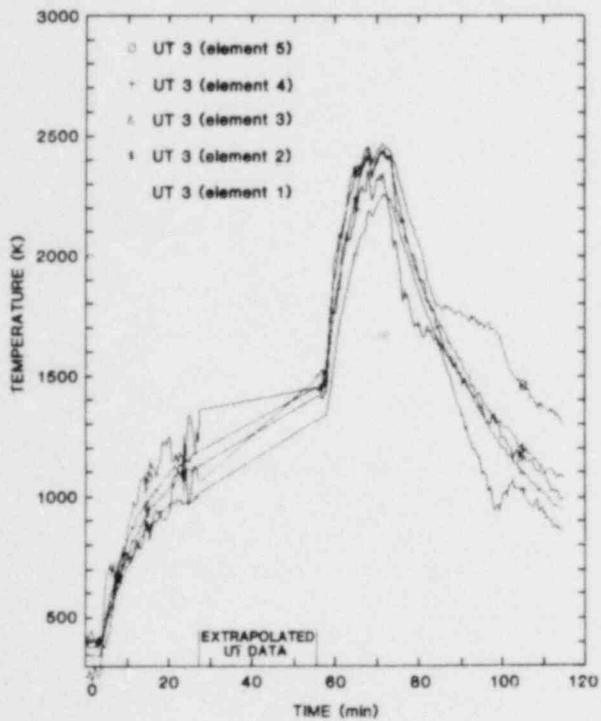


Figure 3.3-6 MP-4 Ultrasonic Thermometer Data
Radius = 25.0 mm

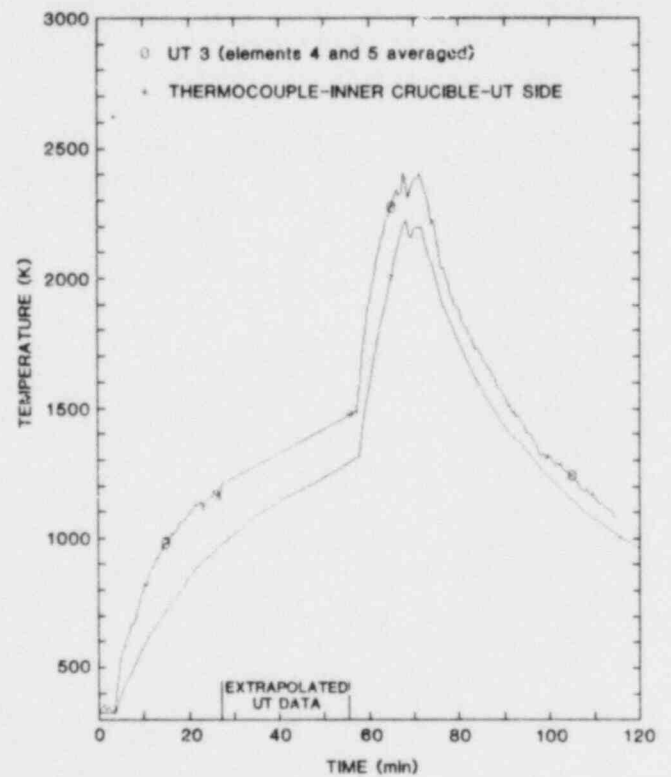


Figure 3.3-8 MP-4 Ultrasonic Thermometer Data
Radius = 25.0 mm - Comparison With Thermocouple Data

Clearly, only selected temperature measurements which do not show significant evidence of UT-signal distortion will provide meaningful data for the thermal analysis of the experiment. Nonetheless, these selected temperatures together with the thermocouple measurements are sufficient to provide a reasonable evaluation of the heat flux distribution in the capsule.

Preliminary calculations have been performed with the heat transfer code TAC2D⁽³⁻³³⁾ to evaluate the ability of current thermal and neutronic models to predict the experimental temperature profiles. Figure 3.3-9 compares measured temperatures near the top of the fuel bed with calculations. The energy deposition, predicted by current models is significantly higher than the experimental data shows. In fact, these models predict that a substantial amount of fuel would melt; however, posttest x-radiographs of the vessel showed no evidence of fuel melting and very little indication of fuel compaction. These indications agree with the experimental data.

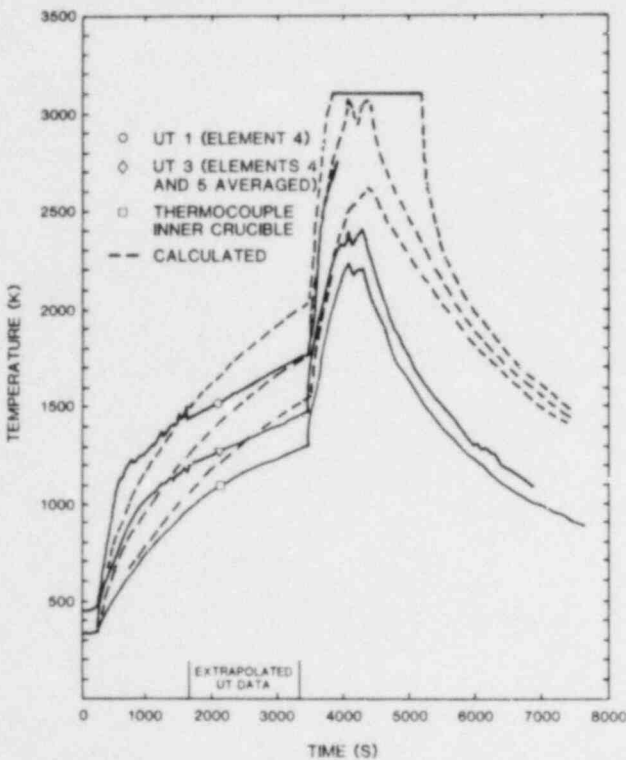


Figure 3.3-9 MP-4 Ultrasonic Thermometer Data Radial Profile Near Top of Fuel Bed (UT1, element 4; UT3, elements 4 and 5)

The agreement between experiment and calculations can be improved significantly by enhancing the conductivity of the UO_2 fuel and the ZrO_2 insulation and slightly increasing the fuel bed power. Figure 3.3-10 shows a new comparison which reflects a 5% increase in power, an increase by a factor of 2.2 in

the ZrO_2 conductivity relative to that used in earlier models, and a radiative term added to the conductivity of UO_2 . These considerations yield an effective conductivity of the form

$$k_e = k_c + k_r$$

where

$$k_r = AT^3.$$

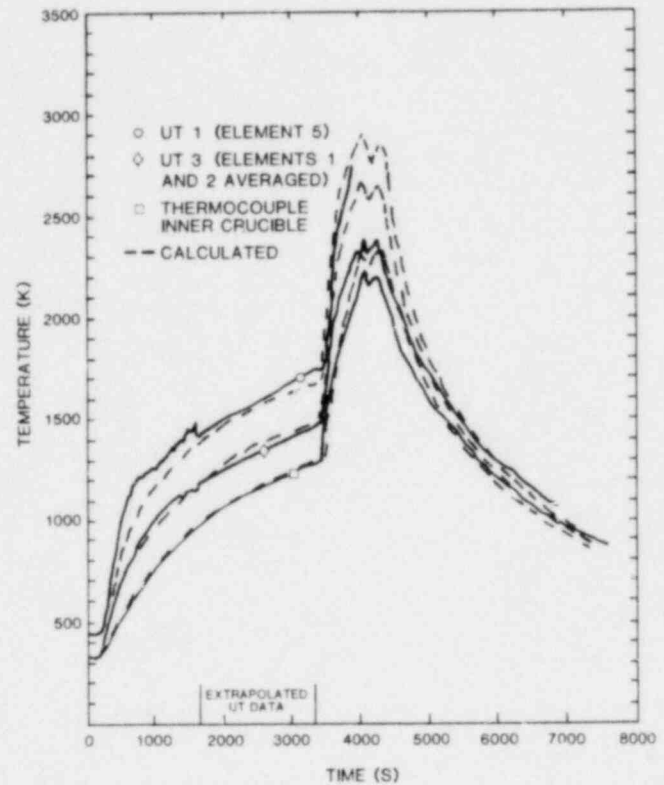


Figure 3.3-10 MP-4 Ultrasonic Thermometer Data Radial Profile Near Top of Fuel Bed

The value of A used in the calculations shown in Figure 3.3-10 is 2.12×10^{10} W/M \cdot K. This value has been calculated to be representative of the type of particle beds being used in the Molten Pool Experiments.⁽³⁻³⁴⁾

The power in the fuel bed was determined by comparing the slopes of the curves during the initial heating period following a power increase. During this period, the energy deposition in the bed is large relative to the heat loss. On this basis, a relatively small increase in the power over that predicted by TWOTRAN would be indicated. The ZrO_2 and UO_2 conductivities were adjusted simultaneously, assuring that both the temperature profiles in the fuel bed and the temperature history of regions away from the bed were in good agreement. Figure 3.3-11 shows a comparison of experimental temperatures measured

at regions away from the bed with calculations performed by using the modified power and conductivity values (these calculations have the same conditions as those shown for the fuel bed calculations in Figure 3.3-10). Note that the cooling conditions on the boundary of the capsule have negligible effect on the fuel bed temperatures during the powered portions of the test. That is, the large amount of high heat capacity and low density insulation considerably limits the amount of heat that can be removed from the bed.

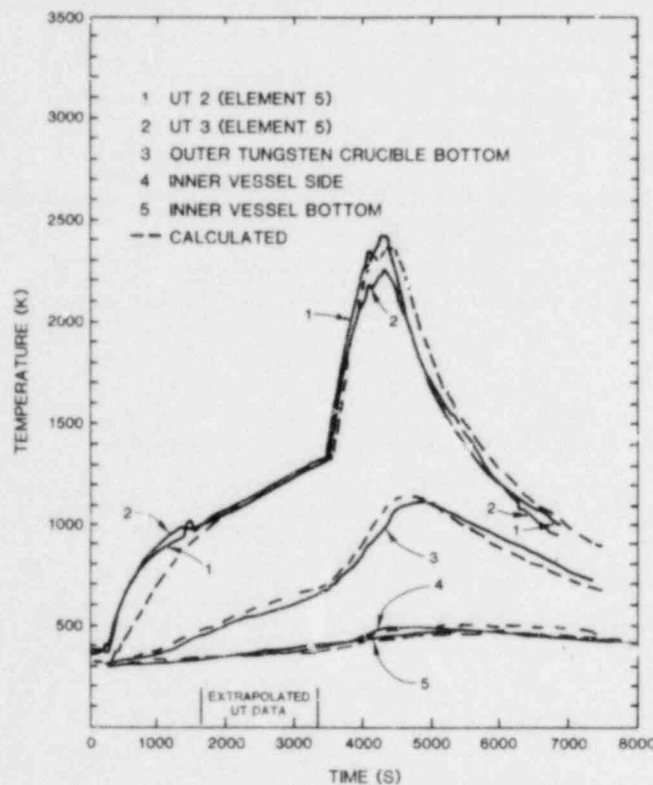


Figure 3.3-11 MP-4 Ultrasonic Thermometer and Thermocouple Data

The above conclusions need to be qualified at this point. The calculations are very preliminary and some aspects need to be analyzed in more detail. At this point, investigators also need to evaluate the extent of the error introduced in the UT and TC measurements as a result of axial heat transfer through the metallic part of the sheaths.

As noted earlier, the unexpected pressurization of the inner vessel caused the termination of the MP-4 experiment. Figure 3.3-12 is a plot of the pressure and the fuel bed power as a function of time. The experiment was initiated with an ambient pressure of 5 psia. The powered portion of the experiment was terminated when the pressure reached the reactor SCRAM set point of 30 psia. Following SCRAM, the pressure continued to increase for ~8 min reaching a

peak value of 32 psia. This pressure was more than twice the pressure expected to result from the heating of the capsule, as predicted by conservative calculations. The posttest ambient pressure remained at ~2.5 times the original pressure, indicating that non-condensable gas may have been generated during the experiment. Unfortunately, the nature and amount of gas in the inner vessel cannot be analyzed until the Sandia hot cell facilities are completed to allow disassembly of the capsule. Until such analysis is performed, summary judgments must be carefully avoided regarding the source of this gas. At this point, an important observation is that the gas may not have been from UO_2/MgO interactions but rather was an artifact of the experiment (i.e., pressure transducer failure, impurities in the system, etc).

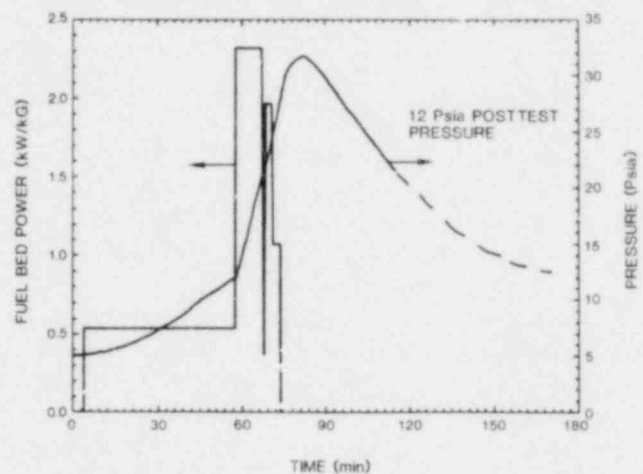


Figure 3.3-12 MP-4 In-Pile Experiment (UO_2/MgO) Power and Pressure Histories

In summary, the MP-4 experiment has produced the first data on the interaction of MgO with internally heated UO_2 fuel. The pressure and temperature data from the experiment have been reduced and preliminary analysis of this data has been performed. Efforts are now underway to determine heat flux distributions in the capsule. Disassembly of the capsule remains to be performed. Upon disassembly, the test section will be microscopically analyzed to determine in detail the interaction of the internally heated fuel with MgO . The results will then be compared with existing out-of-pile correlations.

3.3.3 High Temperature Furnace Tests

Out-of-pile furnace tests were conducted to examine the interaction of $UO_2 + 30$ w/o ZrO_2 and $UO_2 + 30$ w/o La_2O_3 mixtures with MgO . These tests compliment a series of UO_2/MgO experiments discussed in detail in the last two quarterly reports. (3-30,3-31)

In these experiments, the fuel mixture was packed lightly over the MgO disk and was heated rapidly to temperatures between 1773 and 2273 K (1500° and 2400°C), and held at temperature for 15 to 25 min. Table 3-IX shows the test matrix and key test observations.

In all cases, the penetration depth of the fuel mixture into the MgO brick was increased relative to the penetration depth of pure UO₂. For example, a mixture of UO₂ + 30 w/o La₂O₃ held at 2373 K (2100°C) for 900 s will penetrate 12 cm into the MgO brick while pure UO₂ will penetrate only 3.4 mm.⁽³⁻³¹⁾ Further, at higher temperatures where the fuel interacts with the MgO grains, the fuel composition also had a very significant effect on the interaction. For example, when ZrO₂ or La₂O₃ were added to the UO₂ and rapidly heated to 2673 K (2400°C), the mixture foamed momentarily and part of it flowed out of the inner tungsten container. This temperature is about 250 K lower than the temperature at which a UO₂/MgO mixture will foam, and about 300 K lower than the temperature at which MgO will foam by itself.⁽³⁻³⁰⁾ Therefore, at least some gas formation appears to be associated with the formation of the eutectic between fuel material and MgO. These tests performed this quarter do not, however, imply that the temperature of the fuel mixture/MgO eutectic is near 2673 K. In fact, these eutectics could be at substantially lower temperatures but the relatively rapid heating of the tests prevented significant eutectic formation from taking place until the higher temperatures were achieved. That is, the rate of formation of the fuel/MgO eutectic is dependent on the rate of penetration of fuel into the MgO grain boundaries. This dependence in turn is a function of temperature and time at temperature.⁽³⁻³¹⁾ The temperature-dependence is in fact exponential.

The dependence of the UO₂/MgO eutectic on the penetration of fuel into the MgO brick was illustrated with a recent test, shown in Table 3-IX. In this test, a bed of UO₂ particulate was overlaid on an MgO disk and heated at 2573 K (2300°C) for 1 hr. Significant dendritic eutectic formations were found in the SEM examination of this sample. These results contrast with those from the other UO₂/MgO tests exposed to even higher temperatures but for shorter periods of time (i.e., 2773 K for 10 min) where no evidence of a eutectic was found.⁽³⁻³⁰⁾ This temperature is in fact much higher than the UO₂/MgO eutectic temperatures in well inerted systems. These eutectic temperatures have been estimated in the literature to be about 2473 K(2200°C).⁽³⁻³⁵⁾

3.3.4 Activities for Next Quarter

Next quarter will be devoted primarily to the development and testing of a new ultrasonic thermometer system in an effort to improve the accuracy and reliability of this instrument.

3.4 Fragmentation

(T. Y. Chu, 1537)

3.4.1 Data Analysis

Gamma-ray-densitometry measurements were made of core samples from fragmentation test FRAG11. In this test, 23 kg of sodium at 782 K (509°C) were released onto a shallow layer of a thermitically generated UO₂, ZrO₂/stainless steel melt. Tubes of 28-mm ID were driven into the debris bed to obtain the core samples. Out of 19 attempts to sample the

Table 3-IX Description of Fuel/Magnesium Oxide Interaction*

Test	Materials	T _{Max} (°C)	Time of t _{Max} (s)	Observations
1	(UO ₂ + 30 w/o ZrO ₂)/MgO	1500	150	No reaction.
2	(UO ₂ + 30 w/o ZrO ₂)/MgO	2100	900	Grain boundary penetration. Depth ≈ -6 mm.
3	(UO ₂ + 30 w/o ZrO ₂)/MgO	2400	900	Extensive eutectic interaction. Sample foamed indicating gas release upon melt.
4	(UO ₂ + 30 w/o La ₂ O ₃)/MgO	1500	5	Local discoloration of the MgO brick at the UO ₂ interface surface.
5	(UO ₂ + 30 w/o La ₂ O ₃)/MgO	2100	900	Grain boundary penetration. Depth ≈ 12 mm.
6	(UO ₂ + 30 w/o La ₂ O ₃)/MgO	2400	600	Extensive eutectic interaction. Sample foamed indicating gas release upon melt.
7	UO/MgO	2300	3600	Grain boundary penetration followed by UO ₂ /MgO eutectic interaction.

*This table complements a series of UO₂/MgO experiments described and analyzed in References 3-30 and 3-31.

core, 9 were unsuccessful. Apparently the bed contained fragments comparable in size to the core tube diameter. The larger fragments were sparsely distributed (horizontally). A full core sample could usually be obtained within a few centimeters of an unsuccessful attempt. Project personnel believe that at least some of the large fragments came from solidified pieces that were formed before the sodium was released. This problem will be further investigated when the sodium is removed from the bed.

Two typical results are shown in Figures 3.4-1 and 3.4-2. The sample in Figure 3.4-1 was taken from the center of the bed and the sample in Figure 3.4-2 was taken near the wall (15 cm from the center) of the interaction vessel. Gamma-ray scans were made 90 degrees apart for each sample. The density variations between the two directions were quite large and the density variations in the bed were also very large. These variations were due to the large fragments. For the scale of the samples, the bed structure was non-uniform. Comparing the two figures reveals that the high density portion of the bed was not uniform: 2.25 in. thick in the center and 2.75 in. thick near the wall. The average density in both of these regions was about the same, ~ 3.7 g/cm³. These results together with measurements of fragment-weight fraction will give the variation in the void fraction of the bed.

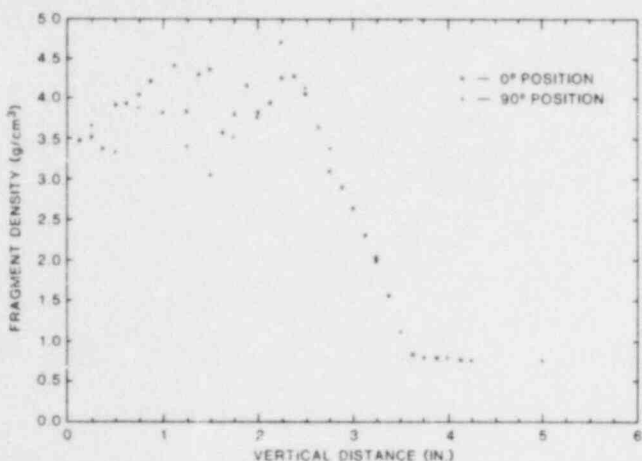


Figure 3.4-1 Fragment Density vs Penetration Distance for Core Sample Taken From the Center of the Bed. (Gamma-ray scans were taken at 0° and 90° positions around the sample.)

3.4.2 New Experiment

Fragmentation test FRAG12 was performed during this quarter. In FRAG12, 20 kg of UO₂, ZrO₂/stainless steel melt were produced in a crucible with a limestone concrete bottom and MgO side walls. A

charge of 23 kg of sodium at 796 K (523°C) was released onto the melt. The experiment was designed to investigate the effect of the melt/concrete and sodium/concrete interactions on the fragmentation process and the formation of the debris bed.

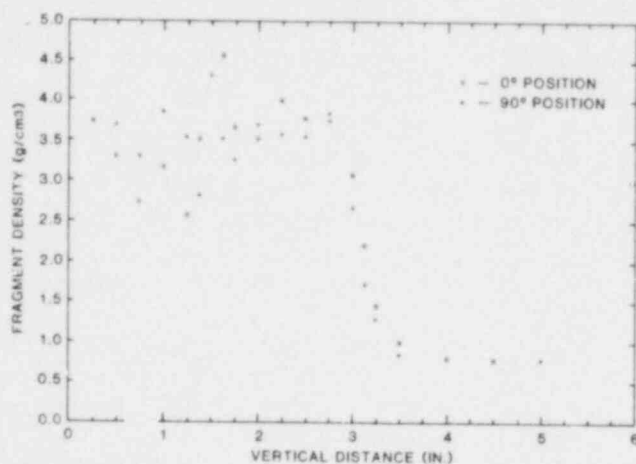


Figure 3.4-2 Fragment Density vs Penetration Distance for Core Sample Taken From the Bed Near the Wall. (Gamma-ray scans were taken at 0° and 90° positions around the sample.)

Sodium was released 10.7 s after ignition of the metallothermic mixture. Audio signals indicated six separate interactions lasting a total of 1.87 s. The interactions caused the 2000-kg test apparatus to move laterally approximately 2 cm. Toward the end of the interaction, fire was observed at the top of the exhaust stack, apparently as a result of hydrogen generated by the sodium/concrete interaction.

Figure 3.4-3 shows the temperature response of the concrete as monitored with thermocouples embedded in the concrete. The reaction front of the sodium/concrete interaction (as indicated by a sharp rise of temperature) reached 6.3 mm at 8 min and 12.7 mm at 21.5 min. The average propagation rate of the reaction front seems to be comparable to the lower range of typical rates for sodium/concrete interactions, 0.5 to 4 mm/min. Assessing the effect of the debris bed on erosion rate (because of its possible effect on the diffusion phenomena near the concrete surface) and the effect of gas generation on the structures of the debris bed (caused by the sodium/concrete interaction) will be interesting in future data analysis.

Posttest analysis is still being carried out. As a result of the sodium/concrete interaction, the MgO sidewalls were heavily eroded up to 20 mm. This phenomenon did not appear in previous fragmentation experiments. The details of the erosion mechanism are yet to be determined.

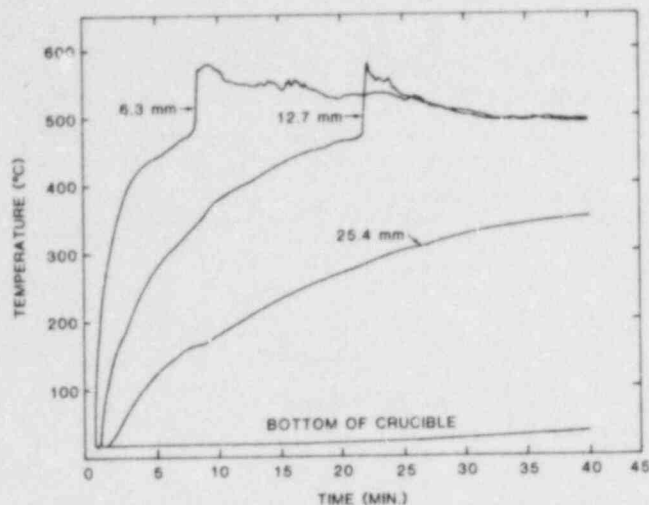


Figure 3.4-3 Elapsed Time vs Temperature (Temperature Response) at Several Selected Concrete Depths, Test FRAG 12

3.5 Sodium Containment and Structural Integrity

(R. U. Acton, 1537; L. A. Kent, 1537; J. E. Smaardyk, 4422; R. L. Sallach, 5846; A. Suo-Anttila, 4425)

3.5.1 Introduction

Preparations for a large-scale sodium/concrete interaction tests were made during this period. Earlier tests were analyzed with the concrete response code USINT.^{*} The next three large-scale tests have been defined. Water-release experiments have been performed on magnetite concrete.

3.5.2 Analyses of Some Previous Na-Concrete Tests

The computer code USINT has been used to calculate the thermal response of the concrete crucible during large-scale tests 5, 11 and 14 for comparison with the actual data. These tests were, respectively, on limestone, basalt, and magnetite concretes. Only temperature data are available from these earlier tests. Each of the tests analyzed involved the interaction of sodium with bare concrete.

In using USINT (and other heat transfer codes as well), it has been found that the sodium pool temperature cannot be used as a boundary condition if a reaction between the sodium and concrete occurs. To

do so yields a much higher heat flux than is found in the actual experiment. This result has also been found by the Hanford Engineering Development Laboratory.⁽³⁻³⁶⁾ When no reaction[†] occurs, the pool temperature may be used as a boundary condition to the concrete. A physical interpretation of this is that, according to the chemical model of the sodium-concrete interaction, concrete penetration does not begin until sodium hydroxide exists as a second phase. The sodium hydroxide is more dense than sodium metal and it therefore settles to the bottom of the pool where it insulates the concrete from the pool.

Test 5 on limestone concrete did not go into an energetic exothermic reaction. Figure 3.5-1 shows the comparison between experimental and computed temperatures in the concrete. In contrast, test 15 produced early energetic reactions in the magnetite concrete. In Figure 3.5-2, the experimental temperatures show evidence of both energetic reactions and spalling. Figure 3.5-3 shows that the USINT code cannot account for these effects. Program personnel are developing a version of USINT that is expected to account for spalling and a moving boundary.

The USINT code calculates pressure inside the concrete; this pressure is caused by the evaporation of water and the release of CO₂. Figure 3.5-4 is a plot of the pressure through the bottom of the basalt concrete crucible at 81.5 min after the start of test 11. No experimental data are available to corroborate the pressure calculation.

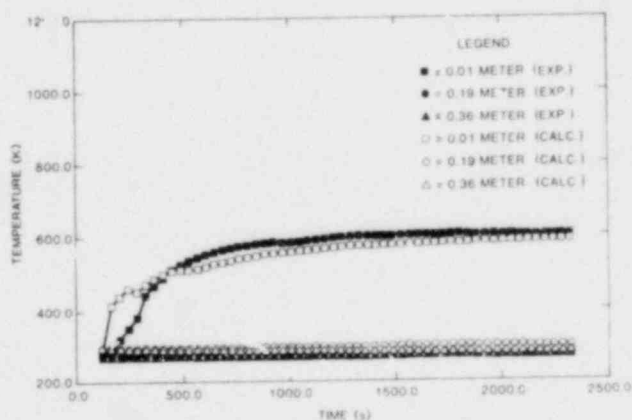


Figure 3.5-1 Experimental and Calculated Temperature, Test 5

[†]Reaction here is defined to be when penetration of the concrete is taking place. The water being thermally driven from the concrete always reacts with the sodium.

^{*}The USINT code is described elsewhere in this report.

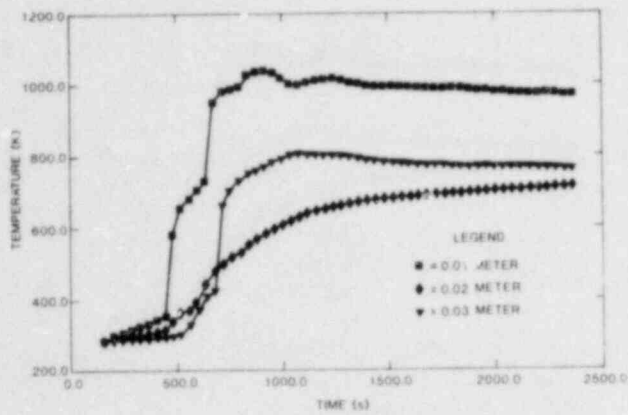


Figure 3.5-2 Experimental Temperature, Test 14

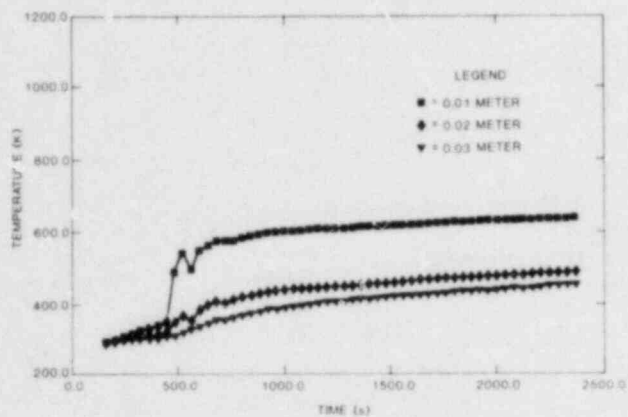


Figure 3.5-3 Calculated Temperature, Test 14

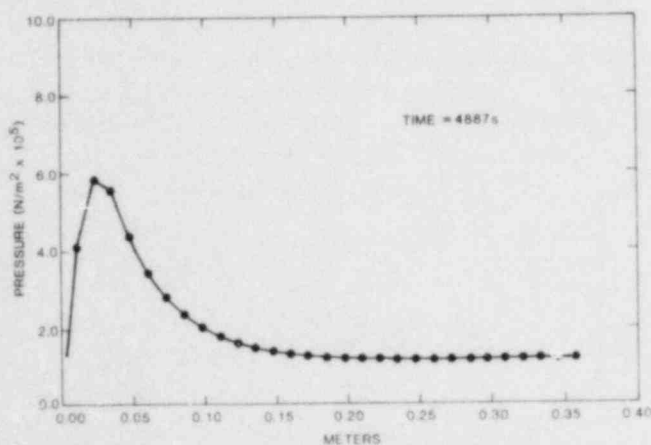
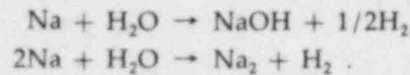


Figure 3.5-4 Pressure Through Concrete, Test 11

3.5.3 Experimental Water Release From Magnetite Concrete on Heating

Some of the reactions that release heat as a result of the contact of molten sodium with concrete involve the water driven from the concrete reacting

with sodium:



The amount of water given off by the concrete is important in analyzing sodium/concrete interactions. To define the amount of water released at a given temperature, two types of experiments are being performed: dehydration and thermal analysis.

The dehydration experiment has been completed. The test samples are from the same batch of concrete from which the crucible of test 14 was cast. Samples were taken and stored at 100% relative humidity for compression test at 7, 14, 28, 90 days. Table 3-X shows the results of tests on these samples.

Table 3-X Strength of Magnetite Concrete

Time After Cast (Days)	Strength (MPa)	Strength (psi)
7	23.91	(3468)
14	27.19	(3944)
28	40.36	(5854)
90	48.00	(6962)

The samples were measured and weighed and then heated to a selected temperature. They were maintained at temperature until repeated weight measurements showed no significant weight change. The temperature was then raised to the next selected value. Figures 3.5-5 and 3.5-6 show the data for the dehydration samples. Interpretation of the results awaits the completion of the thermal analysis experiments.

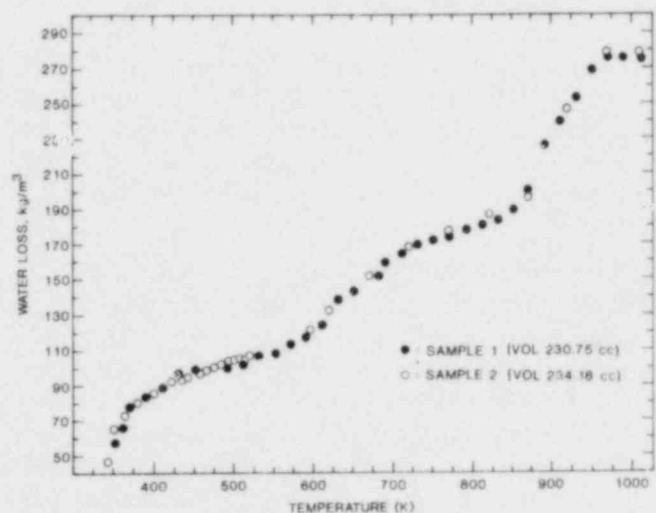


Figure 3.5-5 Water Release Data for Magnetite

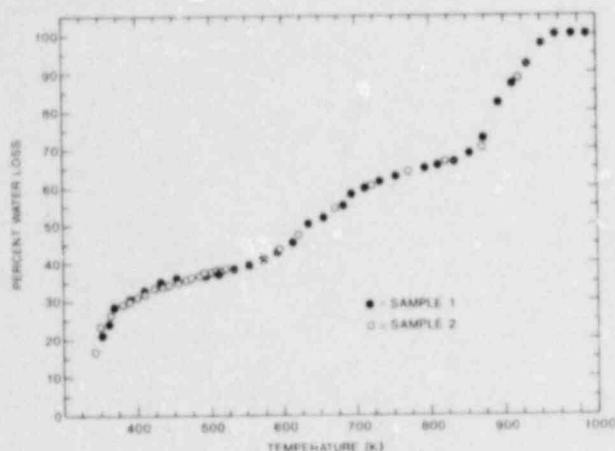


Figure 3.5-6 Relative Water Release Data for Magnetite

3.5.4 Large-Scale Sodium/Concrete Interaction Test Plans

The next three tests have been planned. Table 3-XI shows the test information. Test 17 will probably be conducted in late June.

3.5.5 Physical Separate Effects Test Program

During this period, one physical separate effects test was completed. Figure 3.5-7 is a schematic of the test configuration. The concrete was made from basalt aggregate and sand obtained from FFTF site sources. The concrete was cast in a section of 12-in. schedule 40 pipe to a depth of 30 cm. A sheet metal insert was placed in the upper section of the pipe, and MgO powder was packed in the annulus between the insert and pipe to thermally isolate the sodium pool from the pipe. A tubular heater was placed in the pool area to maintain test temperatures. Next, a steel pan containing 0.9 kg of NaOH was suspended in the test article. This configuration was chosen to provide sufficient NaOH to saturate the sodium pool without creating a thick layer of NaOH at the concrete interface. A deflector was installed above the pan so the sodium flow during the dump would not scatter the NaOH pellets out of the pan.

The sodium charge, 5.4 kg, was heated to 975 K (702°C) before the test. Immediately after the dump, the sodium pool cooled to 683 K (410°C). The pool heater brought the temperature back up to the set-point of 823 K (550°C) in about 2.5 hr. About 3 hr into the test, some exothermic chemical reactions were evident from the thermocouple readings but were not extensive enough to maintain the pool temperature above the set-point.

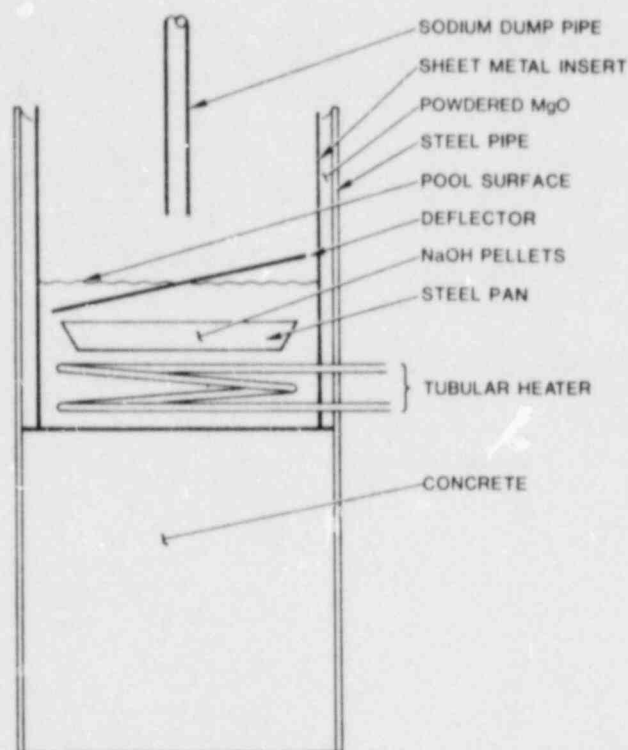


Figure 3.5-7 Key Features of the Physical Separate Effects Test. (The pool and concrete thermocouples were left out of the diagram for clarity.)

At 3.5 hr, most of the sodium leaked from the test article. The heater became uncovered and was turned off. The remaining shallow pool and concrete surface cooled rapidly to about 723 K (450°C). At that point, chemical reactions generated sufficient heat to raise the temperature by about 200 K with brief excursions to 973 K (700°C). These reactions ceased by 4.5 hr into the test and the experiment cooled monotonically. Temperature readings for two of the pool thermocouples and two concrete thermocouples closest to the initial interface are shown in Figure 3.5-8.

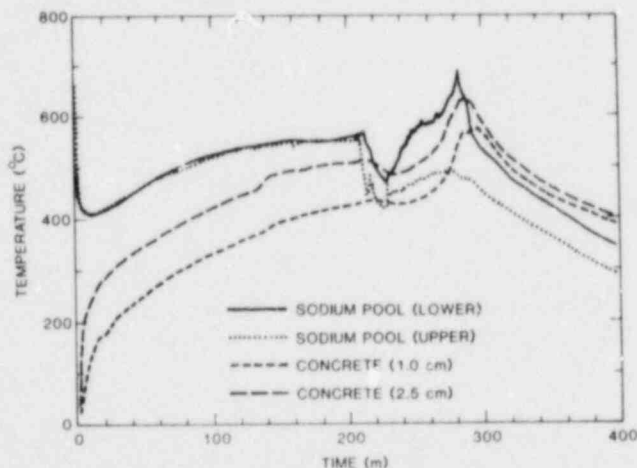


Figure 3.5-8 Sodium Pool and Concrete Temperatures During Physical Separate Effects Test 13 (The dimensions are measured from the original sodium/concrete interface.)

Table 3-XI Future Large Scale Sodium/Concrete Interactions Tests

Large-Scale Test

(Material)

17
(Basalt)

Test Description

Essentially a repeat of Test 16. Bare cavity. 600°C sodium drop temperature. 500°C pool set-point. "Dry" cavity. 27 cm sodium pool depth.

Purpose

To test chemical model hypothesis that sodium pool must saturate with NaOH before concrete attack can occur.

Comments

Both sodium pool depth and free water in surface layer of concrete are important factors. In test 11 with "dry" concrete, there was a 75-min delay before attack started. In test 16, with "Wet"¹ concrete and twice the sodium pool depth of test 11, attack began in a few minutes.

18
(Limestone)

One dimensionalized sodium attack on concrete cavity bottom. Similar to tests 10 and 13. Steel liner in cavity with "standard flaw" in bottom. No firebrick. 700°C sodium drop temp. - 600°C pool set-point. Deep pool. "Wet" concrete.

Because of sodium/water explosion at start of test 10, no data exists for effect of steel liner in limestone concrete.

Test 18 will ascertain if gas/evolution from Na-limestone is sufficient to fail exhaust system.

19
(Limestone)

Bare cavity, shallow sodium pool 13 cm. 700°C sodium drop temp. 550°C pool set-point. "Wet" concrete. Possible multiple sodium drops.

Examine requirements for initiation and sustainment of "phase II" exothermic reactions in limestone concrete-sodium interaction.

Additional sodium drops to look at NaOH saturation of sodium pool and to prevent experiment from becoming sodium limited. This capability may require facility modifications.

¹"Wet" concrete is defined as keeping the concrete of the crucible cavity at conditions of 100% relative humidity for at least 1 mo before crucible is prepared for testing.

Posttest examination showed a layer of reddish, cinder-like material about 3 cm thick. This material is being analyzed to determine its chemical composition and melting point. No metallic sodium remained in the test article.

3.5.6 Sodium Flow Rate Experiment

At the request of NRC, an experiment has been designed to measure the flow rate of molten sodium through a series of cracks in a steel plate. The goal is to obtain quantitative information for use in analyzing a reactor accident in which sodium contacts concrete through a defective or failed steel cell liner.

The apparatus consists of a thin-walled steel bucket with a 9.5-mm-thick bottom plate and a capacity of 5 kg of molten sodium. Five buckets have been fabricated with slots 50 mm long and from 0.23 mm to 2.36 mm wide; these slots simulate cracks or flaws. To weigh the bucket during the experiment, it is attached to a beam with a spring, oscillation damper and position sensor. The complete assembly is placed under the sodium heating/dump tank of the physical separate effects test facility. Provisions are being made to inert the atmosphere, preheat the bucket, and measure appropriate temperatures.

During this period, the apparatus was calibrated by using water at room temperature as the flowing liquid. Typical data are shown in Figure 3.5-9, a plot of the position sensor output as a function of time. Calibration curves are used to convert the data to liquid volume vs time. The slope of the volume vs time curve yields the flow rate as a function of driving head.

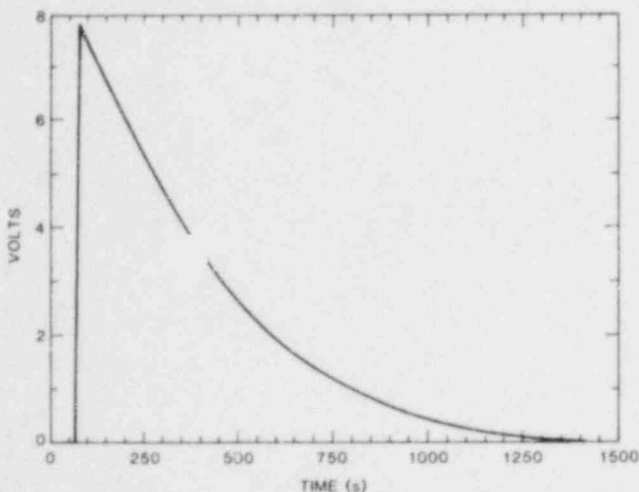


Figure 3.5-9 Flow Rate Data for a 0.23-mm Wide Slot. (Fluid is water at 20°C.)

These results with water have been compared to analytical predictions based on solutions of the Bernoulli equation (the simplest model for fluid flow which neglects such things as viscosity, two-dimensional effects, and vortex effects). Figure 3.5-10 shows the analytical results with experimental data superimposed. The experimental and analytical results agree qualitatively. The actual magnitudes differ by up to 30%. This difference is attributed to the neglected effects in the model. More complex analytical models will be developed when the results with liquid sodium are available.

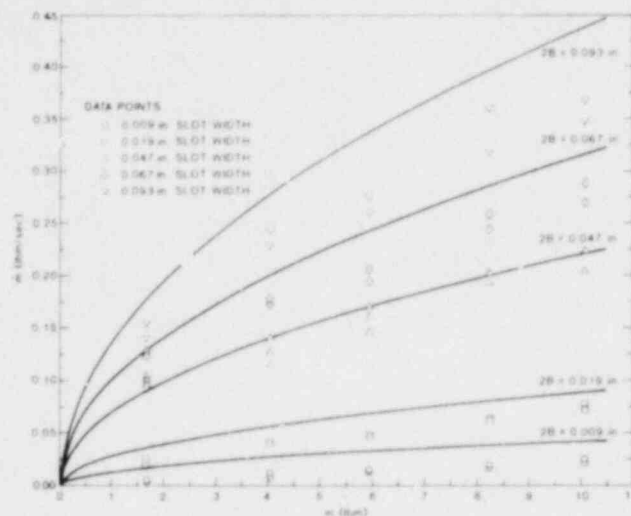


Figure 3.5-10 Mass Flow Rate (m) vs Mass of Water in Reservoir (m). ($W = 2$ in.; $D = 8$ in.) Solid lines represent theoretical calculations assuming quasi-steady, irrotational (inviscid) flow.

3.5.7 Chemical Separate Effects Tests

Investigators have initiated a study of the NaOH ternary system at 973 to 1273 K (700° to 1000°C) to determine the phase boundaries and the thermodynamic properties. No data exist at these temperatures, and such data could help resolve the various, sometimes divergent, results obtained in Na/concrete experiments at different laboratories.

The first experiments concern the hydrogen pressure developed above various Na/NaOH mixtures. The experimental technique is to seal various masses of Na and NaOH within evacuated nickel containers which are then suspended from a microbalance and heated to the desired temperature in a hydrogen atmosphere. A hydrogen pressure is developed within the nickel container as a result of chemical interaction between Na and NaOH. Diffusion of hydrogen through the nickel walls proceeds until the hydrogen pressure within the container is equal to that outside. The equilibrium composition is calculated from the

change in mass. Varying the hydrogen pressure permits a mapping of composition as a function of pressure and temperature. From this mapping, the various phase boundaries can be delineated while thermodynamic information is obtained from the variation of hydrogen pressure with temperature.

To date, data have been obtained at two compositions: at a Na/O ratio of 1.096 (973 K) and at a Na/O ratio of 1.483 (1073 K). These data are shown in Figure 3.5-11 in which the pressure is plotted against the atom fraction of hydrogen. The precision of the data is very good: pressure is ± 0.5 torr and composition is ± 0.0005 atom fraction of hydrogen. Approximately 16 hr are needed at 973 K in order to attain equilibrium and 12 hr at 1073 K.

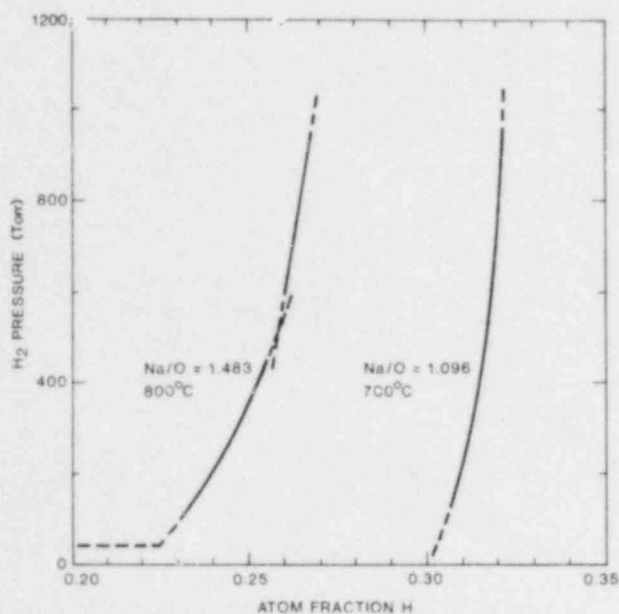


Figure 3.5-11 Data for Two Na/O Compositions

All these composition lie off the (Na + NaOH) pseudo binary composition; i.e., much greater pressures are required to maintain the initial compositions. The curve at Na/O = 1.096 is that expected for a single phase which, in this case, is a predominantly NaOH phase. The data for Na/O = 1.483 are best fitted by two curves. The present interpretation is that the upper curve pertains to the single-phase liquid NaOH while the lower curve pertains to a two-phase region—liquid NaOH and another, as yet unidentified, phase. Not observed in these data is a postulated three-phase region in which the hydrogen pressure is constant.

3.5.8 Sodium/Concrete Ablation Model

3.5.8.1 Introduction

In several recent sodium-concrete experiments performed at Sandia, an energetic chemical ablation

of the concrete has been observed. These experiments yielded several basic facts. First, a delay time occurred before the concrete erosion reaction was initiated. Second, once the reaction began, the rate of concrete penetration was constant until all of the Na was consumed. The delay time was associated with saturation of the pool with NaOH (solubility of about 20 mole %); upon reaching saturation, the NaOH precipitated out and covered the concrete. Temperatures as high as 1200 K were measured indicating that both the Na and water existed in the vapor phase.

A model is proposed to explain the mechanisms involved.

3.5.8.2 Model Description

Initially, saturation and subsequent precipitation of NaOH from the sodium pool is required in order to build up an insulating layer thick enough to promote the formation of Na vapor. Since the concrete is exposed to a very high temperature, it dehydrates leaving behind a porous structure that is easily permeated with vapors. The Na vapor from the pool flows downward into the porous concrete, whereas the water vapor from the saturated concrete flows upwards and meets the Na vapor at a location termed the reaction plane. Both NaOH vapor and H₂ gas are formed in the reaction. The NaOH vapor is rapidly cooled and condenses upon the surrounding porous concrete, producing an evenly distributed coating. The NaOH reacts with the silica in the concrete to produce sodium meta silicate and water vapor. The water vapor that is produced reacts with additional Na vapor producing more NaOH and H₂. The H₂ gas that is produced diffuses against the incoming Na vapor to the Na pool and eventually escapes with the Na vapor bubbles. Figures 3.5-12, -13 and -14 constitute a pictorial representation of the model.

3.5.8.3 Governing Equation

The equations used to describe the concrete ablation model are of four basic types:

- The species diffusion equations

$$D_{i,s} \frac{\partial^2 m_i}{\partial y^2} - v \frac{\partial m_i}{\partial y} = 0,$$

- The energy transport equation

$$K \frac{\partial^2 T}{\partial y^2} - \sum_i \rho_i v_i C_{p,i} \frac{\partial T}{\partial y} = 0,$$

- Enthalpy balance relations, relating the heat of reaction of the enthalpy flow rates.

- Chemical kinetics equations, relating the temperature and composition, to the rate of chemical reaction.

The coordinate system is located at the reaction plane and moves along with it as penetration occurs.

In this model, for the sake of convenience, thermo-physical properties will be held constant at some appropriate average value. The solutions will be separated into two regions representing either the porous dehydrated concrete (region 1) or the porous reaction product layer (region 2).

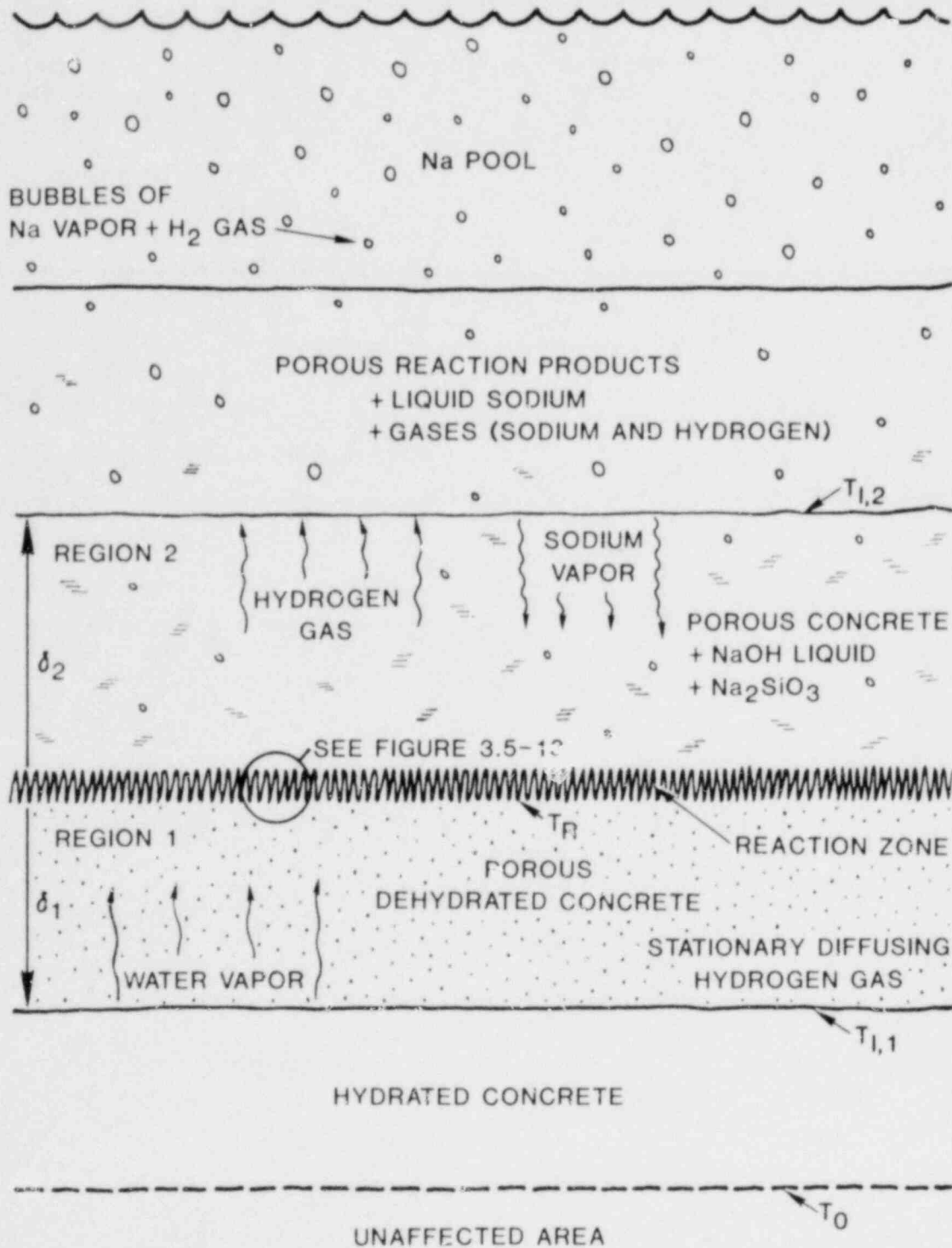


Figure 3.5-12 Sodium/Concrete Ablation Model

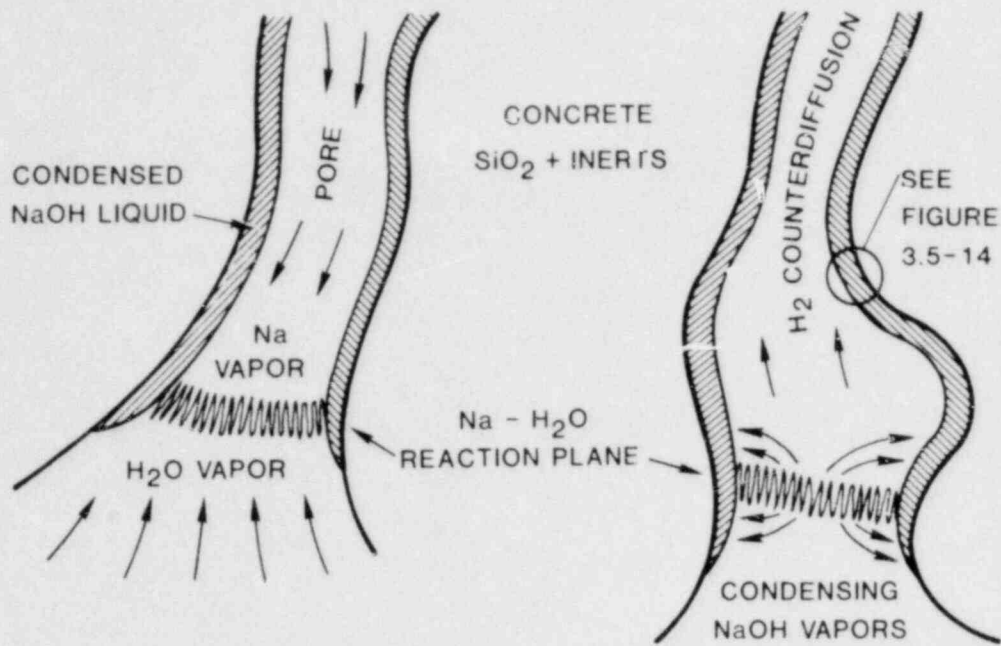


Figure 3.5-13 Closeup View of the Porous Dehydrated Concrete at the Reaction Zone

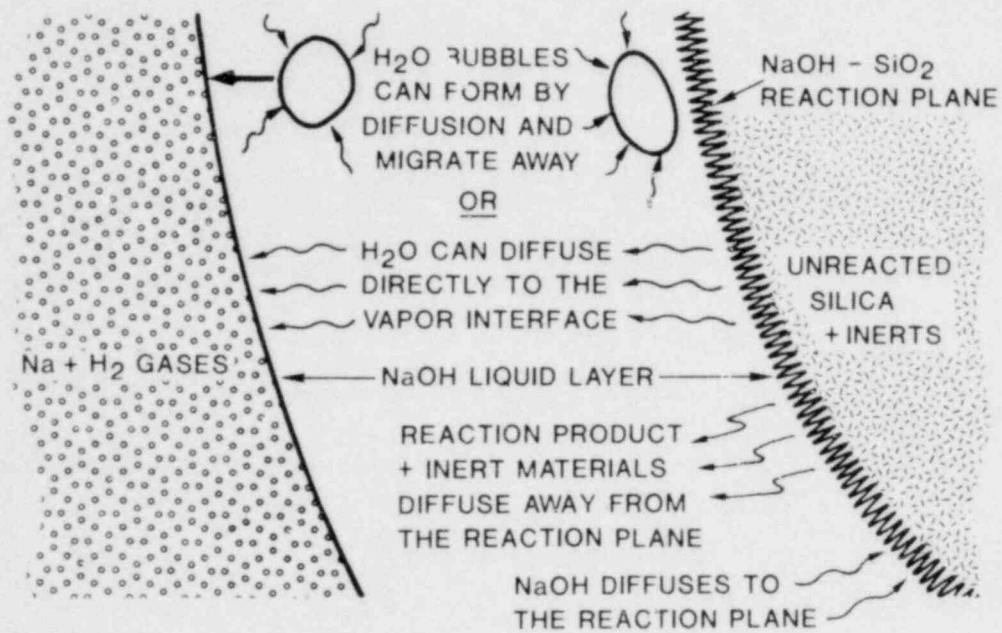


Figure 3.5-14 Closeup View of the Condensed NaOH Liquid Layer

For the species equations,

$$D_{i,g} \frac{\partial^2 m_i}{\partial y^2} - v \frac{\partial m_i}{\partial y} = 0, \quad (3.48)$$

where

- $D_{i,g}$ = porous mass diffusion coefficient of species i through the gas mixture g
- m_i = mass fraction of species i
- v = velocity of the bulk gas mixture
- y = distance from the reaction zone,

a solution may be obtained by integrating and applying the boundary conditions:

- @ $Y = 0$
- @ $Y = \delta_1$ or δ_2
- $m_i = m_{i,r}$
- $m_i = m_{i,e}$

The resulting solution is

$$m_i = \frac{m_{i,e} \left(1 - e^{\frac{vy}{D}}\right) - m_{i,r} \left(e^{\frac{v\delta}{D}} - e^{\frac{vy}{D}}\right)}{1 - e^{\frac{v\delta}{D}}}. \quad (3.49)$$

The energy equation is

$$K \frac{\partial^2 T}{\partial y^2} - \sum_i (\dot{m} C_p)_i \frac{\partial T}{\partial y} = 0 \quad (3.50)$$

where

- K = thermal conductivity of the substrate
- T = temperature
- \dot{m} = mass flow rate of a given species
- C_p = heat capacity at constant pressure of the flowing substance
- Σ = summation over all of the flowing substances
- i = either water vapor, sodium vapor, hydrogen gas, porous concrete or reaction products.

Equation (3.50) is subject to the following boundary conditions:

- @ $Y = 0$
- @ $Y = \delta_1$ or δ_2
- $T = T_r$ = the reaction temperature
- $T = T_{\ell,1,2}$ = the liquid temperature either water-region 1 or sodium-region 2.

The solution is

$$\bar{T} = \frac{T_\ell (1 - e^{(\Sigma \dot{m} C_p) y / K}) - T_r (e^{(\Sigma \dot{m} C_p) \delta / K} - e^{(\Sigma \dot{m} C_p) y / K})}{1 - e^{(\Sigma \dot{m} C_p) \delta / K}}. \quad (3.51)$$

At the boundaries, the conductive heat flux is equal to the evaporative enthalpy flux. Heat transfer from the liquid line into the concrete or sodium pool is ignored for simplicity. Thus at δ

$$\dot{m} L = -K \frac{\partial T}{\partial y} \Big|_{y=\delta} \quad (3.52)$$

where

- \dot{m} = water or sodium evaporative mass flux
- L = latent heat of evaporation of water or sodium.

Differentiating Eq 3.51 and substituting gives:

$$\dot{m} L = \frac{\sum_i \dot{m} C_p (T_\ell - T_r)}{e^{(\Sigma \dot{m} C_p) \delta / K} - 1} \quad (3.53)$$

This expression can be inverted to yield a boundary layer thickness δ

$$\delta = \frac{-K}{\sum_i \dot{m} C_p} \frac{\ln \left(1 + \frac{\sum_i \dot{m} C_p (T_\ell - T_r)}{\dot{m} L}\right)}{\sum_i \dot{m} C_p} \quad (3.54)$$

A similar expression can be obtained from the species equation. An expression for the total mass flux of any vapor species \dot{m}_i can be obtained by integrating the mass diffusion Eq 3.48. This expression is

$$\dot{m}_i = m_{i,\ell} \sum_i \dot{m}_i - \rho D \frac{\partial m_i}{\partial y} \Big|_{y=\delta}. \quad (3.55)$$

Differentiating Eq 3.49, substituting into Eq (3.55) and rearranging terms gives

$$\delta = \frac{-\rho D_{i,g}}{\sum_i \dot{m}_i} \ln \left(1 + \frac{m_{i,\ell} - m_{i,r}}{\dot{m}_i \sum_i \dot{m}_i - m_{i,r} \ell}\right) \quad (3.56)$$

where

- $m_{i,\ell}$ = mass fraction of species i at the boundary
- ρ = macroscopic gas density

The mass fraction of the evaporating liquid at the boundary ($m_{1,e}$) can be related to the temperature of the boundary (T_e) through a simple saturation expression. A more accurate expression, in the case of water, would include the decomposition of concrete; however, this would add considerable complexity without a significant increase in overall accuracy. Thus, the mass fraction of the evaporating liquids at the boundaries is

$$m_{1,e} = \frac{P_1 W_1}{P_1 W_1 + (P - P_1) W_2} \quad (3.57)$$

where

$W_1 = 18$ (molecular weight of water), or 23 (molecular weight of sodium)

$W_2 = 2$ (molecular weight of hydrogen)

$P_1 =$ partial pressure of water or sodium vapor

$P =$ total pressure at the boundary.

The partial pressure of a vapor is given by a saturation pressure formula

$$P_1 = P^* e^{-T^*/T} \quad (3.58)$$

where P^* , T^* are curve fitting constants for the saturated liquid.

3.5.8.3.1 Region 1

To solve the set of equations for region 1, the term $\sum \dot{m} C_p$ needs to be evaluated. Since the concrete ablation occurs as a steady-flow process, the mass flux above and below the water line (δ_1) must be equal and related simply by the composition of concrete. This, of course, assumes that the migration of water below the water line is negligible in comparison to the penetration rate. Thus, in region 1,

$$\sum_i \dot{m} C_p = \dot{m}_w C_{p_w} + \dot{m}_c C_{p_c} + \dot{m}_H C_{p_H}$$

where

w = water

c = concrete

H = hydrogen.

The hydrogen gas is noncondensable and cannot penetrate the water line to any significant extent. Thus $\dot{m}_H = 0$. The concrete-mass flux is related to the water-mass flux by the composition of concrete,

$$\dot{m}_c = \dot{m}_w \frac{\rho_c}{\rho_w}$$

where

$\rho_c =$ concrete density 2200 kg/m³.

$\rho_w =$ water density in concrete 170 kg/m³.

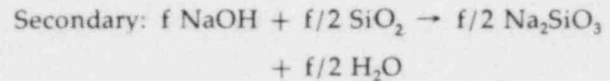
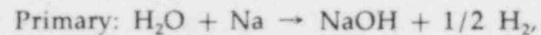
Combining the two foregoing expressions,

$$\sum_i \dot{m} C_p = \dot{m}_w \left(C_{p_w} + \frac{\rho_c}{\rho_w} C_{p_c} \right) \quad (3.59)$$

Equations 3.54, 3.56, 3.57, 3.58, and 3.59 can be solved simultaneously for the unknowns δ_1 and T_1 for given values of \dot{m}_w and T_e .

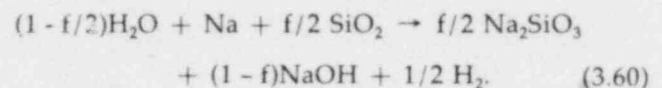
3.5.8.3.2 Region 2

The sodium-vapor flux \dot{m}_{Na} is related to the water-mass flux \dot{m}_w (in region 1) through the stoichiometry of the reaction. The reaction stoichiometry is complicated by the problem that the secondary reaction ($\text{NaOH} + \text{SiO}_2$) is not complete, as is evidenced by the presence of NaOH in the final reaction product mix. A fraction, f (from zero to one), can be introduced to vary the degree of secondary reaction. Thus, the chemical reactions that occur are:



and

summing to obtain the net reaction



From the chemical balance Eq (3.60) and the molecular weights, the mass fluxes of sodium (\dot{m}_{Na}) and hydrogen (\dot{m}_H) can be related to the mass flux of water in region 1 as follows:

$$\dot{m}_{Na} = \frac{-23}{18(1-f/2)} \dot{m}_w$$

and

$$\dot{m}_H = \frac{\dot{m}_w}{18(1-f/2)}$$

Thus, the net mass flux of vapor in region 2 is

$$\dot{m}_g = \dot{m}_{Na} + \dot{m}_H = \frac{-22\dot{m}_w}{18(1-f/2)} \quad (3.61)$$

The minus sign indicates that the direction of the bulk vapor flow is downward to the reaction zone.

The solution for the temperature distribution in region 2 is the same as that in region 1; i.e., Eq (3.51). The differences are that T_ℓ is the temperature of the sodium pool and $\Sigma \dot{m}C_p$ includes the upward concrete and downward gas mass fluxes. In terms of the mass flux of water vapor, the term $\Sigma \dot{m}C_p$ can be evaluated by using Eqs (3.59) and (3.61). Thus

$$\sum \dot{m}C_p = \dot{m}_w \left(\frac{\rho_s C_{p_s}}{\rho_w} - \frac{22C_{p_g}}{18(f/2-1)} \right) \quad (3.62)$$

The heat flux at the upper boundary of region 2 (δ_2) is equal to the enthalpy flow of all the vaporized sodium; i.e.,

$$\dot{m}_{NaT} L_{Na} = -K \frac{\partial T}{\partial y} \Big|_{y=\delta_2} \quad (3.63)$$

The term " $\dot{m}_{NaT} L_{Na}$ " is the total rate of sodium vapor production (or liquid consumption). It includes the sodium vapor that flows upward, out of the pool as bubbles, as well as that which flows downward into the reaction zone.

To solve the set of equations for region 2, the rate of sodium vapor that leaves the pool is required to apply the upper boundary condition, Eq (3.63). This term can be evaluated from an overall enthalpy balance.

3.5.8.4 The Enthalpy Balance Equations

The first law equation for a control volume (cv) with chemical reaction is

$$\begin{aligned} Q_{cv} + \sum_R n_i (h_i + (h-h_{298}))_i \\ = \sum_P n_e (h_e + (h-h_{298}))_e \end{aligned} \quad (3.64)$$

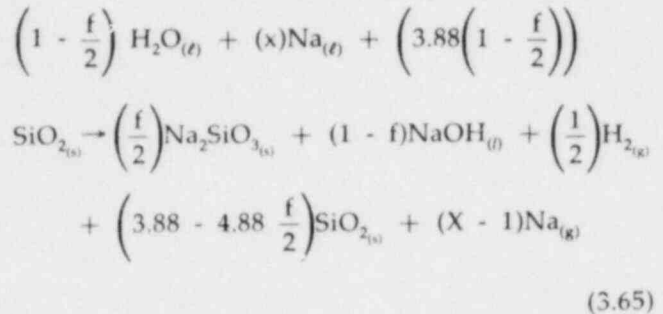
where

- Q_{cv} = net heat transfer to the control volume
- n_i = number of moles of reactant i
- n_e = number of moles of product e
- h_i = heat of formation
- h = enthalpy of material i or e as it crosses the control volume boundary
- h_{298} = enthalpy of material i or e at the reference temperature 298 K.

Selecting a control volume beyond the boundaries δ_1 and δ_2 eliminates Q_{cv} because the temperature gradients are effectively zero. To apply Eq (3.64), the number of moles of reactant and product are required. These numbers are obtained from a general chemical reaction equation that includes all of the

materials that enter and leave the control volume (including inert materials).

The general equation is obtained from Eq (3.60) by adding the inert materials to both sides. The result is



where x is the unknown number of moles of sodium liquid that enters the control volume and subscripts (s), (l), (g) refer to solid, liquid and gas, respectively. The number 3.88 appears because there are about 3.88 moles of SiO_2 per mole of water in hydrated concrete. [Concrete, as modeled here, consists of water (170 kg/m³) and Silica (2200 kg/m³). If water migration is to be considered in the calculations, then the molar ratio of SiO_2/H_2O would have to be modified accordingly.

The change in enthalpy of a material can be approximated by $(h - h_{298}) = C_p(T_\ell - 298)$. Thus for a given value of f , the coefficients from Eq (3.65) can be substituted into Eq (3.66) and the unknown coefficient x can be solved for algebraically. With x known, all of the mass flow rates (in regions 1 and 2) can be solved for as a function of the mass flux of water; thus,

$$\dot{m}_i = \frac{\dot{m}_w n_i w_i}{\left(1 - \frac{f}{2}\right)(18)} \quad (3.66)$$

The mass flow rates \dot{m}_i are required to evaluate the $\Sigma \dot{m}C_p$ terms in Eqs (3.54) and (3.63).

3.5.8.5 Numerical Evaluation

The set of equations described above can be solved simultaneously in an iterative fashion for the unknowns

$$T_{11}, T_{12}, \delta_1, \delta_2, \dot{m}_1,$$

and if desired $T(Z)$ and $M_i(Z)$. The unknowns must be solved for as a function of \dot{m}_w (equivalent to penetration rate), T_R and f . In generating solutions to these equations, "windows" were discovered. That is, only for certain values of \dot{m}_w , T_R , and f are solutions possible.

During the numerical evaluation, several other parameters which were mentioned but not formally included were found to significantly influence the size of the solution windows. The significant parameters are: the liquid water migration rate, the dehydrated concrete and reaction product permeability (these parameters affect the pressure distribution), heat transfer from the lower boundary (water line) to the room temperature concrete, and thermophysical property variations. The solution space is very difficult to represent graphically because there are so many parameters. Selecting the experimentally determined penetration rate and an approximate reaction temperature of 1350 K results in the values shown in Table 3-XII.

Table 3-XII Selected Values for the Solution Space*

$f =$	<0.7	0.8	0.8	1.0
$\delta_1(\text{cm})$	No solution	6.3	6.3	6.3
$\delta_2(\text{cm})$	No solution	2.6	2.1	1.7
$T_{11}(\text{K})$	No solution	392	393	394
$T_{12}(\text{K})$	No solution	1057	1046	1037

* (given $\dot{m}_w = 1.4 \times 10^{-3} \text{ kg/m}^2/\text{s}$, and $T_r = 1350 \text{ K}$)

The exact functional form of f is unknown at present and most likely must be derived from a combination of experimental and analytical methods. However, intuition indicates that f will be large at high T_r and low \dot{m} and small at low T_r and high \dot{m} . At high T_r , both the rate of chemical reaction and diffusion of reactants is enhanced. At low \dot{m} , the time for reaction completion is increased. The opposite effects occur at low T_r and high \dot{m} .

If T_r is increased from its value in Table 3-XII by about 150 K, the driving pressure for sodium flow is insufficient to sustain the reaction. If T_r is decreased from 1350 K, the value of f may drop below 0.7, where solutions are not possible because of insufficient chemical energy.

If T_r is held constant and \dot{m} is increased from its value in Table 3-XII, the parameter f may decrease (due to insufficient time in the reaction zone) to a value less than 0.7 where solutions are not possible. If \dot{m} is decreased from its value in Table 3-XII there is no apparent reason why these solutions are not possible. It may be that the maximum \dot{m} solutions are selected by nature simply because they are reached first in a transient sense. The small \dot{m} solutions have very thick boundary layers and may not even be achievable in the finite size experimental apparatus.

3.5.8.6 Summary and Conclusions

A solution to the equations that describe the ablation of concrete in terms of flowing vapors has been presented. The numbers generated appear to be reasonable when compared with experimental parameters. Solution windows were discovered to exist and are a strong function of the parameters of the problem. The size, shape, and location of the solution windows can be determined better if the fraction f can be quantitatively defined as a function of \dot{m} and T_r . In addition, other experimental parameters such as the permeability of concrete and the reaction products must be defined more accurately before defensible solutions can be generated.

3.5.9 USINT--A Computer Code for Predicting the Thermal Decomposition of Concrete

A computer code has been developed* to predict the thermal decomposition of concretes commonly used for reactor containment. The code models the heat and mass transfer events inside porous concrete when the concrete is exposed to a high temperature environment. It calculates temperature and pressure profiles as a function of time and water release rates at the concrete boundaries.

The USINT code solves the partial differential equations of conservation of energy and mass. The energy equation contains terms that represent conduction in the solid matrix, convection within the pores, energy source terms caused by thermal decomposition of the concrete, and energy storage within the solid matrix and fluid filled pores. Two conservation-of-mass relations are solved: one for water and one for CO_2 . The presence of liquid water is characterized by the term "wet region" while the term "dry region" refers to the existence of water in the vapor form only. For example, the region of concrete near a heated boundary would likely be a "dry region" because of temperatures sufficiently high to vaporize all of the water while the region far removed from the heated boundary would likely be a "wet region" because of the presence of liquid water. The mass conservation relations are different for the wet and dry regions.

The USINT code is limited to one-dimensional geometries; however, it will handle planar, cylindrical, or spherical geometries. The partial differential equations are solved by using the implicit Crank-Nicolson finite difference procedure.

* This code was developed by J. V. Beck and R. H. Knight, former Sandia employees.

A number of subsidiary equations are necessary to mathematically close the USINT model. For example, Darcy's law is used to relate the mean flow velocity to the local pressure gradient. The constant of proportionality is the permeability, which can be empirically related to the porosity if laminar flow through capillary tubes is assumed.

In the wet region, the water liquid and water vapor are assumed to be in equilibrium. The pressure-temperature relationship for a saturated water mixture in a porous medium must be modified to account for surface tension effects; for a given temperature, surface tension increases the vapor pressure. Using the mathematical form of the equation suggested by the Clausius-Clapeyron equation, experimental pressure-temperature data from HEDL⁽³⁻³⁷⁾ was curve-fit to determine constants in the equation.

Thermogravimetric analysis (TGA) experiments by Powers⁽³⁻³⁸⁾ indicate that concrete mass loss is primarily associated with three events:

- Loss of evaporable water, 343 to 523 K (70° to 250°C),
- Loss of chemically constituted water, 623 to 823 K (350° to 550°C),
- Loss of carbon dioxide, 853 to 1323 K (580° to 1050°C).

The rate at which mass is lost through any of the above three events depends not only on temperature but also time at temperature. Physical events of this type are often modeled by an Arrhenius type equation. For each of the above mass-loss events, an activation energy and a rate constant for the Arrhenius expression were determined from the TGA data. Each of the three Arrhenius expressions appears in the energy equation and individually in the appropriate mass conservation equation.

The USINT code has been used to predict the test results of HEDL Test 1.⁽³⁻³⁷⁾ In this test, a magnetite concrete cylinder, 1 ft thick x 2 ft diameter, was heated on one end by placing it in contact with a steel brick at 922 K (1200°F). Figure 3.5-15 compares the USINT temperature prediction with a thermocouple located at 0.0351 m below the heated surface. The temperature agreement is quite good. Figure 3.5-16 compares the USINT pressure predictions with experimental pressure data at a depth of 0.0351 m below the heated surface. The pressure agreement is not as good as the temperature agreement. The computed and integrated water release is compared in Figure 3.5-17; the agreement is quite good.

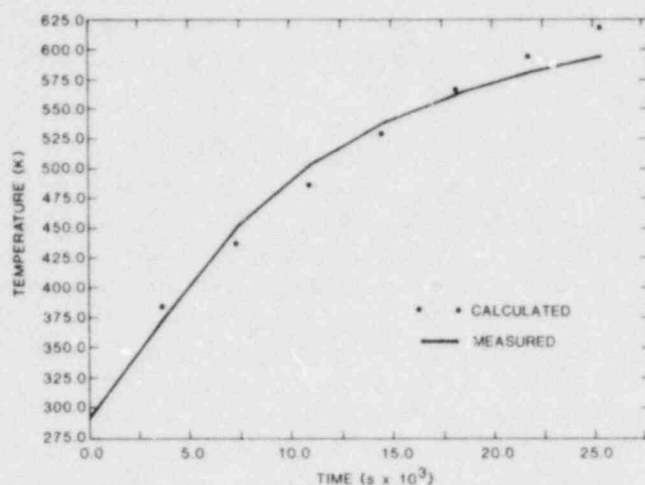


Figure 3.5-15 Calculated and Measured Temperatures at $x = 0.0351$ m for HEDL Test 1 Data

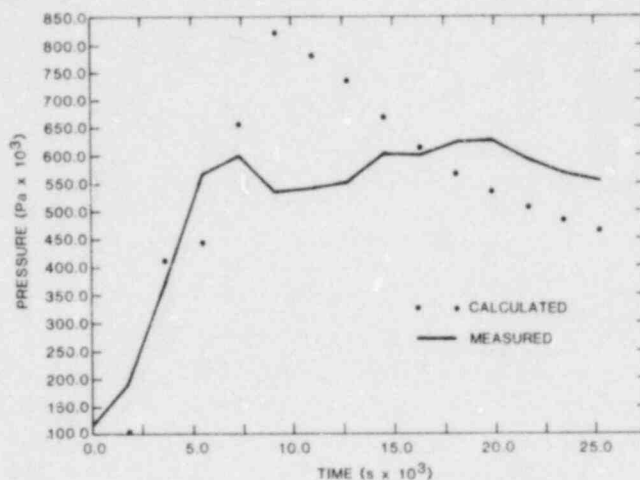


Figure 3.5-16 Plot of Calculated and Measured Pressures at $x = 0.0351$ m for HEDL Test 1 Data

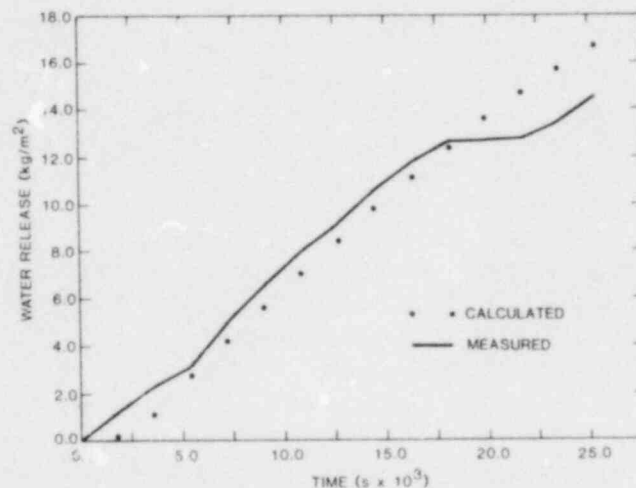


Figure 3.5-17 Plot of Calculated and Measured Value of Integrated Water Release for HEDL Test 1 Data

In general, accurate pressure predictions are more difficult than temperature predictions. This is because the magnitude of the energy events associated with the thermal decomposition are small in comparison to the other events in the energy equation. In fact, reasonably good temperature agreement can be achieved by ignoring the thermal decomposition events. In the mass conservation equations however, the thermal decomposition events are much larger percentage wise. Since pressure is one of the unknowns in the mass conservation equation, it seems reasonable to expect poorer pressure than temperature predictions.

The USINT code is presently being used to perform a sensitivity study to determine how the dependent variables such as temperature, pressure, and water release change with changes in the various input parameters such as thermal conductivity, porosity, permeability, etc. This study will identify those input parameters that have the greatest influence on the computed results. If those parameters with the greatest sensitivity contain large experimental uncertainties, experiments will be designed to measure those parameters more accurately. To date, over 100 runs have been made with the USINT code. Preliminary results indicate that temperature is most sensitive to thermal conductivity while pressure is most sensitive to the activation energy of the evaporable water. This study is being performed by Dr. J. V. Beck of Michigan State University under contract to Sandia.

Some weak points in the code have been identified. The effect of pore size on the water vapor equation of state is not known. The present finite difference procedure requires that the wet-dry interface coincide with a grid point; consequently, when the interface moves from one grid point to the next, a perturbation is introduced into the pressure calculation. The experimental permeability data for magnetite concrete reported by HEDL⁽³⁻³⁷⁾ varies by six orders of magnitude over the temperature range of interest; any parameter that varies this widely should be suspect. The mass decomposition kinetic data was derived from TGA experiments on powder samples; it is not known if this is a valid representation of concrete behavior. The operation of the code at high temperatures where CO₂ production may be important has not been fully checked out. These problem areas will be addressed in the future along with the comparison of the code with additional pressure and temperature data from Muhlestein.⁽³⁻³⁹⁾

Additional details of the USINT code can be found in Beck and Knight.⁽³⁻⁴⁰⁾

References for Section 3

- 3-1 Y. Bottinga and D. F. Weill, "The Viscosity of Magmatic Silicate Liquid: A Model for Calculation," *Am. J. of Sci.*, 272:438, 1972.
- 3-2 D. A. Powers and A. W. Frazier, *VISRHO: A Computer Subroutine for Estimating the Viscosity and Density of Complex Silicate Melts*, SAND76-0649 (Albuquerque, NM: Sandia Laboratories, June, 1977).
- 3-3 Kunitz, *J. Gen. Phys.*, 9:715, 1926.
- 3-4 Ting and Leubbers, *Am. Inst. Chem. Eng. J.*, 3:111, 1957.
- 3-5 W. T. Pratt and R. D. Gasser, BNL-NUREG 27037 (Upton, NY: Brookhaven National Laboratory, December, 1979).
- 3-6 *ENP Core Ladle Design and Safety Evaluation*, Offshore Power System Topical Report No. 36A59, April, 1979.
- 3-7 M. Kampf and G. Karsten, "Effects of Different Types of Void Volumes on the Radial Temperature Distribution of Fuel Pins," *Nucl. Appl. and Tech.*, 1, September 1970.
- 3-8 G. F. Stevens, Personal Communication, April 24, 1980.
- 3-9 H. C. Hardee and R. H. Nilson, *Nucl. Sci. and Eng.*, 63, 119-132, 1977.
- 3-10 V. K. Dhir and I. Catton, *Study of Dryout Heat Fluxes in Beds on Inductively Heated Particles*, NUREG-0252 (Los Angeles: USNRC, June 1977).
- 3-11 R. W. Ostensen Memo to J. B. Rivard (Albuquerque, NM: Sandia Laboratories, February 12, 1979).
- 3-12 As reported in R. B. Bird, W. E. Steward, and E. N. Lightfoot, *Transport Phenomena* (New York: John Wiley and Sons, 1960), pp 196-200.
- 3-13 As reported in A. E. Scheidegger, *The Physics of Flow through Porous Media* (Toronto: U. of Toronto Press, 1974), pp 52, 248.
- 3-14 *Advanced Reactor Safety Research Quarterly Report, October-December 1979* (Albuquerque, NM: Sandia National Laboratories June 1980).
- 3-15 R. J. Lipinski and J. B. Rivard, *Proc. of Fast React. Safety Mtg.*, Seattle, WA, August 19-23, 1979, pp 757-769.
- 3-16 R. S. Keowin, *Dryout of a Fluidized Particle Bed with Internal Heat Generation*, MS Thesis (Los Angeles: UCLA, 1974).
- 3-17 E. S. Sowa, J. D. Gabor, L. Baker, Jr., J. R. Pavlik, J. C. Cassulo, and W. Holloway, *Proc. of Intl Mtg. on Fast Reactor Safety and Related Physics*, CONF-761001, pp 2036-2044.
- 3-18 J. D. Gabor, E. S. Sowa, L. Baker, Jr., and J. C. Cassulo, *Proc. of ANS Fast Reactor Safety Mtg.*, Beverly Hills, CA, April 1974, CONF-740401, pp 823-844.
- 3-19 I. B. Rivard, *Nucl. Tech.*, 46 1979.
- 3-20 J. E. Gronager, to be presented at ANS Annual Meeting, Las Vegas (1980).
- 3-21 L. Barleon, J. Marek, and H. Werle, *Untersuchung zur Kuhlung von Partikelbetten*, IRB-324/79, INR: 994 (Karlsruhe, West Germany: KfK, December 1979).
- 3-22 C. O. LeRigoleur, *Particle Bed Dryout in Sodium* (paper presented at the Post Accident Heat Removal Exchange Meeting, Varesa, Italy, October 10-12, 1978).
- 3-23 V. K. Dhir and I. Catton, *Nucl. Tech.*, 46, pp 356-361, December 1979.
- 3-24 D. A. deVries, Mededel. Landbouwhogeschool Wageningen/Nederland, 52, 1 (1952).
- 3-25 R. O. Wooten and H. I. Aci, *A User's Manual for MARCH (Draft)*, (Columbus, OH: Battelle Memorial Institute, 1979).
- 3-26 T. E. Murley, Ltr. to H. E. Roser, DOE Albuquerque Operations Office, authorizing Zion/Indian Point Study Support (Research Order 60-80-072).

- 3-27 C. N. Kelber, "Zion-Indian Point Review Objectives," presentation made at Sandia National Laboratories, Albuquerque, NM.
- 3-28 *Reactor Safety Study, An Assessment of Accident Risks in U.S. Commercial Power Plants*, WASH-1400, NUREG-75/014 (Washington, DC: Nuclear Regulatory Commission, October 1975).
- 3-29 R. S. Demming, et al, "Methods for the Analysis of Hypothetical Reactor Meltdown Accidents," *Proceedings, Topical Meeting on Thermal Reactor Safety, July-August 1977*, Sun Valley, ID, CONF-770708, pp 3-372.
- 3-30 D. W. Varela in *Advanced Reactor Safety Research Quarterly Report, July-September 1979*, SAND79-2158, NUREG/CR-1141 (Albuquerque, NM: Sandia National Laboratories, April 1980).
- 3-31 D. W. Varela in *Advanced Reactor Safety Research Quarterly Report, October-December 1979* SAND80-1072, NUREG/CR-1572 (Albuquerque, NM: Sandia National Laboratories, October 1980).
- 3-32 K. D. Lathrop and F. W. Brinkley, *Theory and Use of the General-Geometry TWOTRAN Program*, LA-4432 (Los Alamos, NM: Los Alamos Scientific Laboratory, May 1970).
- 3-33 T. F. Petersen, *TAC2D - A General Purpose Two-Dimensional Heat Transfer Computer Code--User's Manual*, GA-8868 (San Diego, CA: Gulf General Atomics, 1969).
- 3-34 R. J. Lipinski in *Advanced Reactor Safety Research Quarterly Report, July-September 1978*, SAND78-2002, NUREG/CR-0470 (Albuquerque, NM: Sandia Laboratories, September 1979).
- 3-35 W. A. Lambertson and M. H. Mueller, *J Am. Ceram Soc*, 36, 10, 332, 1953.
- 3-36 Private Communication with Roy Peak, Hanford Engineering Development Lab, Richland, WA.
- 3-37 A. K. Postma, J. D. McCormack, and J. A. Schur, *A Study of Water and Gas Release from Heated Concrete HEDL TC-996* (Hanford, WA: Hanford Engineering Development Laboratory, December 1977).
- 3-38 D. A. Powers, D. A. Dahlgren, J. F. Muir and W. D. Murfin, *Exploratory Study of Molten Core Material Concrete Interactions, July 1975-March 1977*, SAND77-2042 (Albuquerque, NM: Sandia Laboratories, February 1978).
- 3-39 L. Muhlestein, Private Communication, Hanford Engineering Development Laboratory, February 1980.
- 3-40 J. V. Beck and R. L. Knight, *User's Manual for USINT-A Program for Calculating Heat and Mass Transfer in Concrete Subjected to High Heat Fluxes* SAND79-1694 (Albuquerque, NM: Sandia National Laboratories, May 1980).

4. Aerosol Source Normalization

(R. M. Elrick, 4422)

4.1 Introduction

During an energetic hypothetical core disruptive accident, fuel debris may be produced as vapor or formed as small, particulate debris (molten or solid) which can be transported to the upper vessel regions and through breaks which may have occurred in the vessel. The possibility of transporting this material depends strongly on its initial character.

Aerosol produced from in-pile (ACRR) experiments is being characterized to determine the physical properties of fuel particles resulting from the vaporization and melt breakup of fuel pins subjected to simulated overpower excursions.

Oak Ridge National Laboratory (ORNL) and Sandia National Laboratories have been involved in a collaborative effort to compare the characteristics of debris from UO_2 fuel resistively heated to vapor (at ORNL) and those debris characteristics from fuel heated neutronically (at Sandia). In a recent series of experiments at ORNL, fuel debris was sampled and fuel temperatures measured by methods that had previously been demonstrated with the Annular Core Pulsed Reactor (ACPR) at Sandia.

Previous quarterlies have described the temperature response of an exposed fuel pellet in a stack of fuel pellets when the stack was resistively heated to vapor. Calibrated photographic film was used to measure the temperatures of the fuel surface and of the bottom of a hole drilled to the centerline of the pellet. These centerline and surface temperatures were described for the high preheat and capacitance discharge heating phases. Several tests established the accuracy of the temperature measurements. The thermal condition of the fuel was estimated since sampled fuel debris will be characterized in terms of the temperature state of the fuel.

4.2 Aerosol Source Term During Sodium Concrete Interactions

Initial results have been obtained from a wide spectrum particle-size sampler designed specifically for the sodium containment tests 15 and 16. These results are reported here together with some suggestions for an improved sampler based in part on these results.

4.2.1 General

In test 15 a faulted mild steel liner was used to expose magnetite concrete and firebrick to sodium at

823 K (550°C). This exposure allowed investigators to study vertical wall attack by sodium. Test 16 studied the dependence of reaction time on cavity depth for sodium at 823 K on bare basalt concrete.

To characterize the aerosols, the following specifications were established: (1) chemical composition; (2) aerodynamic behavior: size, shape, effective density, or equivalents; (3) particle size concentration in the reaction chamber; and (4) rate of production, all as functions of time into the reaction. Although the present sampler design does not satisfy all these requirements, it was adequate for studying the scope of the problem.

4.2.2 Sampler Design

To characterize the aerosol source associated with this high temperature environment, the simple, rugged, close-in sampler shown in Figures 4.2-1 and 4.2-2 was designed. As Figure 4.2-1 shows, the sampler was located about 1 m from the reaction vessel, mounted in a straight piece of 5-cm-diameter pipe fastened to the top hat. By opening a ball valve in the pipe, aerosols and gases flowed through the sampler, driven by overpressure in the hat; the other end of the sampler was open to the atmosphere. Flow rate in the sampler was monitored by measuring the pressure drop across the sampler with an inclined oil manometer. Laboratory measurements will relate pressure drop to volume flow rate through the sampler although some flow estimates were calculated from the measured pressure drop and channel geometry.

The sampler itself (Figure 4.2-2) consisted of four long (30 cm), straight flow channels with narrow dimensions of 0.63 cm for two of the channels and 0.16 cm for the other two. The channels were positioned as shown in the figure with the wide dimension extending horizontally. Channel surfaces were made of glass plates for the top two channels and of thin OFHC copper sheets for the lower two channels. The glass plates, or coupons from the copper sheets, could be removed for examining collected particles in optical or electron microscopes. One half of all the collection surfaces were coated with silicone grease for holding particles larger than several hundred micrometres.

4.2.3 Particle Forces

Particles were moved to collection surfaces by three separate forces; gravitational, thermophoretic,

^{*}Radiometric forces are those exerted by a gas on nonuniformly heated objects. In this case, a temperature gradient in the gas causes nonuniform particle heating (thermophoresis).

and thermal diffusive. The relative magnitude of these forces is compared in Figure 4.2-3 where the particle velocity resulting from each force was calculated as a function of size.

The velocity shown for thermal diffusion is actually the average Brownian displacement, $\overline{\Delta X}_B$, of a particle during an interval of 1 s, given by

$$\overline{\Delta X}_B = \sqrt{\frac{4Dt}{\pi}}$$

where D is the diffusion coefficient of the particle and t is the time.

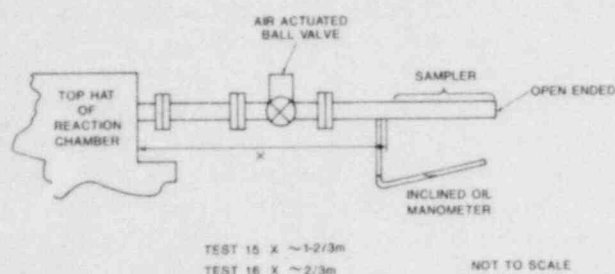


Figure 4.2-1 Schematic of Parallel Plate Sampler Experiment

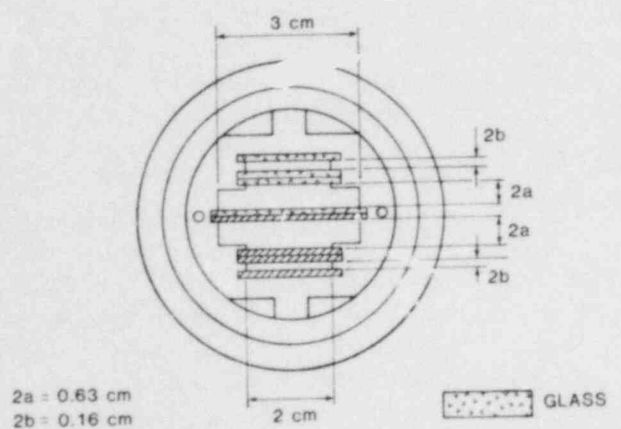


Figure 4.2-2 End View of Sampling Channels

Terminal free fall velocity, v_T , caused by the gravitational force, was calculated by equating the particle weight to the complete drag force, thus

$$v_T = \frac{2r^2g\rho \left(1 + A \frac{\ell}{r} + Q \frac{\ell}{r} e^{-br/\ell} \right)}{9\eta}$$

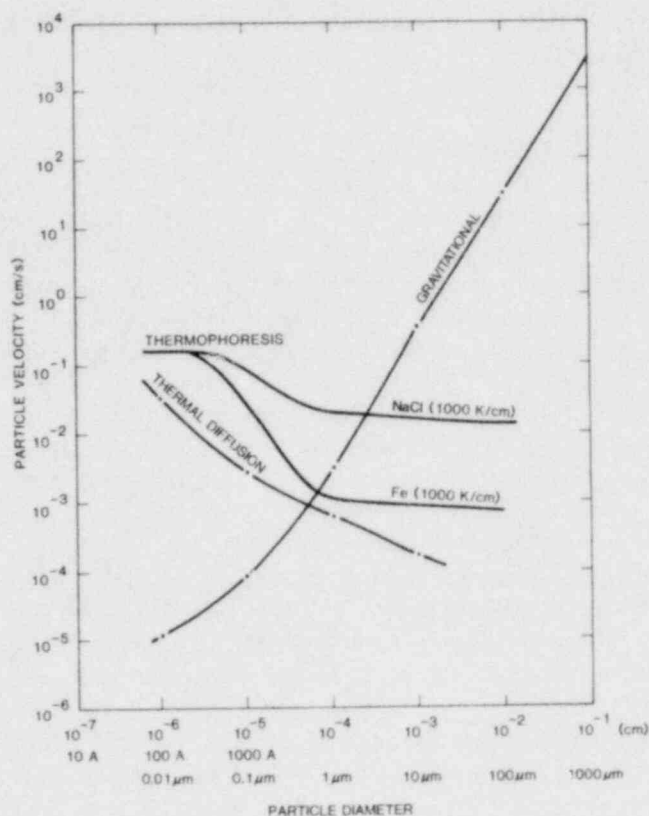


Figure 4.2-3 Comparison of Particle Velocities Arising From Sampling Forces. (1 Gm/cm³ density assumed for gravitational calculation.)

The terms A , Q , and b are constants, r and ρ are particle radius and particle density, η and ℓ are absolute gas viscosity and mean free path of gas molecules and g is the acceleration due to gravity.

An order of magnitude estimate of thermophoretic velocity, v , was obtained by calculating from theory the velocity for the two extremes in particle size: when the particle radius r is much smaller than the mean free path of gas molecules ($r \ll \ell$) and when $r \gg \ell$. These theoretical values were adjusted, based on experimental results, and a curve was smoothed between the values for these extremes in particle size. Figure 4.2-3 shows the resulting curve for iron, a good thermal conductor, and for NaCl with about 1/30 the conductivity of iron. Experimental data were available for particles of these two materials. The appropriate equations in centimetre-gram-second (cgs) units are (4-1).

$$v = - \frac{3 \ell G_g T_a}{8 \left(1 + \frac{\pi \alpha}{8} \right) T} \quad \text{for } r \ll \ell$$

and

$$v = - \frac{3 X_a \eta T_a}{2 (2 X_a + X_i) \gamma_g T} \quad \text{for } r \gg l.$$

For the foregoing equations, the following terms apply:

- G_g = average thermal velocity of gas molecules
- ℓ = mean free path of gas molecules
- α = coefficient of accommodation
- χ_a = thermal conductivity of gas molecules
- χ_i = thermal conductivity of particles
- η = absolute gas viscosity
- γ_g = gas density
- T = absolute temperature
- T_a = temperature gradient

A temperature gradient of 1000 K/cm was assumed in calculating the curves in Figure 4.2-3. This value could be a lower limit assumption in this case where the gas temperature was ~ 773 K (500°C), the wall temperature ~ 323 K (50°C), and the channel height 2 mm. In a developing thermal boundary layer, as would be encountered at the channel entrance, the gradient could exceed 1000 K/cm by a factor of 10 to 100 or so near channel walls.

Based on the experimental results for Fe particles, the thermophoretic velocity of Na particles could be less than that for Fe by a factor of 2 for $r \gg \ell$ since $\chi_{iNa} \sim 2\chi_{iFe}$ and $\chi_a \ll \chi_i$. Note that the thermal diffusive and thermophoretic velocities are independent of particle density, whereas gravitational velocity is proportional to particle density.

Figure 4.2-3 shows that collection by thermal diffusion may dominate for particles less than $0.01 \mu\text{m}$ in size. In a thermal gradient of 1000 K/cm thermophoresis dominates for high conductivity particles from about $0.01 \mu\text{m}$ to less than $1 \mu\text{m}$ diameter and for low conductivity particles from $0.01 \mu\text{m}$ to several micrometres in size. Free fall could control collection for particles larger than several micrometres. Two advantages of using these three forces, which are present anyway, are that they act to collect particles as produced; that is, without breaking aggregates and the particles can easily be separated for individual observation and analysis.

4.2.4 Experimental Conditions

The only differences in sampling between test 15 and test 16 were the sampling time and the sampler position in test 16, about 1 m closer to the reaction

chamber. Sampling for 320 s, beginning 3 min after sodium drop in test 15 produced too thick a coating of particles on the channel surfaces. For test 16 the sampling time was 80 s, beginning 6 min after sodium drop.

As shown below, the flow rates \dot{V} , and mean flow velocities, \bar{u} , were similar in the two tests.

Test 15

$$\dot{V} = 2.1 \text{ cm}^3/\text{s}$$

and

$$\bar{u} = 5.3 \text{ cm/s for } 2b = 0.16 \text{ cm}$$

$$\dot{V} = 137 \text{ cm}^3/\text{s}$$

and

$$\bar{u} = 84.9 \text{ cm/s for } 2a = 0.63 \text{ cm}$$

Test 16

$$\dot{V} = 1.7 \text{ cm}^3/\text{s}$$

and

$$\bar{u} = 4.2 \text{ cm/s for } 2b = 0.16 \text{ cm}$$

$$\dot{V} = 109 \text{ cm}^3/\text{s}$$

and

$$\bar{u} = 67.6 \text{ cm/s for } 2a = 0.63 \text{ cm}$$

These values were calculated from equations for a straight channel of height, $2h$ (h equals either a or b), length L , cross-sectional area A and pressure drop Δp . Absolute gas viscosity is μ .

$$\dot{V} = \bar{u}A$$

where

$$u = \frac{h^2}{6\mu L} \Delta p.$$

Flow in both channel sizes was laminar since the Reynolds numbers were about 2 and 100 for the narrow and the wide channels. Thus there was no particle deposition from turbulence. Also an inlet section without bends eliminated inertial deposition. The channel length for transition flow was about 0.5 cm for the narrow channel and 15 cm for the wide

channel. This is the length required to establish well-developed flow which in this case was parabolic. A known and constant profile can simplify analysis.

Several hours after the reaction subsided, the open end of the sampler was closed with a plastic bag. Several days after the test, the sampler was removed from the facility, disassembled, and the parts sealed in plastic bags containing CaSO_4 desiccant, where they remained until examined. Particle composition and size were possibly altered by chemical reaction with the environment in the time between collection and examination. To reduce this possibility, the sampler could be designed to be purged with inert dry gas immediately after collection while allowing the particles to be desiccated until they are examined.

4.2.5 Collected Particles and Particle Composition

Because most of the analytic effort was concentrated on test 16, those results will be discussed first. Even here a collection time of 80 s proved too long since particle buildup occurred on the front half of the channels. Only on the last 15 cm of the channels were particles isolated from each other so that they could be identified in size, shape, and elemental composition. All reported observations were made by using the SEM.

Particle concentration in the gas stream at the sampler inlet can be determined if all particles of a given size are collected in the sampler. Essentially complete collection was accomplished in tests 15 and 16 as indicated by the rapid decrease in the number of particles on the channel walls with distance from the leading edge. With virtually all particles collected, the concentration as a function of particle size is determined from a particle count vs size on the channel surfaces and a measurement or calculation of the gas volume through the channel during the time of collection. Particle concentration with respect to size could not be measured because of the buildup of particles on some channel areas.

The deposited particulate was white to grayish-white in color. The grayish material was probably sodium hydride since it burst into flame when dropped on water. The whitish deposit could be a sodium oxide or sodium carbonate.

Resolved particles on the glass slides ranged from about $0.1 \mu\text{m}$ to a little larger than $3 \mu\text{m}$ in size. Particles in the 10- to $50\text{-}\mu\text{m}$ size range seem to be agglomerates made up of particles several micrometres in size. General particle shapes could be

characterized as angular as well as spherical. Figure 4.2-4 shows collected particles illustrating some of those characteristics.

Although particles smaller than several micrometres in size got buried in the silicone vacuum grease, the grease was very effective in holding particles larger than several hundred micrometres on both the quartz and the copper. There were more 0.5 mm particles on the greasy side and no particles larger than this on the dry side. However the grease tended to migrate with time onto the dry side of the channel.

OFHC copper provided a collection surface of high purity for identifying particle composition by x-ray energy dispersive analysis (XEDA) on the SEM. However the particles reacted with the copper producing a black deposit and during the reaction the particles several tenths of a micrometre in size disappeared. These particles were visible on glass slides but not on copper coupons taken from the same location in a channel of the same size. On the other hand, the glass that was used produced a dirty background for element identification but was excellent for obtaining particle number, size, and shape since particles did not react with the glass. Other possible high purity substrate metals with high melting points and easily identified characteristic x-ray lines are Ta (although close to the Ag line), Mo (close to the Pb and S lines), W (close to the Si line), Ti (close to the Ba line) and Ni.

The elements identified in the particles collected on glass were identical to those measured in the glass: Na, Si, and Ca (Cl was also found in the particles but not in the glass). However, the Na peak was greater with respect to the Si peak in the signal from particles than from the glass. For the same kind of particles collected on copper (same size channel and same location in the channel) particle elements were Na, Si, and Cl plus Cu from the substrate. (Fe, evidently from the SEM pole pieces, was identified on most of the XEDA traces.) The amount of Cl with respect to Na varies from particle to particle and may be a function of particle size. Identification of chemical species in the particles will be attempted by using electron diffraction in a TEM and x-ray diffraction from a bulk sample. These same techniques will be tried in identifying the black deposit on the copper. This deposit may be only cuprous oxide.

The particles in test 15 appeared similar in size and shape to those collected in test 16. The significant elements detected in test 15 particles by XEDA were Na, Si and, in some areas, Mg. (Also detected were Cu from the substrate and Fe from the SEM pole pieces.)

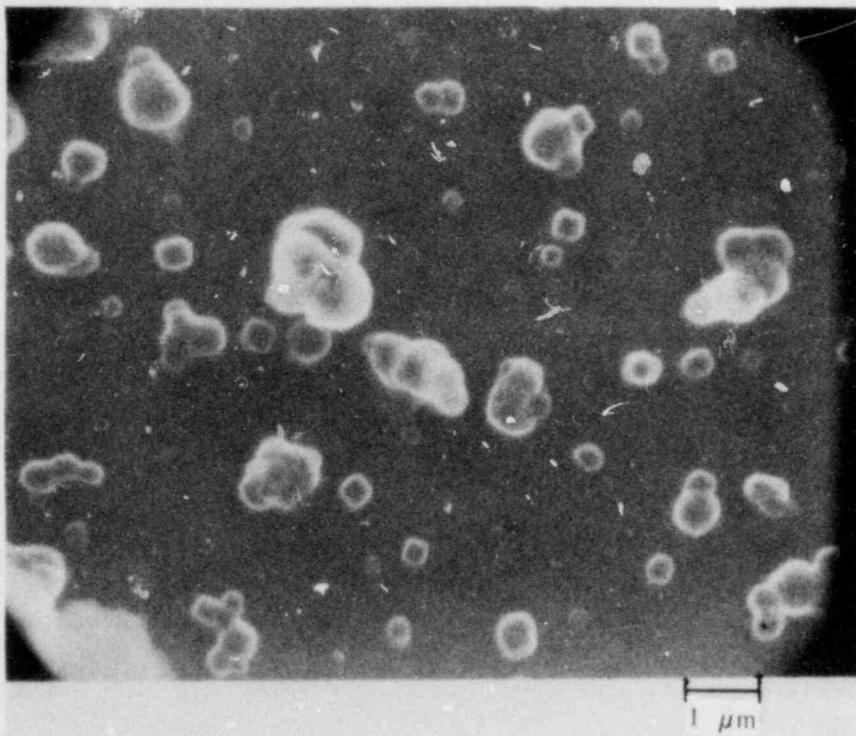
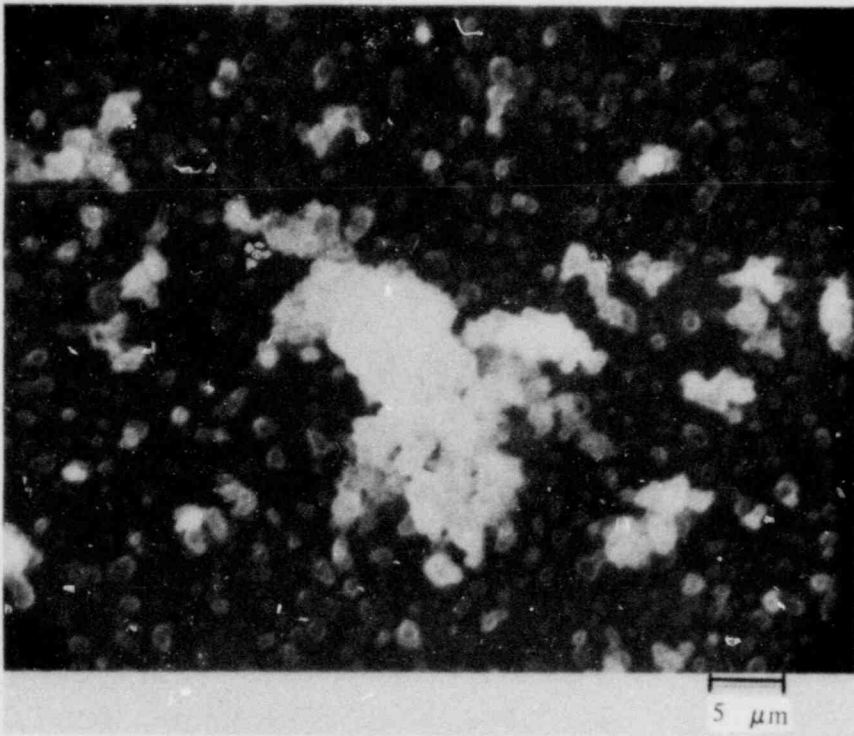


Figure 4.2-4 Aerosol Particles Collected in Sampling Channel on Test 16

4.2.6 Influence of Thermophoretic Force

From the total volume flow rate through the channels, an average flow velocity of 11 cm/s was calculated for the 5-cm-diameter inlet pipe. Particle residence time in the inlet pipe 1 m long was therefore about 9 s, so free-falling particles with terminal velocities larger than 0.6 cm/s, i.e., larger than 10 μm (Figure 4.2-3) should not reach the sampling channels. Actually particles several hundred micrometres in size were found on the top of channels and particles as large as several millimetres were found on the bottom of channels. The explanation is attributed to the thermophoretic force that moves particles from the hot gas to the colder walls. As shown in Figure 4.2-5, particles in the upper half of the channel flow move to the top surface if the thermophoretic force (TP) is larger than the weight, mg , of the particle. If the particle begins to move in this direction, it will continue since the thermal gradient increases nearer the wall. If the particle weight is larger than the TP force, the particle will eventually fall to the bottom of the channel, as will those particles in the lower half of the channel flow. Particles in the upper half of the flow would fall out faster if it were not for the retarding effect of the TP force.

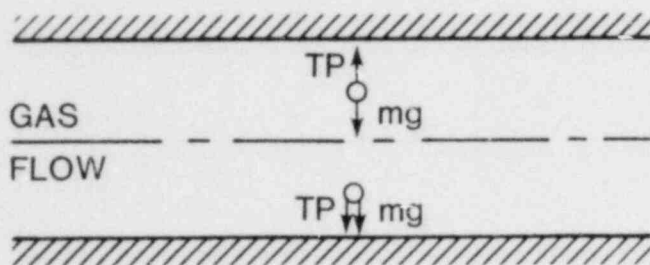


Figure 4.2-5 Particle Migration in the Channel

The thermophoretic force on particles can thus help explain the presence of particles larger than 10 μm in the channels, especially why several-hundred-micrometre particles are found on the top channel surface and why large deposits of particles are found all over the surface of the inlet pipe, nearly as many on the top as on the bottom. The thermophoretic force could be eliminated if the sampler and inlet pipe were heated to the temperature of the reaction gas. A more fruitful approach, especially at higher temperatures (≥ 1273 K) might be to keep the sampler relatively cold as in the present experiments, use the thermophoretic force to collect particles, and attempt to measure the magnitude of this force on the particles. This measurement would give an estimate

of the magnitude of the effect which would be present in all sampling experiments of this type where the particle-containing gas is at a temperature different than that of the sampling equipment. To reduce losses in the inlet pipe, it is possible to eliminate the pipe and extend each sampling channel up to or into the reaction chamber. After sampling, the channel would be withdrawn and sealed; for another sample another channel would be inserted, etc.

While the particle weight is a constant force, the thermophoretic force changes direction according to whether the particle is in the upper or lower half of the channel flow, thus complicating analysis. Perhaps the narrow channels should be positioned in a vertical instead of a horizontal direction (Figure 4.2-6) for sampling. This provides more symmetry and allows the two forces to act at right angles. As particles are collected on either wall, a density pattern for particles of equal aerodynamic size would be established. From this pattern and the velocity profile of the flowing gas, aerodynamic particle size could be estimated. From the same density pattern and velocity profile the thermophoretic force could be estimated knowing the temperature profile in the flow, determined from the temperature measurements and calculations.

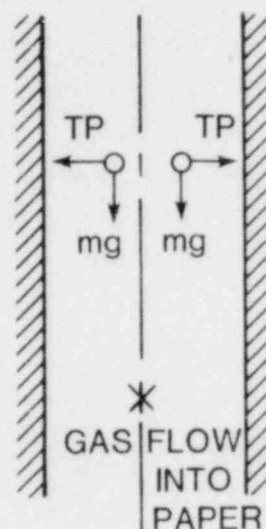


Figure 4.2-6 Sampler Channels Positioned Vertically

4.2.7 Sampling Efficiency

Sampling efficiency here means the efficiency with which particles in a volume of gas in the reaction chamber remain in that same volume when sampled. If the particles had no inertia, they would immediately respond to the flow and be sampled

with 100% efficiency. The larger the particle mass, the larger the inertia and the smaller the sampling efficiency. The stopping distance $V_0\tau$ (V_0 is the initial particle velocity relative to the gas and τ is the characteristic time for a particle and equals the product of particle mass and particle mobility), is the distance a particle of velocity V_0 will travel into a gas at rest before coming to rest, or conversely, the distance traveled by a particle initially at rest before it is entrained in a flow of velocity V_0 with a velocity equal to about $0.9 V_0$.

In the first case above in which a spherical particle of mass m and radius r moves with velocity V_0 into a gas at rest with absolute viscosity η , the equation of motion is

$$\frac{mdv}{dt} = -6\pi\eta rv.$$

(The gravitational force is not considered.) A second integral of the equation of motion gives the particle displacement as

$$x = V_0\tau (1 - e^{-t/\tau}).$$

For large t , x approaches $V_0\tau$, defined as the stopping distance.

In the second case in which the "at-rest" particle becomes entrained in a gas flow of velocity V_0 , the corresponding equation of motion is

$$\frac{mdv}{dt} = 6\pi\eta r (v_0 - v).$$

The Stokes damping force is used in both cases. The first integral results in a particle velocity of

$$v = V_0 (1 - e^{-t/\tau})$$

and the second integral results in particle displacement of

$$x = V_0 t - V_0\tau (1 - e^{-t/\tau}).$$

Thus the stopping distance is a measure of the distance required for a particle to respond to a change in

flow velocity as would be encountered at the sampler inlet.

Based on the results of these equations, high efficiency sampling results when the stopping distance is small with respect to the inlet size of the sampler. For the present case with an inlet pipe 5 cm in diameter and an average pipe flow of 11 cm/s, particles 10 μm and smaller would be sampled with high efficiency (stopping distance ≤ 0.003 cm) but the collection efficiency for 1-mm particles would be significantly smaller (stopping distance ~ 33 cm). A quantitative calculation of sampling efficiency would be complicated by the fact that the trajectories of the source aerosols in the reaction chamber are unknown, unlike particles moving under the influence of gravity alone, for instance. A possible experimental approach for estimating sampler efficiency would be an in-situ calibration of the sampler during the reaction where a known quantity of identifiable tracer particles would be injected into the chamber in a known pattern. Another approach would be to consider a multiple head sampler where each head would sample a skewed particle distribution but the distortions in the total sample would tend to cancel.

4.2.8 Recommendations

In summary, there are several changes and additions to the basic sampler that are suggested in part by these preliminary results.

- Design a sampler with several channels which can be used singly for sampling at different times into the reaction.
- Provide for inserting each sampling channel up to or into the reaction chamber in order to eliminate an inlet section.
- Use vertical channels to separate the effects of gravity and of thermophoresis on particles and thus attempt to measure the aerodynamic particle size and thermophoretic force on the source aerosols.
- After sampling, seal each sampling channel, flush it with dry inert gas, and expose the sample to desiccant.
- Be able to measure and adjust the flow rate before each sample is taken; be able to measure the flow rate during sampling.
- Measure the channel wall temperature and the gas temperature in the channel for calculating temperature gradients in the flow.
- Study the possibility of in-situ calibration of the sampler during sampling by using identifiable tracer particles.

- Because particles at least as large as several millimetres and perhaps as small as vapor exist in the reaction chamber, the sampler must not only be designed to sample at least this size range with an acceptable efficiency, but it must also be possible to identify the physical characteristics of these particles.
- Reduce particle number density on collection surfaces by a combination of increased flow velocity, increased collection surface, and decreased volume sampled so a particle size concentration can be measured. Test results indicate that a sufficiently small collection density can probably be obtained without diluting the source aerosols prior to sampling.
- Use narrow parallel plate geometry of the channel for estimating the charge state of particles by

applying a voltage across the two larger plates to establish a uniform electric field in which the particles move.

This sampler has the potential for collecting a wide range of particle sizes for calculating concentration and size distribution and determining chemical composition. In addition, dynamic characteristics such as thermophoretic effect, particle charge, and aerodynamic size compared to actual size and shape may be estimated for these reaction particles produced at high temperature and at high concentrations.

Reference for Section 4

4.1 N. A. Fuchs, *The Mechanics of Aerosols* (Pergamon Press, 1964).

5. Containment Analysis

(J. P. Odom, 4424; M. E. Senglaub, 4424; P. S. Pickard, 4423; M. J. Clauser, 4424)

5.1 Introduction

During this quarter, CONTAIN's capabilities continued to increase. The principal improvement has been the inclusion of a new aerosol module. F. M. Gelbard (Sandia National Laboratories)⁽⁵⁻¹⁾ has developed MAEROS, a new, state-of-the-art aerosol code which has now been incorporated into CONTAIN. MAEROS uses a sectional treatment of the size-distribution function for aerosol particles. Further, MAEROS allows simulation of multispecies aerosols under the assumption that agglomeration and settling effects are functions solely of particle size. This treatment provides new capabilities in aerosol modeling which will allow more mechanistic treatment of aerosol composition in CONTAIN. MAEROS also calculates the effects of vapor condensation on aerosol dynamics. Section 5.2 below describes MAEROS in detail.

Sensitivity calculations with MAEROS have investigated aerosol behavior in a light water reactor (LWR) TMLB' scenario as part of the Zion-Indian Point (ZIP) Study. These calculations explored the effect of atmospheric conditions on aerosol concentration for several different assumed aerosol particle diameters. The results of these and further CONTAIN calculations will be reported next quarter.

The restructured version of CONTAIN, reported last quarter, has now successfully run a test problem, thus verifying that all of the modules are operational. The code restructuring was undertaken to improve the intelligibility of the code for users.

CONTAIN now has a more general heat transfer model which allows an arbitrary number of heat transfer nodes in a cell. This permits the heat-sink and surface deposition effects of various structures such as piping, equipment, etc. to be modeled in addition to the walls, floor and roof.

A major revision of the plot package is underway. When it is completed, a more useful set of plots will be available to allow more efficient assessment of the voluminous output from CONTAIN.

As part of the ZIP Study, CONTAIN is being modified for application to problems with a condensable atmosphere such as the steam encountered in LWR events. These modifications were originally planned for later inclusion in CONTAIN, but are being implemented now for application in the ZIP Study. When completed, the atmosphere calculation

in CONTAIN will handle mixtures of noncondensable and condensable gases and their condensation on aerosols and structures. Initially, the condensable gas will be steam; subsequently CONTAIN will also treat sodium vapor.

5.2 MAEROS, A Sectional Multispecies Model for Aerosol Dynamics

5.2.1 Introduction to MAEROS

In the study of atmospheric aerosols, much effort has been devoted to understanding the physical and chemical mechanisms of aerosol evolution. For a spatially homogeneous aerosol, particles are characterized by size and chemical composition. Nearly all previous work on solving the governing equations for spatially homogeneous aerosols focused on the evolution of the particle size distribution as affected by coagulation,⁽⁵⁻²⁻⁵⁻⁶⁾ growth due to condensation,⁽⁵⁻⁷⁻⁵⁻⁹⁾ and sources and removal mechanisms.⁽⁵⁻¹⁰⁻⁵⁻¹³⁾ Although investigators often must deal with aerosols that consist of several species, a notable example being atmospheric aerosols, little work has been reported on solving the governing equations for the evolution of the distribution function for aerosols having multiple chemical components. To obtain analytical solutions of the governing equation for a multicomponent aerosol, previous efforts^(5-14, 5-15) resorted to simplified cases which are of limited value in describing actual aerosols. Since chemical composition of particles is very important in determining human health effects, studies restricted to the dynamics of size distribution cannot fully assess the effects of aerosols on health. Furthermore, the chemical composition of a particle often affects its growth rate, and thus the computation of the size distribution often may not be performed independently of that for the composition dynamics of the aerosol.

In this report, which is taken almost entirely from Gelbard,⁽⁵⁻¹⁾ a general method for simulating the evolution of the distribution of chemical species with respect to aerosol particle size is developed. The physical phenomena included (1) coagulation, (2) intra-particle chemical reaction, (3) gas-to-particle conversion, and (4) particle sources and removal mechanisms. Thus, a technique is presented that computes not only the evolving size distribution but also the variation of chemical composition with particle size.

The technique (as discussed for one-component systems⁽⁵⁻¹⁶⁾) is based upon dividing the particle size domain into m arbitrarily located sections and imposing the condition of mass conservation for each component for the four processes given above. Section 5.2.2 presents a detailed derivation of the conservation equations. For a system of s components, a set of $m \times s$ ordinary differential equations results.

5.2.2 Governing Equations for a Multicomponent Sectional Representation

A spatially homogeneous aerosol is assumed in which particle size is characterized by a single variable v , typically particle mass, which is conserved during coagulation and chemical reactions within particles. The size distribution function $n(v, t)$, is defined such that $n(v, t)dv$ is the number concentration of particles in the range $[v, v + dv]$ at time t . By dividing the entire particle size domain into m contiguous arbitrarily sized sections and defining Q_ℓ as the total mass of aerosol per unit volume of fluid in section ℓ at time t ,

$$Q_\ell(t) = \sum_{k=1}^s Q_{\ell,k}(t) = \int_{v_{\ell-1}}^{v_\ell} v n(v, t) dv, \quad (5.1)$$

where $Q_{\ell,k}(t)$ is the mass of component k in section ℓ , s is the total number of components and $v_{\ell-1}$ and v_ℓ denote the size of the smallest and largest particles, respectively, in section ℓ . Note that v_0 is arbitrary and the upper bound of section $\ell-1$ is equal to the lower bound of section ℓ for $\ell = 2, 3, \dots, m$.

In previous work on sectional equations,⁽⁵⁻¹⁶⁾ the general conservation equations were derived such that any integral property of the aerosol size distribution (e.g., number, surface area of volume) was conserved. Since this work is concerned with multicomponent aerosols, the concept of a number or surface area concentration of a single component in a particle composed of a mixture of s components has little physical significance and thus only conservation of mass is considered. Therefore, the objective of this work is to derive the general conservation equations for $Q_{\ell,k}$ ($\ell = 1, 2, \dots, m$ and $k = 1, 2, \dots, s$).

The conservation equations are derived by determining the net rates at which species k is added to each section by (1) coagulation, (2) intraparticle chemical reaction, (3) gas-to-particle conversion, and (4) particle source and removal mechanisms.

The expressions for each of the above mechanisms will be derived in sections 5.2.2.1 to 5.2.2.4, respectively. Section 5.2.2.5 will provide the final set of sectional equations by combining the terms in sections 5.2.2.1 to 5.2.2.4.

5.2.2.1 Coagulation

The derivation of the coagulation equations begins with the assumptions that binary collisions occur and that the rate of coagulation between particles in the mass ranges $[u, u + du]$ and $[v, v + dv]$ is given by $\beta(u, v) n(u, t) n(v, t) dudv$, where " $\beta(u, v) = \beta(v, u)$ " is the coagulation coefficient dependent only on the total masses of the coagulating particles. For particles in sections lower than ℓ , the total rate of coagulation is given by

$$\frac{1}{2} \int_{v_0}^{v_{\ell-1}} \int_{v_0}^{v_{\ell-1}} \beta(u, v) n(u, t) n(v, t) dudv. \quad (5.2)$$

However, only if the resulting particle is in the range $[v_{\ell-1}, v_\ell]$, is it added to section ℓ . Therefore, analysts introduce the function θ , which is equal to one if the specified condition is satisfied and zero if it is not. Hence,

$$\theta(v_{\ell-1} < u + v < v_\ell) = \begin{cases} 1 & v_{\ell-1} < u + v < v_\ell \\ 0 & \text{otherwise} \end{cases} \quad (5.3)$$

Using Eq (5.3), the flux of mass into section ℓ by coagulation of particles in lower sections may be expressed as

$$\frac{1}{2} \int_{v_0}^{v_{\ell-1}} \int_{v_0}^{v_{\ell-1}} \theta(v_{\ell-1} < u + v < v_\ell) (u + v) \beta(u, v) n(u, t) n(v, t) dudv. \quad (5.4)$$

Notice that the factor $(u + v)$ was incorporated into the integrand of Eq (5.4) to determine the mass entering section ℓ . Since the mass of each component is conserved by coagulation, the flux of mass of component k into section ℓ is given by the sum of the masses of component k in the coagulating particles. In general, particles of the same size may have different compositions and thus composition may not be a unique function of particle size. Therefore, a marginal probability density function for the mass fraction, $g_k(v, \eta_k)$, can be defined where $0 \leq \eta_k \leq 1$,

and $g_k(v, \eta_k) d\eta_k$ is the time-dependent fraction of particles in the mass range $[v, v + dv]$ with a mass fraction of component k in the range $[\eta_k, \eta_k + d\eta_k]$. Thus, for $k = 1, 2, \dots, s$,

$$\int_0^1 g_k(v, \eta_k) d\eta_k = 1, \quad (5.5)$$

and $g_k(v, \eta_k) n(v, t) dv d\eta_k$ is the number concentration of particles in the size range $[v, v + dv]$ with a mass fraction of component k in the range $[\eta_k, \eta_k + d\eta_k]$. Since the mass concentration of component k for a particle in the size range $[v, v + dv]$ is given by

$$\left\{ \int_0^1 v \eta_k g_k(v, \eta_k) d\eta_k \right\} n(v, t) dv, \quad (5.6)$$

the mass flux of component k into section ℓ is

$$\frac{1}{2} \int_{v_0}^{v_{\ell-1}} \int_{v_0}^{v_{\ell-1}} (v_{\ell-1} < u + v < v_{\ell}) \int_0^1 \int_0^1 (u \xi_k + v \eta_k) g_k$$

$$(u, \xi_k) g_k(v, \eta_k) d\xi_k d\eta_k \beta(u, v) n(u, t) n(v, t) dudv. \quad (5.7)$$

Using the property of $g_k(v, \eta_k)$ given in Eq (5.5), Eq (5.7) reduces to

$$\begin{aligned} & \frac{1}{2} \int_{v_0}^{v_{\ell-1}} \int_{v_0}^{v_{\ell-1}} \theta(v_{\ell-1} < u + v < v_{\ell}) \left\{ u \int_0^1 \xi_k g_k(u, \xi_k) d\xi_k \right. \\ & \left. + v \int_0^1 \eta_k g_k(v, \eta_k) d\eta_k \right\} \beta(u, v) n(u, t) n(v, t) dudv. \end{aligned} \quad (5.8)$$

By defining the mean mass of component k for all particles having mass in the range $[v, v + dv]$ as

$$\bar{v}_k = \int_0^1 v \eta_k g_k(v, \eta_k) d\eta_k = v \int_0^1 \eta_k g_k(v, \eta_k) d\eta_k, \quad (5.9)$$

Eq (5.8) can be reduced to

$$\frac{1}{2} \int_{v_0}^{v_{\ell-1}} \int_{v_0}^{v_{\ell-1}} (v_{\ell-1} < u + v < v_{\ell}) (\bar{u}_k + \bar{v}_k) \beta(u, v) n(u, t) n(v, t) dudv, \quad (5.10)$$

where

$$\bar{u}_k = \int_0^1 u \xi_k g_k(u, \xi_k) d\xi_k = u \int_0^1 \xi_k g_k(u, \xi_k) d\xi_k. \quad (5.11)$$

Notice that Eq (5.10) is similar to Eq (5.4) except that the mean mass of a component is used instead of the total mass of the particle to determine the mass flux of a specific component into section ℓ .

Particles and hence mass are removed from section ℓ when a particle from section ℓ coagulates with a particle from a lower section and forms a particle larger than v_{ℓ} . The rate at which such events occur is given by

$$\int_{v_0}^{v_{\ell-1}} \int_{v_{\ell-1}}^{v_{\ell}} \theta(u + v > v_{\ell}) \beta(u, v) n(u, t) n(v, t) dudv. \quad (5.12)$$

Therefore, the flux of component k out of section ℓ is given by

$$\int_{v_0}^{v_{\ell-1}} \int_{v_{\ell-1}}^{v_{\ell}} \theta(u + v > v_{\ell}) \bar{u}_k \beta(u, v) n(u, t) n(v, t) dudv. \quad (5.13)$$

However, if a particle in a section lower than ℓ coagulates with a particle in section ℓ and the resulting particle remains in section ℓ , the flux of component k into section is given by

$$\int_{v_0}^{v_{\ell-1}} \int_{v_{\ell-1}}^{v_{\ell}} \theta(u + v < v_{\ell}) \bar{v}_k \beta(u, v) n(u, t) n(v, t) dudv. \quad (5.14)$$

Intrasectional coagulation can only remove mass if the resulting particle size is greater than v_{ℓ} for the ℓ -th section. Therefore, the mass flux of component k out of section ℓ by intrasectional coagulation is given by

$$\frac{1}{2} \int_{v_{\ell-1}}^{v_{\ell}} \int_{v_{\ell-1}}^{v_{\ell}} \theta(u + v > v_{\ell}) (\bar{u}_k + \bar{v}_k) \beta(u, v) n(u, t) n(v, t) dudv. \quad (5.15)$$

Finally, for $\ell < m$ the mass flux of component k leaving section ℓ by coagulation of particles within section ℓ and those of higher sections is given by

$$\int_{v_\ell}^{v_m} \int_{v_{\ell-1}}^{v_\ell} \hat{u}_k \beta(u, v) n(u, t) n(v, t) dudv \quad (5.16)$$

Notice that in Eq (5.16), the θ function is not required since all coagulations of particles in section ℓ with particles in higher sections will remove a particle from section ℓ .

Combining the terms from Eq (5.10) and Eqs (5.13) through (5.16), the sectional equations for $Q_{\ell k}$, ($\ell = 1, 2, \dots, m$ and $k = 1, 2, \dots, s$) for an aerosol undergoing only coagulation are

$$\frac{dQ_{\ell k}}{dt} = \frac{1}{2} \int_{v_0}^{v_{\ell-1}} \int_{v_0}^{v_{\ell-1}} \theta(v_{\ell-1} < u + v < v_\ell) (\hat{u}_k + \hat{v}_k)$$

$$(u, v) n(u, t) n(v, t) dudv - \int_{v_0}^{v_{\ell-1}} \int_{v_{\ell-1}}^{v_\ell} \theta(u + v > v_\ell)$$

$$\hat{u}_k \beta(u, v) n(u, t) n(v, t) dudv$$

$$+ \int_{v_0}^{v_{\ell-1}} \int_{v_{\ell-1}}^{v_\ell} \theta(u + v < v_\ell) \hat{v}_k \beta(u, v) n(u, t)$$

$$n(v, t) dudv - \frac{1}{2} \int_{v_{\ell-1}}^{v_\ell} \int_{v_{\ell-1}}^{v_\ell} \theta(v + v > v_\ell)$$

$$(\hat{u}_k + \hat{v}_k) \beta(u, v) n(u, t) n(v, t) dudv$$

$$- \int_{v_\ell}^{v_m} \int_{v_{\ell-1}}^{v_\ell} \hat{u}_k \beta(u, v) n(u, t) n(v, t) dudv \quad (5.17)$$

To obtain the contribution of the various sections to $Q_{\ell k}$, one replaces the integrals in Eq (5.17) that range over more than one section by a sum of integrals over each section.

$$\frac{dQ_{\ell k}}{dt} = \frac{1}{2} \sum_{i=1}^{\ell-1} \sum_{j=1}^{\ell-1} \int_{v_{i-1}}^{v_i} \int_{v_{j-1}}^{v_j} \theta(v_{\ell-1} < u + v < v_\ell)$$

$$(\hat{u}_k + \hat{v}_k) \beta(u, v) n(u, t) n(v, t) dudv$$

$$- \sum_{i=1}^{\ell-1} \int_{v_{i-1}}^{v_i} \int_{v_{\ell-1}}^{v_\ell} \theta(u + v > v_\ell) \hat{u}_k \beta(u, v) n(u, t)$$

$$n(v, t) dudv + \sum_{i=1}^{\ell-1} \int_{v_{i-1}}^{v_i} \int_{v_{\ell-1}}^{v_\ell} \theta(u + v < v_\ell) \hat{v}_k \beta(u, v)$$

$$n(u, t) n(v, t) dudv - \frac{1}{2} \int_{v_{\ell-1}}^{v_\ell} \int_{v_{\ell-1}}^{v_\ell} \theta(u + v > v_\ell)$$

$$(\hat{u}_k + \hat{v}_k) \beta(u, v) n(u, t) n(v, t) dudv$$

$$- \sum_{i=\ell+1}^m \int_{v_{i-1}}^{v_i} \int_{v_{\ell-1}}^{v_\ell} \hat{u}_k \beta(u, v) n(u, t) n(v, t) dudv \quad (5.18)$$

5.2.2.2 Intraparticle Chemical Reaction

Since mass is conserved by intraparticle chemical reaction, no mass can leave or enter a section by this mechanism. However, the mass of individual components can be changed subject to the constraint given in Eq (5.1). In general, the kinetic expressions for the rates of formation and depletion of a component are functions of the concentration of the reactants, and hence functions of particle composition. If $F_k(\eta_1 v, \eta_2 v, \dots, \eta_s v)$ represents the net mass formation rate of component k for a particle size v with a mass fraction of component i equal to η_i , then

$$\int_{v_{\ell-1}}^{v_\ell} F_k(\eta_1 v, \eta_2 v, \dots, \eta_s v) n(v, t) dv \quad (5.19)$$

is the total mass formation rate of component k in section ℓ per unit volume of fluid. However, since particles of size v may have different compositions, the mass formation rate is given by

$$\int_{v_{\ell-1}}^{v_\ell} \left\{ \int_0^1 \dots \int_0^1 F_k(\eta_1 v, \dots, \eta_s v) P d\eta_1 \dots d\eta_{s-1} \right\} n(v, t) dv \quad (5.20)$$

where $P(\eta_1, \dots, \eta_{s-1}, v, t)$ is the joint mass fraction probability density function defined such that

$$P d\eta_1 d\eta_2 \dots d\eta_{s-1} \quad (5.21)$$

is the fraction of particles in the size range

$[v, v + dv]$ having mass fractions in the ranges

$$[\eta_1, \eta_1 + d\eta_1], \dots, [\eta_{s-1}, \eta_{s-1} + d\eta_{s-1}],$$

and

$$P = 0 \text{ for } \eta_1 + \eta_2 + \dots + \eta_{s-1} > 1.$$

Note that since the sum of η_i , ($i = 1, \dots, s$), must be equal to 1, only $s-1$ mass fractions are independent and therefore only $s-1$ integrations over particle composition are required in Eq (5.20). If F_k is a linear function of its argument, then

$$F_k = \alpha_{0,k} + \alpha_{1,k} \eta_1 v + \alpha_{2,k} \eta_2 v + \dots + \alpha_{s,k} \eta_s v, \quad (5.22)$$

where $\alpha_{i,k}$, ($i = 0, 1, \dots, s$), are arbitrary functions of v and t . Since the expected value of a sum is equal to the sum of the expected values, using Eqs (5.5) and (5.22), Eq (5.20) can be reduced to

$$\int_{v_{\ell-1}}^{v_{\ell}} (\alpha_{0,k} + \alpha_{1,k} \bar{v}_1 + \alpha_{2,k} \bar{v}_2 + \dots + \alpha_{s,k} \bar{v}_s) n(v, t) dv \quad (5.23)$$

for the special case of first order reactions.

5.2.2.3 Particle Growth by Gas-to-Particle Conversion

Heterogeneous processes which incorporate gaseous species into the particulate phase can alter the size and chemical composition of a particle. In general, gaseous species diffuse to the particle surface and either condense or dissolve in the particle. An analysis of particle growth by these mechanisms followed by chemical reaction on the surface or within the particle has been given elsewhere.⁽⁵⁻⁸⁾ Since intraparticle reactions are accounted for by the function F_k as discussed in Section 5.2.2.2, only condensation and dissolution of gaseous species is discussed here.

If the rate at which gaseous molecules of component k of mass v'_k are incorporated into a particle of mass v can be given by

$$G_k(\eta_1 v, \eta_2 v, \dots, \eta_s v),$$

then the mass formation rate of component k in section ℓ is given by

$$\int_{v_{\ell-1}}^{v_{\ell} + v'_k} v'_k G_k(\eta_1 v, \dots, \eta_s v) n(v, t) dv. \quad (5.24)$$

Notice that the upper limit of integration of Eq (5.24) is such that particles do not grow larger than v_{ℓ} .^{*} When molecules of component i , ($i = 1, \dots, s$), of size v'_i are incorporated into particles in the range $[v_{\ell} - v'_i, v_{\ell}]$, the resulting particle will grow into section $\ell + 1$. Assuming that molecular additions to a particle occur in series, two different molecular species cannot simultaneously grow a particle out of section ℓ . Therefore, the flux of component k out of section ℓ is given by the sum of the rates at which molecular species grow particles into section $\ell + 1$. This rate is given by[†]

$$\sum_{i=1}^s \int_{v_{\ell} - v'_i}^{v_{\ell}} v \eta_i G_i(\eta_1 v, \dots, \eta_s v) n(v, t) dv. \quad (5.25)$$

The flux of component k into section $\ell + 1$ is given by

$$\sum_{i=1}^s \int_{v_{\ell} - v'_i}^{v_{\ell}} (v \eta_k + \delta_{i,k} v'_k) G_i(\eta_1 v, \dots, \eta_s v) n(v, t) dv, \quad (5.26)$$

where

$$\delta_{i,k} = \begin{cases} 0 & i \neq k \\ 1 & i = k \end{cases} \quad (5.27)$$

For gas phase diffusion-limited growth, G_k is usually assumed to be proportional to the partial pressure difference of the condensing species in the gas phase and above the particle surface. Since the partial pressure above the particle is generally a function of composition, expressions in Eqs (5.24), (5.25), and (5.26) must be modified to account for particles of the same size but with different compositions. Thus, the mass formation rate of component k in section ℓ is

^{*}It is assumed that v'_k is small enough such that $v_{\ell} - v'_k \geq v_{\ell-1}$, $\ell = 1, 2, \dots, m$ and $k = 1, 2, \dots, s$.

[†]If component i is not undergoing gas-to-particle conversion, $G_i = 0$.

$$\int_{v_{\ell-1}}^{v_{\ell}-v'_k} v'_k \left\{ \int_0^1 \cdots \int_0^1 G_k(\eta_1 v, \dots, \eta_s v) \right. \\ \left. Pd\eta_1 \cdots d\eta_{s-1} \right\} n(v, t) dv \quad (5.28)$$

and the flux of component k out of section ℓ is given by

$$\sum_{i=1}^s \int_{v_{\ell}-v'_i}^{v_{\ell}} v \left\{ \int_0^1 \cdots \int_0^1 \eta_k G_i(\eta_1 v, \dots, \eta_s v) \right. \\ \left. Pd\eta_1 \cdots d\eta_{s-1} \right\} n(v, t) dv. \quad (5.29)$$

Finally, the mass flux of component k into section $\ell + 1$ from section $\ell < m$ is

$$\sum_{i=1}^s \int_{v_{\ell}-v'_i}^{v_{\ell}} \left\{ \int_0^1 \cdots \int_0^1 (\eta_k v + \delta_{i,k} v'_i) G_i(\eta_1 v, \dots, \eta_s v) \right. \\ \left. Pd\eta_1 \cdots d\eta_{s-1} \right\} n(v, t) dv. \quad (5.30)$$

If G_k , ($k = 1, \dots, s$) is a linear function of its arguments, then G_k can be expressed as*

$$G_k = \gamma_{0,k} + \gamma_{1,k} \eta_1 v + \gamma_{2,k} \eta_2 v + \cdots + \gamma_{s,k} \eta_s v, \quad (5.31)$$

where $\gamma_{i,k}$, ($i = 0, 1, \dots, s$) are arbitrary functions of v and t . For the special case of G_k given by Eq (5.31), Eq (5.28) reduces to

$$\int_{v_{\ell-1}}^{v_{\ell}-v'_k} v'_k (\gamma_{0,k} + \gamma_{1,k} \bar{v}_1 + \gamma_{2,k} \bar{v}_2 + \cdots + \gamma_{s,k} \bar{v}_s) \\ n(v, t) dv. \quad (5.32)$$

If the expected value of the product of the mass fraction of component k in a particle of mass v and the rate at which gaseous molecules of mass v'_i are incorporated into that particle is approximated by the product of the expected value of η_k and the expected value of G_i , the terms in Eqs (5.29) and (5.30) for G_i given by Eq (5.31) reduce to†

$$\sum_{i=1}^s \int_{v_{\ell}-v'_i}^{v_{\ell}} \bar{v}_k (\gamma_{0,i} + \gamma_{1,i} \bar{v}_1 + \gamma_{2,i} \bar{v}_2 + \cdots + \gamma_{s,i} \bar{v}_s) \\ n(v, t) dv \quad (5.33)$$

and

$$\sum_{i=1}^s \int_{v_{\ell}-v'_i}^{v_{\ell}} (\bar{v}_k + \delta_{i,k} v'_i) (\gamma_{0,i} + \gamma_{1,i} \bar{v}_1 \\ + \gamma_{2,i} \bar{v}_2 + \cdots + \gamma_{s,i} \bar{v}_s) n(v, t) dv, \quad (5.34)$$

respectively.

5.2.2.4 Source and Removal Mechanisms

Spatially homogeneous sources are usually assumed to be a function of particle size and time. If $S(v, t)$ represents the source rate such that $S(v, t) dv$ is the generation rate of particles per unit volume of fluid in the size range $[v, v + dv]$ at time t , then

$$\int_{v_{\ell-1}}^{v_{\ell}} v S(v, t) dv \quad (5.35)$$

is the mass generation rate into section ℓ . Therefore, the generation rate of component k in section ℓ is given by

$$\int_{v_{\ell-1}}^{v_{\ell}} \bar{v}_k S(v, t) dv. \quad (5.36)$$

To account for a source generating particles of the same size but with different compositions, \bar{v}_k represents the mean mass of component k for generated particles of size v .

In general, removal mechanisms are functions of $n(v, t)$, v , and t . Therefore, if $R[n(v, t), v, t] dv$ is the removal rate of particles in the size range $[v, v + dv]$,

$$\int_{v_{\ell-1}}^{v_{\ell}} \bar{v}_k R[n(v, t), v, t] dv \quad (5.37)$$

is the removal rate of component k in section ℓ . For the often used first order removal rate, i.e., $R = \bar{R}(v, t) n(v, t)$, Eq (5.37) can be expressed as

$$\int_{v_{\ell-1}}^{v_{\ell}} \bar{v}_k \bar{R}(v, t) n(v, t) dv. \quad (5.38)$$

* G_k may be a linear function for diluted solutions.

†In general, the expected value of a product is not equal to the product of the expected values. However, if the partial pressure of the diffusing gaseous species above the particle surface is negligible compared to that in the gas phase, G_i may be independent of particle composition, in which case the expected values can be factored.

5.2.2.5 Multicomponent Sectional Equations

Combining the expressions in Eqs (5.18), (5.20), (5.28), (5.29), (5.30), (5.36), and (5.37) gives for $i = 1, \dots, m$ and $k = 1, \dots, s$.

$$\begin{aligned}
 \frac{dQ_{\ell k}}{dt} = & \frac{1}{2} \sum_{i=1}^{\ell-1} \sum_{j=1}^{\ell-1} \int_{v_{j-1}}^{v_j} \int_{v_{i-1}}^{v_i} \theta(v_{\ell-1} < u + v < v_{\ell}) (\tilde{u}_k + \tilde{v}_k) \beta(u, v) n(u, t) n(v, t) dudv \\
 & - \sum_{i=1}^{\ell-1} \int_{v_{i-1}}^{v_i} \int_{v_{\ell-1}}^{v_{\ell}} \theta(u + v > v_{\ell}) \tilde{u}_k \beta(u, v) n(u, t) n(v, t) dudv \\
 & + \sum_{i=1}^{\ell-1} \int_{v_{i-1}}^{v_i} \int_{v_{\ell-1}}^{v_{\ell}} \theta(u + v < v_{\ell}) \tilde{v}_k \beta(u, v) n(u, t) n(v, t) dudv \\
 & - \frac{1}{2} \int_{v_{\ell-1}}^{v_{\ell}} \int_{v_{\ell-1}}^{v_{\ell}} \theta(u + v > v_{\ell}) (\tilde{u}_k + \tilde{v}_k) \beta(u, v) n(u, t) n(v, t) dudv \\
 & - \sum_{i=\ell+1}^m \int_{v_{i-1}}^{v_i} \int_{v_{\ell-1}}^{v_{\ell}} \tilde{u}_k \beta(u, v) n(u, t) n(v, t) dudv \\
 & + \int_{v_{\ell-1}}^{v_{\ell}} \left\{ \int_0^1 \dots \int_0^1 F_k(\eta_1 v, \dots, \eta_s v) P d\eta_1 \dots d\eta_{s-1} \right\} n(v, t) dv \\
 & + \int_{v_{\ell-1}}^{v_{\ell}-v'_k} v'_k \left\{ \int_0^1 \dots \int_0^1 G_k(\eta_1 v, \dots, \eta_s v) P d\eta_1 \dots d\eta_{s-1} \right\} n(v, t) dv \\
 & - \sum_{i=1}^s \int_{v_{\ell}-v'_i}^{v_{\ell}} v \left\{ \int_0^1 \dots \int_0^1 \eta_k G_i(\eta_1 v, \dots, \eta_s v) P d\eta_1 \dots d\eta_{s-1} \right\} n(v, t) dv \\
 & + \sum_{i=1}^s \int_{v_{\ell}-v'_i}^{v_{\ell+1}} \left\{ \int_0^1 \dots \int_0^1 (\eta_k v + \delta_{i,k} v_i) G_i(\eta_1 v, \dots, \eta_s v) P d\eta_1 \dots d\eta_{s-1} \right\} n(v, t) dv \\
 & + \int_{v_{\ell-1}}^{v_{\ell}} \tilde{v}_k S(v, t) dv - \int_{v_{\ell-1}}^{v_{\ell}} \tilde{v}_k R[n(v, t), v, t] dv. \tag{5.39}
 \end{aligned}$$

Note that the first, second, third, and ninth terms on the right-hand side of Eq (5.39) are evaluated only for $\ell > 1$ and the fifth term is evaluated only for $\ell < m$.

Thus far no mathematical approximations have been required to obtain Eq (5.39). However, this set of equations is unclosed since $G_k(v, \eta_k)$ and $n(v, t)$ are not related to $Q_{\ell k}$. Therefore, one must introduce at least two approximations to close the system.

To eliminate $n(v, t)$ the size distribution may be conveniently approximated as constant within each section. With this approximation it can be shown,⁽⁵⁻¹⁶⁾ that the sectional equations will reduce to the exact integrodifferential equation for one-component aerosols as the number of sections is increased for a fixed particle size domain. Although this is the lowest order and thus the first of an infinite set of possible approximations, using a constant has the advantage that the size distribution, which is a time dependent quantity, generally need not be repeatedly integrated over particle size as one integrates in time. Furthermore, in comparing the sectional solution to a higher order method for a one-component aerosol, excellent agreement was obtained with as few as 10 sections.

Therefore, for the first approximation the distribution of a conveniently chosen size variable will be taken as constant within each section. Although up to this point particle mass has been taken to be the size variable of interest, it would often be desirable to express the distribution on a size basis other than particle mass, for example, particle diameter. Since only an integral constraint on the size distribution exists, i.e.,

$$Q_{\ell}(t) = \int_{v_{\ell-1}}^{v_{\ell}} v n(v, t) dv, \quad (5.40)$$

a size variable other than particle mass for which the distribution is constant within a section can arbitrarily be chosen. Assuming that the size variable of interest is x , and is uniquely related to v by $x = f(v)$, $\bar{q}_{\ell}(t)$, a constant within each section can be defined by

$$v n(v, t) = \bar{q}_{\ell}(t) f'(v), \quad (5.41)$$

where $f'(v) = df/dv$. Substituting Eq (5.41) into Eq (5.40) gives

$$Q_{\ell}(t) = \bar{q}_{\ell}(t) [f(v_{\ell}) - f(v_{\ell-1})]. \quad (5.42)$$

Therefore, a plot of $\bar{q}_{\ell}(t)$ vs x will result in a series of step functions such that the area under each step is equal to $Q_{\ell}(t)$ and

$$n(v, t) = \frac{Q_{\ell} f'(v)}{v(x_{\ell} - x_{\ell-1})}, \quad (5.43)$$

where

$$x_{\ell} = f(v_{\ell}).$$

To eliminate $G_k(v, \eta_k)$ it is convenient to approximate the mean mass fractions of all particles within a section as being equal and thus independent of particle size within a section.* Therefore, for $v_{\ell-1} < v < v_{\ell}$ and $k = 1, \dots, s$,

$$\int_0^1 \eta_k g_k(v, \eta_k) d\eta_k \quad (5.44)$$

is independent of v within section ℓ . By definition

$$\frac{v Q_{\ell k}}{Q_{\ell}} = \frac{v \int_{v_{\ell-1}}^{v_{\ell}} \int_0^1 v \eta_k g_k(v, \eta_k) n(v, t) d\eta_k dv}{\int_{v_{\ell-1}}^{v_{\ell}} v n(v, t) dv}. \quad (5.45)$$

Using the second approximation the double integral in Eq (5.45) can be separated to give

$$\frac{v Q_{\ell k}}{Q_{\ell}} = v \int_0^1 \eta_k g_k(v, \eta_k) d\eta_k. \quad (5.46)$$

Using the definition of \bar{v}_k given in Eq (5.19) gives that in section ℓ

$$\bar{v}_k = \frac{v Q_{\ell k}}{Q_{\ell}}. \quad (5.47)$$

Since all the coagulation and removal terms of Eq (5.39) (i.e., terms 1 through 5 and 11 on the right-hand side, which contain $g_k(v, \eta_k)$) are given in terms of \bar{v}_k , they can be directly related to $Q_{\ell k}$, ($\ell = 1,$

*Note that this approximation does not make any assumptions or restrictions on how composition is distributed for a given particle size. Also, note that as the section sizes decrease to the point that only a single particle size is contained within each section, the mean mass fraction of different particle sizes within a section must be equal since there is only one particle size in the section. Therefore, in the limiting case of a single particle size in each section the first two sectional approximations become exact.

..., m and $k = 1, \dots, s$) by Eq (5.47) without solving for $g_k(v, \eta_k)$. * If F_k and G_k are linear functions, then

$$\int_0^1 \dots \int_0^1 F_k(\eta_1 v, \dots, \eta_s v) P d\eta_1 \dots d\eta_{s-1} = F_k(\bar{v}_1, \dots, \bar{v}_s) \quad (5.48)$$

and

$$\int_0^1 \dots \int_0^1 G_k(\eta_1 v, \dots, \eta_s v) P d\eta_1 \dots d\eta_{s-1} = G_k(\bar{v}_1, \dots, \bar{v}_s) \quad (5.49)$$

as shown by Eqs (5.23) and (5.32), respectively. Hence, the sixth and seventh terms on the right-hand side of Eq (5.39) can be replaced by Eqs (5.23) and (5.32), respectively. If G_i is independent of particle composition, Eqs (5.33) and (5.34) (with all γ 's equal to zero except $\gamma_{0,1}$), can be used to express the eighth and ninth terms of the right-hand side of Eq (5.39), respectively, which would close Eq (5.39).

For those cases in which P is unknown and the conditions needed to eliminate it from the intraparticle chemical reaction and gas-to-particle conversion terms are not valid, Eqs (5.48) and (5.49) may have to be resorted to as a third approximation, regardless of the functional forms of F_k and G_k . Finally, as the fourth approximation, the expected value of $\eta_k G_i$ may have to be approximated by the product of the expected values of η_k and G_i to determine the mass flux crossing section boundaries by gas-to-particle conversion. Note that the errors introduced by using the last two approximations do not vanish in the limiting case of a single particle size within each section.

Using the sectional approximations, Eq (5.39) can be reduced to the final form of the multicomponent sectional equations,

$$\frac{dQ_{\ell,k}}{dt} = \frac{1}{2} \sum_{i=1}^{\ell-1} \sum_{j=1}^{\ell-1} [{}^{1a}\bar{\beta}_{i,j,\ell} Q_{i,k} Q_j + {}^{1b}\bar{\beta}_{i,j,\ell} Q_{i,k} Q_j] - \sum_{i=1}^{\ell-1} [{}^{2a}\bar{\beta}_{i,\ell} Q_i Q_{\ell,k} - {}^{2b}\bar{\beta}_{i,\ell} Q_i Q_{i,k}]$$

*Note that the source term (i.e., the tenth term on the right-hand side of Eq (5.39) is independent of (v, t) and $g_i(v, \eta_k)$ and thus does not have to be related to $Q_{\ell,k}$.

$$- \frac{1}{2} {}^3\bar{\beta}_{\ell,\ell} Q_{\ell} Q_{\ell,k} - Q_{\ell,k} \sum_{i=\ell+1}^m {}^4\bar{\beta}_{i,\ell} Q_i + \bar{F}_{\ell,k} Q_{\ell} + {}^1\bar{G}_{\ell,k} Q_{\ell} - \sum_{i=1}^s {}^2\bar{G}_{\ell,i} Q_{\ell,k} - {}^2\bar{G}_{\ell-1,i} Q_{\ell-1,k} + {}^3\bar{G}_{\ell-1,k} Q_{\ell-1} + \bar{S}_{\ell,k} - \bar{R}_{\ell,k}, \quad (5.50)$$

where the values for $\bar{\beta}$, \bar{G} , \bar{F} , \bar{S} , and \bar{R} are given in Table 5-I. Note that the first, second, third, fourth, tenth, and eleventh terms on the right-hand side of Eq (5.50) are evaluated only for $\ell > 1$ and the sixth term is evaluated only for $\ell < m$. Since there are m sections and s components, Eq (5.50) constitutes a set of $m \times s$ ordinary differential equations which are to be integrated in time.

For the special case of a one-component aerosol, $Q_{i,k} = Q_i$ for all i and Eq (5.50) reduces to Eq (5.19)⁽⁵⁻¹⁵⁾ for a coagulating aerosol in which mass is conserved. Note that ${}^{1a}\bar{\beta} + {}^{1b}\bar{\beta}$ and ${}^{2a}\bar{\beta} - {}^{2b}\bar{\beta}$ are equal to ${}^1\bar{\beta}$ and ${}^2\bar{\beta}$, respectively, from that work.

5.2.3 Comments on Section Size

The sectional equations as given by Eq (5.50) are such that the section size is arbitrary. However, since the particle size range of interest is usually quite large, a geometric constraint can be imposed on the section boundaries (i.e., $v_i \geq 2v_{i-1}$, $i = 1, \dots, m$) without affecting most applications of the equations. With this constraint the minimum number of sectional coefficients is required since

$${}^{1a}\bar{\beta}_{i,j,\ell} = {}^{1b}\bar{\beta}_{i,j,\ell} = 0$$

for $i < \ell - 1$ and $j < \ell - i, \ell$

$${}^{2a}\bar{\beta}_{i,\ell} = {}^{1a}\bar{\beta}_{i,\ell,\ell+1} \text{ and } {}^3\bar{\beta}_{\ell,\ell} = 2{}^{1a}\bar{\beta}_{\ell,\ell,\ell+1}.$$

Furthermore, by imposing the geometric constraint the sectional coagulation coefficients can be simply expressed without resorting to the use of a discontinuous θ function. Thus for some forms of $\beta(u, v)$ it may be possible to determine analytically the $\bar{\beta}$'s.*

*The sectional coagulation coefficients for sections satisfying the geometric constraint are given in Table 5-II. The reasoning by which Table 5-II is obtained from Table 5-I is given in Reference 5-15.

Table 5-1 Sectional Coefficients for Equation (5.50)

Symbol	Remarks	Coefficient*
1. Coagulation ${}^{1a}\tilde{\beta}_{i,j,\ell}$	${}^{1a}\tilde{\beta}_{i,j,\ell} \neq {}^{1a}\tilde{\beta}_{i,j,\ell}$	$\int_{x_{i-1}}^{x_i} \int_{x_{j-1}}^{x_j} \frac{\theta(v_{\ell-1} < u + v < v_{\ell}) u\beta(u, v)}{uv(x_i - x_{i-1})(x_j - x_{j-1})} dydx$
	${}^{1a}\tilde{\beta}_{i,j,\ell} = {}^{1b}\tilde{\beta}_{i,j,\ell}$	
	$1 < \ell \leq m$	
	$1 \leq i < \ell$	
	$1 \leq j < \ell$	
${}^{1b}\tilde{\beta}_{i,j,\ell}$	${}^{1b}\tilde{\beta}_{i,j,\ell} \neq {}^{1b}\tilde{\beta}_{i,j,\ell}$	$\int_{x_{i-1}}^{x_i} \int_{x_{j-1}}^{x_j} \frac{\theta(v_{\ell-1} < u + v < v_{\ell}) v\beta(u, v)}{uv(x_i - x_{i-1})(x_j - x_{j-1})} dydx$
	${}^{1b}\tilde{\beta}_{i,j,\ell} = {}^{1a}\tilde{\beta}_{i,j,\ell}$	
	$1 < \ell \leq m$	
	$1 \leq i < \ell$	
	$1 \leq j < \ell$	
${}^{2a}\tilde{\beta}_{i,\ell}$	${}^{2a}\tilde{\beta}_{i,\ell} \neq {}^{2a}\tilde{\beta}_{i,\ell}$	$\int_{x_{i-1}}^{x_i} \int_{x_{\ell-1}}^{x_{\ell}} \frac{\theta(u + v > v_{\ell}) u\beta(u, v)}{uv(x_i - x_{i-1})(x_{\ell} - x_{\ell-1})} dydx$
	$1 < \ell \leq m$	
	$1 \leq i < \ell$	
${}^{2b}\tilde{\beta}_{i,\ell}$	${}^{2b}\tilde{\beta}_{i,\ell} \neq {}^{2b}\tilde{\beta}_{i,\ell}$	$\int_{x_{i-1}}^{x_i} \int_{x_{\ell-1}}^{x_{\ell}} \frac{\theta(u + v < v_{\ell}) v\beta(u, v)}{uv(x_i - x_{i-1})(x_{\ell} - x_{\ell-1})} dydx$
	$1 < \ell \leq m$	
	$1 \leq i < \ell$	
${}^3\tilde{\beta}_{\ell\ell}$	$1 \leq \ell \leq m$	$\int_{x_{\ell-1}}^{x_{\ell}} \int_{x_{\ell-1}}^{x_{\ell}} \frac{\theta(u + v > v_{\ell}) (u + v)\beta(u, v)}{uv(x_{\ell} - x_{\ell-1})^2} dydx$

* $x_i = f(v_i), u = f^{-1}(y), v = f^{-1}(x), \tilde{v}_i = \frac{vQ_{\ell-1}}{Q_{\ell}}, n(v, t) = \frac{Q_{\ell} f'(v)}{[v(x_{\ell} - x_{\ell-1})]}$

Table 5-1 (cont)

Symbol	Remarks	Coefficient*
1. Coagulation (cont)		
${}^4\bar{\beta}_{i,\ell}$	${}^4\bar{\beta}_{i,\ell} \neq {}^4\bar{\beta}_{\ell,i}$	
	$1 \leq \ell < m$	$\int_{x_{\ell-1}}^{x_i} \int_{x_{\ell-1}}^{x_\ell} \frac{u\beta(u,v)}{uv(x_i - x_{i-1})(x_\ell - x_{\ell-1})} dy dx$
	$\ell < i \leq m$	
2. Gas-to-Particle Conversion		
${}^1\bar{G}_{\ell,k}$	$1 \leq \ell \leq m$	$\int_{x_{\ell-1}}^{f(v_\ell - v'_k)} \frac{v'_k G_k(\tilde{v}_\ell, \dots, \tilde{v}_s)}{v(x_\ell - x_{\ell-1})} dx$
${}^2\bar{G}_{\ell,k}$	$1 \leq \ell \leq m$	$\int_{f(v_\ell - v'_k)}^{x_\ell} \frac{G_k(\tilde{v}_\ell, \dots, \tilde{v}_s)}{(x_\ell - x_{\ell-1})} dx$
${}^3\bar{G}_{\ell,k}$	$1 \leq \ell \leq m$	$\int_{f(v_\ell - v'_k)}^{x_\ell} \frac{v'_k G_k(\tilde{v}_\ell, \dots, \tilde{v}_s)}{v(x_\ell - x_{\ell-1})} dx$
3. Intraparticle Chemical Reaction		
$\bar{F}_{\ell,k}$	$1 \leq \ell \leq m$	$\int_{x_{\ell-1}}^{x_\ell} \frac{F_k(\tilde{v}_\ell, \dots, \tilde{v}_s)}{v(x_\ell - x_{\ell-1})} dx$
4. Sources and Removal Mechanisms		
$\bar{S}_{\ell,k}$	$1 \leq \ell \leq m$	$\int_{v_{\ell-1}}^{v_\ell} \tilde{v}_k S(v, t) dv$
$\bar{R}_{\ell,k}$	$\left\{ \begin{array}{l} \text{arbitrary order} \\ 1 \leq \ell \leq m \end{array} \right.$	$\int_{v_{\ell-1}}^{v_\ell} \tilde{v}_k R[n(v, t), v, t] dv$
		$Q_{\ell,k} \int_{x_{\ell-1}}^{x_\ell} \frac{\bar{R}(v, t)}{(x_\ell - x_{\ell-1})} dx$
	$1 \leq \ell \leq m$	

$$x_i = f(v_i), u = f^{-1}(y), v = f^{-1}(x), \tilde{v}_i = \frac{v Q_{\ell-1}}{Q_\ell}, n(v, t) = \frac{Q_\ell f'(v)}{[v(x_\ell - x_{\ell-1})]}$$

In addition to selecting the section boundaries, considerable flexibility exists in choosing $f(v)$ and hence the type of plot to present the results of a simulation. For atmospheric aerosols, interest is usually shown in the shape of the distribution as represented vs $\log_{10}(D/1 \mu\text{m})$, where D is particle diameter in micrometers. Thus, $f(v)$ for spherical particles

will often be given as

$$f(v) = x = \log_{10} \left[\frac{\left(\frac{6v}{\pi\rho} \right)^{1/3}}{1 \mu\text{m}} \right] \quad (5.51)$$

where ρ is the material density.

Table 5-II Sectional Coagulation Coefficients With Geometric Constraint
 $(v_{i+1} \geq 2v_i, i = 0, 1, 2, \dots, m-1)$

Symbol	Remarks	Coefficient*
${}^{1a}\bar{\beta}_{i,j,\ell} = {}^{1b}\bar{\beta}_{i,j,\ell}$	$i < \ell-1$ $j < \ell-1$	0
${}^{1a}\bar{\beta}_{i,\ell-1,\ell} = {}^{1b}\bar{\beta}_{\ell-1,i,\ell}$	$\left\{ \begin{array}{l} 1 < \ell \leq m \\ i < \ell-1 \end{array} \right.$	$\int_{x_{i-1}}^{x_i} \int_{f(v_{\ell-1}-v)}^{x_{\ell-1}} \frac{u\beta(u,v)}{uv(x_i - x_{i-1})(x_{\ell-1} - x_{\ell-2})} dydx$
	$\left\{ \begin{array}{l} 1 < \ell \leq m \\ i = \ell-1 \end{array} \right.$	$\left\{ \begin{array}{l} \int_{x_{i-1}}^{f(v_i-v_{i-1})} \int_{f(v_{\ell-1}-v)}^{x_{\ell-1}} \frac{u\beta(u,v)}{uv(x_{\ell-1} - x_{\ell-2})^2} dydx \\ + \int_{f(v_i-v_{i-1})}^{x_i} \int_{x_{\ell-2}}^{x_{\ell-1}} \frac{u\beta(u,v)}{uv(x_{\ell-1} - x_{\ell-2})^2} dydx \end{array} \right.$
	$1 < \ell \leq m$	
${}^{1b}\bar{\beta}_{i,\ell-1,\ell} = {}^{1a}\bar{\beta}_{\ell-1,i,\ell}$	$i < \ell-1$	$\int_{x_{i-1}}^{x_i} \int_{f(v_{\ell-1}-v)}^{x_{\ell-1}} \frac{u\beta(u,v)}{uv(x_i - x_{i-1})(x_{\ell-1} - x_{\ell-2})} dydx$

* $x_i = f(v_i)$, $u = f^{-1}(y)$, $v = f^{-1}(x)$.

Note that the expressions given for ${}^3\bar{\beta}$ and ${}^4\bar{\beta}$ are valid even if the geometric constraint is not satisfied. However, if the geometric constraint is not satisfied ${}^3\bar{\beta}_{\ell,\ell+1} > 2{}^{1a}\bar{\beta}_{\ell,\ell,\ell+1}$.

Table 5-II (cont)

Symbol	Remarks	Coefficient*
${}^{2a}\bar{\beta}_{i,\ell} = {}^{1a}\bar{\beta}_{i,\ell,\ell+1}$	$1 < i \leq m$	$\int_{x_{i-1}}^{x_i} \int_{f(v_{i-1})}^{f(v_i)} \frac{u\beta(u,v)}{uv(x_i - x_{i-1})(x_\ell - x_{\ell-1})} dydx$
	$1 \leq i < \ell$	
${}^{2b}\bar{\beta}_{i,\ell}$	$1 < \ell \leq m$	$\int_{x_{i-1}}^{x_i} \int_{x_{\ell-1}}^{f(v_{i-1})} \frac{v\beta(u,v)}{uv(x_i - x_{i-1})(x_\ell - x_{\ell-1})} dydx$
	$1 \leq i < \ell$	
${}^3\bar{\beta}_{\ell,\ell} = 2 {}^{1a}\bar{\beta}_{\ell,\ell,\ell+1}$	$1 \leq \ell \leq m$	$\left\{ \begin{array}{l} \int_{x_{\ell-1}}^{f(v_{\ell-1})} \int_{f(v_{\ell-1})}^{x_\ell} \frac{(u+v)\beta(u,v)}{uv(x_\ell - x_{\ell-1})^2} dydx \\ + \int_{f(v_{\ell-1})}^{x_\ell} \int_{x_{\ell-1}}^{x_\ell} \frac{(u+v)\beta(u,v)}{uv(x_\ell - x_{\ell-1})^2} dydx \end{array} \right.$
${}^4\bar{\beta}_{i,\ell}$	$\left\{ \begin{array}{l} 1 \leq \ell < m \\ \\ \ell < i \leq m \end{array} \right.$	$\int_{x_{i-1}}^{x_i} \int_{x_{\ell-1}}^{x_\ell} \frac{u\beta(u,v)}{uv(x_i - x_{i-1})(x_\ell - x_{\ell-1})} dydx$

* $x_i = f(v_i)$, $u = f^{-1}(y)$, $v = f^{-1}(x)$.

Note that the expressions given for ${}^3\bar{\beta}$ and ${}^4\bar{\beta}$ are valid even if the geometric constraint is not satisfied. However, if the geometric constraint is not satisfied ${}^3\bar{\beta}_{\ell,\ell+1} > 2 {}^{1a}\bar{\beta}_{\ell,\ell,\ell+1}$.

5.2.4 Computational Requirements

A solution is obtained by determining the sectional coefficients and integrating a system of $m \times s$ ordinary differential equations. Since typically more than 90% of the computational effort is devoted to numerically evaluating the sectional coagulation coefficients, the user should try to minimize the number of these coefficients and store them for possible

use in subsequent problems. Because the particle size range, section size, and coagulation mechanism of interest are usually the same for many atmospheric aerosol problems, one set of sectional coagulation coefficients can be used for problems with a different number of components, initial mass and composition distributions, and source, removal, growth, and reaction mechanisms.

The total number of sectional coagulation coefficients can be determined as follows. Using the fact that ${}^{1a}\bar{\beta}_{i,j,\ell} = {}^{1b}\bar{\beta}_{i,j,\ell}$, the number of coefficients for ${}^{1a}\bar{\beta}$ and ${}^{1b}\bar{\beta}$ for section $\ell \geq 2$ is $(\ell - 1)^2$. Therefore for m sections

$$\sum_{\ell=2}^m (\ell - 1)^2 = \frac{2m^3 - 3m^2 + m}{6} \quad (5.52)$$

coefficients have to be determined. For ${}^{2a}\bar{\beta}$, ${}^{2b}\bar{\beta}$, and ${}^4\bar{\beta}$ there are $3m(m - 1)/2$ coefficients and only m coefficients for ${}^3\bar{\beta}$. Thus, the maximum number of coefficients is

$$\frac{m^3 + 3m^2 - m}{3} \quad (5.53)$$

However, if the geometric constraint is satisfied,

$${}^{1a}\bar{\beta}_{i,j,\ell} = {}^{1b}\bar{\beta}_{i,j,\ell} = 0 \text{ for } i < \ell - 1$$

$$\text{and } j < \ell - 1, 2 \text{ } {}^{1a}\bar{\beta}_{\ell,\ell,\ell+1} = 2 \text{ } {}^{1b}\bar{\beta}_{\ell,\ell,\ell+1} = {}^3\bar{\beta}_{\ell,\ell}$$

$$\text{and } {}^{1a}\bar{\beta}_{\ell,\ell,\ell+1} = {}^{2a}\bar{\beta}_{\ell,\ell}$$

Therefore, all ${}^{1a}\bar{\beta}$'s can be determined from the ${}^{2a}\bar{\beta}$'s and ${}^3\bar{\beta}$'s, and are only

$$\sum_{\ell=3}^m \ell - 2 = \frac{(m - 2)(m - 1)}{2} \quad (5.54)$$

nonzero independent coefficients for ${}^{1b}\bar{\beta}$. Since the number of coefficients for ${}^{2a}\bar{\beta}$, ${}^{2b}\bar{\beta}$, ${}^3\bar{\beta}$, and ${}^4\bar{\beta}$ is not affected by the geometric constraint, the total number of sectional coagulation coefficients reduces to its minimum value of $2m^2 - 2m + 1$.

References for Section 5

- 5-1 F. Gelbard and J. H. Seinfeld, "Simulation of Multicomponent Aerosol Dynamics," to be published (1980).
- 5-2 G. M. Hidy, *J Colloid Sci* 20:123, 1965.
- 5-3 E. X. Berry, *J Atmospheric Sci* 24:688, 1967.
- 5-4 W. T. Scott, *J Atmospheric Sci* 25:54, 1968.
- 5-5 R. L. Drake, *Topics in Current Aerosol Research*, (eds G. M. Hidy and J. R. Brock), 3:201-376, Pergamon, Oxford (1972).
- 5-6 S. H. Suck and J. R. Brock, *J Aerosol Sci* 10:518, 1979.
- 5-7 J. R. Brock, *Atmospheric Environment* 5:833, 1971.
- 5-8 J. R. Brock, *J Colloid Interface Sci* 39:32, 1972.
- 5-9 F. Gelbard and J. H. Seinfeld, *J Colloid Interface Sci* 68:173, 1979.
- 5-10 G. C. Lindauer and A. W. Castleman, *Aerosol Sci* 2:85, 1971.
- 5-11 J. W. Burgmeir, I. H. Blifford, and D. A. Gillette, *Water, Air and Soil Pollution* 2:97, 1973.
- 5-12 P. Middleton and J. J. Brock, *J Colloid Interface Sci* 54:249, 1976.
- 5-13 F. Gelbard and J. H. Seinfeld, *J Colloid Interface Sci* 68:363, 1979.
- 5-14 A. A. Lushnikov, *J Colloid Interface Sci* 54:94, 1976.
- 5-15 F. Gelbard and J. H. Seinfeld, *J Colloid Interface Sci* 63:472, 1978.
- 5-16 F. Gelbard, Y. Tambour, and J. H. Seinfeld, *J Colloid Interface Sci* in press (1980).

6. ELEVATED TEMPERATURE DESIGN ASSESSMENT

(J. A. Van Den Avyle, 5835; W. B. Jones, 5835, C. H. Karnes, 5835; D. W. Lobitz, 5521; C. M. Stone, 5521)

6.1 Uniaxial Creep-Fatigue Behavior

6.1.1 Creep Testing

No creep testing was performed during the current reporting period.

6.1.2 Creep-Fatigue Testing

No additional uniaxial testing was performed. See Section 6.1.5 for discussion of biaxial testing.

6.1.3 Nondestructive Test Program

No additional nondestructive examinations were performed.

6.1.4 Microstructural Analysis

Transmission electron microscopy (TEM) examinations were completed on a 2.25 Cr-1 Mo steel specimen obtained from C. R. Brinkman at Oak Ridge National Laboratory. The specimen was cycled at 811 K (538°C) at the low strain range of 0.001 with a 0.05 hr compressive hold period. It ran under these conditions for 8124 hr at which time the strain range was increased to 0.004 and cycling was continued to failure. Of particular interest to Sandia were the dislocation and precipitate substructures. Earlier work at Sandia has shown that cycling at 866 K (593°C) results in significant changes in carbide precipitation that do not occur during thermal aging or creep deformation. Examination of the ORNL sample showed that only thermal aging effects had occurred and that the strain range-temperature combination used in the test did not result in added carbide precipitation. In addition, the dislocation density observed in the foils was very low considering the 3733 cycles at $\Delta\epsilon = 0.004$ given the specimen prior to failure. These observations indicate that accelerated testing of 2.24 Cr-1 Mo steel at higher than service temperatures needs to be re-evaluated.

6.1.5 Multiaxial Test Facility

A series of 13 experiments has been conducted on tubular biaxial specimens of 316 stainless steel at 866 K (593°C). These tests had the purpose of checking out the multiaxial test facility and specimen design under typical operating conditions and to compare the biaxial results with existing uniaxial and biaxial data.

Testing conditions along with cycles-to-specimen failure, and for pressurized specimens, cycles-to-detection-of-a-leak, are listed in Table 6-1. The specimen was a tubular design shown in Figure 6.1-1. Two wall thicknesses were checked: 0.64 mm and 1.27 mm. The tests were run in total axial strain control with simultaneous measurement of axial and diametral strain. Seven tests were cycled uniaxially without internal pressure, and six were cycled with a constant (within ± 7 kPa) internal argon pressure which provided a hoop stress of 41 MPa. Induction heating was employed.

The specimens were cycled until leaking was noted; the pressure system was then shut off, and cycling continued until a crack had propagated approximately 50% around the circumference. The data of Table 6-1 show that at least 90% of the life is required to develop a leak and less than 10% is needed to propagate the crack to failure. Since the cycles required to propagate the leak crack to failure are a low fraction of life, a direct comparison of cyclic lives for the uniaxial and biaxial tubular specimens is reasonable.

Figure 6.1-2 shows a Coffin-Manson type plot of the data from Table 6-1 plotted as plastic strain ranges vs cycles to failure. Also included are reference uniaxial data from solid round-bar (6.35-mm-diameter) specimens generated at Sandia and by Brinkman and North at ORNL.⁽⁶⁻¹⁾ All data fall along straight lines, typical of this type of plot. Several observations can be made:

- The tubular data are consistent and reproducible.
- Uniaxial tubular data show significantly lower lives compared to round-bar data.
- The effect of the 41 MPa hoop stress is negligible for the thin-wall specimen.
- Thicker walled tubular specimens consistently show a slightly longer life than thin walled.
- A 1 min tensile hold period gives about a 50% reduction in life at the strain range tested. This is consistent with round-bar data.

The lower life for tubular versus solid specimens could be due to at least two factors. First, as shown by the thick and thin wall results, greater specimen thickness does influence life by increasing the cycles necessary for propagation. The effect is not thought to be large, however, since crack growth rate increases rapidly with crack length, so a thick section would not contribute much to life. The second factor which could reduce life of the tubular specimen is internal surface finish. For these tests, cracks always

initiated at the inner surface, as would be expected from the strain distribution. Surface finish on the interior is difficult to control, and it is impossible to polish as is typically done with the outside. Any machining grooves present would decrease the cycles necessary to initiate a fatigue crack.

Analysis of this failure data along with cyclic ratcheting results from these tests is continuing and will be further discussed in a topical report to be published later.

Table 6-I Biaxial Creep-Fatigue Tests on 316 Stainless Steel at 593°C

Specimen	$\Delta\epsilon_t$	$\Delta\epsilon_p$	Tensile		t (mm)	N_L	N_f
			Hold (min)	Pressure (Mpa)			
316-BX-1	0.0103	0.0054	--	--	0.64	--	455
316-BX-2	0.0050	0.0014	--	--	0.64	--	4545
316-BX-3	0.0050	0.0015	--	--	0.64	--	4056
316-BX-4	0.0030	0.00014	--	--	0.64	--	227606
316-BX-5	0.0050	0.0016	--	4.7	0.64	3580	3864
316-BX-6	0.0050	0.0016	--	4.7	0.64	3840	4230
316-BX-7	0.0035	0.0006	--	10.5	1.27	41800	42877
316-BX-8	0.0054	0.0020	--	10.5	1.27	--	4523
316-BX-9	0.0050	0.0016	1	10.5	1.27	1637	1665
316-BX-10	0.0050		1	10.5	1.27	--	--
316-BX-11	0.0035	0.0004	--	--	0.64	--	54975
316-BX-12	0.0050	0.0016	1	10.5	1.27	2118	2129
316-BX-13	0.0050	0.0015	--	--	0.64	--	5314
316-BX-14	0.0103	0.0058	--	--	1.27	--	489

$\Delta\epsilon_t$ - total axial strain range

$\Delta\epsilon_p$ - plastic axial strain range

N_L - cycles to pressure leak

N_f - cycles to failure

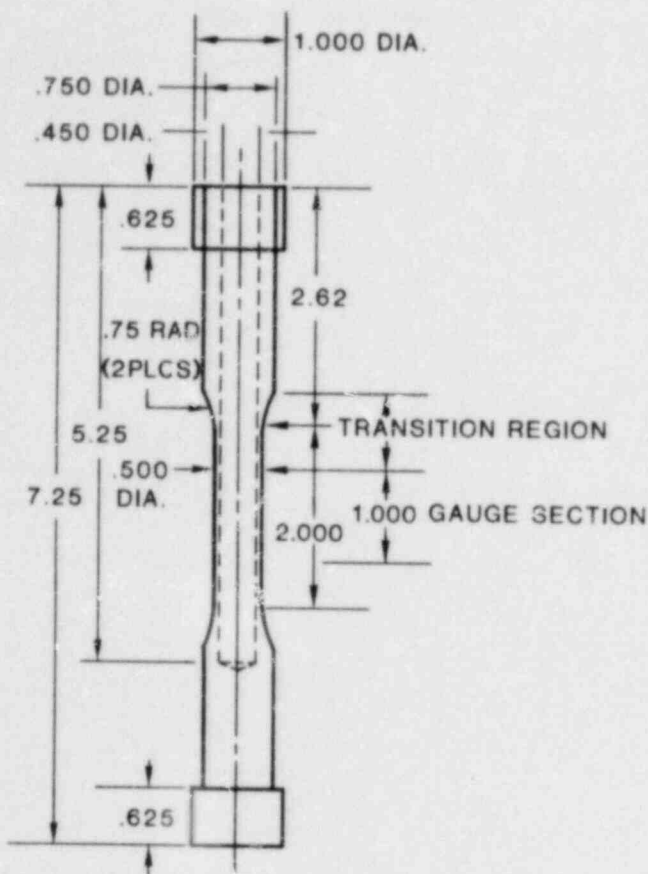


Figure 6.1-1 Multi-axial Specimen Geometry (All dimensions in inches)

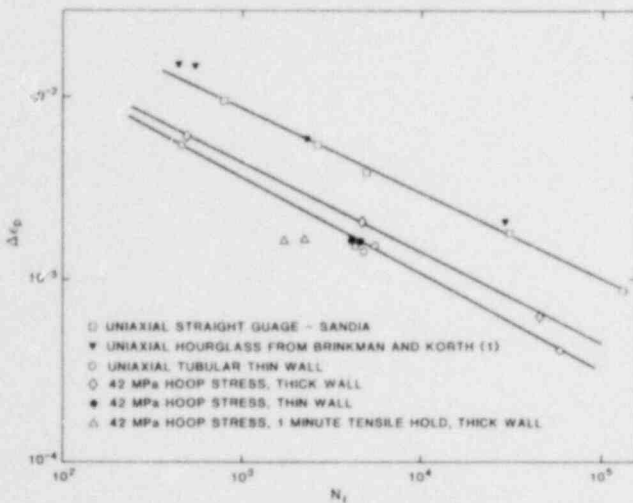


Figure 6.1-2 Low Cycle Fatigue Results for Biaxial Loadings

6.2 Creep-Fatigue Damage Analysis

No additional work was performed in this reporting period.

6.3 Structural Analysis

Work on the report on the piping elbow analysis continued this quarter.

6.4 Structural Evaluation

No work in this area was performed in this reporting period.

Reference for Section 6

6-1 C. R. Brinkman and G. E. Korth, *Metallurgical Transactions* 5:792-794, March 1974.

7. LMFBR Accident Delineation

7.1 Engineered Safety Systems

(J. A. Sholtis, 4424; E. R. Copus, 4424)

During this period, the fault trees under development for detection, SCRAM, and shutdown heat removal system (SHRS) failures in the Clinch River Breeder Reactor Plant (CRBRP) were completed. These fault trees will provide a basis for subsequent relative quantification of CRBRP initiating-accident categories during Phase II of the delineation study. This relative quantification effort will focus on CRBRP as a base case with alternative LMFBR designs and design options to be addressed by sensitivity analysis. Because of the complexity and size of the SHRS fault tree developed for CRBRP and the sensitivity of the SHRS function to common mode and common cause effects, quantification of the SHRS fault tree for all important accident initiators will require a substantial amount of time. This quantification is important in quantifying protected accidents in CRBRP. To provide timely results, therefore, tentative plans for Phase II are to quantify CRBRP unprotected accident categories in a relative sense first and treat the relative quantification of protected accidents in CRBRP over the longer term.

The accident initiation and engineered safety systems (ESS) response sections of the *LMFBR Accident Delineation Study Phase I Final Report* were completed in draft form during this period and will be completed in final form for review in the next quarter.

Sandia staff personnel met with individuals from the University of Arizona recently to discuss the potential for using the BRENDA systems code to characterize the initiation phases of accidents with failures at different points within the system. The University of Arizona will attempt this BRENDA application for both protected and unprotected accidents in CRBRP. This information will be useful to the delineation study.

In preparation for the relative quantification of CRBRP accident initiation during Phase II, several event and fault tree analysis codes were investigated during this period. The Sandia National Laboratories' SETS code for fault-tree evaluation is now available for use and two test cases have been run to acquire familiarity with the SETS code as well as to verify its correct functioning. The AUTOET event-tree evaluation code is presently under consideration and either the AUTOET code or an internally generated equivalent event-tree quantification code will be used during Phase II.

Data collection was also initiated during this period in preparation for the quantification effort during Phase II. This effort will involve the gathering of existing data on initiator recurrence frequencies, component and subsystem failure probabilities, and ESS availability and reliability values; when such data is not available it must be determined analytically or by extrapolation from similar systems.

7.2 Accident Phenomenology

(D. C. Williams, 4424)

The main task this quarter involved preparation of detailed documentation for the *LMFBR Accident Delineation Study, Phase I Final Report*. Topics covered in the accident phenomenology area during this period included:

- Accomplishing a substantial expansion and revision of the delineation of protected accidents
- Delineating the late phase of local fault propagating (LFP) accidents (other aspects of LFP accidents were treated in earlier time periods)
- Revising the delineation of the ULOF late transition phase and the delineation of the fuel dispersal phase to reflect recent results obtained with the SIMMER II code
- Describing the applicability to delineation of two representation techniques other than event trees.

Summaries of these four topics are given below.

7.2.1 Delineation of Protected Accidents

Protected accidents are events in which successful SCRAM action causes neutronic shutdown but a core disruption may still result because of impaired decay heat removal. This accident class has received much less study by the LMFBR safety community than have unprotected accidents. The relative neglect of protected accidents cannot be justified, since they appear to contribute more to the overall probability of a core disruption than do unprotected accidents, and it has not been established that consequences of protected core disruptions are necessarily less severe than unprotected accident consequences. This subject clearly deserves greater emphasis in future LMFBR safety programs.

Protected accidents were delineated by first dividing them into two subclasses:

- Protected transient or failure (PT/F), in which

the core is itself initially undamaged but subsystem failures have occurred which impair decay heat removal capability

- Damaged core scenarios, in which the core itself has suffered sufficient damage to significantly affect its coolability but the damage falls short of a full CDA; additional failure of decay heat removal systems may or may not be involved.

A generic event tree was constructed for protected accidents. It includes questions concerning the availability of key subsystems involved in decay heat removal and also phenomenological questions concerning coolability by natural circulation in the absence of forced flow. The questions included in the tree are sufficient to sort damaged core scenarios from PT/F accidents and, for the latter, to determine the occurrence of a CDA and timing information if it does occur.

Many accident categories falling within the PT/F subclass could be defined, but most of these have received little or no study. Two accident scenarios in CRBRP which have been analyzed at Brookhaven and UCLA were selected for review as illustrative examples. Accidents considered included (1) a protected rupture of the primary boundary in which all capability to remove heat from the primary system is lost due to massive rupture and (2) a much less drastic temporary loss-of-heat-sink transient in which normal heat transport paths are interrupted but heat rejection via the protected air-cooled condensers is ultimately established. In the first accident, a CDA is inevitable and recriticality may be a strong possibility. In the second accident, heating of the clad above the presumed $\sim 900^{\circ}\text{C}$ ($\sim 1600^{\circ}\text{F}$) failure limit is likely if pony flow is not available and the situation is marginal in this regard if pony flow is available; subsequent consequences were not addressed.

Even less information is available concerning damaged core scenarios. Indeed, definition of this subclass in the Accident Delineation Study was motivated largely by the Three Mile Island accident. Such scenarios could conceivably arise in several ways: (1) LFP accidents in which shutdown does not occur until the late phase is reached, (2) initiators which directly damage the core, (3) initiators falling outside the reactor safety system (RSS) design basis (but for which shutdown is achieved albeit not without core damage), (4) partial failure of the RSS with initiators within the design basis, and (5) partial or temporary failure of decay heat removal subsystems after shutdown, including failures due to inappropriate operator actions as at Three Mile Island. The last-mentioned of these five categories is very likely the most important. In all instances, determining the damage

that might result from a specific cause and also determining core coolability limits as a function of damage type and extent are both necessary. In the latter task, at least three sodium flow states should be considered: pony motor flow, natural convection, and full primary pump flow (in case restoration of primary pump flow under these conditions should prove possible and desirable).

7.2.2 Delineation of the Late Phase of LFP Accidents

The LFP accident late phase (beginning with subassembly-scale fuel disruption) was delineated generically. Key questions include: (1) whether fuel dispersal axially or into interassembly gaps can result in a coolable fuel configuration without shutdown, (2) whether pressure-generating events (e.g., FCI) could result in high ramp reactivity insertions or in core distortion that could preclude shutdown, and (3) at what stage might signals calling for RSS action be generated if subassembly-to-subassembly fuel disruption propagates by melting attack. If neutronic shutdown is achieved, a damaged-core scenario results; otherwise a CDA is the outcome. In the latter event, there is a qualitative similarity to UTOP transition phase scenarios.

7.2.3 Delineation Revisions Based Upon SIMMER-II Calculations

Recent calculations at LASL using the SIMMER-II code have led to significant revisions of earlier delineation results in two areas, the ULOF late transition phase and the fuel dispersal phase. In the first area, the SIMMER-II calculations indicate that sequences involving bottled-up pools generally lead to a prompt neutronic burst. Indeed, given certain modeling assumptions (thought to be pessimistic), severe energetics (ramps $> \$100/\text{s}$) can be calculated; whether these results could be realistic under any actual circumstances remains to be determined. The event tree for the ULOF late transition phase was revised to reflect a reduced estimate of the likelihood that molten pools would remain stably boiled-up, and an increased estimate of the likelihood that such sequences will terminate with an energetic disassembly.

Concerning the fuel dispersal phase, calculations have been made at LASL using the SIMMER-II code for a specific ULOF disassembly scenario in CRBRP, with fission energetics in the intermediate range.

Investigators found that work energetics were mitigated by about an order of magnitude relative to the values calculated for isentropic expansion with fuel as working fluid. The calculated mitigation was primarily due to heat and momentum transfer to the above-core structure, and is therefore dependent upon the assumption that this structure remains in place. This assumption is increasingly likely to fail as disassembly severity increases, and also may be invalid for disassemblies arising late in the transition phase, when much of the above-core structure may have been destroyed by melting attack. Interpretation of the SIMMER-II calculations is further complicated by the fact that the principal source of sodium-slug kinetic energy was calculated to result from development of a secondary, ex-core pressure source due to fuel-coolant heat transfer. Without better understanding of the latter process, no assurance can be given that more severe work energetics cannot arise even if SIMMER-II is correct in predicting that the effects of the original pressure source in the core do undergo heavy attenuation before affecting the primary boundary.

7.2.4 Alternative Representational Techniques

Event-tree methodology was the principal representational tool employed in delineating the accident phenomenology area. It proved useful in many respects, but several limitations to event-tree applicability also became clearly apparent. In particular, event trees are not well suited for representing important problem features such as continuously variable parameters, phenomena acting in parallel with the net effect of the combination governing the outcome, cyclic or semicyclic phenomena, feedback relationships, etc.

It seemed desirable to explore means other than event trees for representing accident phenomenology issues, and two such means were developed and applied to the ULOF initiation phase for exploratory purposes. The first of these is a scheme to categorize the phenomenological uncertainties in terms of the magnitude and nature of their impact upon accident

outcome; its primary motivation was to serve as a possible intermediate step in setting research priorities for resolving the outstanding uncertainties. The second approach is an alternative diagrammatic representation of the nature of the interaction between the closely-coupled phenomenologies involved in core disruptive accidents (CDAs). Though program personnel are not convinced that either of these approaches should replace event trees as the main delineation tools, these approaches do display certain problem features more clearly than do event trees and may therefore prove useful as a supplement.

7.3 Postaccident Phenomenology

(F. Sciacca, 4424; P.W. Conrad, 4424)

The event trees defining the postaccident phenomenology were modified somewhat during this quarter. The changes provided a clearer treatment of both in-vessel and ex-vessel energetic recriticality. Primary sodium spills which do not lead to CDAs can also be handled better by the revised tree. This tree modification effort also endeavored to arrange the tree structure, where appropriate, to allow effective feedback interaction from experimentation and analysis information. In the on-going work, this interaction will influence branch-point probabilities and outcomes. The on-going work also seeks to characterize the outcomes of the event-tree branches. Substantial effort during this quarter has been aimed at preparing the *LMFBR Accident Delineation Study Phase I, Final Report*, which will be completed during the next quarter.

Cognizant personnel at Sandia have compiled a list of LMFBR containment research and development needs. The list was formulated in response to an NRC request. The listing presents the R&D needs in three categories: Primary Containment (primary system boundary), Secondary Containment - Reactor Cavity, and Secondary Containment - Upper RCB. Relative priorities of the R&D needs within each category were defined. Both the list and the priorities were established based on available experimental and analytical information. The R&D needs specified and the priorities assigned must be considered preliminary at this time.

8. Test and Facility Technology

8.1 ACRR Fuel Motion Detection System

(J. G. Kelly, 4426; K. T. Stalker, 4426)

A fuel motion detection system has been developed for use with the ACRR. This system, called the Coded Aperture Imaging System (CAIS), will measure nuclear fuel motion in simulated reactor accidents. The evolutionary nature of system development will continue as improvements are incorporated; thus the system is not being described as completed. However, the CAIS achieved a milestone this quarter in tests which show that it will provide important diagnostic information in fuel motion experiments. Therefore, the CAIS is being declared operational and experimenters are planning to use it as a diagnostic tool in upcoming PBE tests scheduled for the summer of 1980.

This quarterly report will (1) review the problems to be addressed during the latest series of tests, (2) review the changes (made since the Phase I proof test of 1979) to improve system performance, (3) describe the Phase II proof tests, and (4) discuss some of the preliminary results. In addition, noise sources in the active system will be analyzed and future plans will be delineated.

System performance has been extensively improved, primarily by alterations in the shield structure. The large reduction in the radiation background at the detector location has led to the opportunity to identify secondary sources of background that were previously obscured. Further, the data obtained in the test series indicate that significant additional improvements can still be made. Section 8.1.2 below elaborates on the enhanced opportunity to identify secondary sources of background.

8.1.1 Problems to be Addressed

Although the Phase I proof tests (February and July 1979) demonstrated that fuel motion can be recorded with the CAIS in a simulated core disruptive accident, the signal-to-noise ratios obtained from coded images recorded on motion picture film were lower than anticipated. Therefore, an extensive series of calculations and subsidiary tests was conducted, leading to design changes in the system. These changes were tested for effectiveness in March 1980. Modification of the system after initial tests had been part of the development effort from its inception.

As earlier reports have outlined, the instrument observes, through a slot in the core, the gamma rays emitted by the fissioning fuel. The geometry is shown in Figure 8.1-1. The gamma rays are divided and introduced into two collimators within which coded apertures and vertical pinhole apertures modulate the beams before they strike the scintillator detectors. The visible light coded images from the detectors are observed with turning mirrors and image intensifiers, and the amplified output signals are recorded by high speed framing cameras. The instrumentation chamber is shielded by a massive shield fabricated of layers of water, steel, borated polyethylene, and lead.

The initial shield was effective enough to permit quality images of the test pin to be reconstructed from x-ray film placed at the detector plane, but the images of the pin recorded with the active system were much poorer. The prudent course for improving the performance of the active system was, therefore, to investigate as many explanations and solutions as were possible. The studies were broken down into the following five areas:

- Scintillator development
- Radiation transport calculations
- Problems with the main shield
- Scene beam studies
- Image reconstruction development.

The first four areas were presented in detail in the previous quarterly report. The principal findings and directions to be taken will now be summarized.

8.1.1.1. Scintillator Development

The scintillator studies indicated no dramatic differences in the calculated gamma ray and neutron responses of various scintillators as compared to x-ray film. However, ZnS activated with silver appeared to be less responsive to low energy gamma rays and neutrons than the standard CaWO_4 screen.

In the experiments, several alternative scintillator configurations were to be compared. The CaWO_4 x-ray intensifying screen (duPont High Plus) was planned for use again because its resolution and sensitivity have been the best in previous tests; a test of CaWO_4 powder was planned to investigate the possible influence of fast neutron-photon recoil interactions in the hydrogenous binder, and a BaSO_4 screen was to be used because of its theoretically lower response to thermal neutrons and soft gamma rays. Also, ZnS activated with silver was to be tested in three configurations: a duPont Cronex D intensifying screen, pure ZnS:Ag powder, and ZnS:Ag powder mixed in a glass binder low in hydrogen.

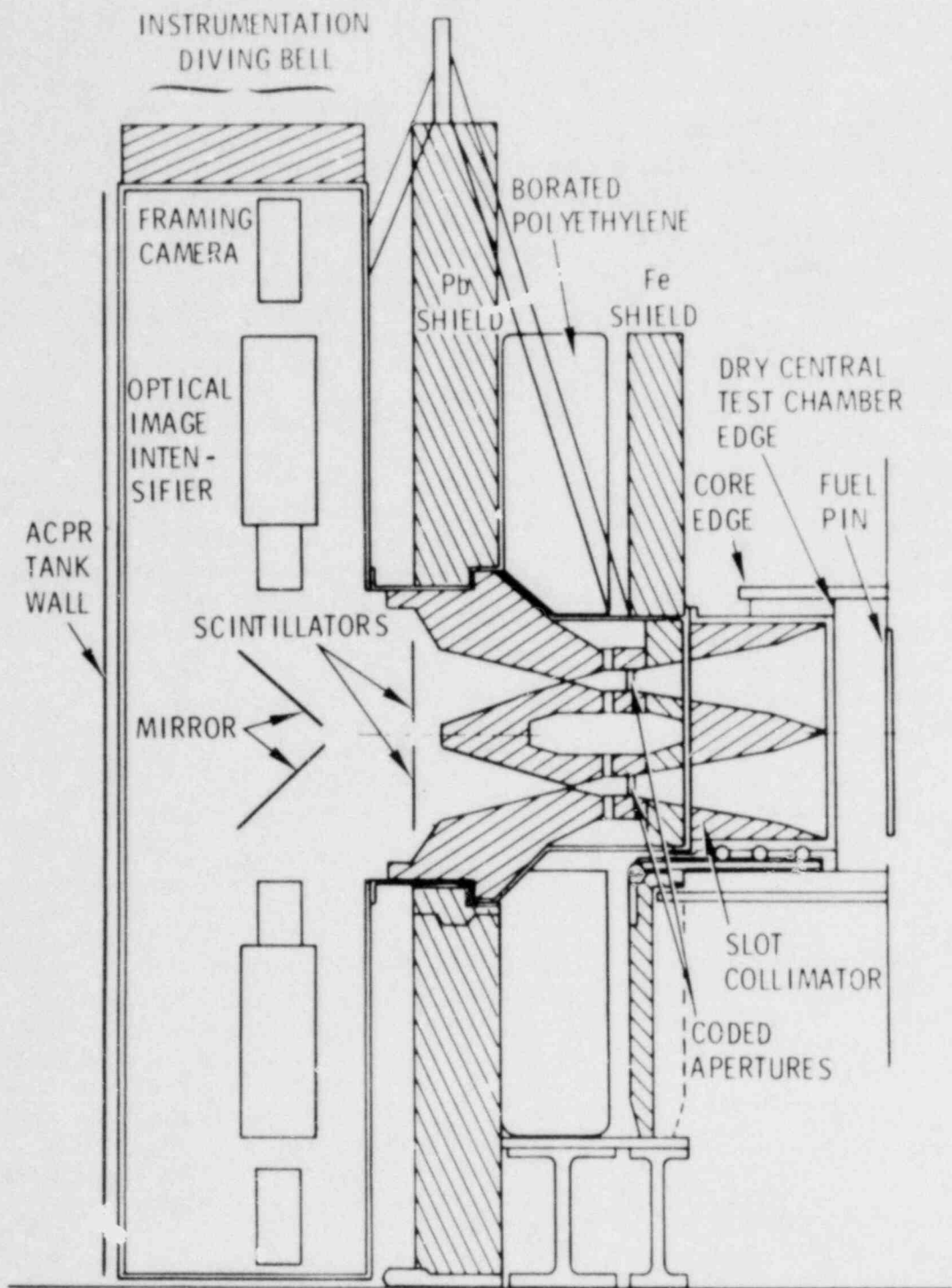


Figure 8.1-1 ACRR Fuel Motion Detection System

8.1.1.2 Radiation Transport

In the bulk shield, the transport calculations revealed that although thermal neutrons are strongly absorbed in the borated polyethylene shield, very thin layers of water will quickly re-establish the thermal flux.

8.1.1.3 Problems With the Main Shield

A comparison of the radiation inside and outside the collimated beams showed that the bulk shielding near the scintillators was inadequate.

A radiation sensitivity was observed in the image intensifiers and additional shielding had to be placed in their vicinity.

8.1.1.4 Scene Beam Studies

The LiH windows placed in the collimators near the core should be very effective in stopping low energy neutrons, but this material could also act as a secondary source of scattered radiation.

The backgrounds generated in the scene beam by the steel wall through which the pin is observed and by the lead wall behind the pin could be substantial.

Thin filters in the beams were not calculated to have a major effect on the backgrounds generated in the scintillator.

8.1.2 Modifications and Test Configurations

8.1.2.1 The Bulk Shield

Drawings of the altered shield configuration in the previous quarterly showed the details of the changes in the bulk shield. The main features were: (1) transferring the LiH window to a position just in front of the coded aperture, (2) embedding a multiple layer (boral and Cd) thermal neutron shield in the collimator behind lead and as a layer just before the final Pb shield in the main shield protecting the intensifiers, (3) filling up of the region around the detectors with lead and borated polyethylene, and (4) adding much more shielding in front of the image intensifiers.

8.1.2.2 Tests of Various Schemes to Reduce Scene Beam Background

Examination of the x-ray film coded images obtained in Phase I indicated that most of the background which arrived at the detectors through the

collimators actually passed through the narrowest portion of the collimation system at the boundary of the core test chamber. This is very important because it means that little radiation arrived from the collimator walls. Most of the scene background was generated within the field of view of the collimator and the sources to consider are therefore limited.

For the latest experiments, several configurations were prepared to determine the source of the backgrounds and to test methods of suppressing them. The major contributors might be the capture gamma rays, scattered gamma rays, inelastic gamma rays and scattered fast neutrons from the following objects:

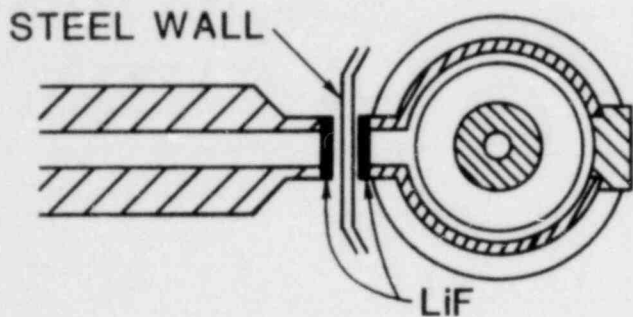
- The 0.635-cm-thick stainless wall of the experimental cavity
- The 1.4-cm-thick tube wall of the Be heat sink around the fuel pin containment vessel
- The Inconel containment vessel around the fuel pin (primarily nickel) with 0.127-cm-thick wall
- The 3.5-cm-thick lead shield block behind the fuel pin
- The reactor structure of the core behind the pin
- The Al canister walls.

Not all of these potential sources could be investigated thoroughly during this set of experiments because of physical and time constraints, but attempts to identify major noise contributors are described below. In a number of cases, the experiment was arranged so that two configurations with only one parameter changed could be compared during the same run with the same detector. (For example, if in one data channel, x-ray film observed a section of the fuel pin configuration in which the beryllium heat sink only covered part of the fuel pin, then the effect of the heat sink material could be evaluated by a comparison of the two regions.)

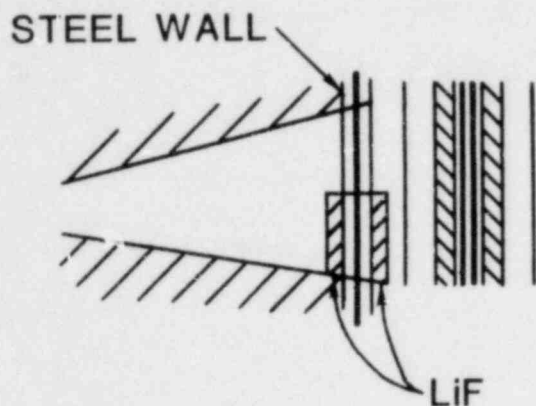
a. *The Stainless Steel Wall of the ACRR Test Chamber* — The possibility exists that the capture gamma rays generated in the steel could be significantly reduced by proper placement of a thermal neutron shield. In one channel, a 0.6-cm-thick layer of LiF was placed on each side of the steel. Figure 8.1-2 shows the configuration. The Li₆ in the LiF should strongly attenuate the thermal neutron fluence passing through it and reduce the gamma-ray production in the steel. Upon capture, the steel emits high energy gamma rays and the Li₆ does not. Geometrical constraints prevented the steel from being shielded from all directions.

b. *The Be Heat Sink* — In a manner similar to the example above, the Be was removed from a portion of the field of view (FOV) of one channel as Figure 8.1-3

shows. Any strong influence on background caused by the Be should be observable. The edge of the Be would be expected to be blurred by the 1.2-cm resolution of the aperture along the fuel pin.



a. Horizontal Cross Section of Canister and Collimator



b. Vertical Cross Section of Canister and Collimator

Figure 8.1-2 Configuration of Thermal Neutron Shield Sandwiching the Stainless Steel Window

c. *The Inconel Containment Vessel* — The vessel extended beyond the fuel and field of view at the top of the pin. Analysis of the coded image in the unfueled region might reveal whether a structure is present in the image which matches the geometry of the vessel. If the fuel itself causes a background to be generated in the vessel, then this background emission would probably not be observable beyond 0.5 cm from the fuel.

d. *The Lead Shield Block Behind the Pin* — A lead block placed behind the fuel pin has already been shown to reduce the scene background by a large factor, but further improvements are still believed possible. In the earlier experiments, the block contained 5% by weight of antimony. Since this material's capture cross section is 33 times larger than that of

lead, its elimination might reduce the capture gamma ray production by factors of 2 or 3. Runs were made in the ACRR using canisters with and without the antimony in the block to test its effect.

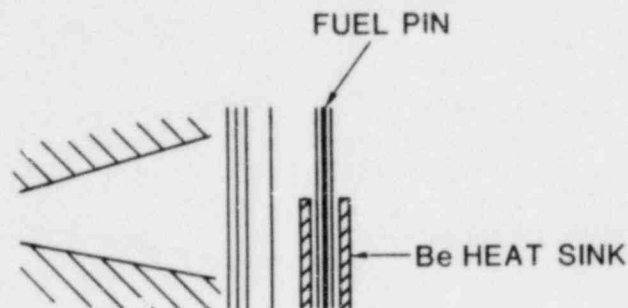


Figure 8.1-3 Geometry for Testing the Effect of the Be Heat Sink on the Scene Background

The experiment with a lead box surrounded by boral indicated that capture gamma-ray production in the lead can be important. Figure 8.1-4 shows how the lead block configuration was modified to permit shielding it from the thermal neutrons in the test section. About 0.6 cm of LiF powder was placed in front of and behind the block and some cadmium protected the sides. Although reason existed for believing that the emission from the lead would be reduced, the LiF itself might be an additional source of radiation because the gamma ray albedo from low Z elements tends to be much higher than for high Z elements.

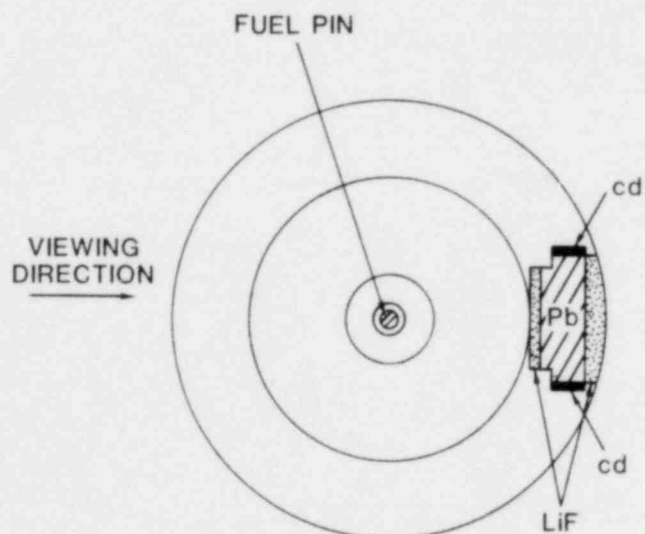


Figure 8.1-4 Thermal Neutron Shielding of the Pb Shield Block

e. *The Reactor Structure Behind the Pin* — The lead block behind the pin reduced the background from

the core. However, a block that is too thick might generate more background than it blocks out. One simple analysis indicated that 1.5 cm would be close to ideal. Two thicknesses were tried: 3.5 cm and 1.5 cm. (The 1.5 cm block was between layers of LiF so more than one parameter was changed between these tests.)

Directly behind the lead block is a fuel rod which can contribute background radiation. The effect of replacing that rod with a lead mockup was tested.

Whether this configuration can be used in maximum pulse experiments is not yet known because the removal of the fuel reduces the available reactivity and further divides the core.

8.1.3 Radiation Measurements

The necessity for having accurate radiation measurements at many locations in and around the detection system has become increasingly evident as the testing of the CAIS has progressed. This is because more detailed information is needed to provide the basis for additional improvements in performance. In particular, although the detector materials and components are most sensitive to gamma rays, local neutron reactions have been found to generate much of the background gamma-ray fluence. Therefore, knowledge of the spatial and energy distributions of the neutrons is needed to devise methods for reduction of the gamma ray backgrounds.

The fluences to be measured in the detector vicinity are much lower for both neutrons and gamma rays than those previously encountered at this work location. In the instrumentation chamber of the CAIS, representative doses of 10^{-2} to 10 rads are encountered. This is in the range of interest for health physics monitoring of employee exposures. Two types of thermoluminescent detectors (TLDs) normally used for personnel dosimetry were obtained, one of which is more sensitive to neutrons (particularly thermal neutrons). Typically, three chips of each type (for statistical accuracy) are inserted into a small plastic vial which is placed at a location of interest. In some cases, chips are placed in cadmium or boron covered cases so that the thermal and slow neutron response can be separated from the total response.

The primary difficulty encountered with the TLD measurement of neutrons is that the neutron response is a very strong function of energy and the neutron spectrum at the detectors is not well known, although the neutron spectrum has been assumed to be the same as that measured in the experimental cavity.

Because of the uncertainty in the neutron response of the TLD, additional neutron dosimetry packages were assembled. The dosimeters in these activation packages are usually exposed at much higher levels because they are read by counting individual gamma rays from activation decays, and the count rates recorded from these experiments were often very low. In a given package, there were four types of detector foils: sulphur pellets (threshold of 3.2 MeV), Indium foils (1 MeV threshold), and two gold foils for thermal and epithermal measurements. In each case one of the gold foils was encased in cadmium. Figure 8.1-5 shows the geometrical arrangement. Since there may be significant changes in the neutron fluence over a distance of a few centimeters (as might be expected in the beam) the measurements may not be entirely consistent. The inaccuracy caused by spatial separation of dosimeters is greatest in the gold foil pair. During the assembly of each test, the location of each radiation detector was recorded on a map of the instrumentation chamber.

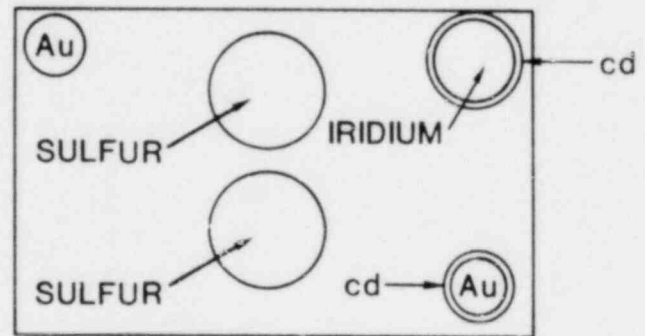


Figure 8.1-5 Neutron Dosimeter Package Layout

8.1.4 Conduct of the Experiment

During the period in which the new shielding hardware and scintillator structures were being prepared, several handling equipment changes were made so that the safety would be increased and the turnaround time between experiments would be shortened. Briefly these included extended bellows tubes which carry the instrumentation cables so that they could be mounted directly to an instrumentation rack, stronger and simpler rigging, a removable support device for the bellows during assembly, rearrangement of the scintillator support structure and mirror mounts so that rapid changes in detector structure could be made through the rear access door (rather than by separating the aperture chamber from instrumentation chamber), altered support structure for the slot collimator, modified structures in the

carts used to support the system outside the reactor, and enlarged access doors to the instrumentation. These changes permitted as many as three complete system assemblies, exposure periods and retrievals from the reactor in 1 day. This capability was important because in a period of 9 reactor days 15 runs were made.

The run schedule used to guide the experiments was subject to some revision part-way through the test series because of time constraints and some re-ordering of priorities. Specifically, two runs were deleted because the effect of antimony in the rear block appeared to be of secondary importance.

In a typical run, the dosimetry packages were mounted within the chamber, the appropriate scintillator or x-ray film detectors were bolted in, the film was loaded into the cameras and the bulkhead doors were sealed. The instrumentation aperture chamber combination was lowered by crane and guided into position within the shield structure. Then a checkout procedure was followed to make certain that the electronics were ready, that cooling air was flowing through the intensifiers, that the film in the cameras was advancing, etc. For these tests, because establishment of the signal-to-background ratio was the primary objective, only steady-state reactor runs were made. In most cases the energy deposited in the core was 50 MJ per run. For a 50-MJ run, the reactor power was operated at 50 kW for 10³s. The cameras used were Nikon reflex 35-mm cameras which have a remote triggering and film advance capability. During a run, sets of 20 to 36 exposures were made for different exposure times and different image intensifier gain settings.

8.1.5 The Results of the Experiments

The results and conclusions which can be drawn from the tests at this time are only preliminary in nature because thorough analysis will take several more months. This is partly because of the immense amount of data obtained. Approximately 800 fuel pin coded images were accumulated in the 9 days of experimenting along with 1200 exposed TLDs and about 40 neutron dosimetry packages. Each film frame must be digitized and processed extensively before an optimized reconstructed image is obtained. Similarly, the 25 x-ray film recorded images must be processed.

The new shield structure brought about a great improvement in the effectiveness of the bulk shield. During the Phase I experiments (conducted in 1979), the ratio of the total gamma ray dose in the direct beam to that dose just outside of the beam was about

2.5. In the latest series, that ratio is about 15. Therefore, the influence of the radiation penetrating the shield or backscattering from the structure behind the detectors is small at the detector plane. This same factor of 15 was found in the fast neutron dosimetry results ($E > 1$ MeV). The thermal neutron fluence appears to have been reduced by at least an order of magnitude (uncertain because of poorer data on the earlier experiments) and appears to be 1/90 as intense as the fast neutron fluence in the beam. Most of this improvement appears to be caused by the multiple layer thermal neutron shield which was placed just outside the lead surfaces. Evidently a large fraction of the former background was generated by thermal neutron capture, in everything around the scintillators. This includes the lead portions of the shield.

The x-ray film exposures taken at the detector plane are very much improved. Because of their linear response and high spatial resolution, they show many important features in the coded images which indicate the sources of other backgrounds. Figure 8.1-6 is a photograph of the coded image obtained at the upper channel in run number 10. The fuel visible in this channel is 93% enriched. The boundary where the top of the fueled region of the pin ends is very evident, and the coded image of the fuel itself stands out clearly. Figure 8.1-7 shows a density scan along the axial direction within the central zone. The step where the fueled region begins is pointed out in the graph. This trace also indicates the magnitude of the fission density variation along the length of the pin. This variation is caused by the thermal neutron flux profile in the core and by aperture transmission variations. Since the upward slope of the exposures on each side of the step are the same, it is easy to extrapolate the background into the region where the fuel is present. The difference in density between the total signal and the background at the same axial position is about $\Delta D = 0.45$. Figure 8.1-8 displays density traces across the coded image at two different radial positions: one above the fuel and one through the fuel region. The lack of higher spatial frequency structure in the background trace is very evident. The form of this background is easy to explain and is quite important. It first consists principally of one trapezoidal structure (which represents the convolution of the opening in the front collimator with the whole coded aperture). The high frequency zones are smeared out because the collimator opening is wide. Outside the first zone, the average transmission of the aperture is about 50%. The second trapezoidal structure that rides on the first is the convolution of the first open zone of the coded aperture with the front collimator. The important

point is that most of the scene background can be accounted for by this structure implying that down-

stream filters and collimator walls contribute very little to the scene background.

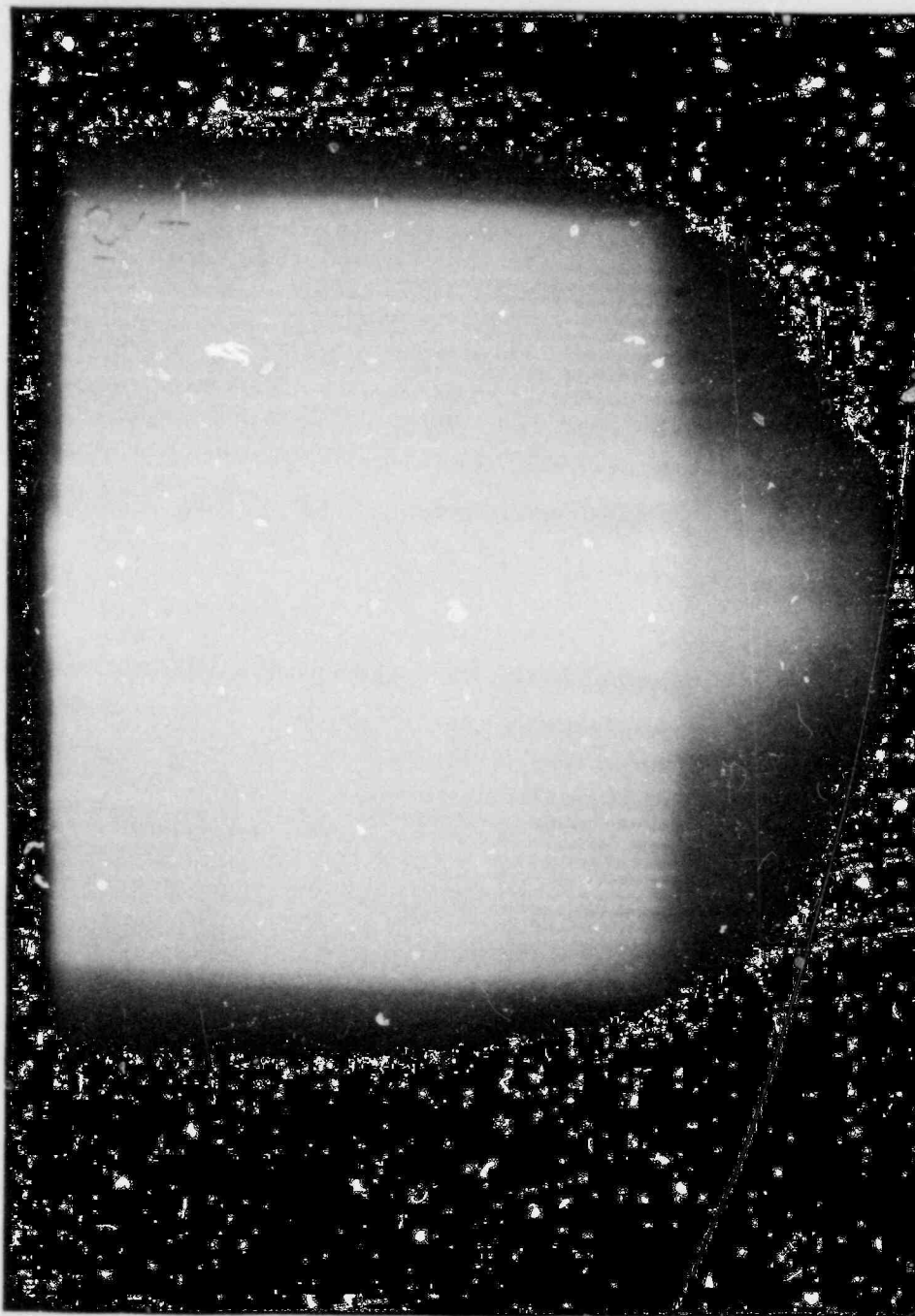


Figure 8.1-6 Photograph of the Coded Image, Upper Channel, Run 10

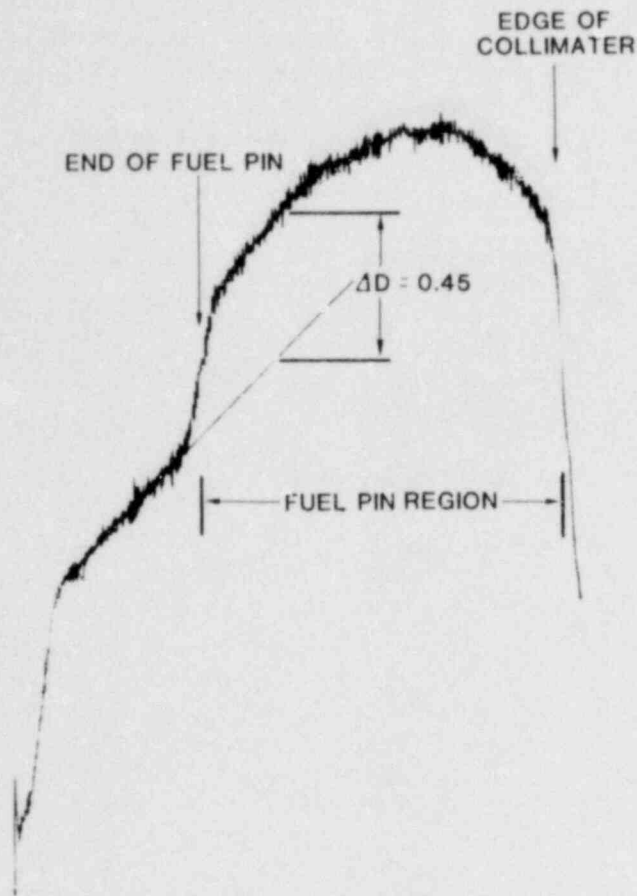


Figure 8.1-7 Axial Scan Along Central Zone of Coded Image

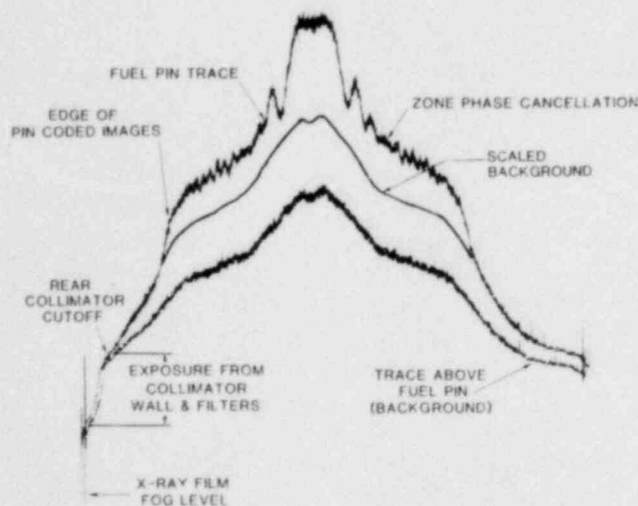


Figure 8.1-8 Radial Scan of the Coded Image

The trace in the fuel region shows structure in the high frequency regions indicating a source with

small dimensional characteristics. This structure can be seen more clearly if the background is subtracted from the total signal by scaling the background trace up until it is $\Delta D = 0.45$ below the total signal as shown in the figure. The signal-to-background ratio under the central peak is $(D_T - D_B)/D_B = 0.23$, almost a factor of 4 higher than that achieved during the Phase I test of 1979. Only part of this increase is caused by the higher enrichment of the pin (93% vs 20%). The reason is that the range of thermal neutrons in both materials is such that most of the neutrons will be absorbed in traversing the pin. The total brightness of the two enriched pins should be close to the same but because most of the fissioning in the highly enriched pin takes place on the surface, the radial structure of the coded image should be different for the two pins if the aperture has the resolution to see it.

The question of differences in radial profile can be investigated even without reconstructing the image. Examination of the coded image in Figure 8.1-6 and the traces in Figure 8.1-8 reveal that the zone shadows disappear at about the third open zone and then reappear as if the coded images from two line sources separated slightly in space were interfering with each other. The geometrical analysis is quite simple but will not be illustrated here in detail. It turns out that if two sources are separated by 3.5 mm their coded images will shift by one full zone at about the 12th zone radius in the code. They will, therefore, add in phase and the zones in this region will be enhanced as these pictures show. This is approximately the separation one finds would exist between the maximum exposure from limbs of a tube shaped source observed from the side if the fissions are concentrated within about 1 mm of the surface in a 5-mm-diameter pin. Thus, a spatial resolution, in the fundamental aperture-detector system, of less than 2 mm in the reactor geometry is demonstrated by this example. The way in which this resolution is carried through the rest of the recording system will depend on the results of detailed analyses of the active system data. Although a more detailed discussion will have to await the next quarterly report, a few general comments can be made at this time about the data acquired with the active system.

- The signal-to-noise ratio in the recorded images has improved by a large factor, but the precise value of the improvement is hard to determine because of the poor data obtained in 1979.
- The CaWO_4 scintillator, commercially made by duPont, still appears to be the best scintillator. Although this scintillator was expected to be

more sensitive to neutrons than ZnS:Ag because of capture in the tungsten, the effect appears to be small because of the large reduction in thermal neutron fluence achieved with the new shielding. In addition, the high density of CaWO_4 compared to ZnS:Ag seems to insure higher resolution in the CaWO_4 because of the shorter range of secondary electrons.

- The partial shielding from thermal neutrons afforded by the steel containment wall through which the fuel pin is observed did not provide an obvious improvement in the signal to background ratio.
- The Be heat sink around the fuel pin does not appear to add a significant background to the "scene" beam.
- Removal of the antimony from the lead behind the pin does appear to reduce the scene beam background. The possibility of using lithium mixed with lead is being investigated because of two potential advantages. First, a 50% x 50% mixture by atomic number of these two materials can have a higher melting point than either material alone, and second, the lithium can absorb thermal neutrons without emitting gamma rays in the process.
- The LiF protected rear block appears to have been close in performance to the thick pure lead block.
- A fuel pin coded image shows clearly on the films even with exposures so short that they would correspond to an exposure time during the peak of the PBE pulse (200 MJ in 10 ms) of about 3 μs . Shorter exposures appear to be degraded by inadequate photon counting statistics in the scintillator.
- At the detector plane the principle background is coming from the scene beam through the front collimator. Therefore improved geometry and materials must be sought for the containment and the canister. If steel and nickel could be replaced by zirconium in the scene beam, the scene background would probably be much smaller.
- The intensifier is susceptible to bulk shield radiation leakage that is unsymmetrical and appears to come from the side. The rigging and instrumentation chamber have been designed to accommodate more side shielding.
- When the reactor is turned off, many delayed gamma rays remain which are emitted by the fuel pin for a few minutes. Fuel pin images taken with

the active system at that time have a far lower background relative to signal (as was the case in 1979). This result again confirms that except for film grain noise in the recording film the largest backgrounds are generated by neutrons.

8.1.6 Noise Sources

If improvement in the system is to continue, the sources of background and noise must be identified and quantified. The active recording system, because of its electro-optical image intensifiers and the use of photographic film has different noise characteristics from x-ray film. The source of these differences and their effect on CAIS performance will be discussed in the next section.

8.1.6.1 Details of Noise Measurement

To determine the ultimate measurement detectivity for the active detector system used in the CAIS, a series of experiments was performed.⁽⁸⁻¹⁾ These experiments were designed to separate the noise contributions of the image intensifier, the film grain noise, and the quantum noise. This was done by first exposing a test film with a step wedge illuminated by a 1-ms pulse of light which was spectrally filtered to closely match the emission from a P-11 phosphor. The film used was Kodak Tri-X pan developed in HC110 Dilution A for 6 min at 20°C. Next, the developed step wedge was digitized with a Perkin-Elmer PDS microdensitometer using a 50- x 50-m aperture. Mean density and density standard deviation were calculated from 200 data samples in each density step. Next, a series of exposures was taken off the P-11 output phosphor of an EMI 9912 four-stage image intensifier tube illuminated by a uniform source of optical radiation at the input. The tube potential was 23 kV, corresponding to a gain of 2.3×10^4 . The exposure time, film, and processing were the same as for the film alone. These films also were scanned with a microdensitometer and the density deviation calculated. Finally, to determine the uncertainty contributed by quantum statistics, the total active detector system was illuminated by a 10-MeV bremsstrahlung source providing a source of x-rays whose spectrum closely approximates the gamma-ray spectrum emitted by fissioning fuel. The x-ray beam was incident on the 0.75-mm-thick CaWO_4 scintillator providing a uniform illumination at the image intensifier. Once again the output was photographed, and the film developed and scanned using the same procedures as before.

Figure 8.1-9 shows the experimental results obtained with an intensifier potential of 23 kV (2.3×10^4

gain). For each film type, a characteristic curve was determined from the data so that density deviation as a function of log exposure is plotted. The image intensifier-film combination (boxed data) is only slightly more noisy than film alone (solid line). Other tests showed that at the maximum gain of 10^6 intensifier noise does become significant. Data obtained when the whole system was exposed to x-radiation also shows good agreement with the film-only situation (even though part of the data was taken for photons passing through 200 mm of lead). The major conclusion to be drawn from these tests is that the most significant noise source for the active detection system operating at a gain of 2.3×10^4 or less is film grain noise.

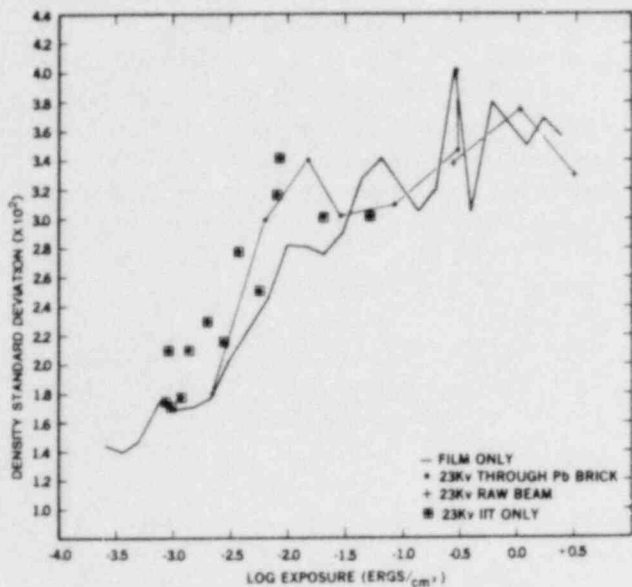


Figure 8.1-9 Density Deviation vs Log Exposures for Three Primary Noise Sources in the CAIS Active Detector System

In the fuel motion tests discussed earlier in the paper, a low gain was used (3×10^3) and a smaller scanning aperture was used ($12.5 \times 66.7 \mu\text{m}$) to scan the film. Although the film used was different, its granularity is comparable to that of Tri-X (0.040 for Double-X in D-19 vs 0.36 for Tri-X at $\text{Log } E = -1.5$ scanned with $50 \times 50 \mu\text{m}$ aperture), so for that experiment the major noise source was definitely film grain noise.

To further explore the impact of film grain noise, a comparison of the electro-optical detection system and x-ray film can be made. In x-ray film the net optical density responds linearly to the energy deposition; i.e.,

$$D = KE \quad (8.1)$$

where D is the net density change above fog; K is a constant; and E is the energy deposited in the film. For an intensified system, the film in the high-speed camera is exposed by optical quanta and in this case the optical density is related to energy deposition in the scintillator by

$$D = \gamma \text{Log } E \quad (8.2)$$

assuming operation in the linear region of the film characteristic curve. In this expression D is the measured film density; γ is the slope of the $D - \text{Log } E$ curve in the linear region; and E is the light energy incident on the film, proportional to energy deposited in the scintillator. Because of this difference in the relationship of E to D , the effective contribution of one significant noise source, film grain noise, is quite different. In the case of x-ray film a ΔD_G caused by film grain produces an equivalent ΔE which is given by

$$\Delta E = \frac{\Delta D_G}{K} \quad (8.3)$$

In the case of photographic film exposed to light, the equivalent ΔE caused by a film grain ΔD_G is given by

$$\Delta E = 2.3 E \frac{\Delta D_G}{\gamma} \quad (8.4)$$

or

$$\frac{\Delta E}{E} = 2.3 \frac{\Delta D_G}{\gamma} \quad (8.5)$$

The Nutting formula relating density deviation to mean density indicates a square root dependence while other investigators indicate a dependence of as low as the cube root.⁽⁸⁻²⁾ This implies that $\Delta E/E$ is a slowly increasing function of deposited energy, thus the percentage uncertainty in E increases only slightly as a function of deposited energy. In the case of x-ray film, the film grain noise is of less concern when used with the CAIS because the resolution element is larger and a large effective scanning aperture can be used ($300 \times 400 \mu\text{m}$). Thus, for x-ray film quantum fluctuations would be expected to be the major noise source and so the signal-to-noise ratio should increase as the energy deposited in the detector.

8.1.6.2 The Effect of Additive Background

Another consequence of the logarithmic response of film to optical radiation is the decrease in signal-to-noise ratio with increased additive background. For a situation with a uniform additive background the density is given by

$$D_{S+B} = \gamma \text{Log}(E_S + E_B) \quad (8.6)$$

where E_S and E_B are the signal and background light energies, respectively. The density change attributable to the signal may be found by subtracting the density due to the background alone or

$$\Delta D_S = \gamma \text{Log}(E_S + E_B) - \gamma \text{Log} E_B \quad (8.7a)$$

$$= \gamma E_B \left(1 + \frac{E_S}{E_B}\right) - \gamma \text{Log} E_B \quad (8.7b)$$

$$= \gamma \text{Log} \left(1 + \frac{E_S}{E_B}\right) \quad (8.7c)$$

Assuming that film noise is the dominant noise source as was indicated in the previous section, the signal-to-noise ratio is given by

$$\text{SNR} = \frac{\Delta D_S}{\Delta D_G} = \frac{\gamma \text{Log} \left(1 + \frac{E_S}{E_B}\right)}{\Delta D_G} \quad (8.8)$$

where ΔD_G is the density deviation due to film grain. For the fuel motion test using Double-X film developed in D-19 developer and scanned with a 12.5- x 67- μm aperture, a typical measured value for D_{FG}/γ was 0.06. Thus, to obtain a signal-to-noise ratio of 1, the ratio of signal-to-background must be 0.15 (corresponding to a background level 6.75 times the signal level). Theoretical estimates of the signal-to-background ratio for the shielding geometry used in the first prototypic fuel motion tests are about 0.05, yielding a SNR of 0.35.

Two ways of improving this situation are to reduce the film grain level or reduce the background present caused by shield penetration. The film grain noise may be reduced by changing film or scanning with a bigger aperture. For example, by using Tri-X film developed in HC110 Dilution A and scanned

with a 50- x 50- μm aperture ($\Delta D_G/\gamma = 0.036$) a signal-to-background ratio of 0.086 could be tolerated ($E_B = 11.6 E_S$). Keeping the same film as before but increasing the signal-to-background ratio by a factor of 2 from 0.15 to 0.30 would result in an increase in SNR from 1.0 to 1.9. Both methods will be used in future tests to increase signal-to-noise ratio when possible. In experiments requiring a time resolution of less than 200 fr/s, a 35-mm framing camera will be used and the film will be scanned with a larger aperture to provide less film grain noise. Modifications have already been made to the bulk shielding which would theoretically reduce the nonscene background by about one third and should provide a 60% increase in SNR.

The scene and nonscene areas are both equally affected by the above noise sources. Additional sources of background within the scene, such as penetrating gamma rays from the reactor core behind the fuel pin being imaged and scattered radiation from the containment structures, are also present. These sources may have a significant effect on the total signal-to-noise ratio in the reconstructed image. This is because a broad low-level background which fills the field of view acts the same as a broad source in reducing the signal-to-noise advantage of the coded aperture over a pinhole camera of comparable resolution. For this reason the inclusion of additional shielding within the area around the test fuel pin is being investigated in an effort to reduce these background sources.

8.1.7 Future Plans

The CAIS is now being prepared for a full-scale PBE test to be conducted in August of 1980 with a 14% enriched pin in stagnant sodium. The intention at this time is to use phase-locked cameras at 500 fr/s and two new image intensifier tubes which have fewer stages of amplification. Fewer stages in the tube will mean higher resolution and contrast in the images and is permitted because of the high light output of the CaWO_4 scintillators. Additional shielding which has been modified will be placed around the intensifiers.

Major calculational and experimental efforts will continue to be directed toward identifying sources of and reducing scene beam backgrounds. The members of the IEFM task group will be consulted to assure that the sodium loop design is compatible with the CAIS.

8.2 ACRR Status

(T. R. Schmidt, 4451)

During this quarter, modification of the ACRR continued with the objective of improving its performance in several ways including giving it a capacity for increased power levels, faster control rod drive speeds, and enhanced pulse shaping capability. This modification was not only applicable to the reactor itself, but also involved installing and testing several pieces of auxiliary equipment for programming ACRR operating modes.

The programmable transient rod withdrawal equipment was installed and the zero-power mechanical and functional tests were performed.

The new shield plug, incorporating a hole through the center for access to experiments such as the fuel dynamics experiments located in the central loading tube, was installed and a radiation survey conducted.

Over the end-of-year shutdown, fuel storage holes up to 32 ft deep were installed in the floor of the ACRR high bay to accommodate storage of full length PBE and DBE experiments. The holes are aligned with the penthouse crane so that experiments may be removed from the reactor and placed in storage by remote control.

The hardware and B_4C poison for the previously installed new high-worth transient rods were received.

The preoperational survey by the DOE Albuquerque Operations Office on the Transient Rod Withdrawal (TRW) mode was completed for the hard-wired rod-drive programmer.

A new external cavity (used primarily for DOE weapons experiments) was installed and tested in February. It provides a 38-cm-diameter dry cavity next to the "flat" of the core (same side as the CAIS system). The cavity system consists of a 16-in. OD aluminum tube 7.9 m long which extends to the surface of the pool, a lead ballast, and a composite shield plug. Ten additional fuel elements were added to the core on the side toward the cavity to enhance the leakage fluence. The consequence of the additional fuel was to reduce the worth of the transient rod bank by \$0.15.

The initial characterization of the programmed transient rod withdrawal (TRW) mode was performed under control of the eight-segment hard-wired programmer. The initial attempt at a high-power square wave resulted in a power level of 37 ± 5 MW for 4 s with an energy release of 150 MJ.

References for Section 8

- 8-1 K. T. Stalker, L. M. Choate, and L. D. Posey, "The Potential for High Speed X-Ray Cinematography as a Fuel Motion Diagnostic for Safety Test Facilities," *Proceedings of the International Meeting on Fast Reactor Safety Technology*, Seattle, WA, August 19-23, 1979, Vol. 5, kp. 2270.
- 8-2 F. Naderi and A. A. Sawchuck, "Estimation of Images Degraded by Film-Grain Noise," *Appl. Opt.* 17:1228, 1978.

DISTRIBUTION:

U. S. Nuclear Regulatory Commission
(380 copies for R7)
Division of Document Control
Distribution Services Branch
7920 Norfolk Avenue
Bethesda, MD 20014

U. S. Nuclear Regulatory Commission (4)
Division of Reactor Safety Research
Office of Nuclear Regulatory Research
Washington, DC 20555
Attn: C. N. Kelber, Asst Dir
Advanced Reactor Safety Research
R. T. Curtis, Chief
Analytical Advanced Reactor Safety
Research, ARSR
M. Silberberg, Chief
Experimental Fast Reactor Safety
R. W. Wright
Experimental Fast Reactor Safety

U. S. Department of Energy
Office of Nuclear Safety Coordination
Washington, DC 20545
Attn: R. W. Barber

U. S. Department of Energy (2)
Albuquerque Operations Office
P. O. Box 5400
Albuquerque, NM 87185
Attn: J. R. Roeder, Dir
Operational Safety Div
D. K. Nowlin, Dir
Special Programs Div
For: C. B. Quinn & D. Plymale

University of Michigan
Nuclear Engineering Dept
Ann Arbor, MI 48104

General Electric Corporation (7)
310 De Guigne Drive
Sunnyvale, CA 94086
Attn: J. O. Bradfute, Mgr, Dynamics and Safety
R. A. Meyer, Mgr, Analytical Engineering
S. M. Davies, Mgr, Conceptual Design Study
J. W. McDonald, Mgr, Containment &
Radiological Evaluation
N. W. Brown, Mgr, Licensing & Systems Eng.
M. I. Temme, Mgr, Safety Criteria &
Assessments
K. H. Chen, M/C S-54

K Tech Corp
901 Pennsylvania NE
Albuquerque, NM 87110
Attn: W. Tarbel

Projekt Schneller Brueter (4)
Kernforschungszentrum Karlsruhe GMBH
Postfach 3640
D75 Karlsruhe
West Germany
Attn: Dr. Kessler (2)
Dr. Heusener (2)

UKAEA (3)
Safety and Reliability Directorate
Wigshaw Lane
Culcheth
Warrington, WA3 4NE
England
Attn: H. J. Teague (3)

Reactor Fuels Group
AERE Harwell
Oxfordshire, OX11 0RA
England
Attn: R. G. Bellamy

UKAEA - Atomic Energy Establishment
Reactor Development Division
Winfrith, Dorchester
Dorset
England
Attn: R. G. Tyror, Head

Power Reactor & Nuclear Fuel (3)
Development Corporation (PNC)
Fast Breeder Reactor Development Project (FBR)
9-13, 1-Chome, Akasaka
Minato-Ku, Tokyo
Japan
Attn: Dr. Mochizuki
Dr. Watanabe (2)

Joint Research Centre (2)
Ispra Establishment
21020 Ispra (Varese)
Italy
Attn: R. Klersy
H. Holtbecker

W. E. Nyer
P. O. Box 1845
Idaho Falls, ID 83401

DISTRIBUTION: (cont)

1100	C. D. Broyles Attn: J. D. Plimpton, 1110 T. L. Pace, 1120 G. L. Ogle, 1125	4424	D. C. Williams
1537	N. R. Keltner	4425	W. J. Camp
1537	R. U. Acton	4425	E. D. Bergeron
1537	T. Y. Chu	4425	W. M. Breitung
1550	F. W. Neilson Attn: O. J. Burchett, 1552 J. H. Gieske, 1552	4425	P. Briscoe
2150	C. B. McCampbell	4425	R. J. Lipinski
3434	B. N. Yates	4425	K. K. Murata
4000	A. Narath	4425	M. L. Schwarz
4231	T. P. Wright	4425	A. Suo-Anttila
4400	A. W. Snyder	4425	M. F. Young
4410	D. J. McCloskey	4426	G. L. Cano
4420	J. V. Walker (5)	4426	J. G. Kelly
4420	Secretary (7)	4426	H. L. Scott
4421	R. L. Coats	4426	K. T. Stalker
4421	J. E. Gronager	4426	W. H. Sullivan
4421	G. W. Mitchell	4426	S. A. Wright
4421	C. Ottinger	4441	M. L. Corradini
4421	J. B. Rivard	4450	J. A. Reuscher
4422	D. A. Powers	4451	T. R. Schmidt
4422	R. M. Elrick	4452	M. F. Aker
4422	J. E. Smaardyk	4723	D. O. Lee
4422	D. W. Varela	5500	O. E. Jones
4423	P. S. Pickard	5530	W. Herrmann
4423	A. C. Marshall	5534	D. A. Benson
4423	D. A. McArthur	5541	W. L. Luth
4423	K. O. Reil	5800	R. S. Claassen
4424	M. J. Clauser	5820	R. E. Whan
4424	E. R. Copus	5822	K. H. Eckelmeyer
4424	F. E. Haskin	5830	M. J. Davis
4424	J. T. Hitchcock	5835	C. H. Karnes
4424	P. J. McDaniel	5846	E. K. Beauchamp
4424	J. P. O'Connell	5846	R. A. Sallach
4424	F. W. Sciacca	8214	M. A. Pound
4424	M. E. Senglaub	3141	L. J. Erickson (5)
		3151	W. L. Garner (3)
			For: DOE/TIC (Unlimited Release)
		3154-3	C. Dalin (25)
			For: NRC Distribution to NTIS